UNIVERSITAT DE BARCELONA

Molecular mechanisms underlying radioresistance of glioblastoma initiating cells

Elisabetta Stanzani

Doctoral program in Biomedicine
2016

MOLECULAR MECHANISMS UNDERLYING RADIORESISTANCE OF GLIOBLASTOMA INITIATING CELLS

Doctoral thesis
submitted by
ELISABETTA STANZANI

Thesis conducted under
the guidance of
Dra. AVELINA TORTOSA I MORENO

Dra. FINA MARTÍNEZ-SOLER

Dra. PEPITA GIMÉNEZ-BONAFÉ

Unitat de Fisiologia del Departament de Ciències Fisiològiques
Campus Ciències de la Salut de Bellvitge
Facultat de Medicina i Ciències de la Salut

Dedicated to those who did not lose hope
facing research frustrations and failure
and still keep seeking the objective truth
with passionate and creative soul.

ACKNOWLEDGEMENT

RINGRAZIAMENTI

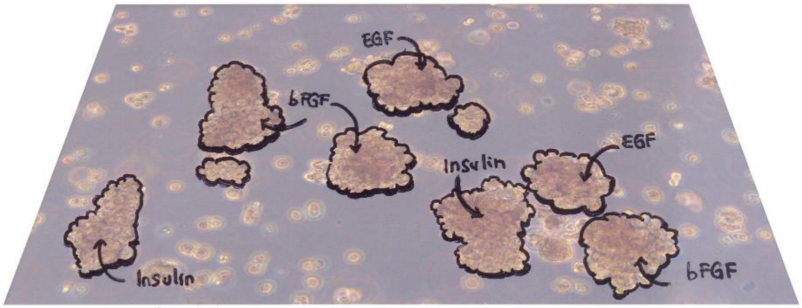

AGRADECIMIENTOS

Tal y como las neuroesferas no crecerían sin los suplementos del medio *Stem*, esta tesis no existiría si yo no hubiera tenido el soporte de algunas personas… Con este apartado quiero agradecer mis *EGF*, *bFGF* e *Insulin*.

Similarly to the neurospheres that would not grow and proliferate without the supplements of the *Stem* media, this thesis wouldn't be without the endorsement of several people… With this section I want to thank my *EGF*, *bFGF* and *Insulin*.

Allo stesso modo in cui le neurosfere non potrebbero crescere senza i supplementi al terreno di coltura *Stem*, questa tesi non potrebbe esistere senza l'aiuto di alcune persone… Con questo capitolo vorrei ringraziare i miei *EGF*, *bFGF* e *Insulin*.

Primero de todo quería agradecer a mis jefas. Avelina, gracias para haberme dado la oportunidad de compartir contigo estos años de doctorado y por haberme dejado experimentar y seguir mis teorías. Fina, gracias para haberme apoyado y ayudado siempre en todo. Pepita, gracias por haber creído en mí y por darme la gran oportunidad de sustituirte en las clases... Ha sido una impresionante experiencia y te lo agradezco.

Otra persona que tengo que agradecer es Joan. Sin ti no hubiera podido acabar el doctorado con serenidad y no hubiera podido terminar mucha de la parte experimental. Tu soporte absolutamente inesperado ha hecho que mis últimos dos años aquí fueran los que han sido.

Gracias a Ruth y a Roser, que me acogieron en el equipo y me enseñaron las bases. Quiero agradecer también todos los demás estudiantes que han pasado por el laboratorio a lo largo de estos años. Con ellos he aprendido a enseñar y a vivir el labo con mucha alegría. Gracias a Sedu, con tu *black humor* y tus tantos porcientos. Siento mucho que las cosas no hayan ido como tu querías. Te he echado de menos en este tiempo. Gracias a mis chicas guapas Aneru, Karen, Teresa, Lidia, Verónica, y gracias en especial a ti, Aleix. No hubiera podido pedir un compañero mejor para los últimos meses de tesis. Eres genial y te deseo todo lo mejor de aquí en adelante.

Y ahora mis grandes compañeras, mis gordikukins. Habéis hecho de mi doctorado una experiencia tan espectacular, tan divertida que no me la podía ni imaginar en mis mejores sueños. Lo de hablar de cosas muy personales en *open air* no es exactamente lo mío, pero espero haberlo transmitido cada día… Pero sí, quiero agradeceros por lo que me habéis enseñado a nivel profesional, porque creo que podría no es tan obvio. Beuki, eres la persona más curiosa que he conocido en mi vida, tu sed insaciable de conocimiento es algo que no tiene precio y espero de haberla absorbido un poco. Petrushi, sweet Petrushi. You have taught me to be accurate in all thing I'm doing. Most of the time that I'm sitting for planning a new experiment I'm asking to myself "How would Petrushi do it?", because for sure is the right way. Cris, a parte del catalán, que claro sin ti estaría todavía al nivel *m'agrada, així, això, de res, adéu*… quiero agradecerte tu energía, por haberme enseñado a no tener miedo de nadie, y que sí, nadie nos puede pisar.

Gracias también a los profes, y en particular a Francesc y José Carlos, por los consejos y por ser fuente de inspiración. José Carlos gracias también por haberme guiado en el mundo del metabolismo y haberme hecho una apasionada del tema. Gracias también a Aurea y Alejandro. Gracias por haberme ayudado en todas las maneras posibles con las clases.

Gracias a Ene y Joan, os echo y os echaré mucho de menos. Gracias para los muchos momentos bonitos. Ha sido un encanto compartir el tiempo con vosotros y espero que de verdad nuestras vidas vuelvan a cruzarse muchas veces. Como no agradecer al gran equipo cerveza, lástima que hemos tardado tanto en montarlo… Sonia, José, Helga, Tai, Susana, Ana, Carol. Ha sido un placer compartir con vosotros estos años. Aun en los peores días, *you made my day!!!*

Gracias también a Ana Mari y Dani. Gracias para las risas, los consejos y el apoyo. No sabéis lo bonito que es venir a hacer bolsitas a vuestro labo. ¡Bendito el día que se estropeó nuestra maquina!

Gracias a José y a los técnicos del servicio de radioterapia por haber conseguido siempre compaginar pacientes y células.

Y ahora mi compañera de doctorado lejana. Gracias Vero, me ha encantado compartir contigo esta experiencia, y no me lo puedo creer que de verdad terminamos la tesis con un par de días de diferencia…

Grazie alle mie amiche scientifiche di sempre: Alice e Benny. Per quanto ci si veda poco, so di per certo che alla prima occasione ci sarà sempre così tanto da dirsi da riempire le ore. Il vostro incoraggiamento e la possibilità di confrontarmi con voi sono sempre stati qualcosa di prezioso, soprattutto perché credo fermamente nell'obiettività della vostra opinione. Ali, il tuo aiuto è stato fondamentale, senza la tua visione clinica non sarei mai riuscita a fare luce sul maledetto LQM. Grazie, grazie, grazie.. *y hasta siempre!!!!*

Grazie ai miei genitori e alla mia grande e affettuosa famiglia. Grazie per il sostegno e l'interesse che avete sempre dimostrato nei confronti di ciò che faccio. Per quanto sia difficile e lontano dalla realtà quotidiana, non avete mai rinunciato a capire cosa fosse il glioblastoma o un *western blot*. Siete insostituibili.

E un ultimo grazie a Dado, il mio amico di sempre e grande compagno. Con la tua calma, forza, determinazione e saggezza hai saputo illuminare le mie ombre più profonde.

Per sapere chi sei non mi basta una notte (…)
Non mi basterai come a una vela non basterà il vento
ma mi mancheresti come al mare mancherebbe il sale.
[Marta sui Tubi – I nostri segreti]

No importa que no te tenga,
no importa que no te vea.
Lo que yo te pido
es que la corpórea
pasajera ausencia
no nos sea olvido,
ni fuga, ni falta:
sino que me sea
posesión total
del alma lejana,
eterna presencia.
[Pedro Salinas - Eterna presencia]

A voi,
Mario e Carla
perché anche se non fate più parte
di questo mondo
farete per sempre parte
del mio.

INDEX

FIGURE AND TABLE LEGEND

Introduction – Figures and Tables:

Materials and Methods - Tables:

Materials and Methods - Figures:

Results – Tables and figures:

ABBREVIATION

A	AB	AlamarBlue
	AUC	Area Under the Curve
B	BCA	Bicinchoninic Acid Assay
	BER	Base Excision Repair
	bFGF	Basal Fibroblast Growth Factor
	BrEt	Ethidium Bromide
	BSA	Bovine serum albumin
C	CAMs	Cell Adhesion Molecules
	CFC	Colony Forming Capacity
	CHAPS	3-[(3-cholamidopropyl)dimethylammonio]-1-propanesulfonate
	CL	Classical
	CNS	Central Nervous System
	CSC	Cancer Stem Cells
	CST	Cell Signaling Technology
	CT	Control sample
	CTC	Circulating Tumor Cells
D	DAPI	4',6-Diamidino-2-Phenylindole
	DDR	DNA Damage Response
	DFS	Disease Free Survival
	DGC	Differentiated Glial Cells
	DMSO	Dimethyl Sulfoxide
	DNA	Deoxyribonucleic Acid
	dNTP	Deoxynucleotide
	DSB	Double-Strand Break
	DTT	Dithiothreitol
E	EANO	European Association of Neuro-Oncology
	EBRT	External Beam Radiation Therapy
	ECM	Extracellular Matrix
	EDTA	Ethylenediaminetetraacetic acid
	EGF	Epidermal Growth Factor
	EGFR	Epidermal Growth Factor Receptor
	ELDA	Extreme Limiting Dilution Assay
	EORTC	European Organization for Research and Treatment of Cancer
	EMT	Epithelial-to-Mesenchymal Transition
	ES	Embryonic Stem
	ES*	Enrichment Score **within Gorilla analysis*

	ESCs	Embryonic Stem Cells
	ESMO	European Society for Medical Oncology
	EtOH	Ethanol
F	FACS	Fluorescence-activated cell sorting
	FAK	Focal adhesion kinase
	FBS	Fetal Bovine Serum
	FDR	False Discovery Rate
G	GBM	Glioblastoma Multiforme
	G-CIMP	Glioma CpG Island Methylator Phenotype
	GFP	Green Fluorescent Protein
	GICs	Glioblastoma Initiating Cells
	GO	Gene Ontology
	GSEA	Gene Set Expression Analysis
H	H/E	Hematoxylin and eosin stain
	HBSS	Hanks' Balanced Salt Solution
	HEPES	4-(2-hydroxyethyl)-1-piperazineethanesulfonic acid
	HR	Homologous Recombination
I	IDH	Isocitrate dehydrogenase
	IMRT	Intensity Modulated Radiation Therapy
	IR	Ionizing Radiation
K	KEGG	Kyoto Encyclopedia of Genes and Genomes
L	LQ	Linear Quadratic
	LQM	Linear Quadratic Model
M	Mes	Mesenchymal
	MetOH	Methanol
	MGMT	O6-Methylguanine Methyltransferase
	MLPA	Multiplex Ligation-dependent Probe Amplification
	MSP	Methylation Specific PCR
	MTT	3-(4,5-Dimethylthiazol-2-yl)-2,5-Diphenyltetrazolium Bromide
N	N	Neural
	NAM	Nicotinamide
	NCIC	National Cancer Institute of Canada
	NES	Normalized Enrichment Score
	NGS	Normal Goat Serum
	NHEJ	Non-Homologous End Joining
	NSC	Neural Stem Cell

O	OCR	Oxygen Consumption Rate
	OS	Overall Survival
	OXPHOS	Oxidative Phosphorylation
P	PBS	Phosphate-Buffered Saline
	PCA	Principal Component Analysis
	PCR	Polymerase Chain Reaction
	PDGFR	Platelet-derived growth factor receptor
	PDH	Pyruvate dehydrogenase
	PE	Plating Efficiency
	PEP	Phosphoenolpyruvate
	PEPCK	Phosphoenolpyruvate carboxykinase
	PFA	Paraformaldehyde
	PFS	Progression Free Survival
	PI3K	Phosphatidylinositol-3-kinases
	PN	Proneural
	PVDF	Poly-Vinylidene Di-Fluoride
	PTPase	Protein Tyrosine Phosphatase
Q	qPCR	Quantitative PCR
R	ROS	Reactive Oxygen Species
	RNA	Ribonucleic Acid
	RNS	Reactive Nitrogen Species
	RT	Radiotherapy
	RTKs	Receptor tyrosine kinases
	RT-PCR	Reverse Transcription PCR
S	SEM	Standard Error of the Mean
	SF2	Surviving Fraction at 2 Gy
	SF4	Surviving Fraction at 4 Gy
	SF8	Surviving Fraction at 8 Gy
	shRNA	Short Hairpin RNA
	SRY	Sex Determining Region Y
	SSB	Single-Strand Break
	SVZ	Subventricular Zone
T	TAMs	Tumor Associated Macrophages
	TBS	Tris-Buffered Saline
	TBS-T	TBS-Tween
	TCA	Tricarboxylic Acid

	TCGA	The Cancer Genomic Atlas
	TF	Transcription Factor
	TMZ	Temozolomide
V	VEGF	Vascular Endothelial Growth Factor
W	WHO	World Health Organization
1-9	3D-CRT	Three-Dimensional Conformal Radiation Therapy

INTRODUCTION

"Imperfect engines (...) have lent themselves to the game of selection, as happened for the first vertebrate's brain appeared on our planet between 300 and 400 million years ago. The empty vesicles of that ancestral brain lent themselves to the selective pressure of evolution by creating endless variations, expressed now in the diverse brains of the living and extinct forms of vertebrates. The most recent among them is the wonderful and utterly imperfect brain of *Homo sapiens*. On the contrary, the solid and perfect brain of invertebrates did not play the game of selective pressure, and propagated in submerged and emerged areas of the planet. Among them, in particular, stands the model that it can be considered the most successful: the insects. However, neither Hitler nor Einstein will rise ever from their progeny, even if their descendants will survive in all likelihood for the next hundreds of millions of years."
RITA LEVI MONTALCINI – *Praise upon imperfection*

1 GLIOBLASTOMA MULTIFORME

1.1 CLASSIFICATION

Glioblastoma Multiforme (GBM) is the most frequent and malignant primary brain tumor. According to the World Health Organization (WHO), GBM is assigned to the WHO grade IV, typically characterized by cytologically malignant, mitotically active, necrosis-prone neoplasms typically associated with rapid pre- and postoperative disease evolution and a fatal outcome (Louis et al., 2007b). In developed countries, every year 3 to 4 new cases are diagnosed per 100.000 persons (Louis et al., 2007a). The vast majority of GBM develops rapidly *de novo* in elderly patients (primary GBM; 90%). In those cases, the diagnosis of GBM occurs at the first biopsy without clinical or histologic evidences of a preexisting less malignant precursor lesion. Oppositely, secondary GBM progresses from preceding low-grade or anaplastic astrocytoma, accounts for 10 % of all GBM and preferentially arises in younger patients (Ohgaki & Kleihues, 2013). Primary and secondary GBM bear distinct clinical, prognostic and genetic features (Figure 1), but until 2008, with the identification of mutation in *IDH1/2* (Parsons et al., 2008; Yan et al., 2009), it was not possible to separate the two types unequivocally on a molecular basis. These findings set the stage for a major revision of the last Central Nervous System (CNS) WHO classification (2007 CNS WHO; Louis et al., 2007a). The new CNS WHO classification (2016 CNS WHO; Louis et al., 2016) combines as diagnostic tools the old, well-established histopathological features with new molecular parameters. The use of this "integrated" approach is hoped to help improved diagnostic accuracy and patient management. According to the 2016 CNS WHO, GBM are divided into Glioblastoma, IDH-wildtype that roughly correspond to the clinically defined primary GBM, and Glioblastoma, IDH-mutant, which correspond to the so-called secondary GBM (Figure 1). The study of primary GBM (WHO grade IV) was at the core of this PhD thesis.

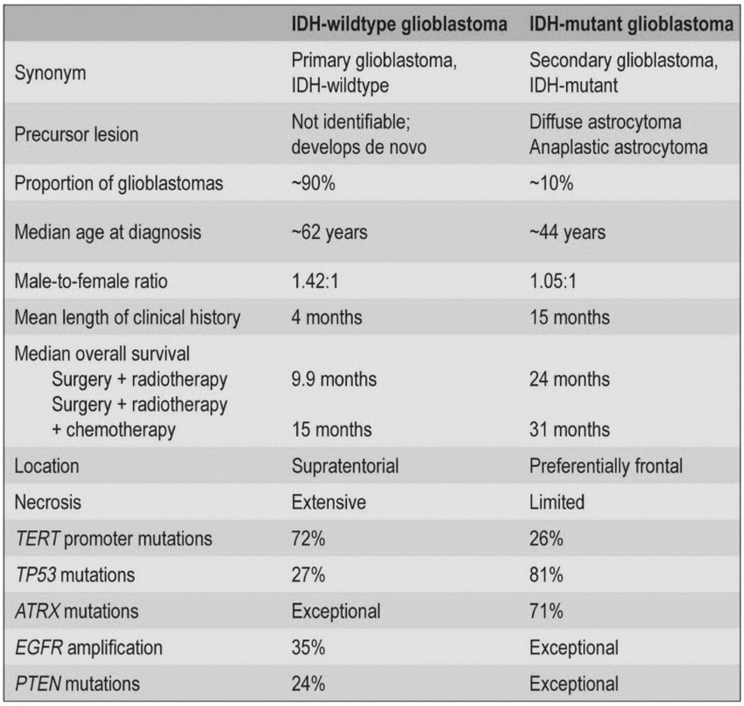

	IDH-wildtype glioblastoma	IDH-mutant glioblastoma
Synonym	Primary glioblastoma, IDH-wildtype	Secondary glioblastoma, IDH-mutant
Precursor lesion	Not identifiable; develops de novo	Diffuse astrocytoma Anaplastic astrocytoma
Proportion of glioblastomas	~90%	~10%
Median age at diagnosis	~62 years	~44 years
Male-to-female ratio	1.42:1	1.05:1
Mean length of clinical history	4 months	15 months
Median overall survival		
Surgery + radiotherapy	9.9 months	24 months
Surgery + radiotherapy + chemotherapy	15 months	31 months
Location	Supratentorial	Preferentially frontal
Necrosis	Extensive	Limited
TERT promoter mutations	72%	26%
TP53 mutations	27%	81%
ATRX mutations	Exceptional	71%
EGFR amplification	35%	Exceptional
PTEN mutations	24%	Exceptional

Figure 1: Key characteristics of IDH-wildtype and IDH-mutant glioblastomas
(Modified from Louis et al., 2016)

1.2 CLINICAL DATA, STANDARD THERAPEUTIC STRATEGY AND TREATMENT FAILURE

Clinical GBM presentation includes headaches, seizures, focal neurologic deficits, confusion, memory loss, cognitive dysfunction, and personality changes and symptoms typically worsen rapidly (Wen & Kesari, 2008).

According to EANO (The European Association of Neuro-Oncology) and ESMO (The European Society for Medical Oncology) guidelines' the current standard of care for adult patient with diagnosed GBM is surgery followed by radiotherapy (RT) plus concomitant and adjuvant temozolomide (TMZ) chemotherapy (Stupp et al., 2014a; Weller et al., 2014). The protocol, also called "Stupp regimen", was established in 2005 following the pivotal randomized trial coordinated by the European Organization for Research and Treatment of Cancer (EORTC)/National Cancer Institute of Canada (NCIC; Stupp et al., 2005).

Surgery is the key initial therapeutic approach, useful for both tumor debulking and collection of diagnostic biopsies. Due to the infiltrative nature of GBM, the lesion cannot be eliminated completely. Even though, maximal extensive resection is attempted if feasible within protection of neurological functions. In addition to the diagnostic value of biopsies, surgical removal reduces significantly symptoms associated to mass effect and intracranial pressure (Wen & Kesari, 2008).

Surgery is followed by fractionated focal radiotherapy administered Monday to Friday for 6–7 weeks (60 Gy, 30–33 fractions of 1.8–2 Gy, or equivalent doses/fractionations). TMZ, an oral alkylating agent capable to cross the blood-brain barrier, is administered to patient, on a daily basis during radiotherapy, and in six five-days long cycles as maintenance (adjuvant) treatment after the end of radiation (Stupp et al., 2014a). Concomitant and adjuvant TMZ chemotherapy significantly improved median, 2- and 5-year survival, and is the current standard of care for patients with glioblastoma up to age 70 (Stupp et al., 2005).

Patients with IDH-wildtype GBM, have a mean length of preceding clinical symptoms of 4 months, and a median overall survival of 15 month when treated after surgery with chemo radiotherapy (Figure 1; Louis et al., 2016). Only a limited fraction of patient (3-5%) survives for more than 3 years. A comparative study of the so-called "long-survivors", revealed that favorable outcome is significantly associated with young age at diagnosis, a good initial performance score, and importantly *MGMT* promoter hypermethylation (Krex et al., 2007). *MGMT* (O6-methylguanine methyltransferase) encodes for a DNA repair protein capable to restore guanine from O-6-methylguanine, which is the type of genomic lesion induced by alkylating agents, TMZ included. Consequently, MGMT likely can modulate sensitivity and cause resistance to alkylating drugs. Apart from long-survivors, it has been described prominent benefit for TMZ in patients with MGMT promoter methylation (Stupp et al., 2009). Even though, recent investigation on TCGA samples, revealed significant MGMT prognostic value exclusively for GBM classical subtype but not for GBM expressing other molecular profiles (Brennan et al., 2013).

Despite intense patient management, conventional therapies are not able to achieve long-term remissions and eventually almost every tumor recurs. The rapid tumor recurrence or even the tumor progression despite aggressive treatments, result in patients' mortality. The impossibility of extensive tumor debulking, the marked heterogeneity of lesions and the poor drug delivery in the brain contribute significantly to the lack of effective treatment options. These features make of GBM one of the most challenging cancers to treat.

Standards of care for patients with recurrent or progressive GBM are not established yet. Repeat surgery as well as re-irradiation remain controversial. The therapeutic values of different treatment regimens including DNA alkylating agents as nitrosoureas (e.g., carmustine [BCNU], lomustine [CCNU], nimustine [ACNU]) or TMZ, anti-angiogenic agents, targeted therapies, administered as either monotherapy or in combination regimens, or novel concepts including immunotherapy are still under revision (Seystahl et al., 2016).

1.3 HETEROGENEITY IN HISTOPATHOLOGICAL AND GENETIC FEATURES

Glioblastoma are named “Multiforme” due to their high degree of heterogeneity at both histological and genomic level. Most of GBM are poorly delineated and show epicenter in the white matter. Macroscopically, tumor mass presents central area of necrosis with an extensive peritumoral edema. Despite the short clinical history, these tumors are often surprisingly extended at diagnosis, occupying most of the cerebral lobe (Louis et al., 2007a; Figure 2-A). Interestingly, GBM lacking IDH mutations show widespread anatomic distribution within the supratentorial region, in contrast with IDH-mutant glioblastomas that predominantly involve the frontal lobe (Figure 1 and Figure 2).

Glioblastoma is characterized by a remarkable intratumoral histological heterogeneity and cell are often poorly differentiated. According to the 2007 CNS WHO classification, histologic criteria for GBM diagnosis include nuclear atypia, cellular pleomorphism, mitotic activity, vascular thrombosis, microvascular proliferation and the distinctive necrotic area typically specified as pseudopalisading necrosis (Louis et al., 2007b; Figure 2-C).

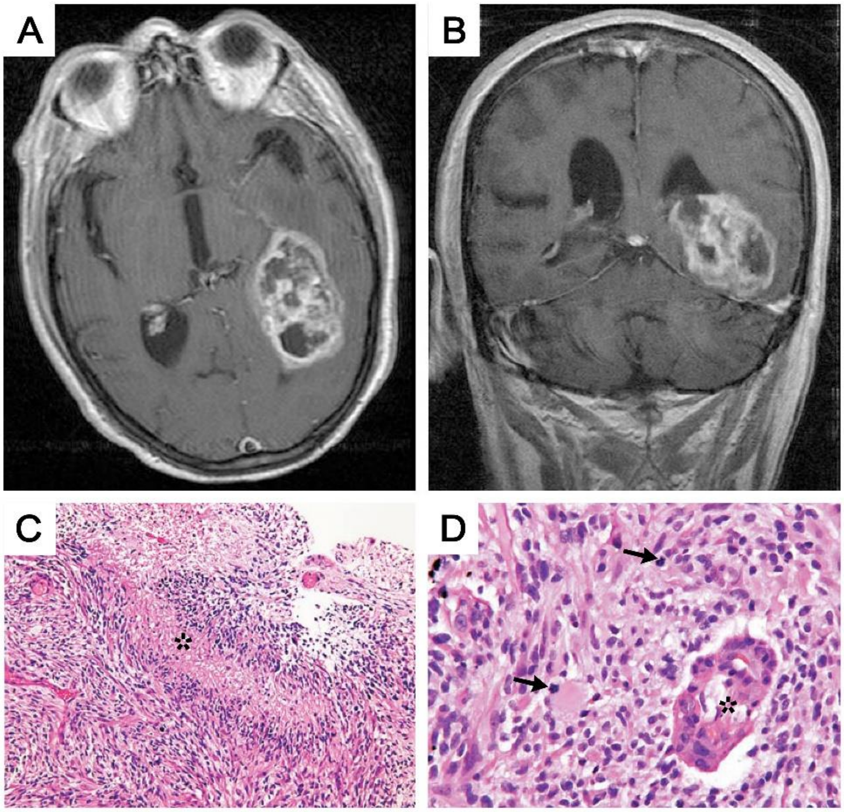

Figure 2: Macroscopic and Microscopic features of GBM
(A-B) Axial (A) and coronal (B) magnetic resonance images showing a heterogeneously enhancing mass with central necrosis (A and B modified from Altman et al., 2007). (C-D) Histologic appearance of a glioblastoma in hematoxylin and eosin stain. (C) Picture with recognizable nuclear pleomorphism, dense cellularity and pseudopalisading necrosis (asterisk). (D) Panel showing vascular endothelial proliferation (asterisk) and mitotic figures (arrows) (C and D modified from Wen & Kesari, 2008).

On the genomic point of view, large scale molecular profiling of gliomas, coordinated by The Cancer Genomic Atlas (TCGA) network, have led to an improved insight of the pathways commonly disrupted in several cancer types. GBM was among the earliest tumor types investigated by the network. In the first GBM TCGA report (TCGA network, 2008) a highly interconnected network of aberrations has been identified, suggesting a marked intertumoral genetic heterogeneity. Using an integrative approach, three core pathways were found dysregulated: the p53 and RB tumor suppressor pathways, and PI3K pathway (Figure 3).

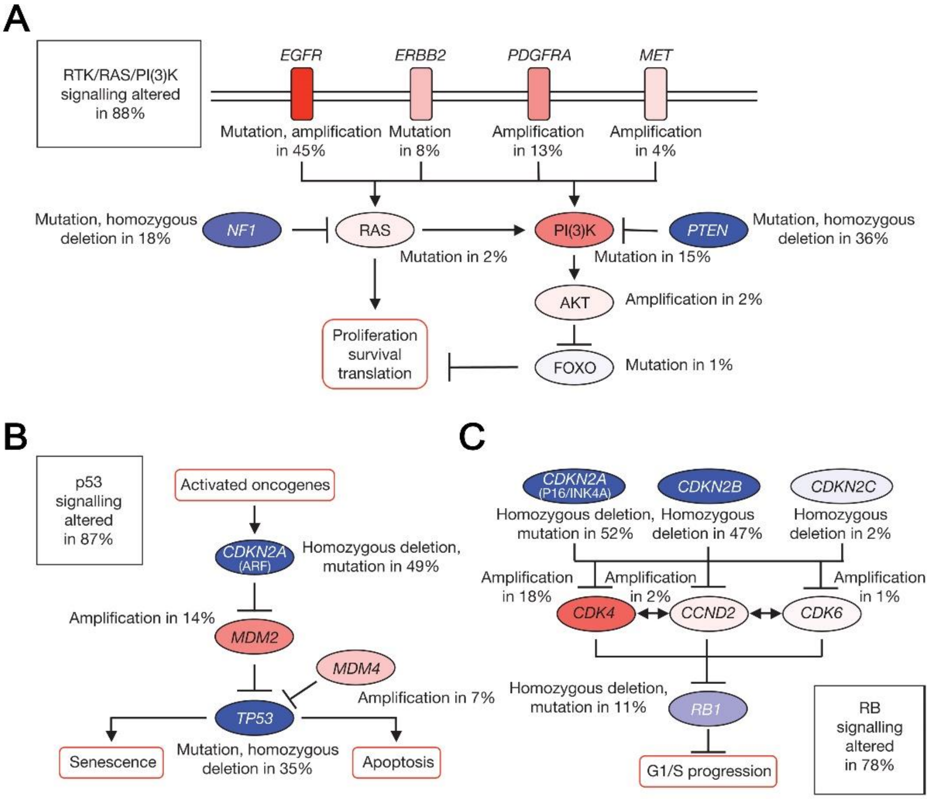

Figure 3: Core signaling pathways found altered in GBM

Most of the identified GBM genetic aberrations can be connected to three major signaling pathways: (A) RTK/RAS/PI3K, (B) p53 and (C) RB. (A-C) Red indicates both activating mutations and genetic amplifications, blue indicates inactivating alterations (loss-of-function mutations or deletions). Darker shades correspond to higher percentage of tumors affected by the single alteration. Boxes contain the percentages of GBM specimens with alterations in at least one component gene of the indicated pathway (picture from TCGA network, 2008).

The key tumor suppressor gene *CDKN2A* report in GBM frequent homozygous deletion. *CDKN2A* encodes for both Ink4A (p16) and Arf ($p14^{ARF}$) that are activators of Rb and p53 respectively. *MDM2* (p53 repressor) and *CDK4* (upstream inhibitor of Rb) are often amplified, leading to a significant repression of p53 and Rb signaling pathways.

Receptor tyrosine kinases (RTKs) upstream of PI3K, catalytic and regulatory PI3K domains, and the key PI3K negative regulator, PTEN, are all frequently altered in GBM. Briefly, genomic amplification of *EGFR*, often depicted by the constitutively active variant III (EGFRvIII), along with *PDGFRA* and *MET* point to a global activation of RTKs pathways. Activating mutation of the PI3K complex and deletion, silencing mutations or deletion of *PTEN* or mutation in the Ras antagonist *NF1* suggest an unconditional activation of PI3K in GBM specimens. Even though, proteomic profiling of TCGA samples lysates revealed that RTKs amplification do not reflect significantly RTKs downstream pathway activation as measured by p-AKT, p-S6 and p-MAPK clusters (Brennan et al., 2013). Conversely, *PTEN* loss match with a significant enhancement of AKT pathway, and mutant PI3K samples have lower PI3K activity when compared to samples lacking PI3K mutation. Similarly, samples harboring *NF1* mutation/deletion show elevated MAP kinase activity (via p-ERK and p-MEK; Brennan et al., 2013).

Subsequently, several studies have drawn attention to a significant intratumoral heterogeneity. Importantly, it has been described that focal amplification of two or more RTKs (most commonly PDGFRA and EGFR) can occur redundantly within the same GBM (Figure 4-A). Nevertheless, the genetic landscape of these amplifications is not homogeneous as documented by in situ hybridization (Little et al., 2012; Snuderl et al., 2011; Szerlip et al., 2012). The majority of the amplifications exhibit a mutual exclusivity, with distinct cellular subclones containing diverse amplified receptor genes reflecting a pattern of intratumoral heterogeneity (Figure 4-B). In a wider picture, Sottoriva and colleagues interrogated the mutational spectrum of GBM in a spatial point of view (Sottoriva et al., 2013). Through multiple sampling of spatially separated tumor regions, it was possible to uncover extensive intratumoral heterogeneity based on a number of different mutations. More recently, analysis of single-cells derived from the same GBM sample showed distinct somatic aberration supporting a marked intratumoral heterogeneity even at single cell level (Patel et al., 2014; Figure 4-C). Intratumoral heterogeneity together with redundant signaling routes are one of the possible drivers of treatment failure. This peculiar GBM feature reflects genomic instability and focal new clones arising from the bulk as a result of additional genetic alterations (Ohgaki & Kleihues, 2013).

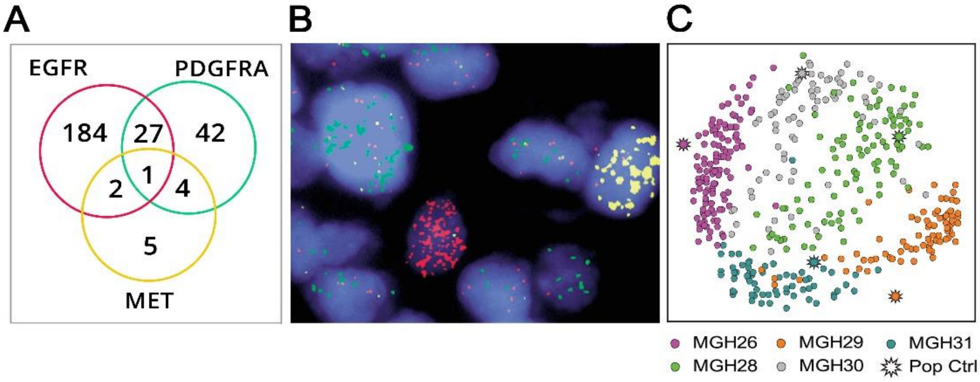

Figure 4: Molecular intratumoral heterogeneity

(A-B) Mosaic amplification of RTKs. (A) Venn diagram depicting the incidence of individual RTK amplifications and the co-occurrence of two or more RTKs amplification in the same tumor (picture from Szerlip et al., 2012). (B) Multicolor FISH mapping for multiple RTKs amplification. Three subpopulations of GBM cells with mutually exclusive amplification of EGFR (red), MET (green) and PDGFRA (yellow) (picture from Villanueva, 2012). (C) Multidimensional scaling plot illustrates the single-cell distribution according to expression profiles. Color code indicates the five different tumors of origin, whereas the control samples (Pop Ctrl) are non-tumorigenic cells derived from the same patient. The distance between any two cells reflects the similarity of their expression profiles. Cells group by tumor, but each tumor also contains outliers that are more similar to cells derived from other tumors (picture from Patel et al., 2014).

1.4 TRANSCRIPTIONAL SUBTYPES

The analysis of high-throughput genomic platforms for mRNA expression has allowed the identification of distinct transcriptional profiles within TCGA samples. Based on four consistent transcriptomic signatures, TCGA network described four GBM subtypes, termed classical (CL), proneural (PN), neural (N) and mesenchymal (Mes; Verhaak et al., 2010). Interestingly, the majority of genetic aberrations already identified in GBM were found particularly enriched in specific subtypes: *EGFR* (CL), *PDGFRA, TP53* and *IDH1/2* (PN) and *NF1* (Mes; Figure 5; Brennan et al., 2013; Verhaak et al., 2010). In the case of N-GBMs, particular molecular abnormalities remain unidentified. Importantly, the PN subtype is further subdivided into two subgroups based on the DNA methylation patterns. GBM displaying coordinated hypermethylation at a large number of loci are defined as Glioma CpG Island Methylator Phenotype (G-CIMP). All G-CIMP tumors display *IDH1* mutation and even if at transcriptional level resemble PN subtype, their biology is significantly different and are associated with improved prognosis (Noushmehr et al., 2010).

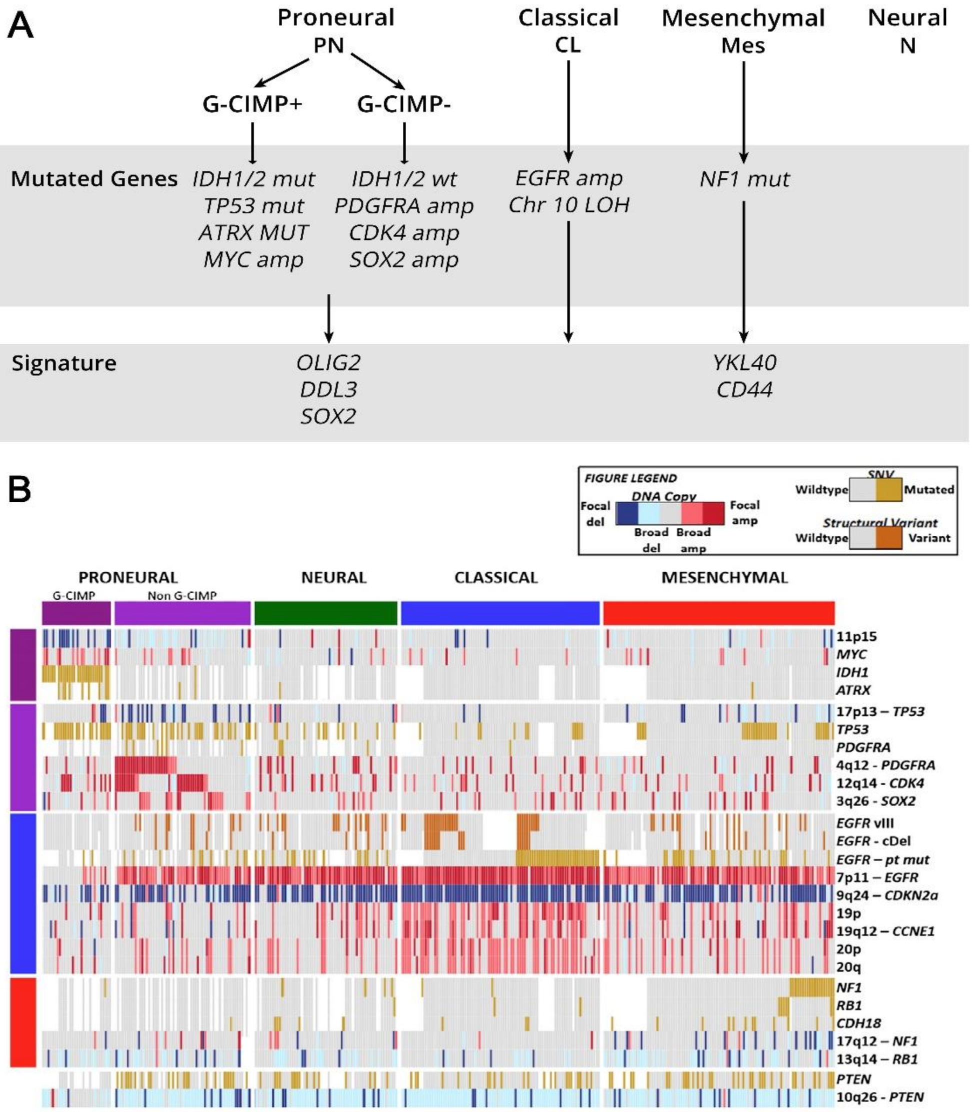

Figure 5: Transcriptional subtypes of Glioblastomas

(A) The common patterns of somatic mutations and DNA copy number alterations along with key gene defining the transcriptional signature are indicated for each subtype. (B) Genomic alterations associated with GBM molecular subtypes (picture from Brennan et al., 2013).

It has been reported that each profile significantly correlates with distinct CNS cell types' transcriptional signature. In its initial description, the PN signature was associated to oligodendrocytic signature, whereas CL and Mes to astrocytic and N to astrocytic and oligodendrocytic (Verhaak et al., 2010). Conversely, according to more recent findings, PN and CL subtypes are strongly associated to stemness signature, thus resembling progenitor compartment, while Mes and N profiles are close to astrocytic and oligodendrocytic lineages respectively (Patel et al., 2014).

In addition, proteomic profiling of TCGA samples revealed diverse key pathways activated in the different GBM subtypes. Classical subtype shows relative downregulation of MAPK signaling and proapoptotic proteins (cleaved caspase 7 and 9, Bid and Bak). Mesenchymal profile exhibits elevated amount of endothelial markers (CD31 and VEGFR2), inflammation markers (FN1 and COX2) and activation of MAPK pathway (high levels of p-Raf, p-MEK and p-ERK). Proneural GBMs show relatively elevated activation of PI3K pathway. G-CIMP samples share features with their PN superfamily and in addition exhibited decreased amount of several proteins, including COX2, IGFRBP2 and Annexin 1 (Brennan et al., 2013).

Given the heterogeneous nature of GBM, it was not surprising to discover fragments from the same tumor expressing different subtype profiles (Sottoriva et al., 2013) and mixed population of cells expressing multiple subtypes within a dominant transcriptional program, which coincides with the profile detected globally for each sample (Patel et al., 2014; Figure 6-A).

On the predictive power of GBM subtypes for the patient outcome, full agreement has not been reached yet. A clear and unquestionable prognostic advantage has been demonstrated for G-CIMP patients (Noushmehr et al., 2010). Whether the non-G-CIMP PN and Mes signatures, as well as the other GBM subtypes, could serve as predictor factors for patient outcome is still being investigated. Initially, the proneural signature was associated with a better outcome (Phillips et al., 2006). Then, following G-CIMP phenotype description, it was uncovered that prognostic advantage was likely provoked by those G-CIMP IDH1/2 mutant gliomas initially included in PN group as transcriptionally indistinguishable from their superfamily (Brennan et al., 2013). Conversely, Bhat and colleagues reported correlation among PN/Mes status and radiation response, being Mes-GBM associated to progression following RT and PN-GBM to initial response, even in patient with *IDH*-wt tumors (Bhat et al., 2013; Figure 6-B). Patel and colleagues described as well significant clinical advantage for pure PN tumors when compared with samples showing global PN transcriptome mixed with either modest or strong signal for other subtypes (Patel et al., 2014; Figure 6-C).

In addition, the recent interest on Circulating Tumor Cells (CTC) in GBM patient blood samples leads to uncover their predominant Mes identity regardless the prevailing trait of the original tumor (Sullivan et al., 2014).

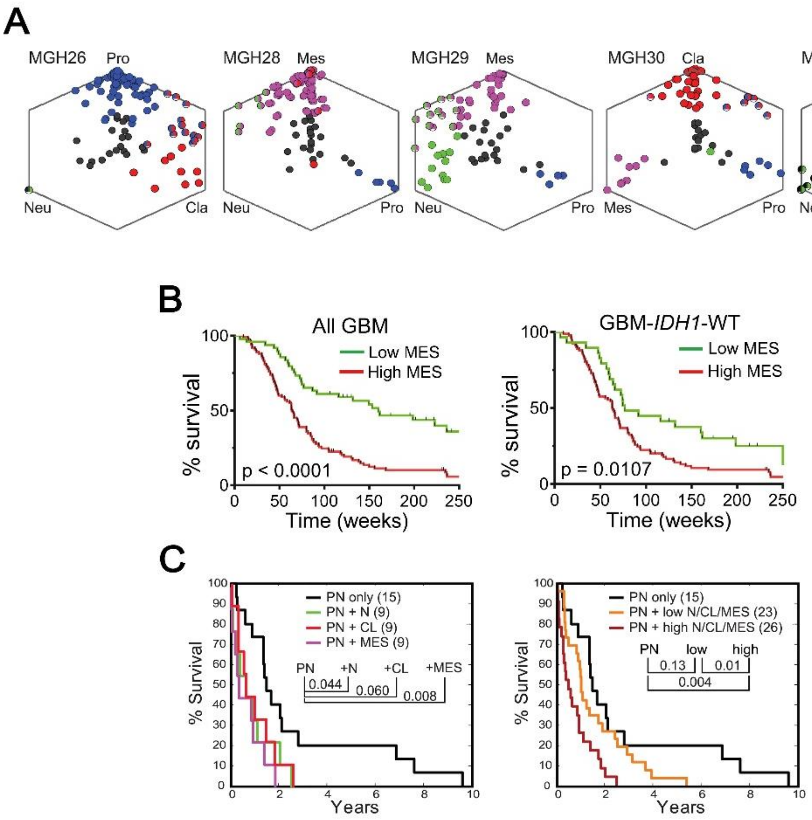

Figure 6: heterogeneous expression of GBM subtypes and their clinical implications

(A) Individual tumors contain a spectrum of glioblastoma subtypes and hybrid cellular states. Plots indicates expression subtype scores for single cells extracted from each tumor (five different samples are depicted). Each data point corresponds to a single-cell and it is plotted along three axes according to its relative scores for the indicated subtypes (picture from Patel et al., 2014). (B) Kaplan Meier curves show survival of GBM patients based on PN/MES subtype considering or not the *IDH1* status (picture from Bhat et al., 2013). (C) Kaplan-Meier survival curves for PN tumors analyzed by TCGA network. Samples were grouped according to estimated heterogeneity, based on the detection of alternative subtypes within the predominant PN trait or on the relative strength of alternative subtype signatures (group size in parentheses; picture from Patel et al., 2014).

In view of the fact thart CTC intravasate in the absence of therapy-mediated blood-brain barrier disruption, CTC are expected to provide biologic insights into the process of GBM invasion. Consequently, it was not surprising to find cells with predominant Mes trait at the invasive edge of the deep white-matter tracts and surrounding the necrotic foci of patient's tumors and patient-derived xenografts in mouse (Sullivan et al., 2014).

1.5 TUMOR PROGRESSION AND TRANSDIFFERENTIATION

The extensive heterogeneity of GBM leads to infer complex tumor evolution, with divergent development of cancer cells subpopulations within the same lesion (Ozawa et al., 2014; Sottoriva et al., 2013). Particularly, Ozawa and colleagues suggest a temporal sequence of genetic alterations during tumorigenesis being PN the profile of primordial tumors, and the other subtypes evolve from them. This evolutionary view is consistent with the detection of cells exhibiting a PN signature in all GBM analyzed regardless of the dominant subtype of the tumor (Patel et al., 2014). Despite these studies, the tumor evolution in GBM is still point at issue, especially for the difficulties related to ascertain the influence of microenvironment in the early stages of GBM.

Importantly, STAT3 along with C/EBPβ and TAZ were described as master regulators of Mes related transcriptome (Carro et al., 2010). In addition, it has been described a potential crosstalk between macrophages/glia in the surrounding tissue and cancer cells via TNF-α/NF-κB in triggering the transdifferentiation of PN GBM to Mes (Bhat et al., 2013). Finally, several studies reported a shift in molecular subtype toward Mes signature upon recurrence in astrocytomas (Phillips et al., 2006; Figure 7). This GBM molecular subtype shift, which resemble the known epithelial-to-mesenchymal transition process (EMT), has been recently described to occur *in vivo* in irradiated proneural GBM (Halliday et al., 2014).

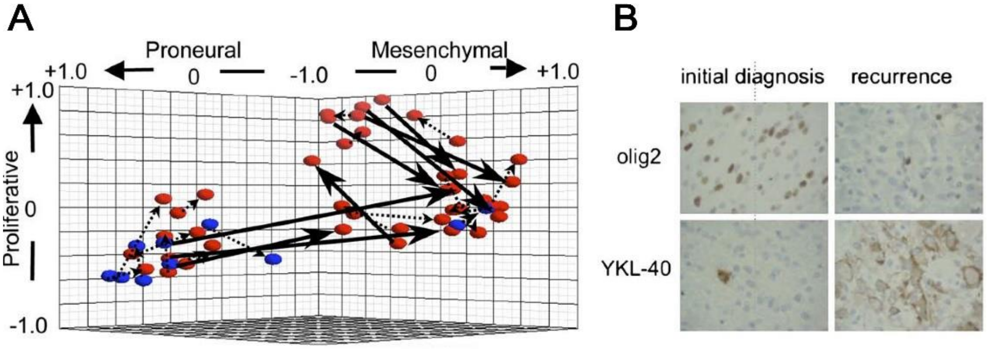

Figure 7: Tumors tend to shift toward the Mes phenotype upon recurrence

(A) Matched specimens that represent primary and recurrent astrocytomas from the same patients. Each pair of matched specimens is connected by an arrow that is solid and boldin case of signature class shift. Proliferative subgroup in Phillips classification has been divided into Neural and Classical subtypes (Verhaak et al., 2010). (B) Immunohistochemistry of YKL40 and OLIG2 in matched primary and recurrent tumors (picture from Phillips et al., 2006).

2 RADIOTHERAPY

Radiation therapy (RT) remains a mainstay of modern cancer management for both benign and malignant tumors. In high-income countries, half of newly diagnosed cancer patients benefit from receiving RT (alone or multimodality treatment) at some point during the course of their treatment (Atun et al., 2015). Therefore, RT is an integral component of localized cancer's treatment. It allows to achieve cancer regression or local control and palliation in case of incurable and metastatic tumors. As anti-cancer tools, RT is characterized by high-energy beam of Ionizing Radiation (IR) capable to free electrons from targeted atoms, thereby ionizing them (Figure 8).

At present, in the context of GBM, patients are treated with radiotherapy in order to reduce as much as possible the radiation-related adverse effects, including neurotoxicity and cognitive impairment. Thanks to significant technological advances IR now can selectively target the post-surgical cavity with nearly acceptable side effects on normal surrounding tissues. Indeed, nowadays IR are usually delivered with External Beam Radiation Therapy (EBRT) administrated mainly following two distinct procedures: three-dimensional Conformal Radiotherapy (3D-CRT) or Intensity-modulated radiotherapy (IMRT; Clarke et al., 2010). The latter strategy corresponds to a more sophisticated 3D-CRT, as it is able to precisely target tumor volumes and spare the surrounding radiosensitive organs often located in close proximity (brainstem, optic chiasm, lens, optic nerves, and cerebral cortex). Several studies compared IMRT to 3D-CRT and reported equal local control without exhibiting clear survival benefit (Chen et al., 2013; Fuller et al., 2007). EBRT can deliver two types of radiations: photons, such as X-rays and γ-rays, and charged particles, such as protons and electrons. Photons are conventionally used as standard treatment, and even though they differ in the source of generation, X-rays and γ-rays share the same radio-physical properties (Miao et al., 2014; Figure 8).

The main objective of RT in cancer is the impairment of tumoral cell capacity for unlimited proliferation (Barendsen, 1997). The biological effects of ionizing radiation on cells are different and mainly related to DNA damage: single strand break (SSB), double strand break (DSB) and other lesions leading to chromosomal aberrations. Damaged cells that are not able to repair lesions undergo severe consequences, including mutagenesis and eventually cell death via G2/M arrest, mitotic catastrophe, senescence and apoptosis (Ivanov & Hei, 2014; Tu et al., 2013). Importantly, radiation sterilizes cells not properly kills them, meaning that cells do not die immediately, but at the time of the next cell division, or a few divisions later (Fowler, 2006).

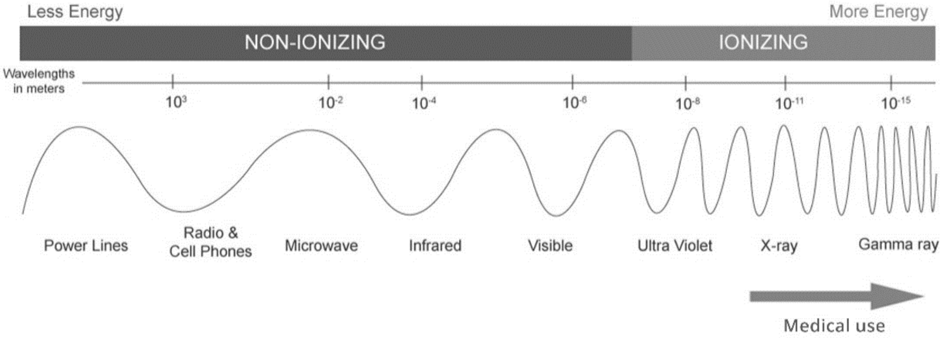

Figure 8: Electromagnetic spectrum of radiation

Ionizing radiations, as X-ray and γ-ray, are employed as treatment tools against cancer. Picture modified from Miao et al., 2014.

2.1 BIOLOGICAL CONSEQUENCES OF RADIATION

In living cells, the energy deposition from ionizing radiation tracks can either directly disrupt biomolecules, producing chemical modifications, or act indirectly through radiolysis of water (Figure 9; Azzam et al., 2012). Being water the major component of cells (~80%), the indirect effect, with the consequent generation of Reactive Oxygen Species (ROS), represents the most likely occurring event after ionizing radiation exposure. Indeed, only ~1/3 of the IR-dependent DNA damage is thought to be generated from direct interaction of the radiation tracks with biomolecules (Azzam et al., 2012). Endogenous bursts of ROS are recorded in and around the radiation track within targeted cells and in the extracellular matrix. Moreover, IR can also stimulate inducible nitric oxide synthase (NOS) activity in targeted cells, thereby producing large amounts of Reactive Nitrogen Species (RNS; Azzam et al., 2012; Hei et al., 2008). Free radicals can rapidly diffuse, damage critical biomolecules (DNA, protein and lipid) and trigger the activation of signaling cascades to compensate the oxidative stress. Moreover, imbalance of ROS intracellular amount may significantly lead to perturbation in the *redox*-based reactions and mitochondrial respiratory chain. In addition, excess of radicals may cause mutation in mitochondrial DNA (mtDNA) leading to the disruption of expression and assembly of proteins required for the electron transport chain. Changes in the structure of mitochondrial respiratory chain proteins driven by mutations in mtDNA can give rise to increased oxidative metabolism-derived ROS production and consequent enhancement of DNA damage (Azzam et al., 2012; Richardson & Harper, 2016).

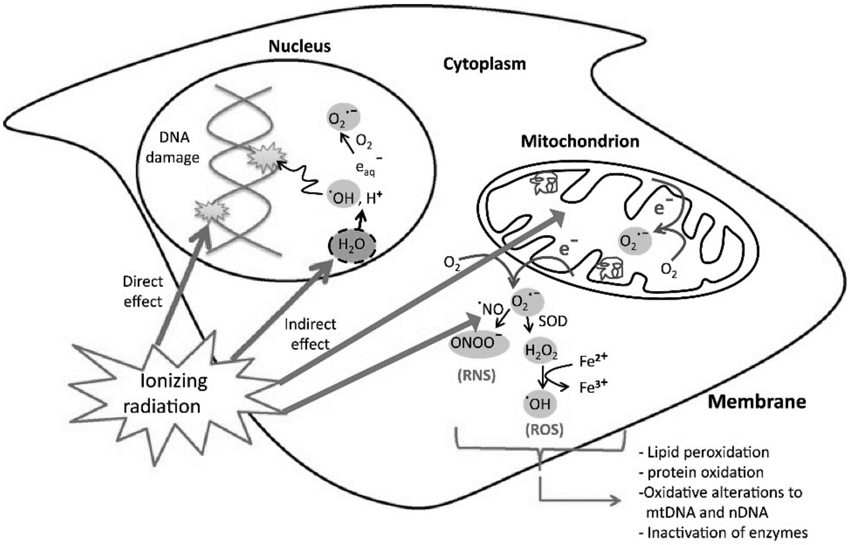

Figure 9: The direct and indirect cellular effects of ionizing radiation on macromolecules
Picture modified from Azzam et al., 2012.

Beyond the induction of DNA damage, ionizing radiation (IR) triggers a complex series of signaling cascades (Allen & Tresini, 2000; Azzam et al., 2012; Hamada et al., 2007; Maier et al., 2016; Miao et al., 2014; Valerie et al., 2007). RT-dependent pathways' activation is believed to be mediated mostly by free radical production after water radiolysis, which get possibly amplified via mitochondria. Most of the studies reported a substantial alteration in cytokines' expression (e.g. IL1β, IL6, IL8, TNF-α and TGB-β) leading to activation of MAPK superfamily and crucial transcription factors, mostly NF-κB, AP-1 and STATs, thereby modulating target genes' expression and in turn upregulating cytokines in a positive feedback loop (Miao et al., 2014). Moreover, the generated positive loop can amplify the radiation or ROS-induced oxidative stress and inflammation, which may persist chronically (Miao et al., 2014). In addition, large amount of ROS and RNS inhibits protein tyrosine phosphatases (PTPase) activity which leads to RTKs constitutive activation and downstream enhancement of prosurvival pathways (Herrlich & Böhmer, 2000; Valerie et al., 2007). Importantly, even though the exact function of these pathway's activation remains unclear, some of them are likely to contribute to radioresistance phenomenon and tumor progression (Craft & Hallahan, 2012; Miao et al., 2014).

Remarkably, damaging effects can be maintained after the initial exposure for days and months, and even in the progeny of irradiated cells. Particularly, radiation-induced mitochondrial dysfunctions may be involved in the persistence of ROS in irradiated cells' progeny (Azzam et al., 2012). In addition, oxidative stress may spread from targeted cells to neighboring non-irradiated cells though bystander effect. The bystander phenomenon involves intercellular communication mechanisms and/or key soluble factors, especially cytokines and ROS, which might mediate the activation of critical pathways ending up enhancing the inflammatory response, thus providing a continuous supply of radicals in surrounding unirradiated cells, eventually (Hei et al., 2008; Prise & O'Sullivan, 2009).

2.2 DNA DAMAGE RESPONSE PATHWAYS

RT response studies mainly focus on induced DNA damage as it represents the major biomolecule of interest. Particularly, IR-effects on DNA molecule either by direct ionization or indirect radicals formation include DNA breaks, base damage, destruction of sugars, telomere dysfunction and DNA–DNA/DNA-protein crosslinks (Kakarougkas & Jeggo, 2014; Maier et al., 2016; Figure 10). Approximately 3000 damaged bases, 1000 SSBs and 40 DSBs are induced in a cell by an X-ray dose of 1 Gy. DNA breaks (SSB and DSB) are disruptions in the phosphodiester backbone which can occur within both strands, separated by up to 10 bp (DSB), or on single strand (SSB). Due to its cytotoxicity, DSB are thought to be the most RT-induced deleterious lesion. Contrarily base damage and SSB are of minor relevance for cell survival, as these lesions are essentially all repaired by the highly efficient Base Excision Repair (BER) mechanism, explained in details later. DSB are processed by either non-homologous end joining (NHEJ) or homologous recombination (HR). The DSB repair pathway's choice depend mainly on the cell-cycle phase of the damaged cell (Shrivastav et al., 2008). Irrespectively from the activated pathway, the DNA Damage Response (DDR) is carried out by a plethora of enzymes able to chemically modify DNA (e.g. nucleases, helicases, polymerases, topoisomerases, recombinases, ligases, glycosylases, demethylases, kinases, and phosphatases; Ciccia & Elledge, 2010). Importantly, the most of the proteins involved in DDR, are tightly regulated by post-translational modifications, as phosphorylation, ubiquitination and sumoylation.

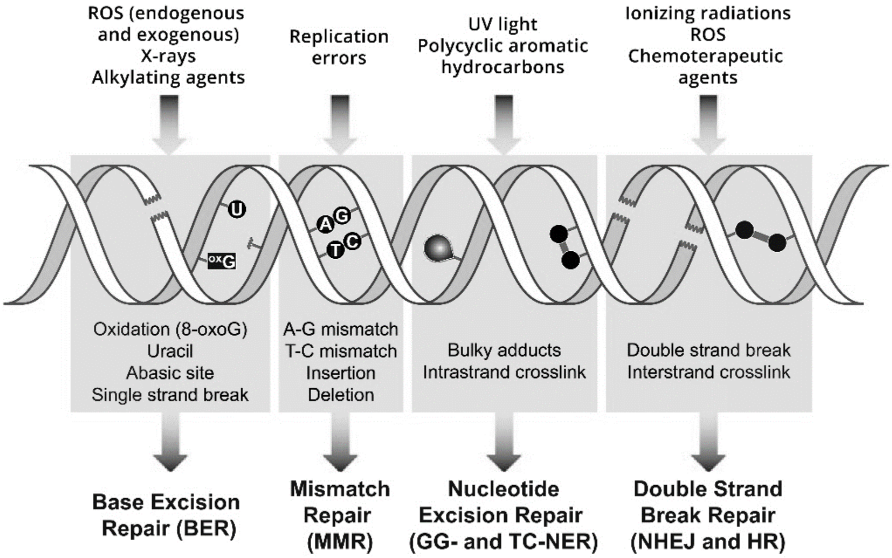

Figure 10: DNA damage induced by various genotoxic events

The diagram illustrates common DNA lesions caused by specific DNA damaging agents and the corresponding DNA repair mechanisms. Picture modified from Dexheimer, 2013.

The early DDR following DNA lesions formation is mediated by proteins of the phosphatidylinositol 3-kinase-like protein kinase (PIKKs) family — ATM, ATR, and DNA-PK — and by members of the poly(ADP-ribose) polymerase (PARP) family (Ciccia & Elledge, 2010). Both ATM and DNA-PK are activated by DSBs generated by IR, while ATR is mainly rectruited following stalled replication forks or UV light and chemoterapic genotoxic effects. PARP family members exert their major role on SSB repair via BER.

ATM is constitutively present in its dimer-inactive form and, given its activity on a vast number of substrates, ATM activation represents the master regulator of DDR sensing DSB induced by IR. After recruitment at the DNA break site, ATM dissociates and autophosphorylates on multiple residues and subsequently mediates the activation of key signaling cascades: phosphorylation of Chk2, which in turns mark CDC25A/B/C for proteosomal degradation, resulting in G1/S arrest; phosphorylation and activation of p53, which transactivates p21, thus inhibiting CDK2 and CDK4, two G1/S-promoting Cyclin-Dependent Kinases (CDKs); phosphorylation of the key histone variant H2AX on Ser139 residues (pH2AX or γH2AX) close to the break site (Figure 11). The described cascade massively leads to G1 arrest (Hakem, 2008) and help recruit to the DNA lesion site the DNA repair machinery. The arrest of the cell cycle is an essential part of DDR as it facilitates DNA repair and maintenance of genomic stability. Importantly, if the DNA lesion can not be repaired, p53 activates the pro-apoptotic program through the induction of *BAX* and *PUMA* expression (Ciccia & Elledge, 2010). Histone H2AX undergo rapid phosphorylation and marks the presence of damage, thus directing the recruitment of DNA repair complexes (Chapman et al., 2012). Phosphorylation at H2AX can be conveniently visualized by immunofluorescence like aggregates frequently named as "foci". Generation of γH2AX foci corresponds to IR-induced DNA DSBs and their decay correlates with DSB repair, thus providing a measure of radiosensitivity (Jamal et al., 2012; Revet et al., 2011; Ropolo et al., 2009). Moreover, H2AX removal of phosphorylations is important for attenuating the checkpoint signal in order to allow the cell cycle to resume (Shrivastav et al., 2008).

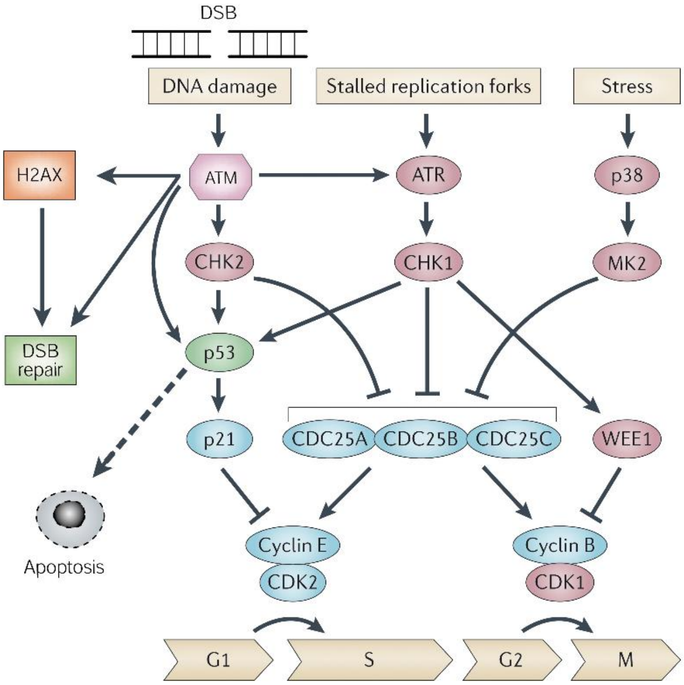

Figure 11: Induction of cell cycle arrest after irradiation

In response to DNA lesion, ATM phosphorylates the checkpoint effector kinase CHK2, which can arrest cell cycle at the intra-S phase or G2/M checkpoints by inhibiting via phosphorylation the cell division cycle 25A (CDC25A), CDC25B and CDC25C. Picture adapted from Bouwman & Jonkers, 2012.

After cell cycle arrest, either NHEJ or HR mechanisms are activated (Figure 12). The phosphorylation of H2AX recruits on site MDC1 and either 53BP1 or BRCA1, as upstream regulators of NHEJ and HR repair respectively (Chapman et al., 2012).

The NHEJ corresponds to the main mechanism by which the DSBs get repaired throughout all the phases of cell cycle with a preferential activation in G1. However, NHEJ provides less repair fidelity than HR (Chapman et al., 2012). NHEJ involves the recruitment of Ku70/80 heterodimer and DNA-PKcs to the DSB loci, followed by processing of the DSB by the DNA Ligase IV and Artemis among others. Importantly, while Ku70/80 is recruited to all DSB, DNA-PKcs is involved only in the repair of initially unsolved DSB (Lomax et al., 2013). Once Ku70/80 is recruited on the DSB, NHEJ machinery promotes direct ligation of the DSB ends, but in an error-prone fashion, leading frequently to small insertions, deletion or substitution at the break site (Chapman et al., 2012). Furthermore, misrepair due to ligation of DNA ends of different DSBs will cause translocations, rearrangements and di- or acentric chromosomes, which results in chromosomic aberration and formation of micronuclei (Maier et al., 2016).

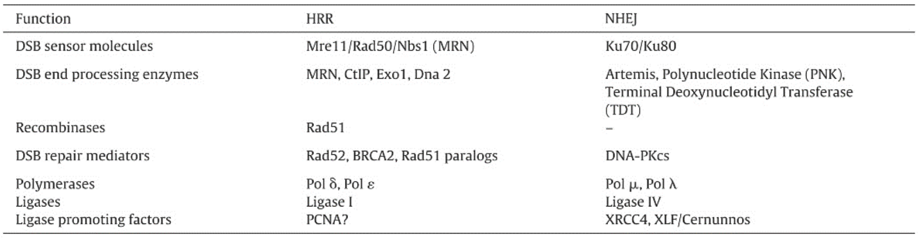

Function	HRR	NHEJ
DSB sensor molecules	Mre11/Rad50/Nbs1 (MRN)	Ku70/Ku80
DSB end processing enzymes	MRN, CtIP, Exo1, Dna 2	Artemis, Polynucleotide Kinase (PNK), Terminal Deoxynucleotidyl Transferase (TDT)
Recombinases	Rad51	–
DSB repair mediators	Rad52, BRCA2, Rad51 paralogs	DNA-PKcs
Polymerases	Pol δ, Pol ε	Pol μ, Pol λ
Ligases	Ligase I	Ligase IV
Ligase promoting factors	PCNA?	XRCC4, XLF/Cernunnos

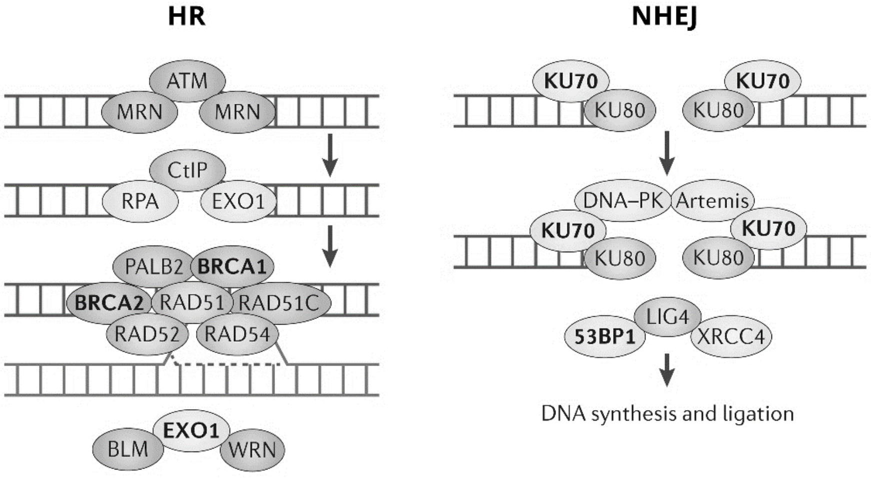

Figure 12: Non-Homologous End-Joining (NHEJ) and Homologous Recombination (HR)
Summary of the DSB repair key proteins involved in HRR and NHEJ are shown separated based on protein function (modified from Bouwman & Jonkers, 2012; Mladenov & Iliakis, 2011).

On the contrary, HR is largely error-free and prevalent after DNA replication (late S/G2 phase), since an identical sister chromatid is available as a template for repair. The HR damage sensor is the MNR complex (MRE11-RAD50-NBS1) and recruits subsequently the HR core repair machinery to the DNA lesion. The HR mediators are RAD51, RAD52 and BRCA2 among others (Kakarougkas & Jeggo, 2014).

Importantly, while most of the DSBs repair proteins seems to function exclusively in NHEJ or HR, a core of common proteins is believed to interact with both. ATM, H2AX, DNA-PK and the MNR complex are required, even if at different levels, for both NHEJ and HR programs (Ciccia & Elledge, 2010; Shrivastav et al., 2008).

SSB lesions and base damages are repaired in cells by the BER pathway, mainly promoted by Poly (ADP-ribose) polymerase (PARP; Javle & Curtin, 2011). Especially, BER removes very efficiently DNA bases that are damaged by oxidation (Bouwman & Jonkers, 2012). Incomplete repair, caused by PARP inhibitor, lead to cell death (Figure 13). Unsolved SSB can be converted to DSB upon DNA replication, as the replication fork meet the unrepaired SSB foci (Lomax et al., 2013), and then can be equally repaired or not.

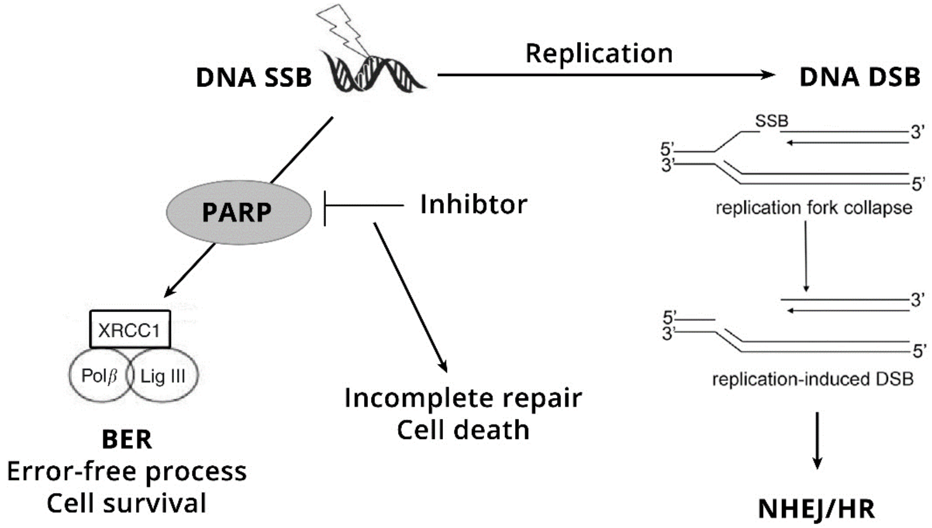

Figure 13: DNA SSB repair

DNA SSBs are repaired by PARP-dependent BER/SSBR. PARP inhibition leads to stall in BER, incomplete SSB accumulation and eventually cell death. If repair is incomplete, then in proliferating cells, the SSBs will cause replication fork stalling and replication-associated DSBs. These are preferentially repaired by error-free HR, but in case of defective HR, DSBs are repaired by error-prone NHEJ (picture modified from Javle & Curtin, 2011; Lomax et al., 2013).

2.3 LINEAR QUADRATIC MODEL

The Linear Quadratic Model (LQM) is a well-validated mathematical model used in clinical radiation oncology (Astrahan, 2008; Emami et al., 2015; Fowler, 2006). It allows quantitative prediction of dose/fractionation dependencies and biological effects with an experimental-based approach. The model has been applied to normal tissues, tumors and cell cultures as well. To date, LQM represent the most common tool used to fit cell survival curves obtained with fractionated doses *in-vitro*. The model is based upon the assumption that the biological response to radiation can be described by an equation with two principle components: one proportional to the dose (α) and another proportional to the square of the dose (β).

$$SF = e^{-(\alpha D+\beta D^2)}$$

Where D is the fraction dose, α is the linear component, β the quadratic component and SF is the cells' surviving fraction.

Alpha is associated to the non-repairable Sublethal Damage (SLD) induced by ionizing radiation on DNA. In terms of radiobiological meaning, α corresponds to cell/tissue intrinsic radiosensitivity, defined as how many logs (to the exponential base *e*) of cell are killed (sterilized) per Gy in a "non-repairable" way. In the equation α is the linear component, being the SLD directly proportional to the dose received.

Conversely, β is associated to the repairable portion of DNA damage, also called Potentially Lethal Damage (PLD). Cell repair include both good-repair and mis-repair, being the mis-repair the accountable of cell mitotic death. β-component, in terms of radiobiological meaning, corresponds to cell/tissue repair capacity.

The β-component derives from evidences of strong association between mitotic death and presence of chromosome aberrations (e.g., dicentric, acentric or centric ring chromosomes; Figure 14). Mis-repair requires cell wrong rejoin of two nearby chromosome breaks caused in a reduced period by two different charged particles. The probability that two chromosomes will be hit by two independent events is proportional to the square of the dose (Brenner, 2008). Consequently, β is the quadratic component of the Linear Quadratic (LQ) equation.

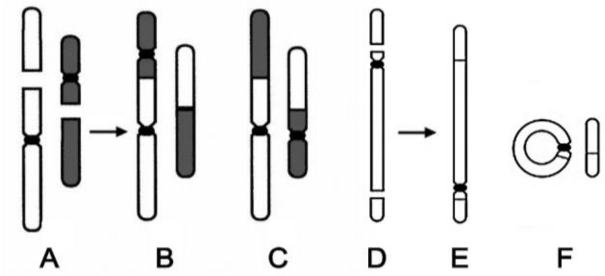

Figure 14: Examples of chromosome aberrations

(A) The picture shows two chromosomes, each one with a DSB. Most DSB are correctly repaired, but a few undergo wrong rejoining. (B) Binary mis-repair can result in dicentric and acentric fragments that generally destroy the proliferative capacity of the cell. (C) Sometimes, the binary mis-repair events produce chromosome reciprocal translocations, which generate large-scale rearrangements and possible oncogenic transformation. (D) A single chromosome with two breaks. (E) Mis-rejoining can give simple intrachromosomal aberrations as pericentric inversion. (F) A second possibility is production of a centric ring with accompanying acentric fragment. DSB are indicated as a gap, centromeres are shown as black constrictions (modified from Brenner, 2008).

Analysis of α and β individual contributions to the LQ curve (Figure 15) shows that lethal lesions, defined by α, determine the initial slope of the curve. Conversely, at low dose β-contribution is highly restricted, indicating that SLD is fully repaired. The β-component starts to dominate at larger doses, where the increasing accumulation of SLD lead to a progressive bend of the curves (Barendsen, 1997). For these characteristics, the LQM describes with a good fit the mammalian cell survival curves that show on a semilogarithmic scale a gradual bending until at least 10 Gy and a trend close to linearity at higher doses (Fowler, 2006).

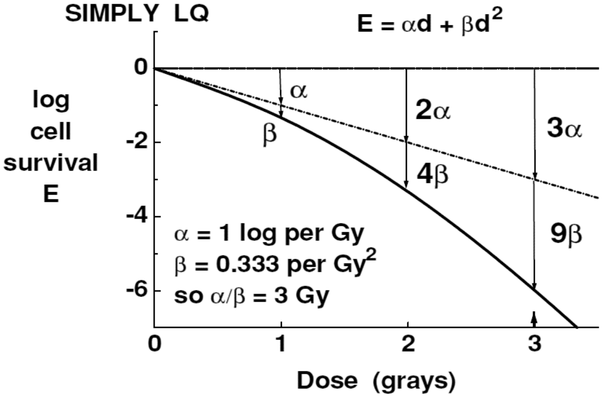

Figure 15: Individual contribution of α- and β-component to the LQ curve

The cell survival curve interpreted by the LQ model. *(legend continued on next page)*

The α-component increases linearly with dose. The β-component increases with the square of the dose (D^2), thus contributing to bend the curve (image from Fowler, 2006).

The third radiobiological parameter is α/β ratio and corresponds to the dose in which single and multi-target mechanisms contribute equally to cell killing *in-vitro*. If α- and β- component curves are plotted individually (Figure 16) the ratio represent the point of intersection between the two curves (Astrahan, 2008).

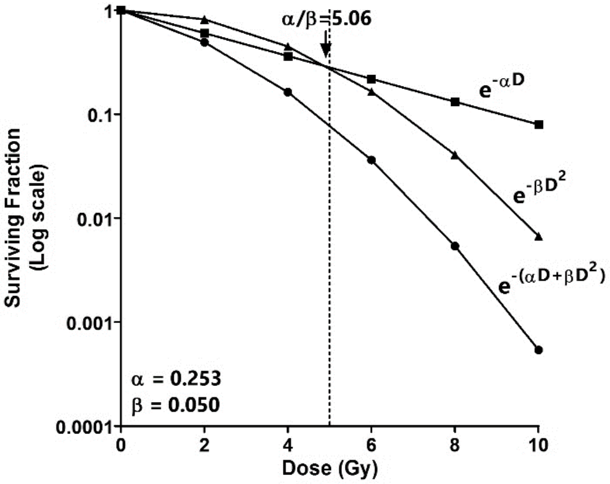

Figure 16: Survival curve according to LQ formula with α- and β- individual curves
The components of cell killing are equal where the curves $e^{-\alpha D}$ and $e^{-\beta D2}$ intersect. This occurs at dose D = α/β (5.06 Gy in this example).

Importantly, the LQ model and its radiobiological parameters can be employed in order to quantify cultures radiosensitivity. In fact, as indicated in Figure 17, a curve with high α describes a radiosensitive cultures, being higher the initial slope with increasing values of α. Similarly, high values of β are associated with a more bended curve and reduced cells' capacity to repair DNA damage (Astrahan, 2008).

On the contrary, the α/β value is mainly employed to evaluate the efficacy of non-conventional fractionation therapy. Briefly, in cultures with high α/β, it is the irreparable PLD produced by single-hit events that exclusively determines the efficacy of fractionated radiotherapy, with no effective benefit given by hypofractionated regimens. In cultures with low α/β ratio, the hypofractionation acquires significant benefit, as β-inactivation mechanism plays a significant role in tumor response (Chapman, 2003; Emami et al., 2015).

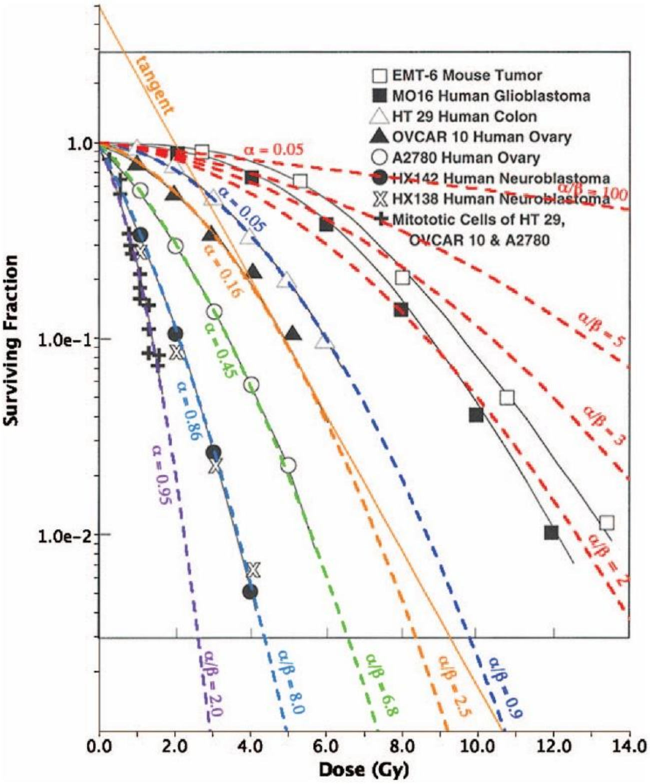

α	β	α/β
0.05	0.001	100.0
0.05	0.010	5.0
0.05	0.017	3.0
0.05	0.025	2.0
0.05	0.056	0.9
0.16	0.064	2.5
0.45	0.066	6.8
0.86	0.108	8.0
0.95	0.475	2.0

Figure 17: Experimental survival curves fitted according the LQM

The LQ model has been applied to survival curves of a number of human and rodent cell lines (modified from Astrahan, 2008). For a better understanding α, β values and their ratio are reported for every curve following the color code. Red curves are all characterized by α = 0.05 and increasing β. The other curves are characterized by increasing values of α and consequently show higher radiosensitivity. The relative α/β ratios are also indicated at the end of every curves.

3 GLIOBLASTOMA INITIATING CELLS

The Cancer Stem Cell (CSC) hypothesis postulated at the beginning of this century provided a new concept to understand the biology of several tumors (Reya et al., 2001). Briefly, the CSC hypothesis proposes that only a limited population of transformed cells within the bulk of the tumor is able to give rise to cancer and to infinitely drive its growth. CSCs are defined as cancer cells that share stem cell properties: self-renewal, asymmetric cell division, infinite growth, and multipotency, the latter exerted by the capacity to differentiate into distinct mature cell types (Vescovi et al., 2006). In addition, CSCs should demonstrate the capability to generate a tumor that summarize key histopathological features of the parental tumor when injected orthotopically in nude mice. Among solid tumors, GBM became paradigmatic for the crucial role of CSC. In fact, although CSCs account for the minority of the cells within the bulk tumor, they appear to be critical for the generation of GBM (Wen & Kesari, 2008).

Within normal tissues, organogenesis and tissue homeostasis occur following a stiff hierarchical organization. In the apex, few somatic organ-specific multipotent stem cells give rise to a progressively differentiated progeny covering the complex architecture of distinct tissues (Figure 18). In a similar fashion, it was hypothesized that some cancers might mirror the same organization, with cancer-stem like cells being capable to generate a wide array of phenotypically different cells within a single tumor (Figure 18). The above mentioned theory, along with the belief that GBM originated mostly from the subventricular zone (SVZ; Hopewell & Wright, 1969), which contains the highest density of astrocyte-like stem cells (Alvarez-Buylla et al., 2002), push researchers efforts toward the isolation and characterization of Glioblastoma Initiating Cells (GICs) within GBM (Galli et al., 2004; Hemmati et al., 2003; Sanai et al., 2005). Remarkably, it is still under investigation whether GICs arise from transformed Neural Stem Cells (NSC) or from differentiated cell type that loses tissue commitment and acquires stem-like features (Figure 18; Zhou et al., 2009).

The CSC hypothesis also suggests that CSCs may contribute to the therapeutic resistance (Reya et al., 2001; Wen & Kesari, 2008). According to that, a therapy will always fail if it is not able to eliminate residual CSC, eventually (Baumann et al., 2008). Consequently, efficacy of the treatment strategies virtually depends on their capability to eradicate both the CSCs and cells composing the bulk tumor (Figure 18).

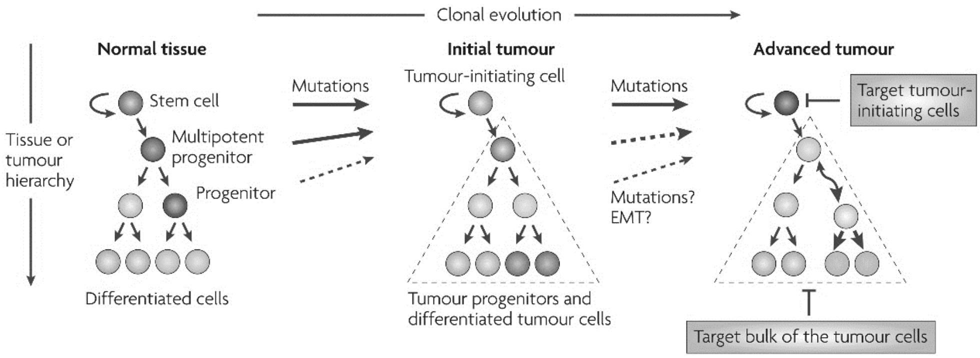

Figure 18: Normal tissue hierarchy and proposed tumor organization
The heterogeneity of cells in normal tissues reflects a hierarchical program of differentiation in which a plethora of differentiated cell types are derived from a common multipotent stem cell through intermediate progenitors. Heterogeneous tumor may be the result of both acquired mutations and aberrant but hierarchical differentiation programs. Picture from Zhou et al., 2009.

In GBM a number of studies proved GICs radio- and chemo-resistance (Bao et al., 2006; Beier et al., 2011; Liu et al., 2006), but still better understanding is needed. In particular, GICs radioresistance was related to preferential activation of DNA damage checkpoint (Bao et al., 2006) and to nuclear translocation of L1CAM intracellular domain (Cheng et al., 2011). Concerning chemoresistance, many potential mechanisms were identified (e.g. *MGMT* promoter methylation, mutations of the mismatch repair system, insufficient drug delivery and presence of drug efflux pumps), but still the issue remains controversial (Beier et al., 2011).

Recent works investigated whether GICs share the same molecular profiles described in GBM (proneural, neural, mesenchymal and classical; Verhaak et al., 2010). Bhat and colleagues identified two mutually exclusive GICs populations bearing distinct molecular signatures (Bhat et al., 2013; Figure 19). The two populations described in Bhat’s work strikingly matched with already described Mes and PN GBM subtypes, with the first class showing marked activation of NF-κB pathway while the second relied more on Notch and PDGFR downstream pathways. In addition, Mes GICs transcriptome showed enrichment of wound response, vasculature formation, and cell motility signatures, whereas PN GICs correlates with differentiated neural or glial cell functions gene sets (Figure 19). Importantly, Mes GICs displayed a more aggressive and radio-resistant phenotype when compared with PN GICs (Bhat et al., 2013). Improved survival after RT of PN mice model was associated to better capacity of PN GICs to induce heterogeneous cell death, including apoptosis and mitotic arrest with

G2/M blockade (Bhat et al., 2013; Halliday et al., 2014). Likewise GBM, in GICs context has been identified the same molecular drivers of the PN to Mes transition, being NF-κB, STAT3, C/EBPβ and TAZ the leading transcription factors (Bhat et al., 2013).

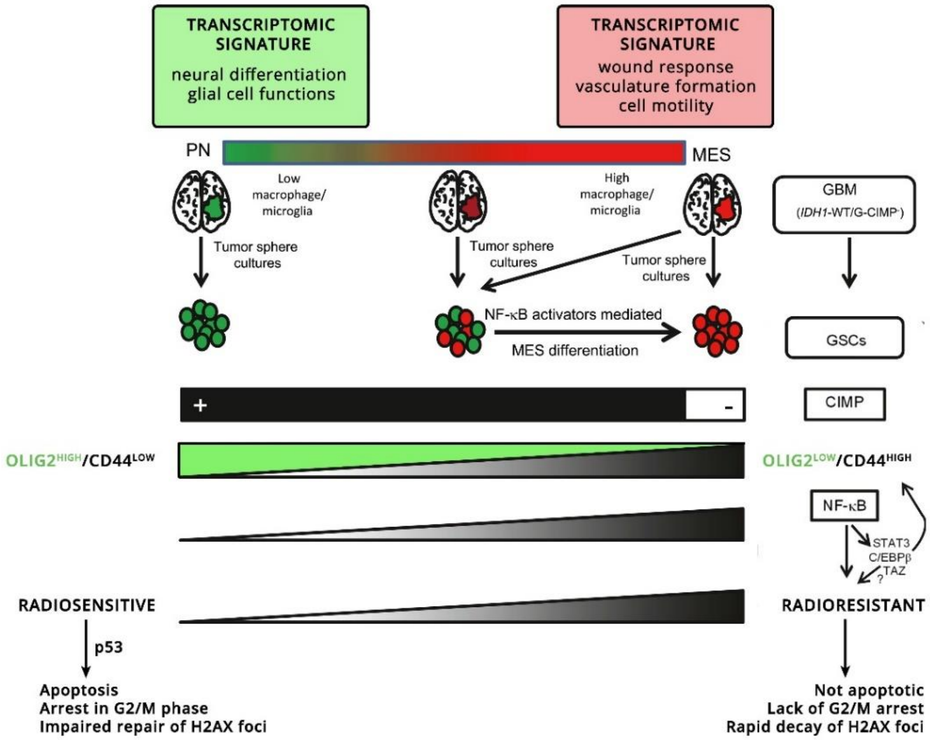

Figure 19: Features Associated with PN and MES transcriptome in GICs

PN GICs tend to be CIMP+ although derived from G-CIMP- tumors that lack the IDH1 mutation. In contrast, MES GICs are CIMP-, predominantly express CD44, are radioresistant, and exhibit constitutive activation of NF-κB and downstream master regulator TFs (STAT3, C/EBPβ, and TAZ). Modified from Bhat et al., 2013.

3.1 ISOLATION OF GICS

Given the increasing interest on GICs for their potential role in GBM outbreak, progression and relapse, many laboratories have tried to selectively isolate and culture them *in-vitro* in order to investigate GICs' biology and learn how to sensitize them to therapies. Nowadays, there is still a lack of overall standardization concerning methods to isolate GICs efficiently. Many efforts have been made to define a set of molecular markers capable to identify selectively GICs within a GBM specimen (see Table 1; Table 2). Despite that, current techniques have not yet defined a molecular profile absolutely representative of the stem-like subpopulation in GBM. Although several markers may be informative, there is still no universal and specific marker that might be faithfully used to discriminate NSCs from CSCs as well as CSCs from their derived progenitors (Brescia et al., 2012).

NAME	SYNONIMS	ROLE
CD15	*FUT4; SSEA-1;* Lewis X	Expressed in adult NSCs and ESC during neural development.
CD133	Prominin-1	Unknown biological function
CD44	-	Cell-surface glycoprotein involved in cell-cell interactions, cell adhesion and migration. Receptor for hyaluronic acid, but can also interact with other ligands (osteopontin, collagens, and matrix metalloproteinases)
L1CAM	L1 cell adhesion molecule; NCAM-L1	Glycoprotein belonging to the immunoglobulin supergene family. Plays an important role in nervous system development, including neuronal migration and differentiation
ITGA6	Integrin subunit α6	Upon heterodimer formation, ITGA6 interacts with ECM proteins including members of the laminin family. In addition, it plays a critical structural role in the hemidesmosome

Table 1: Surface markers commonly used to isolate via FACS cells with CSC features
Data collected from bibliography (Hemmati et al., 2003) and the GeneCards human gene database (Weizmann Institute of Science; www.genecards.org).

NAME	SYNONIMS	FUNCTION	ROLE
NANOG	-	Transcription factor	Involved in ES-cells proliferation, renewal and pluripotency.
OCT4	*POU5F1*	Transcription factor	Plays a key role in embryonic development and ES cells pluripotency.
SOX2	SRY-related HMG-box gene 2	Transcription factor	Works in partnership with OCT4. Expressed in NSCs and the developing neural tube. Required for embryonic development and determination of cell fate, involved in stem-cell maintenance in the CNS.
NES	Nestin	Intermediate filament protein	Required for brain and eye development. Expressed in neural progenitor cells.
CD15	*FUT4; SSEA-1;* Lewis X	Surface protein	Expressed in adult NSCs and ESC during neural development.
CD133	Prominin-1	Surface protein	Unknown biological function
MSI1	Musashi-1	RNA-binding protein	Plays central roles in post-transcriptional gene regulation.

Table 2: Common Embryonic Stem Cell Markers

Data collected from bibliography (Hemmati et al., 2003) and the GeneCards human gene database (Weizmann Institute of Science; www.genecards.org).

A lot of disagreement exists regarding the use of a specific marker or a combination of different markers to selectively identify and isolate GBM CSCs *in-vitro*. Particularly, any of the surface proteins used for isolate CSCs have shown to be necessary or sufficient to isolate cells with stem-cell-like properties. The main concern is given by the expression instability of most of the markers that oscillate in a cell-cycle-dependent manner or in response to environmental clues. Contrarily, there is strong agreement regarding the steps required to validate CSCs stemness. The assessment of indefinite proliferation, self-renewal capability, multi-lineage differentiation and tumor initiating capacity are thought to reliably corroborate the stemness of isolated cells (Vescovi et al., 2006).

3.2 GBM MICROENVIRONMENT AND GICS NICHE

An additional layer of complexity and heterogeneity has been added to GBM biology since different GICs types were detected within the same GBM (Chen et al., 2010) and the key microenvironmental influence on GICs pool has been emphasized (Hambardzumyan & Bergers, 2015). GBM microenvironment is heavily infiltrated with endothelial cells, astrocytes, fibroblast, pericytes, brain-resident microglia, peripheral macrophages and myeloid-derived suppressor cells (Charles et al., 2011). Consequently, it is likely to believe that those non-neoplastic stromal and myeloid cells are establishing fundamental interactions with cancer cells.

It is well known that normal stem cells are tightly regulated and influenced by the surrounding microenvironment or by stem cell niche (Zhou et al., 2009). The stem cell niche is a complex and dynamic microenvironment that actively provides unique support and instructional hint to the stem cells in order to generate and maintain a stable functional stem cell pool (Ellis & Tanentzapf, 2010). In a bidirectional fashion stem cells, as well, appear to influence and modulate the microenvironment that support and fuel their own maintenance. Experimental evidences on GBM reported that GICs are enriched in specific niches, located around tumor vessels or close to areas of necrosis (Heddleston et al., 2011). Recently, three distinct specialized tumor niches have been extensively described in GBM even within the same tumor: the perivascular niche, the invasive niche and the hypoxic niche (Figure 20; Hambardzumyan & Bergers, 2015). All three niches display different morphology and elicit different and specific key functions, including tumor growth, angiogenesis, and tumor invasion. Similarly to normal stem-cell’s niche, it has been reported that the composition of GICs niche and various microenvironmental clues, mainly the hypoxic state, may modulate the GICs phenotype, or selectively promote the growth of a specific GICs subtype (Stopschinski et al., 2013). Similarly, GICs niche are believed to not only harbor GICs cells, but also to actively support their growth and crosstalk with tumor stroma via cell-to-cell contact or paracrine stimuli (Gilbertson & Rich, 2007). In addition, GICs niche has been suggested to potentially contribute to the therapeutical resistance through the stimulation of prosurvival and proangiogenic pathways (Fidoamore et al., 2016). An intriguing hypothesis still to be confirmed, is that alterations of the niche itself might drive the transformation of stem cells into cancer stem cells (Ellis & Tanentzapf, 2010).

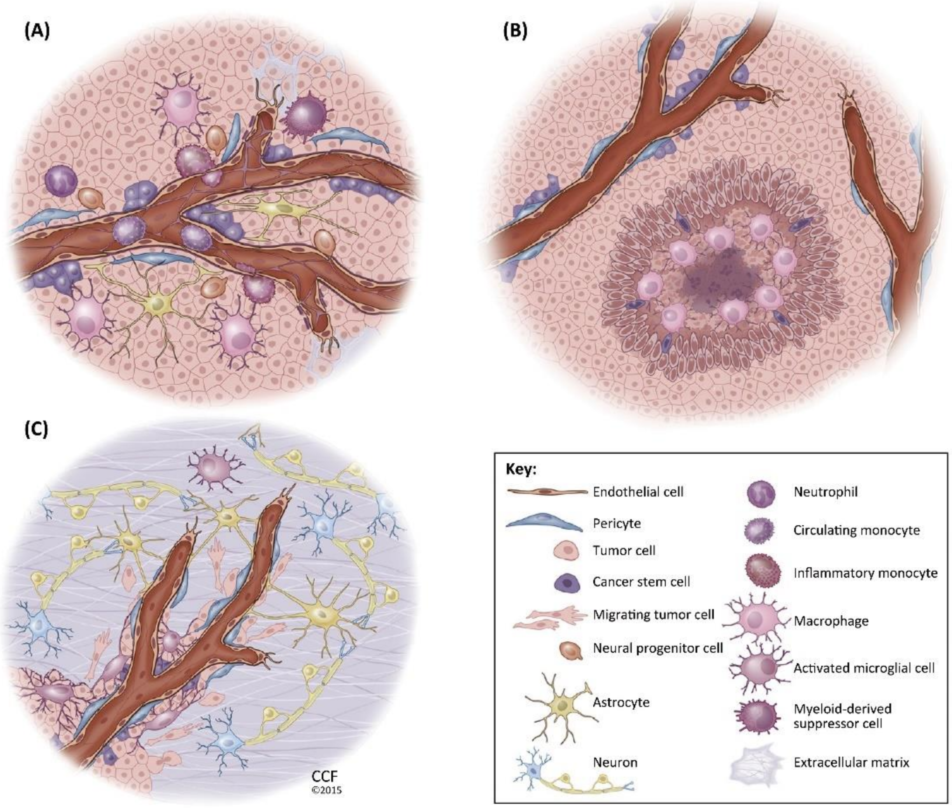

Figure 20: Different Glioblastoma niches

The perivascular GBM niche (A), the hypoxic GBM niche (B) and the invasive GBM niche (C). Picture modified from Hambardzumyan & Bergers, 2015.

The constitutive components of normal stem-cell niches are variable, but commonly include various stromal cell types, matrix glycoproteins, locally and distally secreted signal proteins and local metabolites (Gilbertson & Rich, 2007). In CNS context, the mayor components of the NSC niche Extracellular Matrix (ECM), are chondroitin sulfate proteoglycans, heparan sulfate proteoglycan, laminin, collagen and fibronectin (Bernstock et al., 2014; Mannino & Chalmers, 2011). Importantly, ECM components in GBM are expected to influence GICs survival, migration and resistance to treatment (Fidoamore et al., 2016).

Abnormal degradation and remodeling of ECM occurs during neo-angiogenesis and tumor invasion processes, both crucial hallmarks of GBM and key events of GBM progression (Shimizu et al., 2016). Neo-angiogenesis is the formation of new vessels by redirection of preexisting vascular networks to sustain the avid demands for nutrients of the rapidly growing tumor (Gilbertson & Rich, 2007). After the breakdown of basement membrane mediated by MMPs, ADAM, uPA/uPAR and cathepsin B (Nakada et al., 2007), endothelial cells are able to proliferate and migrate toward cancer cells following chemotactic and pro-angiogenic molecules (VEGF, angiopoietin-1/2). The neo-angiogenic process requires a complex crosstalk between endothelia, tumor cells, ECM components and stromal element of the host microenvironment. Importantly, the GBM abnormal vessel proliferation is believed to potentially generate aberrant cancer stem cell niches, thus favoring GBM progression (Gilbertson & Rich, 2007).

3.3 INTEGRIN FAMILY AND α6 SUBUNIT

The effects of the ECM alteration and remodeling on cells are mainly mediated by the integrins. Integrins are cell type-I transmembrane proteins that establish a bidirectional communication between ECM and adjacent cells. These cell surface receptors essentially bind to ECM and simultaneously establish connection with the cytoskeleton inside the cytoplasmic membrane (Bellail et al., 2004; Shattil et al., 2010). Integrin activation can be triggered by interactions of their cytoplasmic domain with different cytoplasmic factors (inside-out activation) or by the interactions with extracellular ligands (outside-in activation; Shattil et al., 2010). In GBM context, integrins mediate the interaction of cancer cells with ECM and with non-neoplastic elements of the perivascular niche like pericytes and endothelial cells, thus regulating the niche functions (Fidoamore et al., 2016).

Integrin is a large family, composed by several α and β subunit that form heterodimers to constitute a complete integrin receptor. Each combination of heterodimers can recognize distinct ECM components, including laminin, fibronectin, vitronectin, collagen, thrombospondin, and osteopontin; or specific cell surface counter-receptors of the immunoglobulin superfamily (Figure 21).

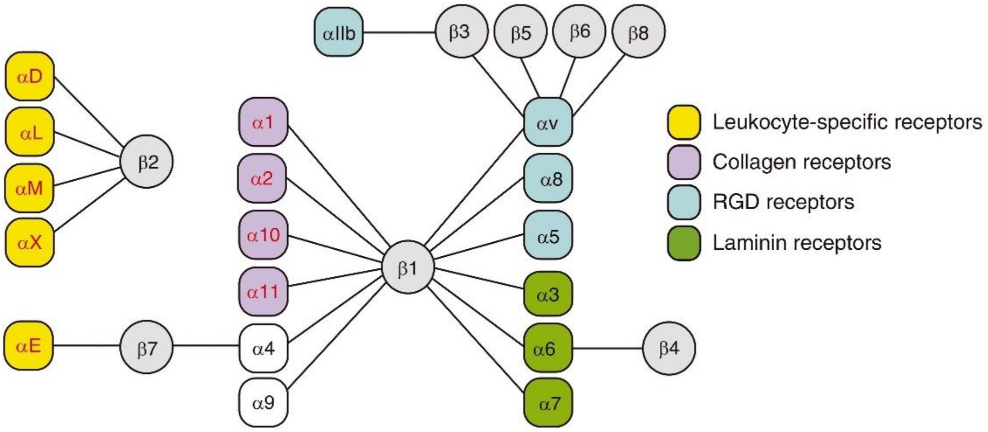

Figure 21: Classification of integrin family of heterodimers based on their ECM affinity
Subunits depicted as line-connected are able to form heterodimers. Picture from Srichai & Zent, 2010.

The link of integrin to ECM establishes cell polarity and mediates cell adhesion, motility and migration, through the reorganization of the cytoskeleton. In addition, integrins regulates proliferation, gene expression and the production of ECM and proteases, leading to the ECM remodeling (Bellail et al., 2004). Unlike growth factor receptors, integrins have no intrinsic enzymatic or kinase activities, but promote signaling cascades by co-clustering with kinases and adaptor proteins in focal adhesion complexes. In detail, the signaling cascades activated by complexed integrins pass through the phosphorylation of the second messenger Focal Adhesion Kinase (FAK) and consequent activation of MAPK, PI3K, NF-κB, and Src cascades (Figure 22; Guo & Giancotti, 2004). Further complexity arises from the existence of integrin-specific downstream pathways. For example, the α6β4 integrin has been reported to specifically cooperate with members of the growth factor receptor family (ERBB2 and MET) and it is likely to promote tumor growth via PI3K (Gambaletta et al., 2000; Trusolino et al., 2001). Importantly, integrins have the ability to enhance either cell survival or apoptotic death depending on their interaction with ECM. Unbounded integrin complex can promote pro-apoptotic cascade via activation of caspase 8 in a process termed integrin-mediated death (Desgrosellier & Cheresh, 2010).

In the stem niche, integrins help define and shape the niche architecture. In particular, they are involved in stem cells homing and maintenance into their niche, they regulate stem cell proliferation and self-renewal, and finally, control the orientation of dividing stem cells (Ellis & Tanentzapf, 2010).

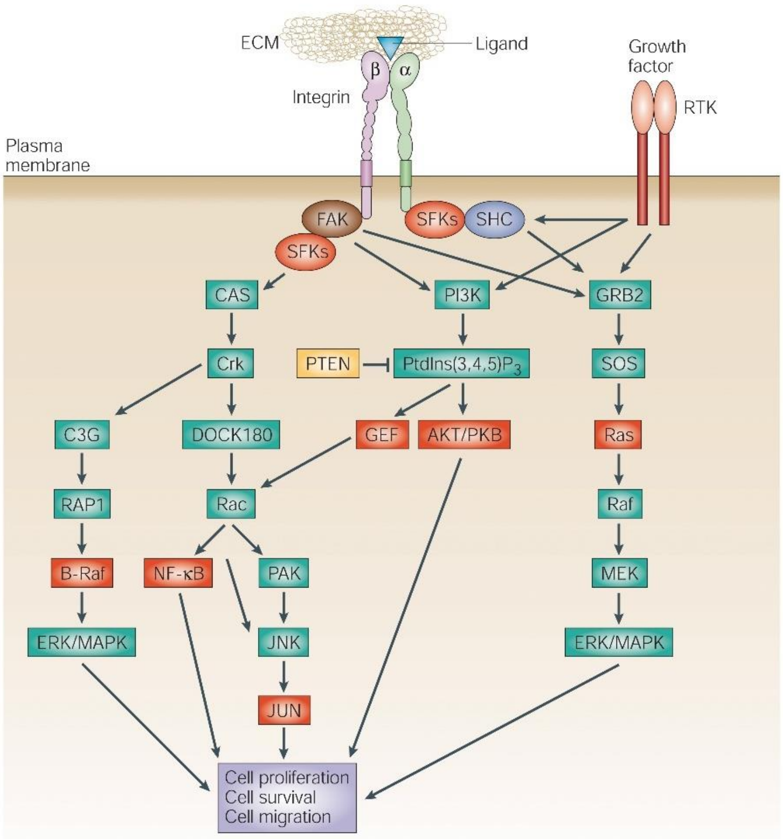

Figure 22: Integrin signaling

Most integrins through their β subunit recruit FAK that once phosphorylated functions as scaffold for the Src-family kinases (SFKs). Complexed SFKs lead to activate NF-κB and JUN TFs, while FAK has been reported to activate also PI3K and ERK/MAPK cascades. Integrin α6β4 has been demonstrated to actively communicate with RTKs for enhancement of downstream signaling pathways. Picture from Guo & Giancotti, 2004.

Integrin subunit α6 (ITGA6; CD49f) forms heterodimer with integrin β1 or β4 subunits to generate the surface receptor for laminin. *ITGA6* was reported to be commonly expressed in independent signatures describing *stemness* identity in ESC, NSC and hematopoietic stem cells (Fortunel et al., 2003). In human mesenchymal stem cells Integrin α6 has been described to maintain pluripotency through prolonged activation of PI3K/AKT pathway and suppression of p53 levels (Yu et al., 2012). Furthermore, adult progenitor cells of the SVZ express on their surface the Integrin α6β1 receptor, which has been demonstrated to play a central role in binding SVZ stem cells to the vascular niche (Shen et al., 2008). In GBM, ITGα6 has been described as hallmark of GICs, being capable to enrich GICs more efficiently than CD133 (Lathia et al., 2010). In this work, Lathia and coworkers underlined the crucial role of ITGA6 in regulating GICs within the GBM perivascular niche and in sustaining GICs stemness and maintenance.

AIMS

“The limits of my language are the limits of my mind. All I know is what I have words for.” LUDWIG WITTGENSTEIN – *Tractatus Logico-Philosophicus* – Proposition number 5.6

The main goal of this PhD thesis was to uncover the mechanisms driving GBM resistance to radiotherapy, with a strong in-focus investigation on Glioblastoma Initiating Cells (GICs).

Toward this end, the research process was developed following these three particular projects:

1. To establish and characterize GICs from patient-derived cultures.
2. To study the radiation-induced molecular mechanisms of established GICs in comparison to non-GICs.
3. To assess the role of Integrin subunit α6 in GICs radioresistance.

MATERIALS AND METHODS

"Imagine two engines, the one being driven by complete and the other by incomplete combustion of coal. A man who knows nothing at all about engines, their structure, and their purpose, may discover the difference. He may, for example, smell it." OTTO WARBURG – *On Respiratory Impairment in Cancer Cells* (1956)

1 GLIOBLASTOMA PRIMARY CULTURES

1.1 SAMPLING AND CULTURES ESTABLISHMENT

Tumor samples were collected during surgery according to the protocol approved by the *Hospital de Bellvitge* Ethics Committee. Histological diagnosis was Glioblastoma multiforme (GBM, W.H.O grade IV; Louis et al., 2007a). Specimens were collected in sterile FBS-free DMEM/F12 media (Invitrogen) supplemented with penicillin and streptomycin cocktail at final concentration 100 U/ml and 0.1 mg/ml respectively. Tissue pieces were rinsed several times in HBSS (GIBCO) previously warmed at 37ºC and then weighted in a sterile eppendorf. Finally, in accordance to laboratory timing, samples were processed or stored at -80ºC in FBS + 10 % DMSO. In particular, samples collected within 1 month from great days off were not processed, as the establishment of primary cultures requires an intense follow-up. Moreover, to frost cells before the achievement of a full-established culture is not recommended.

To achieve a good rate of culture establishment *in vitro*, tissue piece should weigh at least 300 mg. Samples weighting more than 400 mg were processed following two different protocols: one for the establishment of primary Differentiated Glioblastoma Cells (DGC) and one for the establishment of Glioblastoma Initiating Cells (GICs). In case of smaller piece of tissue, samples were processed exclusively following the protocol for the establishment of GICs. When specimen exceed 500 mg, a small piece of tissue was collected and stored for further molecular analysis at -80ºC without FBS.

! *PAY ATTENTION!!! Expect lower establishment efficiency when:*

- *Specimen has been stored at -80ªC*
- *Sample weight less than 300 m*

Either processed or not, each specimen was recorded following the internal lab code (PG* for DGC and PG*s for GICs). Clinical data of each patient (age, gender, PFS, OS) were noted as well.

1.1.1 *ESTABLISHMENT OF PRIMARY DIFFERENTIATED GLIOBLASTOMA CELLS (DGC)*

1. Move the tissue to an empty 100 mm plate and start to break it up mechanically with a pair of sterile tweezers and bistoury. Obtained pieces should pass easily through a 5 ml pipette.

2. Add 9 ml of HBSS previously warmed at 37ºC and move the suspension to a 50 ml falcon.
3. Add 1 ml of collagenase type I (2000 U/ml; Sigma-Aldrich).
4. Incubate the sample at 37ºC for 1 hour on a shaking surface.
5. Ensure that the suspension can pass through a 1000 µl tip.
6. Centrifuge at 300 g for 5 min.
7. Remove all the supernatant and add 1 ml of red blood lysis buffer ACK (Lonza). Dissociate the pellet with a 1000 µl tip. Add 2-3 ml more of ACK and incubate the sample for 4 min at 4ºC. At the end of the incubation time, add 20-30 ml of *Primary* media (see Table M1) to stop the lysing process.

   ! *In case of not clear and defined pellet, it is better to keep the entire suspension through the following steps, in order to avoid culture loss. Erythrocytes will autonomously decrease through time.*

8. Filter the suspension using a 70 µm cell strainer (BD Falcon).

   ! *In case of low cells yield, tissue pieces that remained unstrained in the upper part of filter could be placed in culture as last attempt, even if normally cells are not able to migrate out of the tissue pieces that remained undigested.*

9. Centrifuge at 300 g for 5 min. Remove the supernatant.

   ! *Once again, in case of not clear and defined pellet do not discard the supernatant and seed it too to culture, in order to avoid culture loss.*

10. Suspend the pellet in 3 ml of *Primary* media and seed the cells in a 6-well plate.

REAGENT	CONCENTRATION	COMPANY
DMEM High Glucose, w/o Sodium Pyruvate, w/o L-Glutamine		Biological industries
iFBS	10%	Biological industries
L-Glutamine	2 mM	Biological industries
Penicillin	100 U/ml	Biological industries
Streptomycin	0.1 mg/ml	Biological industries

Table M1: Primary media used for maintenance of primary DGC cultures

FBS was previously heat inactivated (iFBS) at 56ºC for 30 min and then rapidly cooled down on ice.

1.1.2 ESTABLISHMENT OF PRIMARY GLIOBLASTMA INITIATING CELLS (GICS)

1. Move the tissue to an empty plate and start to break it up mechanically using sterile tweezers and bistoury. Pieces should pass easily through a 5 ml pipette.
2. Add 10 ml of pre-warmed and filtered digestion buffer (see Table M2) and transfer the suspension to a 50 ml falcon.
3. Incubate the sample at 37ºC for 20-30 min on a shaking surface.
4. Ensure that the suspension can pass through a 1000 µl tip.
5. Centrifuge at 300 g for 5 min.
6. Remove all the supernatant and add 1 ml of red blood lysis buffer ACK (Lonza). Dissociate the pellet with a 1000 µl tip. Add 2-3 ml more of ACK and incubate the sample for 4 min at 4ºC. At the end of the incubation time, add 20-30 ml of primary media to cells suspension to stop action of the lysing process.

   ! *In case of not clear and defined pellet, it is better to skip this step and keep the entire suspension through the following steps, in order to avoid culture loss. Erythrocytes will autonomously decrease through time.*

7. Filter the suspension in 50 ml falcon using 70 µm cell strainer (BD Falcon).

   ! *In case of low cells yield, tissue pieces that remain unstrained in the upper part of filter could be placed in culture, even if normally cells are not able to migrate out of the tissue pieces that remain undigested.*

8. Centrifuge at 300 g for 5 min. Remove the supernatant.

   ! *Once again, in case of not clear and defined pellet do not discard the supernatant and seed it too to culture, in order to avoid culture loss.*

9. Suspend the pellet in 3 ml of *Stem* media (see Table M3) and seed the cells in a 6-well plate.

REAGENT	CONCENTRATION	COMPANY
Papain	900 µg/ml	Worthington
Cysteine	100 µg/ml	Sigma-Aldrich
EDTA	100 µg/ml (0.34 mM)	Panreac
DNase I	10 µg/ml	Roche

Table M2: Digestion buffer recipe

Prepare fresh 10 ml digestion buffer per sample. Dissolve reagents in HBSS with exception of DNase and filter it with 0.22 µm membrane. Add then DNase under flow hood. Warm it to 37ºC.

1.2 MAINTENANCE OF CULTURES

Cultures were maintained ad 37ºC and 5% CO_2 and experiments were always performed before passage 20. All cultures were routinely tested to be Mycoplasma-free (see paragraph 1.2.3).

1.2.1 MAINTENANCE OF DGC

Differentiated Glioblastoma Cells were maintained in *Primary* media (Table M1). Cells were passed after rinsing with Ca^{2+}/Mg^{2+} free PBS, by means of Trypsin-EDTA digestion (Biological Industries). A sub-cultivation rate of 1:10 was performed twice a week. In order to maintain primary cultures at low working passages cells were stored at -80ºC or in liquid nitrogen. Primary DGC were frosted in FBS + 10 % DMSO.

1.2.2 MAINTENANCE OF GICS

Primary GICs were maintained in *Stem* media (see Table M3). Cultures were passed every week with a sub-cultivation rate of 1:10. Spheroid clusters were mechanically dissociated at every passage with P200 pipette set at 180 µl until the achievement of a single cell suspension.

> ! *The best seeding concentration for fully established primary GICs is around 15-20.000 cell/ml.*

Stem media was prepared following the S. Raffaele Hospital Stem Cell Research Institute (Milan, IT) instructions (Galli et al., 2004; Gritti et al., 1996). *Stem* media and *Hormone mix* (Table M4) should be prepared under the flow hood and then filtered with 0.22 µm vacuum filtration systems (Sarstedt). In order to maintain primary cultures at low working passages cells were stored at -80ºC or in liquid nitrogen in *Stem* media + 10 % DMSO. All experiments were performed before passage 20. Sometimes, in order to clean up culture from cellular debris and fibers, a differential centrifugation was performed. Cells were collected in 50-ml falcon and centrifuged at 70 g during 15 minutes prior addition of DMEM/F12 until 40 ml of total volume.

REAGENT	CONCENTRATION	COMPANY
DMEM/F12	1X	Invitrogen
D-Glucose	33 mM	Sigma-Aldrich
$NaHCO_3$	0.105%	GIBCO Invitrogen
HEPES	5 mM	GIBCO Invitrogen
L-Glutamine	2 mM	Biological industries
Penicillin	100 u/ml	Biological industries
Streptomycin	0,1 mg/ml	Biological industries
Heparin	4 μg/ml	GIBCO Invitrogen
Hormone Mix (see Table M4)	1X	
BSA	2 μg/ml	Sigma-Aldrich
EGF	20 ng/ml	PrepoTech
bFGF	10 ng/ml	PrepoTech

Table M3: "Stem" media recipe

Final concentration of each reagent is reported. Add BSA to Milli-Q® water during continuous stirring and then add remaining reagents under the flow hood. Stock solution concentrations of all reagents are reported in Table M5.

REAGENT	CONCENTRATION	COMPANY
D-Glucose	33 mM	Sigma-Aldrich
$NaHCO_3$	0.1125%	GIBCO Invitrogen
HEPES	5 mM	GIBCO Invitrogen
Putrescine	96.5 μg/ml	Sigma-Aldrich
Insulin	0.25 mg/ml	Sigma-Aldrich
Apo-transferrin	1 mg/ml	Sigma-Aldrich
Selenium	0.3 μM	Sigma-Aldrich
Progesterone	0.2 μM	Sigma-Aldrich
Penicillin	100 u/ml	Biological industries
Streptomycin	0.1 mg/ml	Biological industries

Table M4: "Hormone mix" 10X recipe

Final concentration of each reagent is reported. Add putrescine, apo-transferrin, insulin, selenium and progesterone to Milli-Q® water while stirring. Then, complete the mix under flow hood. Stock solution concentrations of different reagents are reported in Table M5.

REAGENT	CONCENTRATION	SOLUTION PREPARED IN
DMEM/F12	10X	Milli-Q® H_2O
D-Glucose	1.66 M	Milli-Q® H_2O
Heparin	2 mg/ml	Milli-Q® H_2O
EGF	500 µg/ml	Milli-Q® H_2O+ 0.1% BSA
bFGF	25 µg/ml	10 mM Tris+ 0.1% BSA
Insulin	4 mg/ml	HCl 0.1N
Selenium	3 mM	Milli-Q® H_2O
Progesterone	2 mM	EtOH 95%

Table M5: Stem media reagent stock solution preparation

Elution buffer for each reagent and relative stock solution concentrations are reported. After preparation DMEM/F12, D-Glucose and Heparin should be filtered with 0.22 µm pore membrane (Millipore). EGF and bFGF should be prepared under flow hood.

1.2.3 MYCOPLASMA DETECTION TEST

Mycoplasma is a prokaryotic organism that is a frequent contaminant of cell cultures. Because of their small size, Mycoplasmas can be maintained in culture as occult contamination. This organism can modify many aspects of cell physiology, rendering experiments that are conducted with contaminated cells unreproducible and worthless.

Mycoplasma detection was performed by DAPI staining (1 µg/ml) or PCR following published guidelines (Young et al., 2010). In case of mycoplasma contamination of highly valuable cultures, cells were treated with Plasmocin (InvivoGen) following the company guideline. Briefly, cells underwent 2 weeks of intensive treatment with Plasmocin at 25 µg/ml in combination with penicillin and streptomycin. Media and reagent were replaced every 3-4 days. Subsequently, cells were maintained for a month with Plasmocin at 5 µg/ml as a prophylactic measure. Effective Mycoplasma decontamination was always performed at the end of every treatment.

2 PROTEIN DETECTION

2.1 WESTERN BLOT

Protein were extracted from samples after being snap-frozen in liquid nitrogen. DGCs samples were previously PBS rinsed and cells were collected by scraping. Trypsin digestion was not employed to detach cells in order to avoid disruption of membrane proteins. Extraction was performed with 0.3% CHAPS buffer supplemented with protease and phosphatase inhibitors (Table M6). Proteins were then kept on shacking surface for 40-60 min at 4ºC and finally sonicated (Branson Sonifier) following these parameters:

- Timer: Hold
- Duty Cycle: 20%
- Output Control: 3
- Sonicate 3 times

> ! *Do not escape the sonication! Samples would be extremely mucous and impossible to load otherwise.*
>
> ! *Do not centrifuge samples to clarify proteins if you are interested in analyzing membrane proteins!*

Glycerol was added at 10 % concentration to support protein stability once stored at -20ºC. Samples were quantified using Pierce™ BCA Protein Assay Kit (Thermo-Scientific) following the manufacturer instructions.

> ! *Protein concentration can be increased if needed by evaporation. Samples can be concentrated in SpeedVac™ System (Thermo-Scientific) or Concentrator 5301 (Eppendorf) set at 45ºC/max with vacuum for 10-20 minutes. Check the tube at 10, 15 and 20 minutes.*

Samples were then mixed with Protein Loading Buffer (Table M8) at 1 µg/ml protein concentration and boiled for 10 min at 98ºC. Twenty µg of protein per sample was loaded into Acrylamide/Bis-Acrylamide gel 37.5:1 (Bio-Rad) prepared at different concentration (8%, 12% or 15%) depending on which proteins were analyzed. Protein electrophoresis was carried out at constant 110 mV (Mini-Protean, Bio-Rad). The buffer used for protein electrophoresis is described in Table M8. Resolved protein were then blotted onto a PVDF membrane with 0.45 µm pores size (Millipore). Over the years protein blotting was achieved by means of two different equipment: wet

(Mini Trans-Blot, Bio-Rad) and semi-dry (Trans-Blot Turbo, Bio-Rad) transference systems. Wet transference was performed at constant 350 mA for 90 min, whereas semi-dry blotting system allows protein transference in 30 min at 1 A set as maximum and constant 25 V.

REAGENT	FINAL CONCENTRATION	COMPANY
Tris-HCl pH 7.5	10 mM	
NaCl	100 mM	
DTT	1 mM	Sigma-Aldrich
CHAPS	0.3%	Sigma-Aldrich
Phosphatase inhibitors		
NaF	50 mM	AppliChem
B-glycerophosphate	50 mM	Fluka
PhosSTOP	1X	Roche
Protease inhibitors		
Pepstatin A	1 µg/ml	AppliChem
Complete	1X	Roche

Table M6: Protein lysis buffer

DTT, Pepstatin, Complete and PhosSTOP should be added at the moment of use. Other reagents could be mixed and stored at 4ºC. When needed stock solution concentration and preparation of reagent are reported in Table M7.

REAGENT	CONCENTRATION	SOLUTION PREPARED IN
PhosSTOP	10X	Water
DTT	1 M	Water
Pepstatin A	1 mg/ml	MetOH + 10% Acetic acid
Complete	25X	Water

Table M7: Reagents stock solution for protein lysis buffer

For the preparation of Pepstatin A, heat may be required. Warm solution at 37ºC as long as required to dissolve the powder.

Blotted membrane was blocked at room temperature during 1 h with TBS-T 5% non-fat dry milk, and subsequently incubated overnight at 4ºC with the primary antibody chosen (see Table M9). The day after, membrane was washed for 7 min three times with TBS-S and then incubated for 1 h at room temperature with secondary antibody horseradish peroxidase-conjugated. After three further washes of 7 min each in TBS-T, membrane was finally incubated with ECL-Prime (GE Healthcare). Buffers used for protein blotting and detection are listed in Table M8. Capture of chemo-luminescence was performed with LAS-3000 (FujiFilm) by means of ImageReader software (version 2.2, FujiFilm). Images were captured with machine set as described:

- Lite version
- Exposure type: Increment
- Exposure time: 30 sec
- Sensitivity: standard

> ! *Amino acids phosphorylation and difficult proteins detection could benefit from longer exposure time (3 minutes, 5 minutes or even 10 minutes) with Exposure type still set in Increment mode.*

Densitometric analysis were carried out using Multi-Gauge software (FujiFilm Corporation). Unless otherwise specified, densitometric data were normalized to β-actin expression.

> ! *Membrane could be re-incubated with further primary antibody, after being re-blocked with TBS-T 5% nonfat dry milk for at least 30 min.*

BUFFER	COMPOSITION
Protein Loading Buffer	1X Sample Buffer (4X) 100 mM DTT 0.002% bromophenol blue
Sample Buffer (4X)	320 mM Tris-HCl pH 6.8 8% SDS 10% Glycerol
Running Buffer (10X)	250 mM Tris-base 1.92 M Glycine 1% SDS pH 8.3
Transfer Buffer (10X)	250 mM Tris-base 1.92 M Glycine pH 8.3
Transfer Buffer	1X Transfer Buffer (10X) 20 % MetOH
Anode Transfer Buffer	0.3 M Tris-base 20% MetOH
Cathode Transfer Buffer	40 mM 6-aminocaproic acid 20% MetOH
TBS (10X)	200 mM Tris-HCl 1.37 mM NaCl pH 7.6
TBS-T	1x TBS (10X) 0.1 % Tween

Table M8: Buffers used for Protein Manipulation

When not indicated, buffers concentration correspond to 1X. Transfer Buffer was applied for wet protein blotting system, whereas Anode and Cathode Transfer Buffer were employed for semi-dry transference.

ANTIGEN	DIL.	S.	DILUTED IN	CLONE / #REF	COMPANY
			Primary antibodies		
L1CAM	1:1000	[M]	5% BSA	2C2	Abcam
ITGA6	1:500	[R]	5% BSA	HPA012696	Novus Biologicals
CD44	1:100	[M]	5% BSA	156-3C11	Thermo-Scientific
p-STAT3 (Tyr705)	1:2000	[R]	5% BSA	D3A7	CST
p-STAT3 (Ser727)	1:500	[M]	5% BSA	788335	RD System
STAT3	1:2000	[R]	5% BSA	79D7	CST
p-AKT (Ser473)	1:1000	[R]	5% BSA	#9271	CST
p-PDH (Ser293)	1:10000	[R]	5% BSA	AP1062	Calbiochem
PEPCK-M	1:1000	[R]	5% BSA	70359	Abcam
β-Actin	1:5000	[M]	5% dry milk	AC-15	Sigma-Aldrich
			Secondary antibodies		
anti-Mouse	1:5000	[S]	5% dry milk	#NA931V	GE Healthcare
anti-Rabbit	1:5000	[D]	5% dry milk	#NA934V	GE Healthcare
anti-Mouse	1:80,000	[G]	5% dry milk	#A9917	Sigma-Aldrich
anti-Rabbit	1:50,000	[G]	5% dry milk	#A0545	Sigma-Aldrich
anti-Rabbit	1:10,000	[G]	5% dry milk	R-05072	Advasta

Table M9: Antibodies employed in Western Blot detection

For all antibodies used it is reported the working dilution (DIL.), the biological source (S.), the dilution buffer, the clone number or antibody reference (#REF) and the company. Biological source of both primary and secondary antibodies is indicated as [M] mouse; [R] rabbit; [S] sheep; [D] donkey; [G] goat. Antibodies were diluted in TBS-T plus either 5% BSA or 5% nonfat dry milk. Sigma-Aldrich secondary antibodies were previously diluted 1:20 in TBS-T with 5% BSA.

2.2 IMMUNOFLUORESCENCE

Cells were seeded in 12-well plate onto Ø15 mm sterile coverslips at specific concentration defined for both DGC and GICs in following paragraphs (2.2.1 and 2.2.2). Then, cells were PBS rinsed and fixed with fresh 4% paraformaldehyde (PFA) during 20 min at room temperature. The following steps were then executed:

1. Rinse twice coverslip with PBS.

   - ! *Cells can be stored over a month at 4ºC after this step, if abundantly covered with PBS.*

2. Permeabilize samples with PBS containing 0.1% Triton X-100 during 10 minutes at room temperature.
3. Block unspecific interaction throughout 2 hours with 10% Normal Goat Serum (NGS; GIBCO) in PBS containing 0.1% Triton X-100.
4. Incubate samples overnight at 4ºC with selected primary antibody (Table M10). Incubate negative control sample with only PBS containing 0.1% Triton-X and 1% of NGS.

   - ! *Samples were incubated in a humid chamber with antibody diluted in a 40 µl drop upon the coverslip. It's a good tip to reduce significantly the amount of reagent employed.*
   - ! *If co-localization of two or three antigens is required, incubate cells together with all antibodies. In this case, it is mandatory to add all negative controls needed to exclude antibodies cross-reactivity.*

5. Rinse three times coverslip with PBS.
6. Incubate samples along with negative controls with secondary antibody during 1 hour at room temperature and protected from the light (see Table M11).
7. Rinse three times coverslip with PBS.
8. Incubate samples with DRAQ5 (1:2500; Biostatus) during 1 hour at room temperature and protected from the light.
9. Rinse three times coverslip with PBS.
10. Mount coverslips onto slides with a drop of Fluoroshield (Sigma-Aldrich).

Samples were stored protected from light at 4ºC and evaluated within a month. Micrographs were captured with a Leica TCS-SL Spectral Confocal Microscope (Leica Microsystems) coupled with LCS image processing software (Leica).

2.2.1 IMMUNOFLUORESCENCE OF DGC

Primary DGC were seeded onto sterile coverslip at defined concentration of 4 x 10^4 cells/well. Then, cells were allowed to settle down and to grow for 24 hours before proceeding with staining procedure.

2.2.2 IMMUNOFLUORESCENCE OF GICS

GICs samples were processed following the same procedure described previously (paragraph 2.2) with minor modification. According to previous works (Sasaki et al., 2010) samples were left without moving for 5 minutes after every steps, especially rinses, to reduce the cell loss during staining protocol.

The protein expression assessment of GICs in single-cell culture was carried out by seeding 1 x 10^5 cells per coverslip. GICs were seeded in excess due to the high percentage of cell loss throughout the protocol. Then, cells were allowed to settle down for 24 hours and subsequently samples were processed as described previously. On the contrary, when the protein distribution was analyzed in cells associated in spheres, an additional step was required. Cells were grown and let proliferate until the state of spheres in 75 cm^2 flask. Then, 1 ml was collected from culture. Cells were pelleted down, dissociated and counted. Then, the volume of culture needed to catch 3 x 10^5 cells was seeded onto each coverslip. Cells were allowed to settle down for 3-6 hours and then were processed for immunofluorescence.

2.2.3 γ-H2AX ASSAY

The detection of histone H2AX phosphorylated at Ser139 (γ-H2AX) was performed by immunofluorescence. Cells were irradiated with the indicated doses, and at the indicated time, samples were rinsed, fixed and processed as described below (paragraph 2.2). Nuclei and foci were counted using Image J software (National Institute of Health, United States) following these parameters:

- Binary
- Particles size: 3-140 cm^2
- Particles circularity: 0.00-1.00

Between five and eight images were analyzed for each condition.

ANTIGEN	DILUTION	SOURCE	CLONE / #REFERENCE	COMPANY
CNPase	1:100	[M]	11-5B	Sigma
GFAP	1:50	[R]	#Z0334	Dako
TUJ1	1:1000	[R]	#PRB-435P	Covance
MAP2	1:100	[M]	HM-2	Sigma
VIMENTIN	1:100	[M]	3B4	Dako
CD44	1:100	[M]	AC-15	Thermo-scientific
L1CAM	1:1000	[M]	2C2	Abcam
ITGA6	1:100	[Rt]	NKI-GoH3	Millipore
γ-H2AX (Ser139)	1:500	[M]	JBW301	Millipore

Table M10: Primary antibodies employed in Immunofluorescence protocol

Antibodies were prepared in PBS containing 0.1% Triton-X and 1% of Normal Goat Serum (GIBCO). Biological source of primary antibodies is indicated as [M] mouse; [R] rabbit; [Rt] rat.

SPECIFICITY	DYE		COMPANY	REFERENCE
anti-Rat	Alexa-488	Goat IgG (H+L)	Invitrogen	A11006
anti-Mouse	Alexa-488	Goat IgG (H+L)	Invitrogen	A11001
anti-Rabbit	Alexa-488	Goat IgG (H+L)	Invitrogen	A11034
anti-rabbit	Alexa-555	Goat IgG (H+L)	Invitrogen	A21430
anti-mouse	Alexa-555	Donkey IgG (H+L)	Invitrogen	A31570
anti-mouse	Alexa-647	Donkey IgG (H+L)	Invitrogen	A31571
anti-mouse	Cy3	Donkey IgG (H+L)	Jackson	715-166-151

Table M11: Secondary antibodies employed in immunofluorescence technique

Secondary antibodies and DRAQ5 were diluted in PBS at a working concentration of 1:400.

2.3 HISTOLOGICAL TECHNIQUES

Histological samples were obtained from mouse brain after intracranial injection and patient post-surgical specimens, both paraffin embedded. Mouse brains were sampled in proper cassette, fixed with 4% PFA for 6 hours at 4ºC and then dehydrated with increasing EtOH concentration. The dehydration process is accomplished by passing the tissue through the steps indicated below:

1. Incubate samples 3 hours in EtOH 70º
2. Leave sample overnight in EtOH 96º
3. Incubate 4 hours in absolute EtOH

After dehydration, the tissues were cleared in xylene during 30-45 minutes and then immersed in paraffin: 1-step paraffin for 3 hours plus a 2-step with pure paraffin overnight. Finally, brain pieces were included in paraffin wax individually.

> ! *Each change should be performed at least into 4-times more volume compared to the volume of the cassettes treated.*
>
> ! *The paraffin tissue block can be stored at room temperature for years.*

Section were cut at 4-µm thickness in a microtome and mounted on 0.05% poly-L-lysine (Sigma-Aldrich; dilution 1:1 in water) coated glass microscope slide. Slides were then heated at 56ºC for 1 hour and left overnight at 37ºC.

2.3.1 HEMATOXYLIN/EOSIN STAINING

Slides were stained in rectangular staining glass dishes as indicated below:

1. Deparaffinize slides in four changes of xylene, 5 min each.
2. Re-hydrate section in a series of decreasing ethanols: three changes in 100º EtOH, three changes in 96º, final transfer in 70º and 50º EtOH, respectively for 5 minutes each.
3. Stain in Harris Hematoxylin (Sigma-Aldrich) during 5 minutes

> ! *Filter hematoxylin with a filter paper every time before use.*

4. Wash in running tap water for 5 minutes.

> ! *BE CAREFULL, tap water stream should be placed at the corner of the cuvette, to avoid section detachment and lost.*

5. Differentiate in 1% Acid alcohol (1% HCl in 100º EtOH) with three quick dips. Hematoxylin stain turn into a winy red-purple color.
6. Wash in running tap water for 5 minutes.

7. Bluing in 0.2% ammonia water for 5-9 dips until sections turn into shiny blue color.
8. Wash in running tap water for 5 minutes.
9. Counterstain in Eosin solution (Sigma-Aldrich) for 9 dips.
10. Dehydrate sections through a series of ethanols, three changes at 96º EtOH plus three more changes in 100º EtOH. Passages are direct, with no incubation time.
11. Clear in four changes of xylene.
12. Mount section with DPX mounting medium (Sigma-Aldrich).

2.3.2 IMMUNOHISTOCHEMISTRY

Immunohistochemistry was performed in rectangular staining glass dishes until step n.6 following the protocol indicated below:

1. Deparaffinize slides in four changes of xylene, 5 min each.

   ! *For human brain sections elongate dewaxing period from 5 minutes to 10 minutes.*

2. Re-hydrate section in a series of decreasing ethanols: three changes in 100º EtOH, three changes in 96º, final transfer in 70º and 50º EtOH, respectively for 5 minutes each.
3. Wash sections in distilled H_2O for 10 minutes and after in PBS for 10 more minutes.
4. Block endogenous peroxidases with 3% hydrogen peroxide solution (3% H_2O_2 + 30% MetOH in PBS) during 15 minutes protected from light.
5. Rinse sections in distilled H_2O for 10 minutes and then perform two changes in PBS of 5 minutes each.
6. Treat slides for heat-mediated antigen unmasking using boiling citrate buffer (1.8 mM citric acid monohydrate and 8.2 mM tri-sodium citrate, pH 6.0) during 20 minutes.
7. After antigen-retrieval assemble slices in Sequenza Slide Rack (Shandon) coupled with Coverplate™ (Shandon).

   ! *The volume/sample of reagent from now on is 100 µl.*

> ! *Sections of human brain should be maintained in rectangular glass dishes, until incubation with NGS blocking solution or antibodies. Incubations are performed horizontally with reagent-drop placed onto the slice and covered with a piece of Parafilm®. Slides were then placed into a humidified chamber for the indicated incubation time.*

8. Rinse slides with two changes of PBS of 5 minutes each, plus three additional washes with 0.2% PBS-Triton X (PBS-T) of 5 minutes each.
9. Block non-specific staining with 10% NGS in 0.2% PBS-T during 2 hours protected from light.
10. Incubate samples overnight at 4ºC with the indicated concentration of primary antibody (see Table M12) diluted in 1% NGS in 0.2% PBS-T or in Dako REAL™ antibody diluent (Dako; S2022).

> ! *Dako REAL™ antibody diluent ensures a better and cleaner stain of sections. Use it preferentially for human brain slices.*

11. Leave slide rack 30 minutes at room temperature and then rinse samples with three changes of 0.2% PBS-T, and three changes of PBS, of 5 minute each.
12. Incubate sections during 1 hour at room temperature with biotinylated secondary antibody (see Table M13) prepared at 1:100 and diluted in PBS with 0.1% NGS.
13. Rinse slides three times with PBS with 5 minutes incubation time.
14. Incubated sections during 1 hour at room temperature with streptavidin-HRP diluted 1:400 in PBS.
15. Rinse slides with three changes of PBS of 5 minutes each.
16. Develop sections with DAB+ Chromogen (DAKO) diluted 1:50 in PBS. Incubation time could vary between 2 and 20 minutes.

> ! *Do not forget that DAB is a suspected carcinogen.*

17. Counterstain with pure Harris Hematoxylin (Sigma-Aldrich) for 3 minutes.
18. Stop reaction with running tap water for 5 minutes.

> ! *BE CAREFULL, tap water stream should be placed at the corner of the cuvette, to avoid section detachment and lost.*

19. Dehydrate sections through a series of ethanols, three changes at 96º EtOH plus three more changes in 100º EtOH. Passages are direct, with no incubation time.
20. Clear in four changes of clean xylene.
21. Mount section with DPX mounting medium (Sigma-Aldrich).

ANTIGEN	DILUTION-M	DILUTION-H	CLONE	COMPANY
Vimentin [M]	1:100	1:10	3B4	Dako
GFAP [R]	1:500 (*)	1:500 (*)	6F2	Dako
CD44 [M]	1:100	1:5	AC-15	Thermo-Scientific

Table M12: Antibodies employed for immunohistochemistry

Dilution is differentially specified for mouse brain samples (M) and for human brain samples (H). Biological source of reported antibodies is indicated as [M] mouse; [R] rabbit. (*) Performed in the pathological service of Bellvitge Hospital.

REAGENT		REFERENCE	COMPANY
Biotinylated horse anti-mouse	IgG (H+L)	BA-2001	Vector
Biotinylated goat anti-rabbit	IgG (H+L)	BA-1000	Vector
Streptavidin-biotinylated horseradish peroxidase complex	-	RPN1051V	GE Healthcare

Table M13: Reagent used for immunohistochemistry

3 FLUORESCENCE-ACTIVATED CELL SORTING (FACS)

Cells were collected, dissociated and counted to prepare tubes with 2 x 10^6 cells (GICs samples), 5 x 10^5 cells (DGC samples) plus 2 x 10^5 cells per control tube. ITGA6 was labeled indirectly by means of immunofluorescence staining method (protocol detailed below). Dilution and washes were performed in dilution buffer (0.5% BSA and 2 mM EDTA dissolved in PBS; pH 7.2) warmed at 37ºC. Tubes not incubated with primary antibody were added to the experiment as negative control. Cells were sorted using MoFlo Astrios (Beckman Coulter).

1. To prevent unspecific signals block cells during 15 minutes with 300-µl/sample (1 ml for GICs tubes) of 10% NGS prepared in dilution buffer. Perform incubation at room temperature protected from light.
2. Add dilution buffer to samples and then centrifuge at 300 g for 5 minutes.
3. Resuspend cells with 200 µl of anti-ITGA6 antibody solution prepared at 1:100 (500 µl for GICs tubes; Table M10) in dilution buffer with 10% NGS. Incubate samples protected from light during 8 minutes at room temperature and then 8 additional minutes at 4ºC.
4. Add dilution buffer to samples and then centrifuge at 300 g for 5 minutes.
5. Rinse cells twice with 500 µl of dilution buffer. Between washes, pellet down cells at 300 g for 5 minutes.

   ! *From now on samples should be kept protected from light to avoid decay of fluorescent signal.*

6. Incubate samples during 15 minutes at 4ºC with 100 µ of secondary antibody (Alexa-488 anti-rat; Table M11) diluted at 1:400 in dilution buffer with 1% NGS (500 µl for GICs tubes).
7. Add dilution buffer to samples and then centrifuge at 300 g for 5 minutes.
8. Rinse cells twice with 500 µl of dilution buffer. Between washes, pellet down cells at 300 g for 5 minutes.
9. Resuspend cells in 500 µl of dilution buffer and then filter cells with cell-strainer (polystyrene round-bottom tube with cell-strainer cap, Falcon) to avoid cell aggregates.

   ! *A part of the sample could be stained with DAPI to set gate and to discard dead cells.*

4 RNA DETECTION

RNA was retro-transcribed and expression was normally analyzed by means of Real-Time PCR assay (qPCR, paragraph 4.1). Semi-quantitative RNA detection by PCR is illustrated in paragraph 4.3. Instead, the extraction of whole transcriptome and analysis by means of Microarray chip are described aside in paragraph 4.4.

4.1 RNA EXTRACTION AND REVERSE-TRANSCRIPTION

Total RNA was extracted from either tissue or cells after being snap-frozen in liquid nitrogen. In particular, DGCs samples were previously PBS rinsed and cells were collected by scraping. Extraction was performed with TRIsure (Bioline) following the manufacturer guidelines. For details on brain-tissue RNA extraction and analysis see paragraph 4.2.1.

! *4 µl of Glycogen type III (20 mg/ml, Sigma-Aldrich) were added per 500 µto each tube along with isopropyl alcohol, to ease pellet visualization.*

! *Pellets were air-dried for 1-2 hours underneath a light at room temperature, paying attention not to over-dry.*

Total RNA concentration and quality were assessed by Nanodrop® Spectrophotometer (Thermo-Scientific).

! *RNA concentration can be increased if needed by evaporation. Samples can be concentrated in SpeedVac™ System (Thermo-Scientific) or Concentrator 5301 (Eppendorf) set at 30°C/max with vacuum for 10-20 minutes. Just be careful not to over-dry. Check the tube at 10, 15 and 20 minutes.*

Reverse transcription was performed with the High Capacity cDNA Reverse Transcription kit (Applied Biosystems) following manufacturer's instruction.

4.2 REAL-TIME PCR

To quantify the gene expression the quantitative Real-Time PCR (qPCR) was employed. Some of the assay probes used do not span an exon-exon boundary and may detect genomic DNA as well. Consequently, RNA was treated with RNase-free DNase I (Thermo-Scientific) prior to Reverse-Transcription reaction. 1 µg of RNA was treated per 10-µl reaction (100 ng/µl reaction concentration) and RNA concentration was newly determined by spectrophotometry (Nanodrop®).

! *Exclusively probes with Assay ID suffix "_m1" span an exon junction.*

Reverse transcription was then performed with minor modification required by the drastic decrease of RNA concentration induced because of DNase treatment. In particular, only 1 µg of treated RNA was retro transcribed per 20-µl reaction. Finally, qPCR was performed in the ABI Prism 7900HT fast real-time PCR System (Applied Biosystems) employing SensiFAST™ Probe Hi-ROX mix (Bioline) and the validated Taqman® Gene Expression Assays (Applied Biosystems, see table). Samples were loaded on MicroAmp® Optical 384-well plate (Applied Biosystems) in duplicate following the 11-µl reaction mix indicated below:

SensiFAST™ Hi-ROX mix (2x)	5.5 µl
Assay Probe (20x)	0.5 µl
50 ng cDNA	5 µl
Mix total volume	11 µl

! *cDNA was diluted in Milli-Q® water recently collected.*

Gene expression analysis was performed with SDS Software (version 2.2.2, Applied Biosystems). Data analysis is based on ΔCt method. The ΔCt value was obtained by subtracting the mean of Ct values from housekeeping genes to the target gene Ct value, as detailed below. Housekeeping genes used were *GAPDH* and *GUSB* if not otherwise specified (see Table M14). In particular, for RNA extracted from tissue samples, specific genes were employed as normalizer (see paragraph 4.2.1).

$$\Delta Ct = Ct_{target} - \frac{(Ct_{GAPDH} + Ct_{GUSB})}{2}$$

The relative mRNA expression level of each gene was obtained by the formula [$2^{-\Delta Ct}$]. When plot indicates gene relative amount, data were obtained by the ΔΔCt method. The ΔΔCt value was calculated as follow:

$$\Delta\Delta Ct = \frac{2^{-\Delta Ct_{sample}}}{2^{-\Delta Ct_{control\,samples}}}$$

In case of molecular subtype analysis, data are presented in a comparative heatmap as metagene score after Z-score correction (see paragraph 4.2.2). For details on the transcriptomic response to RT displayed as clusters see paragraph 4.2.3.

GENE NAME	ALIAS	FUNCTION
GAPDH	Glyceraldehyde-3-Phosphate Dehydrogenase	Glycolytic and gluconeogenic enzyme
GUSB	Glucuronidase β	Lysosomal hydrolase, degradates glycosaminoglycans
IPO8	Importin 8	Nuclear import of proteins
HPRT1	Hypoxanthine Phosphoribosyltransferase 1	Synthesis of purine nucleotides
TBP	TATA Box Binding Protein	Subunit of TFIID which coordinates the initiation of transcription by RNA polymerase II

Table M14: Housekeeping genes employed for RealTime-qPCR normalization

GAPDH and *GUSB* were employed to normalize mRNA levels obtained from *in-vitro* samples, either GICs or DGC. IPO8, HRPT1 and TBP were tested as housekeeping genes for normalization of mRNA content in GBM tissue samples (further details in paragraph 4.2.1).

4.2.1 RNA DETECTION IN TISSUE

Samples previously stored at -80ºC were weighted and 20-50 mg of tissue was crushed with a pestle in a ceramic mortar maintained in liquid nitrogen. The frost powder obtained were dissolved in 1 ml of Trisure per 25 mg of weight. Samples were then were processed as described above. Gene expression level of tissue samples were indicated as gene relative amount after standardization with a control sample. Brain frontal cortex sample from healthy donor was kindly provided by I. Ferrer's lab (Sample code: #07A9CF). The microdissection of the control sample was performed trying to achieve the maximum amount possible of white matter.

According to bibliography (Kreth et al., 2010; Valente et al., 2009), it was necessary to define suitable endogenous control genes for the normalization of mRNA levels in GBM tissue samples. Consequently, it was investigated the stability of a pool of five putative housekeeping genes: TBP, IPO8, HRPT1, GUSB and GAPDH. Transcriptional levels of the selected genes were determined by q-PCR in a panel of 11 different tissue samples, including 7 GBT and 4 control tissues. To compare the expression levels among samples, the cycle threshold values were directly plotted (Figure M1). Among the analyzed set of genes, GAPDH displayed a diverse tendency and consequently it was discarded. Within the group of candidates with better correlation, TBP and IPO8 were selected as putative endogenous controls to normalize the expression of target genes.

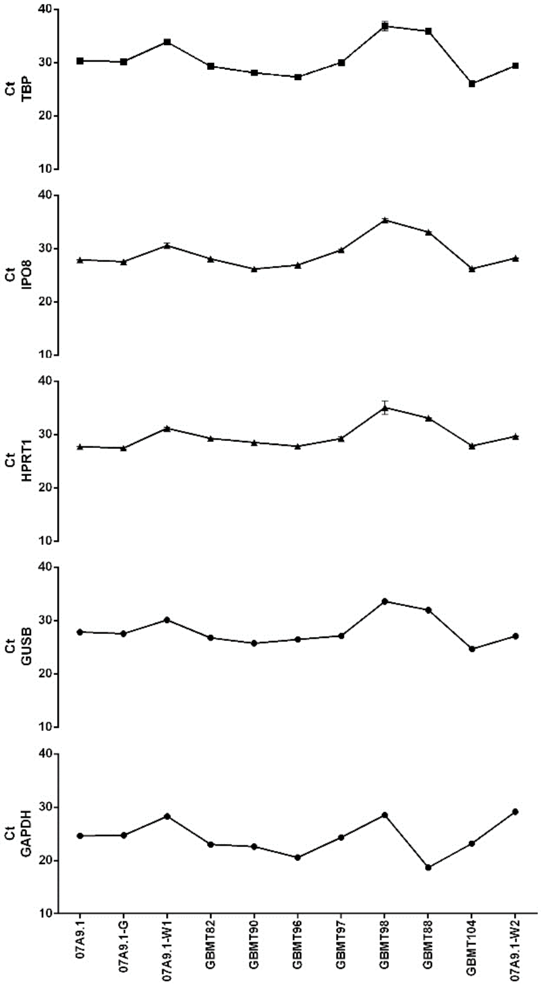

Figure M1: Selection of Housekeeping genes for tissue GBM sample

Ct values were plotted as raw data. Sample 07A9.1 was the internal control from a healthy brain specimen. Samples 07A9.1-G and 07A9.1-W1/2 were extracted from the internal control trying to isolate respectively grey matter (G) and white matter (W).

4.2.2 METAGENE SCORE AND Z-SCORE CORRECTION

A Z-Score is a statistical tool to standardize individual element in a group. It is a measure of the relationship between the specific element and the mean of the group. A Z-score of zero means that the element is equal to the mean. A Z-score can also be positive or negative, indicating whether the element in analysis is above or below the mean and by how many standard deviations it is from the mean.

For the PN/Mes metagene calculation, the expression of four PN (SOX9, OLIG2, SOX2 and CD133) and four Mes (FN1, YLK-40, CD44 and CTGF) genes were analyzed by q-PCR. The relative mRNA expression level of each gene was calculated by the formula [$2^{-\Delta Ct}$]. For each *in*-vitro sample the mRNA expression level of genes were obtained from at least three independent samples. Conversely, genes expression level from post-surgical specimens were obtained from one-single tissue piece. Individual mRNA expression level for each gene was then corrected with Z-score as indicated.

$$Z_i = \frac{X_i - \frac{\sum_{i=1}^{n} X_i}{n}}{\sigma}$$

"i" stands for the individual gene analyzed, Z_i indicates the Z-score, X_i indicates the calculated [$2^{-\Delta Ct}$] value for a gene and σ is the standard deviation between all mRNA level obtained within the analyzed sample for the genes analyzed.

Subsequently, individual PN and Mes scores were calculated for each sample by averaging respectively PN and Mes gene expression level after Z-score correction. To generate values for a comparative heatmap, composite metagenes were obtained within each sample by subtracting from the calculated Mes score the PN score (Bhat et al., 2013). Heatmaps were visualized using GENE-E software (Broad Intitute).

4.2.3 UNSUPERVISED CLUSTERING AND HEATPLOT

The unsupervised hierarchical clustering and heatmaps were obtained in collaboration with Miquel Angel Pujana's team (IDIBELL; Breast cancer unit) using the R (http://www.r-project.org/) functions *hclust* and heatmap.3 in Bioconductor. Data analyzed through indicated softwares correspond to gene relative amount and the values were calculated by the ΔΔCt method as detailed before (chapter 4.1).
To generate unclustered comparative heatmap, the software GENE-E was employed (Broad Intitute).

4.3 RT-PCR

The RT-PCR method can be used not only to detect specific mRNAs but also to semi-quantitate their levels. Thus, one can compare levels of transcripts in different samples as a pilot study.

Total RNA was extracted and retro-transcribed as above indicated in paragraph 4.1. PCR reaction was performed using GeneAmp® PCR System 9700 thermocycler (Applied Biosystems). The sequences of primers used were chosen among the ones described in bibliography (Table M15). Sequences were analyzed with Primer-BLAST tool (NCBI web site) and primers selection was carried out taking into account PCR product size, primer length, GC%, predicted melting temperature and self-complementarity.

PCR cycle conditions were optimized individually for each primer pair (see Table M16). In particular, the following parameters were adjusted in order to achieve the most efficient amplification of specific template:

- $MgCl_2$ concentration, which could span among 1.5 and 2.2 mM
- Annealing temperature
- Number of cycles

To identify quickly the best combination of annealing temperature and cycles, the PCR optimization was performed using C1000™ Thermal Cycler (BIO-RAD) which allows simultaneously the amplification of template with a gradient range of annealing temperature along the block and two different possibilities of cycle number. In conclusion, PCR conditions were set as indicated below:

Hot-Start (*)	95°C	5 minutes	
Cycles (**)	94°C	15 seconds	*[denaturation step]*
	Ta (***)	30 seconds	*[annealing step]*
	72°C	30 seconds (****)	*[extension step]*
Extension	72°C	5 minutes	*[final extension]*
End	4°C	indefinite period	

(*) AmpliTaq Gold is a Hot-Start polymerase and requires a preliminary activation step at 95°C for 5 minutes. (**) and (***) Optimized cycles and annealing temperatures were specified in Table M16 for every primer pair. (****) Unless otherwise specified. Ta indicates the annealing temperature.

TARGET GENE	FORWARD PRIMER SEQUENCE	REVERSE PRIMERS SEQUENCE	PRODUCT SIZE	BIBLIOGRAPHY
CD133-L	CTGGGGCTGCTGTTTATTATTCTG	ACGCCTTGTCCTTGGTAGTGTTG	337 bp	
CD133-s	TCACTGCTTATGCTTCCAG	TACGGCACTCTTCACCTG	83 bp	
SOX2	CCAGCTCGCAGACCTAC	GAGTGGGAGGAAGAGGTAAC	151 bp	Raso et al., 2012
MSI1	AGCCCAAGATGGTGACTC	GTCCACCTTCCCAAACTG	107 bp	Raso et al., 2012
OCT4	CCTGGGGGTTCTATTTGG	ACGAGGGTTTCTGCTTTG	171 bp	Raso et al., 2012
NES	CGCACCTCAAGATGTCC	GAGCAAAGATCCAAGACGC	179 bp	Raso et al., 2012
CD15	CTCGCAGCACCTGGATTA	GCGGTCGAGGAAAAGCA	187 bp	Raso et al., 2012
CD44	AAGGTGGAGCAAACACAACC	AGCTTTTTCTTCTGCCCACA	151 bp	Clement et al., 2007
L1CAM	TGCTCATCCTCTGCTTCATC	TCCTCGTTGTCACTCTCC	145 bp	Cheng et al., 2011
GAPDH	AGTGGGTGTCGCTGTTGAAGT	AACGTGTCAGTGGTGGACCTG	160 bp	

Table M15: Forward and Reverse Primer sequences

Primers were purchased to Roche and eluted at 50 µM in Milli-Q® water.

TARGET GENE	CYCLE NUMBER	Ta (ºC)	EXTENSION (sec)
CD133-L	40	56	60
CD133-S	37	58	30
SOX2	37	57	60
MUSH1	37	57	30
OCT4	37	55	30
NESTIN	37	58	30
CD15	37	57	30
CD44	37	59	30
L1CAM	37	62	30
GAPDH	40	54	30

Table M16: RT-PCR conditions for every primer used

Ta indicates the annealing temperature. To optimize CD133 amplification program, RNA extracted from Saos-2 osteosarcoma cell line was used as control positive (Tirino et al., 2008).

PCR reaction was performed in 20-µl total volume employing AmpliTaq Gold® (Applied Biosystems) and 1 µg of cDNA according to Table M17.

REAGENT	CONCENTRATION
cDNA	1 µg
AmpliTaq Gold® (5 U/µl)	1 U
PCR Gold Buffer (10X)	1X
$MgCl_2$ (25 mM)	2 mM
dNTPs (10 mM)	0.2 mM
Primer F (20 µM)	0.2 µM
Primer R (20 µM)	0.2 µM

Table M17: RT-PCR reaction mix

Mix was prepared on iced-block to maintain the stability of parts.

PCR fragments were separated and visualized in 4%, 6% or 8% 19:1 Acrylamide (AppliChem) gel depending on the expected product size. Gels were polymerized in Tris-borate-EDTA (TBE) buffer (89 mM Tris-Base, 89 mM Boric acid and 2 mM EDTA), and PCR fragment were loaded 1:1 with STOP buffer (95% Formamide, 20 mM EDTA and 0.05% Bromophenol Blue). Electrophoresis was carried out at constant 90 mV (Mini-Protean, Bio-Rad) and gels were then stained in TBE with BrEt for 10 minutes. Product were finally visualized under a transilluminator with a UV filter. Gene expression level was approximated by means of signal quantification after normalization with *GAPDH* density using ImageJ (National Institute of Health, USA).

4.4 WHOLE TRANSCRIPTOME ANALYSIS

Whole transcriptome was measured by means of GeneChip® Human Gene 1.0 ST array (Affymetrix). RNA was extracted from samples after one hour from the last 2 Gy fraction using RNeasy® Mini Kit (Qiagen) that ensures extraction of higher RNA quality. Microarray technique requires sample with RNA absorbance ratios at 260/280 and 260/230 equal or higher than 2. In order to achieve the necessary level of RNA purity some additional steps were added to manufacturer instruction:

- Add 10 µl of β-mercaptoetahnol to each 1 ml RTL lysis buffer (optional in company instruction)
- Warm RTL lysis buffer at 37ºC before use
- Use 70% EtOH prepared exclusively at the moment of use (it increases the RNA yield)
- Aspire the flow through out of the collection tubes with vacuum device instead of just dumping them out
- During washes (RW1 and RPE) invert and roll the column several times to make sure the buffer has really washed the inside of the tube
- Let RW1 wash remain in the cartridge for about 2 minutes
- Perform an extra wash with RW1 (it helps to decrease 280 nm contamination)
- Perform an extra wash with RPE and let it on the cartridge for about 2 minutes to make sure all the salt is removed
- Allow the columns to air dry & evaporate EtOH with the caps open for ~5min before elution (it increases yield and decreases 230 peak)
- Pre-warm the water (~45ºC) before elution and let it sit for 2-3 minutes (it increases yield)

Ten µl of RNA at concentration of 100 ng/µl were then sent to *Centro de Investigación del Cáncer* (Universidad de Salamanca-CSIC). RNA quality control was performed in a 2100 Bioanalyzer (Agilent Technologies). In all cases, the RNA integrity number was equal to 10. Following quality control, samples were labelled and hybridized according to protocols from Affymetrix. Briefly, 100-300 ng of total RNA were amplified and labeled using the WT Expression Kit de Ambion and then hybridized to Human Gene 1.0 ST Array (Affymetrix). Washing and scanning were performed using GeneChip System of Affymetrix (GeneChip Hybridization Oven 640, GeneChip Fluidics Station 450 and GeneChip Scanner 7G).

5 BIOINFORMATIC TOOLS

5.1 MICROARRAY DATA ANALYSIS

The data were analysed in collaboration with Miquel Angel Pujana's team (IDIBELL; Breast cancer unit) using Microarray Suite version 5.0 (MAS 5.0), Affymetrix default analysis settings and global scaling as normalization method. The data were deposited under the GEO reference GSE82139 (private data). Principal Component Analysis (PCA) was realized using the R (http://www.r-project.org/) in Bioconductor.

To correct for multiple hypothesis testing, a False Discovery Rate (FDR) of 5% was used (FDR < 0.05).

Microarray data were also examined using the Gene Set Expression Analysis (GSEA) tool, run using default values for all parameters (Subramanian et al., 2005). GSEA pathways enrichment was evaluated using pathways annotation from the Kyoto Encyclopedia of Genes and Genomes (KEGG; Kanehisa et al., 2012), BioCarta (National Cancer Institute) and Reactome (Croft et al., 2014; Fabregat et al., 2016). GSEA tool was interrogated also to estimate Transcription Factor (TF) binding site enrichment, by means of TFT collection, and to identify specific well-defined biological states or processes, through the Hallmark collection (H).

The Gene Ontology (GO) biological processes were identified using GO enRIchment anaLysis and visuaLizAtion tool (GOrilla; http://cbl-gorilla.cs.technion.ac.il/; Eden et al., 2009). The list of genes differentially expressed in cluster 3 compared to cluster 2 (R-fold higher than 2.00 and FDR < 0.05) were run against the background list, corresponding to the whole genes composing Microarray platform. A *P*-value threshold of 10^{-09} was used.

DAVID conversion tool (https://david.ncifcrf.gov/conversion.jsp; Huang et al., 2009) and WebGestalt (http://www.webgestalt.org/; Wang et al., 2013) were used to convert Affymetrix gene ID format to the universally accepted gene symbol.

5.2 TCGA DATABASES

5.2.1 ITGA6 EXPRESSION IN PUBLIC DATASETS

In order to analyze *ITGA6* expression within public multidimensional cancer genomics data, various databases were examined. The cBio Cancer Genomics Portal (cBioPortal;

http://www.cbioportal.org/; Cerami et al., 2012; Gao et al., 2013) was employed to compare two provisional data sets from TCGA project:

- Glioblastoma Multiforme (TCGA, Provisional)
- Brain Lower Grade Glioma (TCGA, Provisional)

Oncomine database (www.oncomine.org) was employed to compare *ITGA6* expression in a restricted set of human glial brain tumors (Bredel et al., 2005) and in TCGA healthy brain and GBM specimens, data extracted from Human Genome U133A Array platform (no associated paper).

In addition, the following TCGA GBM gene expression datasets were extracted from the Cancer Genomic Browser (UC Santa Cruz; https://genome-cancer.ucsc.edu/) and analyzed:

- AgilentG4502A_07_2 array (Data set ID: TCGA_GBM_G4502A_07_2) measured experimentally using Agilent 244K custom gene expression G4502A_07_2 microarrays from 483 samples (University of North Carolina TCGA genomic characterization center)
- AffyU133a array (Data set ID: TCGA_GBM_exp_u133a) measured experimentally using the Affymetrix HT Human Genome U133a microarray platform from 539 samples (Broad Institute of MIT and Harvard University cancer genomic characterization center)

5.2.2 EXPRESSION IN PUBLIC DATASETS OF THE GENESET DEFINED AFTER TRANSCRIPTOMIC ANALYSIS OF IRRADIATED SAMPLES

Data extracted from the Cancer Genomic Browser (UC Santa Cruz; https://genome-cancer.ucsc.edu/) belongs to the up-mentioned AgilentG4502A_07_2 array (Data set ID: TCGA_GBM_G4502A_07_2). Unsupervised hierarchical clustering was performed as indicated in paragraph 4.2.3 "Unsupervised clustering".

In order to analyze *COX2*, *LIF*, *ICAM1*, *IL6* and *NNMT* expression impact on GBM clinical attributes, it was employed the cBio Cancer Genomics Portal (cBioPortal; http://www.cbioportal.org/; Cerami et al., 2012; Gao et al., 2013). Public multidimensional data were extracted from Glioblastoma Multiforme (TCGA, Provisional) and Overall Survival/Progression Free Survival were analyzed.

6 DNA ANALYSIS

DNA was extracted from both cell cultures and flash-freeze brain tissues with QIAamp® DNA Mini Kit (Qiagen) following the manufacturer guidelines. In order to obtain RNA-free genomic DNA, it was performed the optional treatment with RNase A suggested by the company at final concentration of 1.8 µg/µl (AppliChem).

6.1 MLPA TECHNIQUE

Multiplex Ligation-dependent Probe Amplification (MLPA) is a semi-quantitative technique employed to determine amplifications or deletions of several target genes in a single multiplex PCR-based reaction. This method can evaluate gross alteration in the relative copy number variation but does not detect point mutation that could lead to protein loss or gain-of-function.

Copy number alteration of genes *PDGFRA*, *EGFR*, *CDKN2A*, *PTEN*, *CDK4*, *MIR26A2*, *MDM2*, *NFKBIA* and *TP53* were investigated through SALSA MLPA (kit P105, MRC-Holland) following the company guidelines. DNA from both primary cells and brain tissue were analyzed. Among 100-400 ng of DNA was loaded in 5-µl total volume with AE buffer (Quiagen). A minimum of two reference samples extracted from healthy donors and a No-DNA control tube (5-µl of AE buffer) were included per MLPA run. The product of PCR reaction was load into MicroAmp™ Optical 96-well plate (Applied Biosystems) along with Size Standard GeneScan™ 500 LIZ (Applied Biosystems) and Hi-Di™ Formamide (Applied Biosystems). PCR product were then submitted to capillary electrophoresis employing the ABI-Prism 3730 Genetic Analyzer (Applied Biosystems). Peaks area were finally analyzed using Coffalyzer freeware software (Coffalyser.net; MRC-Holland). Only those samples that pass quality control, evaluated by means of D-fragment and Q-fragment, were considered. For each sample, copy number were determined the Final Probe Ratio (FPR) obtained by comparing each gene relative probe peak to peaks detected in reference samples. Following the company guidelines, the FPR was interpreted as explained in Table M18.

FINAL PROBE RATIO (FPR)	COPY NUMBER STATUS
FPR = 0	0 copies (homologous deletion)
0.40 < FPR < 0.65	1 copy (heterozygous deletion)
0.80 < FPR < 1.20	Normal copy number (identical to reference samples)
FPR < 1.30	>2 copies (duplication)
All other values	Ambiguous results

Table M18: Relation between copy number status and the obtained FPR
Ambiguous results were interpreted considering FPR of all samples replica.

6.2 MGMT PROMOTER METHYLATION STATUS

This assay allows to analyze MGMT promoter methylation pattern in the CpG islands and consequently to infer the presence or absence of MGMT protein in samples. The methylation status was determined by sodium bisulfite conversion, a chemical modification of unmethylated, but not methylated, cytosine to uracil (Herman et al., 1996), followed by PCR amplification with primers specific for either methylated or the modified unmethylated DNA (MSP, Methylation-Specific PCR).

Around to 200-500 ng DNA per sample was treated with EZ DNA Methylation-Gold kit™ (Zymo Research) following manufacturer instruction. A universally methylated sample and Human genomic DNA (Roche) were added to the analysis as positive and negative control respectively. Sample without DNA was used as negative PCR control. Complete bisulfite conversion was followed by a two-stage MSP amplification for MGMT promoter (Palmisano et al., 2000). In particular, the primers chosen for stage-1 recognize a portion of MGMT CpG-rich promoter region, but do not discriminate between methylated and unmethylated alleles. PCR products from stage-1 were then diluted 50-fold in H_2O, and subjected to a stage-2 PCR in which primers specific to methylated or unmethylated template were used. Primers employed are detailed in Table M19. PCR reaction mix PCR reaction was performed in both stages loading 1-µl of DNA, either bisulfite treated or 1-step product, in 20-µl total volume as indicated in Table M17.

	PRIMER SEQUENCE	PRODUCT SIZE	Ta	REF
MGMT-F	GGATATGTTGGGATAGTT	289 bp	52ºC	(*)
MGMT-R	CCAAAAACCCCAAACCC			
MET-F	TTTCGACGTTCGTAGGTTTTCGC	80 bp	62ºC	(**)
MET-R	GCACTCTTCCGAAAACGAAACG			
UM-F	TTTGTGTTTTGATGTTTGTAGGTTTTTGT	90 bp	62ºC	(**)
UM-R	AACTCCACACTCTTCCAAAAACAAAACA			

Table M19: MGMT Primer sequences and MSP specific conditions

MGMT primers were employed for the stage-1 PCR, whereas MET/UM methylation specific primers were used for stage-2 PCR. Ta indicates the annealing temperature. (*) Primer sequences from Palmisano et al., 2000. (**) Primer sequences from Esteller et al., 1999.

PCR conditions were set as indicated below:

Hot-Start (*)	95°C	5 minutes	
30 Cycles	95°C	30 seconds	*[denaturation step]*
	Ta (**)	30 seconds	*[annealing step]*
	72°C	30 seconds	*[extension step]*
Extension	72°C	10 minutes	*[final extension]*
End	4°C	indefinite period	

(*) AmpliTaq Gold is a Hot-Start polymerase and requires a preliminary activation step at 95ºC for 5 minutes. (**) Annealing temperatures were specified in Table M19 for 1- and 2-step PCR.

PCR fragments were visualized as described in paragraph 4.3.

7 CSCs FUNCTIONAL FEATURES ASSESSMENT

7.1 COLONY FORMING CAPACITY

Colony Forming Capacity (CFC) is the ability of cell to proliferate at low cell density as multicellular clusters, either colonies or neurospheres. CFC could be obtained by the Plating Efficiency (PE) that is the ratio of the number of colonies or spheres to the number of cells seeded.

Low numbers of cells were seeded as single-cell suspension at two different densities as indicated in Table M20. Seeding concentrations were established according to preliminary studies about the growth rate of each primary culture in both *Monolayer* and *Neurospheres* condition (details in paragraph 7.1.3). Cells were maintained for 14 days in their culturing condition without any media renewal. At the fixed end-point, plates were evaluated with different approaches depending on culture conditions for the formation either of colonies or of neurospheres (see paragraphs 7.1.1 and 7.1.2). Plating Efficiency (PE) was calculated according to Franken et al., 2006:

$$PE = \frac{n. of\ colonies\ formed}{n. of\ cells\ seeded}\%$$

PRIMARY CULTURE	CELL SEEDED - DGC	CELL SEEDED - GICs
#35	750, 1000	100, 200
#82	750, 1000	50, 100
#88	500, 750	40, 80
#90	500, 750	25, 50

Table M20: Seeding concentration for the Colony forming assay
Indicated numbers stand for number of cells/well.

7.1.1 CFC EVALUATION IN MONOLAYER CONDITION

DGC were seeded in 6-well plates at the indicated concentrations in triplicates. At the end-point, wells were processed as indicated below:

1. Rinse gently wells once with PBS.
2. Fix-stain colonies with 0.2% Crystal Violet + 2% EtOH in PBS. Incubate plates at 37°C for 30 minutes.

3. Score wells by manual counting, consider as colonies only multicellular aggregates dimensionally bigger than a 50-cells colony size.
4. Scan plates to digitalize the experiment.

7.1.2 CFC EVALUATION IN NEUROSPHERE CONDITION

GICs were seeded in 96-well flat-bottomed plate at the indicated concentrations in quadruplicates. At the end-point, wells were visually scanned using the inverted light microscope DM-IRB (Leica). Spheres were measured by means of ProgRes CapturePro software (Jenoptik) and only multicellular clusters exceeding 100 µm were counted as neurospheres. Diameter value was calculated as mean of all radius*2 obtained from each ProgRes output parameters (width, height, circumference and area).

7.1.3 PLATING EFFICIENCY ESTIMATION

Plating efficiency detection should be optimized to determine the best cell seeding concentration in a specific growth condition. Especially, linearity of PE should be tested first within a range, before choosing the cell seeding concentration in a clonogenic assays. In fact, PE is strongly dependent on the number of cell seeded, as with increasing numbers of cells the plating efficiency decreases (Pomp et al., 1996).

To optimize the seeding concentration of each primary cultures established, cells were seeded at increasing concentrations in triplicates, maintained in culture for 14 days and then, growth as either colonies or neurospheres was assessed as detailed in paragraph 7.1.1 and 7.1.2, respectively. Cell seeding concentration for DGC cultures were 250, 500, 750, 1000, 1250, 1500, 1750 and 2000. Cell seeding concentration for GICs cultures varied among cultures analyzed. The optimal concentrations were chosen in order to be in a range of PE linearity and to avoid overcrowded conditions that were making wells almost uncountable (Figure M2 and Figure M3).

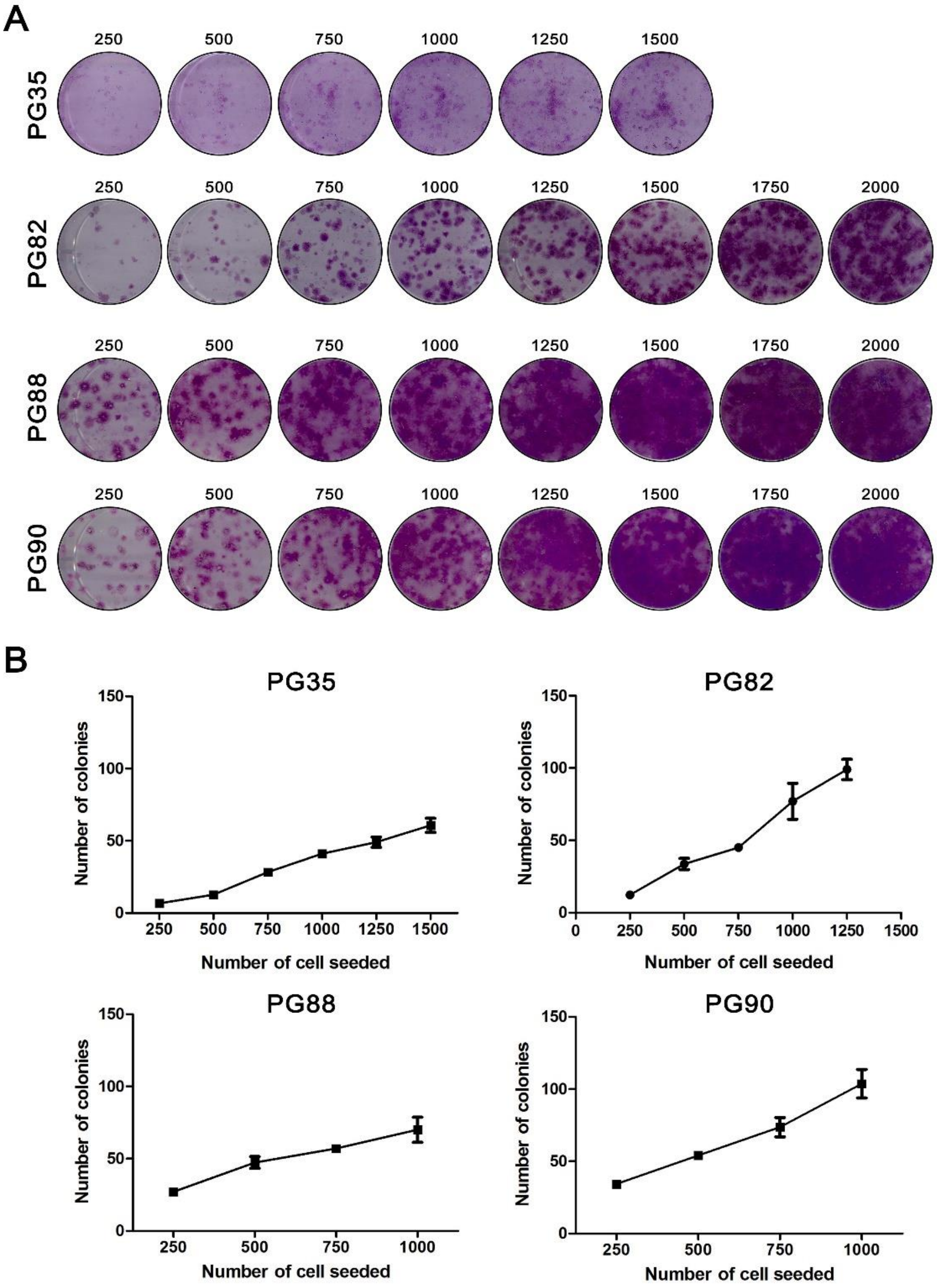

Figure M2: Plating Efficiency assessment of DGC culture

(A) Representative picture of PE analysis of DGC cultures PG35, PG82, PG88 and PG90 after Crystal Violet staining. (B) Number of colonies counted per cell seeded of PG35, PG82, PG88 and PG90. Data are presented as mean ± SEM (n=3).

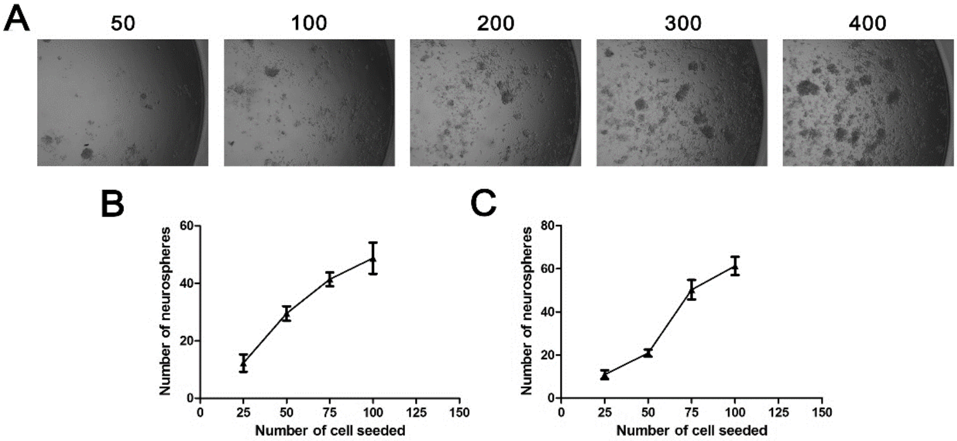

Figure M3: Plating Efficiency assessment of GICs culture

(A) Representative picture of PE analysis in GICs culture PG35s. (B-C) Number of neurospheres counted per cell seeded for PG88s (A) and PG90s (B).

7.2 SOFT AGAR COLONY FORMATION ASSAY

The Soft Agar assay allows evaluating the capacity of cell to growth in an anchorage-independent condition. This method is considered as a highly stringent *in-vitro* assay to confirm the tumorigenic potential of transformed cells.

The Soft Agar assay was performed over a 0.5% agar layer, with single-cell suspension dissolved in 0.3% agar as thereafter indicated in details. GICs were seeded in triplicate at two different concentrations: 1000 and 2000 cells per well. DGC were seeded as well in triplicate but at four different concentrations: 1000, 2000, 5000 and 20000 cells per well.

1. Prepare in 6-well plates the first layer of Agar 0.5% (w/v). Place Bacto™ Agar (BD) in Erlenmeyer flask containing the correct proportion of sterile PBS. Tap the flask with cotton cap and with the aid of microwave dissolve the powder. Quickly pour 1 ml of the prepared solution in each well of a 6-well plate under sterile conditions. Let the plates to cool down uncovered for 15 minutes at room temperature. Finally, place the plates at 4°C closed and upside down.

   ! *Use 10-ml pipette to aliquot the hot solution inside the well. P-1000 is not suitable to handle this dense and hot solution.*

   ! *Plates can be prepared up to one month before use. Store plates at 4°C in a sealed plastic bag with a bit of PBS in it, to maintain humidity.*

2. Pellet down and suspend cells to count their concentration. In case of GICs, dissociate spheres and strain sample with 70 µm Cell Strainer (BD Falcon) in order to avoid carrying spheres along in the single-cell suspension.
3. In 1.5-ml eppendorf, seed the desired number of cell in 500-µl total volume of their growing media.
4. Set the thermoblock at 38ºC and warm up the plates with 0.5% Agar layer.

   - ! *This is a very crucial step; check the thermometer to ensure the correct temperature. One degree less will polymerize agar. Then, to avoid killing the cell, cool down agarose for a couple of second right before mixing it with the cell suspension.*

5. Prepare Agar 0.6% solution (w/v) placing Agarose (Ecogene) in Erlenmeyer flask containing the correct proportion of sterile PBS. Tap the flask with cotton cap and with the aid of microwave dissolve the powder. Aliquot the solution placing 500 µl in 1.5-ml eppendorfs. Maintain the agarose unpolymerized by placing eppendorfs in the heated thermoblock.

   - ! *Again, use 5-ml pipette to aliquot 0.6% Agar.*
   - ! *Prepare Agarose solution in excess and leave it in the warm bath, in case it polymerizes and a supplement will be needed.*
   - ! *Meanwhile, cell-aliquots should be stored in the incubator.*

6. Mix one-to-one the Agar aliquot with the cell suspension. Homogenize properly and seed the mixture onto 0.5% Agar layer. Allow the new layer to polymerize and store the plate in the incubator. After 15 minutes add 500 µl of corresponding media on top.

Cells were maintained in culture for three weeks and media layer was replenished every 4-5 days. Then, plates were stained after removing media layer with 150 µl of 0.5 mg/ml MTT diluted in the proper growth media. Staining was carried out in the incubator, at 37ºC during six hours.
Stained colonies were counted by ImageJ (National Institute of Health, USA) following these parameters:

- Binary
- Particles size: 8-600 Pixel^2
- Particles circularity: 0.00-1.00

Counted colonies were then plotted referred to number of cells seeded.

7.3 SINGLE-CELL PROLIFERATION ASSAY

For the self-renewal assay, neurosphere were mechanically dissociated and then seeded in 96-well flat-bottomed plate with 200-µl media. Cells were seeded by means of serial dilution at extremely low cell density: expected concentration of one cell per well. Cells were then allowed to settle down overnight in the incubator. After 24 hours from seeding, plates were visually scanned with inverted light microscope DM-IRB (Leica) to select well containing indeed a single cell. Fourteen days after seeding plates were again visually scanned at inverted light microscope. Spheres were measured by means of ProgRes CapturePro software (Jenoptik) and only multicellular clusters exceeding 100 µm were counted as neurospheres. Sphere formation was scored from selected well and the percentage of growth as neurosphere was calculated.

7.4 DIFFERENTIATION ASSAY

In order to assess GICs capacity to differentiate along the main CNS lineages, differentiation was induced with 10% FBS. Briefly, cells were seeded and maintained in *Primary* media for 14 days, samples were sub-cultured following the ratio required to avoid cell confluency. 24 hours before the end-point cells were seeded onto coverslips and then processed for detection of selected markers by immunofluorescence (see paragraph 2.2).

7.5 INTRACANIAL TUMOR-INITIATING CAPACITY ASSESSMENT

All mouse experiments were approved by and performed according to the guidelines of the IDIBELL Animal Care Committee in agreement with the European Union and national directives. Per culture analyzed, five male athymic mice (Harlan) aged 7 weeks were anesthetized with isoflurane and were inoculated with 10^5 viable cells. Single-cell suspension was prepared in 30 µl of Hank's balanced salt solution (NaCl 0.9% B. Braun) and was injected into the right hemisphere using a U-100 insuline syringe (BD) syringe with an unbeveled 29-gauge needle. Animals were followed daily for the development of neurologic deficits. After 7 weeks mice were euthanatized, brain collected, formalin-fixed and paraffin-embedded. Details of tissue processing and paraffin section analysis are indicated in paragraph 2.3.

8 RADIATION SCHEDULE

Treatment of cells was carried out at room temperature using the X-ray beam from the Varian linear accelerator unit (Clinac 600 CD, M/S Varian AG) located at *Institut Català d'Oncologia* (ICO-Hospitalet). Dose was absorbed at dose-rate of 2.67 Gy/minute with the machine set with these parameters:

- Nominal energy: 6 MV
- Distance: 100 cm
- Field: 40x40 cm
- Arm rotation: 180° (from the bottom)

Samples were irradiated every 24 hours following an increasing fractionated schedule as indicated in Figure M4. Experiment were performed using 2.0 Gy/fraction as repeated unit and total absorbed doses were 2.0, 4.0, 6.0 and 8.0 Gy. Control plates underwent the same handling procedure with exception of being irradiated.

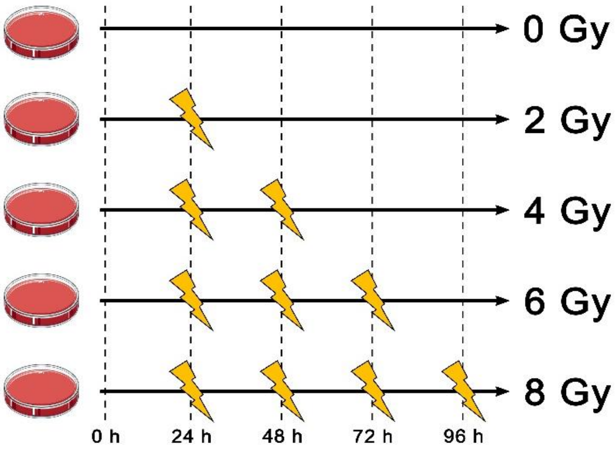

Figure M4: Radiation schedule of fractionated dose
Single radiation dose of 2 Gy every 24 hours.

9 CELL VIABILITY EVALUTATION

9.1 CLONOGENIC ASSAY

Clonogenic assay (or colony formation assay) is an *in-vitro* cell survival assay based on the ability of a single cell to grow indefinitely even at low density. The assay essentially tests every cell in the population for its ability to form colonies of more than 50 cells, equivalent to six cell divisions, in a period of 1-3 weeks. Clonogenic assay is the method of choice to establish cells residual proliferative potential after treatment with either ionizing radiation or cytotoxic agents. In fact, from a treated pool of cells only a fraction is able to retain the capacity to form colonies (Franken et al., 2006).

Cultures were dissociated, counted and seeded as single-cell suspension at the indicated concentration (Table M21).
Cells were let to settle down for 24 hours and then plates were irradiated according to the defined schedule (paragraph 8). Cells were allowed to proliferate for 14 days without any media renewal and finally cell proliferation in either colonies or neurospheres was evaluated as detailed in paragraph 9.1.1 and 9.1.2, respectively. The Surviving Fraction (SF) at each RT dose (D) was calculated after normalization with PE of non-irradiated control sample, indicated as PE(0).

$$SF(D) = \frac{n.of\ colonies\ formed(\mathrm{D})}{n.cell\ seeded \times PE(0)}$$

PE(0) was calculated as indicated in paragraph 7.1 from control sample. Doses evaluated (D) were 2, 4, 6 and 8 Gy.

Mean SF obtained from at least four independent experiment of each primary culture were fit by a linear regression according to the linear–quadratic formula (LQ):

$$SF = e^{-(\alpha D+\beta D^2)}$$

To estimate the α and β parameters of the LQ model, it was used the least square regression method of the function:

$$Y = \ln(SF) = -(\alpha D + \beta D^2)$$

SF at 2 Gy (SF2) was used to determine α and β parameters presented in the results.

We evaluated differential radiosensitivity by means of the surviving fraction after 2 Gy (SF2) and 8 Gy (SF8), the area under the curve (AUC) calculated using GraphPad Prism (v 5.0; GraphPad Software) along with LQ values α, β and their ratio α/β (Brenner, 2008; De Llobet et al., 2013; Franken et al., 2002, 2006).

PRIMARY CULTURE	DGC – CTR, 2 GY	DGC – 4, 6, 8 GY	GICs
#35	750, 1000	1500, 2000	100, 200
#82	500, 750	1500, 2000	50, 100
#88	750, 1000	1750, 2000	40, 80
#90	250, 500	750, 1000	25, 50

Table M21: Seeding concentration for Clonogenic assay

Indicated numbers stand for number of cells/well.

9.1.1 CLONOGENIC ASSAY FOR DGC

DGC were seeded in 6-well plates in triplicate at two different concentrations (3-ml volume), which were optimized for each primary culture as detailed in paragraph 7.1 (Table M21). Clonogenic assay plates were divided into two groups according to the treatment dose received. Control plates and samples treated with 2 Gy were composing the first group, whereas second group was made up of plates receiving 4, 6, and 8 Gy. Seeding concentrations of the first group were comparable to the one defined for CFC, while cell number for the second group was increased in order to better define the drop down of Surviving Fraction noticed at high doses.

At the end-point, cells were fixed with 2% ethanol and stained with 0.2% crystal violet as described in paragraph 7.1.1. Colonies of 50 cells or more were scored as capable to proliferate after radiation treatment. Furthermore, an additional step was performed to the protocol detailed before:

1. Dissolve Crystal Violet in 1-ml of 1% SDS in PBS on gentle shaking during 1 hour.
2. Aliquot 100-µl of each 6-well dissolved dye in triplicate in 96-well flat-bottomed plate.
3. Quantify absorbance with Sunrise spectrophotometer microplate reader (TECAN) coupled with XFluor4™ software (version 4.51; Tecan) at 550 nm.

Absorbance was referred to values detected in control samples and were plotted together with manual counting to improve accuracy of colony formation score.

9.1.2 CLONOGENIC ASSAY FOR GICS

Clonogenic assay was adapted to peculiar condition of free-floating spheres. GICs were seeded at low density (Table M21) in quadruplicate in 96-well flat-bottomed plate along with 200-µl of *Stem* media. Optimal concentration of cell per well for each GICs culture was defined considering Colony Forming Capacity (see paragraph 7.1.3) and reduction rate of AlamarBlue (see paragraph 9.2.1). At the end-point plates were visually scanned using the inverted light microscope DM-IRB (Leica) coupled with ProgRes CapturePro software (Jenoptik). Total number of formed neurospheres with diameter bigger than 100 mm was scored. Diameter value was calculated as mean of all radius*2 obtained from each ProgRes output parameters (width, height, circumference and area). Diameter of every single sphere bigger than 70 µm was plotted for each treatment dose in order to appreciate the variation of sphere dimension.

9.2 ALAMARBLUE VIABILITY ASSAY

AlamarBlue® proliferation assay is an *in-vitro* assay based on indirect measurement of cell metabolic activity. Resazurin, the active ingredient of AlamarBlue® reagent (AB), is a non-toxic, cell-permeable compound, non-fluorescent and blue in color. Upon entering cells, Resazurin is reduced to Resorufin, as it acts as an intermediate electron acceptor in the electron transport chain (Pagé et al., 1993). The reduced compound is red in color and highly fluorescent. By using the reducing power of living cells, it allows to measure quantitatively cell proliferation. Viable cells continuously convert the reagent, thus increasing the overall fluorescence of media. The amount of Resorufin can be detected by fluorescence (excitation/emission peaks at 570/585 nm) or absorbance (570 nm; Figure M5). Furthermore, AB is extremely stable and allows *live* monitoring of cultures.

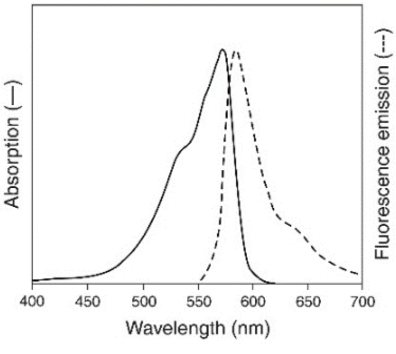

Figure M5: Absorbance and emission spectra of Resorufin (reduced AB reagent)

The assay was carried out on clonogenic assay plates after microscope count, about 17 days after the seeding of experiment. AlamarBlue® proliferation assay was performed in order to confirm data obtained from microscope counting and to improve accuracy of neurosphere formation score. AB assay was optimized for every GICs primary culture according to the manufacturer's guidelines (see paragraph 9.2.1). 50-µl of media was removed from each well and replaced with 50-µl of 40% AlamarBlue® (AB, Invitrogen) diluted in *Stem* media (final concentration in the well of 10%).

- ! *Add to unseeded well 150 µl of Stem media + 50 µl of 40% AB solution as negative control.*
- ! *Add at least to one well per experiment 100%-reduced sample, required as internal control. To obtain 100%-reduced AB, autoclave at 121°C for 15 min a solution of 10% AB prepared in Stem media, as suggested by AB technical datasheet (AdD Serotec).*

Plates were then incubated in humidified condition at 37°C and 5% CO2. Then, reagent detection was performed every hour until achievement of 5 hour post AB addition. AB reduction was measured through fluorescence emission using the FLUOstar OPTIMA microplate reader (BMG labtech; λ_{exc} = 550 nm, λ_{em} = 590 nm). Data obtained were referred to non-irradiated control condition and then, calculated average values for each treatment point detected at various hours were plotted.

9.2.1 ALAMARBLUE ASSAY OPTIMIZATION

In order to establish the best reagent incubation time and the optimal range of cell concentration, a pilot test was carried out. Cells were seeded at increasing concentrations in 96-well plate in quadruplicate and then were let proliferate for 14 days. At the end-point, AB reagent was added to wells as indicated in paragraph 9.2. Plates were then incubated in humidified condition at 37°C and 5% CO2 and fluorescence was detected every hour until 5-6 hours. According to data obtained and plotted in Figure M6, the optimal cell seeding concentrations were diverse for every GICs culture. The chosen concentrations, which were plotted with dashed lines, exhibited separated curves and consequently they allowed to discriminate a reduction in cell number. Moreover, the fluorescence intensity for selected concentrations was raising linearly from 1 hour up to 5 hour, with exception of PG90s that reached already at 5 hour the reduction plateau. Consequently, the time of reagent incubation was scheduled at 1, 2, 3, 4 and 5 hours, with exception of PG90s that was incubated until a maximum of 4 hours.

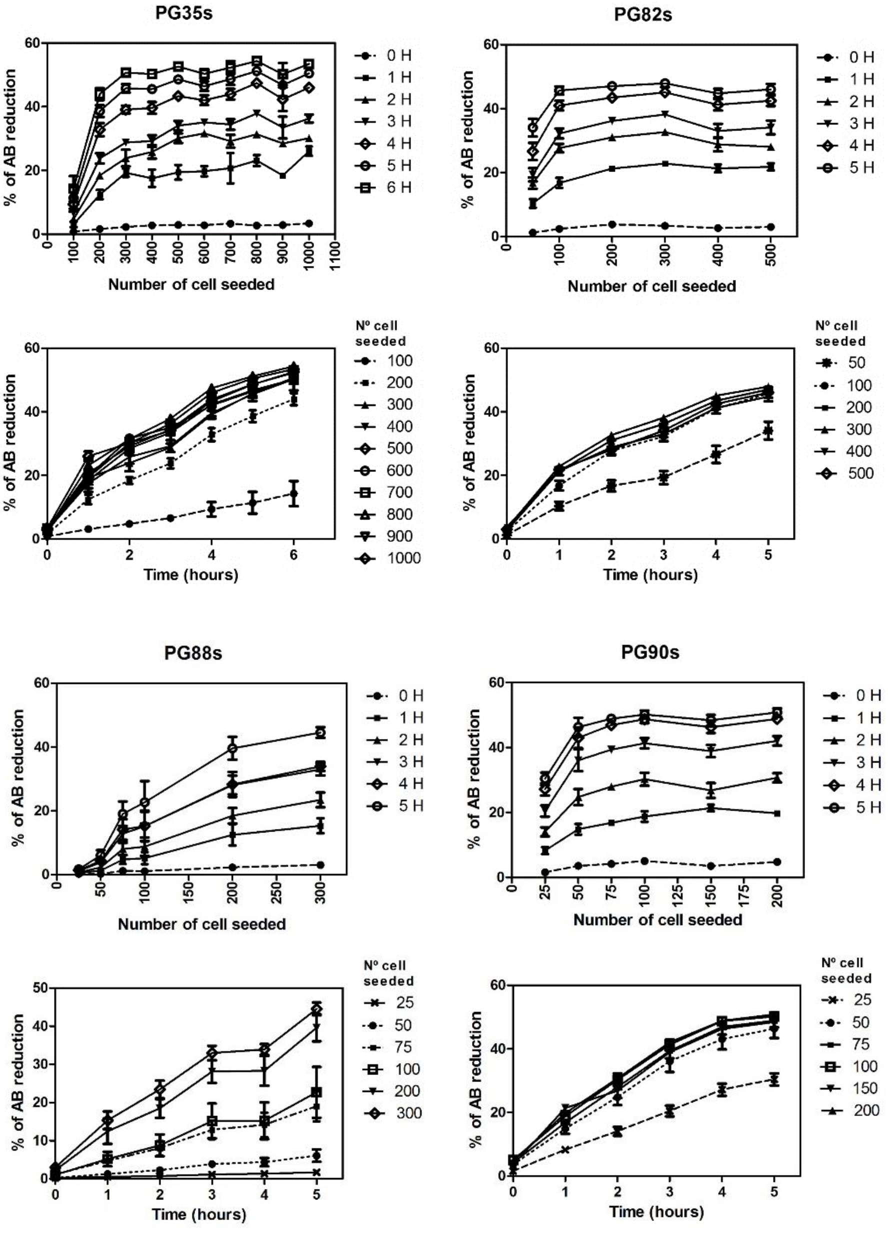
PG35s

PG82s

PG88s

PG90s

Figure M6: AlamarBlue® incubation time optimization

Percentage of reduction of AB referred to AB 100%-reduced is plotted in relation to either number of cell seeded or incubation time.

9.3 DOUBLING TIME

Cells were plated in triplicate at a density of 2.5×10^4 per well in 6-well plates, irradiated following standard fractionated radiation schedule (see paragraph 8 Radiation schedule) and then prepared for doubling time determination. Unirradiated control plates were processed alongside following the same procedure. Samples were manually counted after 4, 7, 10, 15 and 21 days from the beginning of the experiment. At each time-point samples were dissociated and counted. Triplicate samples were then mixed together to avoid clonal selection, re-counted and seeded in triplicate for the next time point at $2.5 \mathrm{x} 10^4$ cell density. Doubling time (T_d) was calculated from the following equation:

$$T_d = (t_2 - t_1) \times \frac{\log(2)}{\log\left(\frac{q_2}{q_1}\right)}$$

Parameters q1 and q2 represent the average number of cells at times t1 and t2, respectively.

9.4 EXTREME LIMITING DILUTION ASSAY

Extreme Limiting Dilution Assay (ELDA) is an *in*-vitro experimental technique for quantifying the proportion of biologically active particles in a population. ELDA it has been used also to quantify Glioblastoma cells bearing stem features within a mixed population (Flavahan et al., 2013).

GICs cells were sorted by FACS selecting for GFP+ cells with decreasing numbers of cells per well (10, 5 and 1) plated in 96-well plates containing *Stem* media. Cells were then allowed to settle down overnight in the incubator. After 24 hours from seeding, plates were visually scanned with inverted light microscope DM-IRB (Leica) to verify the exact number of cell seeded. The same day plates were irradiated with the first dose of 2 Gy. Plates underwent 8 Gy total exposure in fractioned doses following the schedule indicated in paragraph 8. A control non-irradiated plate seeded and handled under the same conditions was always included to each experiment. Fourteen days after seeding, plates were again visually scanned at inverted light microscope. Spheres were measured by means of ProgRes CapturePro software (Jenoptik) and only multicellular clusters exceeding 100 µm were counted as neurospheres. Sphere formation was scored and analysis was performed using the web-based tool available at http://bioinf.wehi.edu.au/software/elda/ (Walter and Eliza Hall Institute of Medical Research) following bibliography instructions (Hu & Smyth, 2009). ELDA tool accepts an input data table of data with three or four columns, separated by any combination of commas, spaces or tabs. The input columns are:

1. Dose, that indicates the number of cells seeded per well
2. Tested, that specifies number of wells bearing the concentration specified in Dose
3. Response, which indicates the number of wells exhibiting at least one neurosphere with size bigger than 100 µm.
4. Group, that stands for the experimental group code analyzed (typically CTR and RDT).

Below is indicated an example text input for the ELDA web tool:

```
1      26     17     CTR
2      11     10     CTR
3      8      6      CTR
4      6      5      CTR
5      3      3      CTR
6      2      2      CTR
8      1      1      CTR
9      2      2      CTR
1      23     4      RDT
2      15     7      RDT
3      12     7      RDT
4      4      3      RDT
5      3      2      RDT
6      1      1      RDT
9      1      1      RDT
```

Analysis was performed with default 95% confidence, selecting checkboxes in order to test for inequality in stem cell frequency between multiple groups and stating that the input numbers correspond to the actual number of cells observed.

ELDA web tool return a file displaying the estimated confidence interval for stem cell frequency in each group (1 cell bearing stem features every X number of cell seeded) and a statistical test for pair-wise differences in stem cell frequencies between the groups analyzed.

10 LENTIVIRAL INHIBITION

Lentiviral infection was implemented to inhibit *ITGA6* translation by means of shRNA approach (Short hairpin RNA). Lentiviral vector can infect both non-dividing and actively dividing cell types and can integrate their genomes into host cell chromosomes achieving a stable inhibition of target gene.

Lentiviral particles were purchased from Thermo-Scientific (Catalog Number: VGH5523; Lot Number: V14051506). ITGA6 shRNA constructs were cloned into the pGIPZ™ lentiviral vector which allows gene silencing with minimized cellular toxicity. Features of the Thermo-Scientific™ pGIPZ™ lentiviral vector were indicated in Figure M7 and Table M22 (for a more detailed view see Figure M8). In particular, the pGIPZ lentiviral vector includes among others:

- microRNA-adapted shRNA for gene knockdown, based on Human miR-30 (Figure M9). The hairpin stem consists of approximately 22 nt from target gene dsRNA and a 19 nt loop from human miR-30. The addition of miR-30 loop and further 125 nt of miR-30 flanking sequence on either side of the hairpin results in 10-fold increase in Drosha and Dicer processing of the expressed hairpins when compared with conventional shRNA designs. This implies greater shRNA production.
- TurboGFP (tGFP, Evrogen; excitation/ emission max = 482/ 502 nm), an improved variant of the green fluorescent protein which appears earlier than other green fluorescent proteins (reduced maturation half time).
- PuromycinR, a drug resistance flag to allow selection of stable cell lines.

Moreover, tGFP and shRNAmir are part of a bicistronic transcript allowing the visual marking of shRNAmir expressing cells.

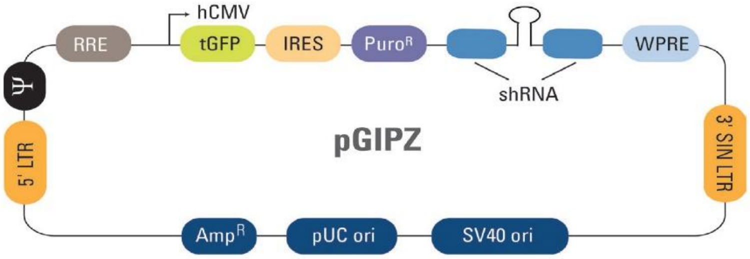

Figure M7: pGIPZ lentiviral vector
Picture from the manufacturer datasheet.

VECTOR ELEMENT	UTILITY
hCMV	Human cytomegalovirus promoter drives strong transgene expression
tGFP	TurboGFP reporter for visual tracking of transduction and expression
PuroR	Puromycin resistance permits antibiotic-selective pressure and propagation of stable integrants
IRES	Internal ribosomal entry site allows expression of TurboGFP and puromycin resistance genes in a single transcript
shRNA	microRNA-adapted shRNA (based on miR-30) for gene knockdown
5' LTR	5' long terminal repeat
3' SIN LTR	3' self-inactivating long terminal repeat for increased lentivirus safety
Ψ	Psi packaging sequence allows viral genome packaging using lentiviral packaging systems
RRE	Rev response element enhances titer by increasing packaging efficiency of full-length viral genomes
WPRE	Woodchuck hepatitis posttranscriptional regulatory element enhances transgene expression in the target cells

Table M22: Features of the pGIPZ vector

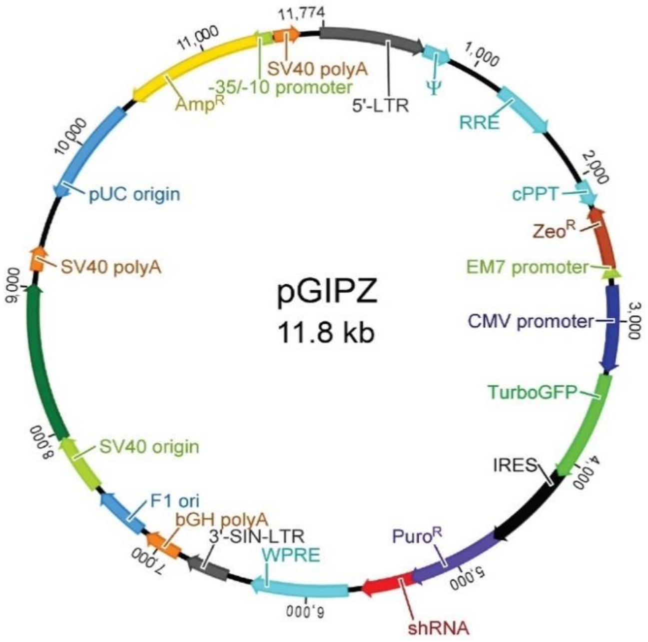

Figure M8: Detailed vector map of pGIPZ lentiviral vector.

Picture from the manufacturer datasheet.

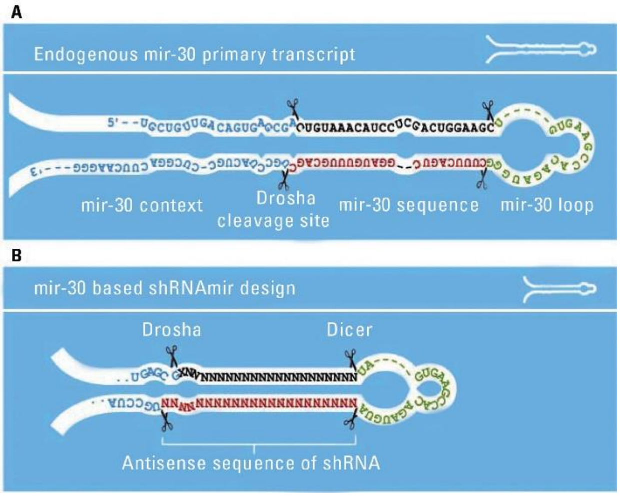

Figure M9: microRNA-30 Based hairpin design
Picture from the manufacturer datasheet.

Primary cultures were seeded in a 24-well plate with 500 µl of media (5x10^4 cells per well). After a minimum of 4 hours, cells were infected with lentiviral particles using MOI (Multiplicity of Infection) equal to 5.

> ! *Due to the absence of FBS in GICs culture media, a preliminary period of serum removal was not necessary.*

Each well was infected individually with one of the purchased particle (see Table M23), plus an additional well infected with non-silencing-pGIPZ sequence (mock viral particle). To ease transduction, Polybrene was added at 5 µg/ml (Hexadimethrine bromide, Sigma-Aldrich) and plates were centrifuged at 300 g for 5 minutes (Avanti™ J-20XP centrifuge, Beckman Coulter). At 24 hours post-transduction, cells were collected, washed by centrifugation (300 g for 5 min) and re-seeded in 1 ml of fresh media. At 48 hours post-transduction, cells were examined microscopically for the presence of reporter gene expression (tGFP). At 96 hours post-transduction, cultures were selected with Puromycin 5 µg/ml during 48 hours (Sigma-Aldrich). Even if lentiviral infection should ensure a long-term RNAi effect, a decay in ITGA6 inhibition was detected. Consequently, Puromycin selection pressure was maintained at 1 µg/ml concentration over all culture handling and even during experiments.

> ! *It is important to seed an additional uninfected well in order to verify the proper and effective antibiotic selection.*

PARTICLE	SOURCE CLONE ID	GENE TARGET SEQUENCE	EXON
shITGA6_1	V2LHS_77129	CAGCAAGGCAGATGGAATA	7
shITGA6_2	V2LHS_77130	CTCTCAGATTCAGTAACTA	9
shITGA6_3	V3LHS_326014	AGGATATTGCTTTAGAAAT	15
shGAPDH	RHS4372	-	-
mock	RHS4348	Non-silencing sequence	-

Table M23: Lentiviral particles

Particles were stored at -80°C in small aliquots corresponding to 5 MOI in a well containing $5x10^4$ cells. shGAPDH was a GAPDH-GIPZ viral particle employed as positive control, to set up the infection protocol. Mock particle bears a non-silencing-GIPZ sequence, and it was used in all experiment as negative control.

The Puromycin treatment concentration of 5 µg/ml was chosen among a range of doses: 1, 3, 5 and 7 µg/ml. The indicated concentrations were tested in two different un-infected GICs cultures, and samples were visually scanned after 24 and 48 hours of treatment. The lowest dose with 100% of dead cell after 48 hours was designated as treatment dose.

The conditions of lentiviral infection were optimized in a pilot study employing shGAPDH lentiviral particles (Figure M10).

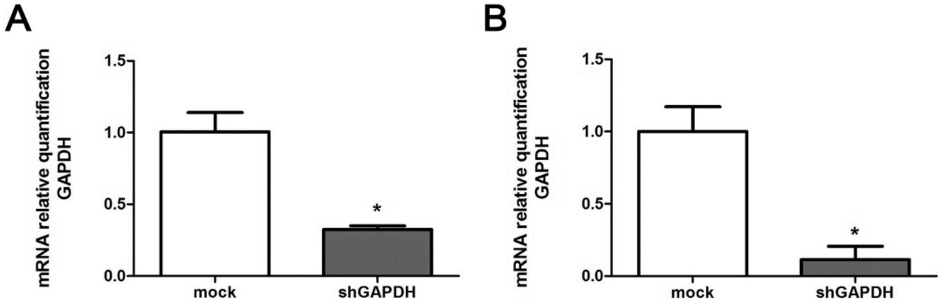

Figure M10: shGAPDH lentiviral infection

GAPDH fold inhibition after infection with shGAPDH lentiviral particles. GICs primary cultures tested were PG82s (A) and PG88s (B). Expression levels were calculated after normalization to *GUSB* expression. Data are presented as mean ± SEM (n=2); * *P* < .05; with unpaired t-test in comparison to control sample.

11 METABOLITES ANALYSIS

The detection of metabolites from DGC and GICs samples was performed in collaboration with Jose Carlos Perales group (Unit of Biophysics: Cellular Bioenergetics).

11.1 LACTATE QUANTIFICATION

Lactic dehydrogenase (LDH) may be used for the indirect quantitative enzymatic determination of either lactate or pyruvate. LDH catalyzes the reversible conversion of lactate to pyruvate in presence of excess nicotinamide adenine dinucleotide oxidized-form (NAD) or, for the opposite reaction, of nicotinamide adenine dinucleotide reduced-form (NADH). To force the reaction to completion in the reduced-form direction, it is necessary to trap the formed pyruvate with hydrazine. Because the reduced forms of these molecules differ from the oxidized forms in their ability to absorb light, it is possible to quantitate amount of NADH based on light absorbance at 340 nm or by the fluorescent emission of light at 445 nm. Consequently, the catalytic action of LDH allows measurement of lactate in terms of the generation of NADH, which is proportional to the lactate content originally present in the sample.

The quantitation of lactate production was performed on both D GC and GICs in triplicate from 10 cm plates containing 3x10^5 cells. 200 µl of media from culturing plates was collected every 24 hours until day four. An aliquot at time zero was sampled as well. Aliquots were maintained at -80ºC until end-point analysis. Lactate was quantified indirectly in terms of NADH production during the reaction catalyzed by LDH enzyme. The standard curve was realized from decreasing concentrations of sodium L-lactate (Sigma-Aldrich; dilutions realized in water: 10, 5, 2.5, 1.25, 0.625 and 0.3125 mM). A blank sample, containing exclusively water, was prepared as well. Measurement of lactate was performed following the protocol detailed below:

1. In a 96-well black plate (Corning) place 10 µl of each sample/blank/standards, one sample per well, and mix with 200 µl Reaction mix (see Table M24) which contains excess NAD and glycine-hydrazine buffer.
2. Measure absorbance at 360 nm using FLUOstar OPTIMA microplate reader (BMG labtech). This measurement represent time T0.
3. Add to each well add 20 µl of LDH solution (see Table M24).
4. Incubate samples at room temperature protected from light during 20 minutes.

5. Measure absorbance again at 360 nm using FLUOstar OPTIMA microplate reader.

Absorbance at T0 was subtracted to absorbance detected at T1. In order to estimate lactate concentration, the calculated T1-T0 was interpolated into the obtained absorbance standard curve.

SOLUTION	COMPOSITION
Reaction mix	0.3 M Hydrazine sulfate (Merk) 0.87 M Glycine (AppliChem) 2.5 M NAD (Roche) 0.19 M EDTA (Panreac) pH 9.5
LDH solution	0.15 M Hydrazine sulfate (Merk) 0.435 M Glycine (AppliChem) 344 U/ml LDH pH 9.5

Table M24: Solutions used for Lactate quantification

LDH solution is prepared diluted in Milli-Q® water.

11.2 GLUCOSE QUANTIFICATION

Glucose may be quantified indirectly from aqueous solutions by the coupled enzymatic reaction of Glucose Oxidase/Peroxidase (PGO). In the first reaction step, glucose is employed as substrate of Glucose oxidase enzyme to produce Gluconic acid and H_2O_2. Hydrogen peroxide itself works as substrate for the second reaction, which converts colorless o-Dianisidine (ODD) to brown oxidized o-Dianisidine. The amount of oxidized ODD could be measured at 425-475 nm. The final absorbance is proportional to the glucose amount contained in analyzed sample.

The analysis of glucose consumption was performed on both DGC and GICs in triplicate from 10 cm plates containing $3x10^5$ cells. 200 µl of media from culturing plates was collected every 24 hours until day four. An aliquot at time zero was sampled as well. Aliquots were maintained at -80ºC until end-point analysis. Glucose concentration measurement was carried out by means of Glucose Oxidase/Peroxidase enzymes reaction solution (PGO; Sigma-Aldrich) according to manufacturer instructions. The PGO solution was prepared by mixing 100 ml of the PGO enzyme solution with 1.6 ml of the o-Dianisidine solution (ODD; Sigma-Aldrich). The standard curve was realized from decreasing concentrations of glucose stock solution prepared at 1 mg/ml corresponding to glucose 5.55 mM (dilutions realized in water: 1, 0.5, 0.25, 0.125, 0.0625 and 0.03125 mg/ml). According to all media component's datasheet, the estimated concentration of Glucose was 55 mM for *Stem* media and 25 mM for DGC media. Consequently, media sampled during experiment was respectively diluted 1:60 and 1:30 in order to drag Glucose concentration between ranges covered by standard curve. A blank sample, containing exclusively water, was prepared as well. Enzymatic reaction was carried out mixing 15 µl of sample/blank/standards with 200 µl of PGO solution in a 96-well plate. Plate was then incubated 30 minutes at 37ºC and absorbance detected at 450 nm with Sunrise spectrophotometer microplate reader (TECAN) coupled with XFluor4™ software (version 4.51; Tecan).

11.3 OXYGEN CONSUMPTION

The measure of cells' oxygen consumption rate was performed employing the Oxygraph-2k device (Oroboros). The oxygen consumption was detected from 2.3 ml of a suspension prepared at $5x10^5$ single-cells per ml diluted in growth media.

12 STATISTICAL ANALYSIS

Data graphs are usually presented as means ± standard error of the mean (SEM). Unpaired Student's t-test, Mann-Whitney test and two-way ANOVA were performed for statistical analysis using GraphPad Prism (v 5.0; GraphPad Software). All tests were two-sided and differences were considered statistically significant at $P < .05$: * $P < .05$, ** $P < .01$, and *** $P < .001$.

RESULTS

“And the air was full of Thoughts and Things to Say. But at times like these, only the Small Things are ever said. Big Things lurk unsaid inside.” ARUNDHATI ROY – *The God of Small Things*

1 PRIMARY CULTURES ESTABLISHMENT

During this PhD thesis, 27 patient-derived brain tissue samples (classified as GBT) were collected from the pathology service of *Hospital Universitari de Bellvitge* (Table R1). Sampling was performed from consenting patients in accordance to protocol approved by the Hospital de Bellvitge Ethics Committee. Fifteen specimens were directly processed within 1 hour from the surgical resection. Mechanical and enzymatic disruption were performed following the protocols defined for the establishment of Differentiated Glioblastoma Cells (DGC) and Glioblastoma Initiating Cells (GICs). In particular, DGC were maintained under conditions optimal for growth of glioblastoma and most of other cancer cell lines ("*Monolayer*" culture conditions: DMEM media containing 10% fetal bovine *serum*). Conversely, GICs were cultured under conditions optimal for propagation and non-differentiation of normal NSCs ("*Neurosphere*" culture conditions: serum-free media supplemented with bFGF and EGF). Of note, GICs were not selected based on specific marker, but exclusively employing the neurosphere culture method (Galli et al., 2004; Gritti et al., 1996; Lee et al., 2006). In this media stem-like cells were capable to expand and were positively selected *in-vitro*, whereas differentiating/differentiated cells were automatically selected away.

Among the fifteen processed specimens, 12 were further diagnosed as GBM (WHO grade IV) and five samples were successfully established in both culture conditions: #82, #88, #90, #94 and #104 (Table R1). According to this data, the establishment rate of patient-derived culture was 42%. Primary culture pair #35 was formerly settled up in both conditions. Interestingly, only GBM tissue samples were capable to grow under the selected *in-vitro* conditions. The molecular IDH state of processed GBM was not defined, as the IDH detection was not yet included as diagnostic tool in neuropathological service routines.

Given the composite nomenclature used to identify established cultures and samples, a short guide has been included (Figure R1).

SAMPLE	WEIGHT (mg)	DIAGNOSIS		OUTCOME	YEAR
GBT81	-	GBM	Processed	Only DGC	2011
GBT82	2765	GBM	Processed	Established	2011
GBT83	498	GBM	Processed	Not growing	2012
GBT84	873	Metastasis	Processed	Not growing	2012
GBT85	134	OA III	Processed	Not growing	2012
GBT86	253	Meningioma	Processed	Not growing	2012
GBT87	833	GBM	Processed	Not growing	2012
GBT88	340	GBM	Processed	Established	2012
GBT89	326	GBM	Processed	Not growing	2012
GBT90	579	GBM	Processed	Established	2012
GBT91	277	GBM	Processed	Not growing	2012
GBT92	492	GBM	Stored	-	2012
GBT93	660	GBM	Processed	Not growing	2012
GBT94	1014	GBM	Processed	Established	2012
GBT95	389	GBM	Stored	-	2012
GBT96	755	GBM	Stored	-	2012
GBT97	499	GBM	Stored	-	2013
GBT98	704	GBM	Stored	-	2013
GBT99	535	Infectious	Discarded	-	2013
GBT100	322	GBM	Stored	-	2013
GBT101	245	GBM	Stored	-	2013
GBT102	519	GBM	Stored	-	2014
GBT103	593	GBM	Stored	-	2014
GBT104	391	GBM	Processed	Established	2014
GBT105	700	GBM	Stored	-	2014
GBT106	673	GBM	Processed	Not growing	2015
GBT107	683	GBM	Stored	-	2015

Table R1: Post-surgical specimens collected

For each tissue sample, it is indicated whether they were stored at -80ºC or directly processed following the two protocols. Moreover, among processed samples it is specified if the establishment was successful (Established) or not (Not growing). GBT81 was processed but only the *Monolayer* counterpart was capable to grow under the established *in*-vitro conditions (only DGC). GBT35 was established in 2006 from a GBM post-surgical specimen of 407 mg. OA III stands for oligoastrocytomas (WHO grade III).

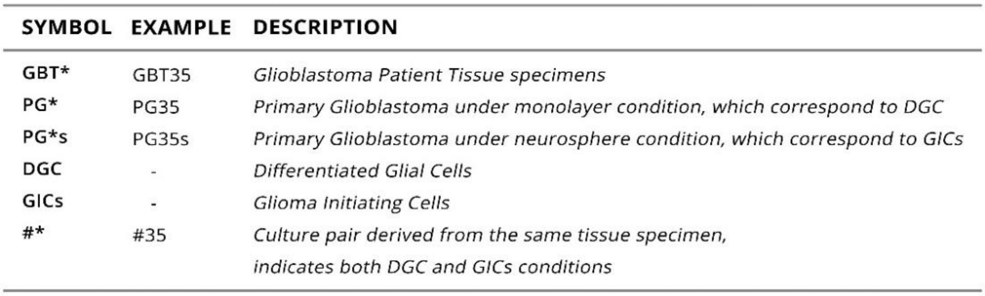

SYMBOL	EXAMPLE	DESCRIPTION
GBT*	GBT35	*Glioblastoma Patient Tissue specimens*
PG*	PG35	*Primary Glioblastoma under monolayer condition, which correspond to DGC*
PG*s	PG35s	*Primary Glioblastoma under neurosphere condition, which correspond to GICs*
DGC	-	*Differentiated Glial Cells*
GICs	-	*Glioma Initiating Cells*
#*	#35	*Culture pair derived from the same tissue specimen,* *indicates both DGC and GICs conditions*

Figure R1: Nomenclature used to identify cultures and samples

Initially, cultures presented highly heterogeneous morphology, while within a month, expanding cells turned out as more homogeneous culture (Figure R2). Established cells maintained in *Neurosphere* condition proliferated as floating phase-bright cells organized in multicellular clusters with spheroid-shape. Whereas, *Monolayer* cultures were growing with a highly varied morphology, sometimes as fibrous or protoplasmic astrocytes together with cells with morphology similar to fibroblasts or epithelial cells. Once cells reached a stable and constant proliferation rate, cultures were considered as effectively established *in-vitro* and samples were subjected to all experiments. Analysis were always performed before passage 15. Of note, single cells obtained from dissociation of *Neurospheres* showed diverse proliferative potentials; some form abortive non-growing colonies, whereas others form spheres varying in size.

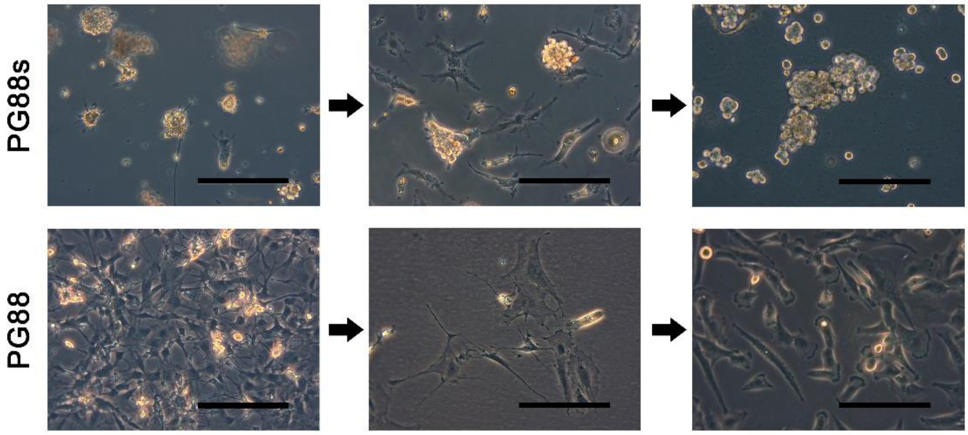

Figure R2: Primary derived culture establishment in "Stem" or "Monolayer" media

Sequence showing autonomous selection of proliferating clones during time. Scale bar of 200 µm.

2 CHARACTERIZATION OF ESTABLISHED CULTURES

2.1 PATIENT-DERIVED CULTURES RETAIN MAJOR ALTERATION FROM ORIGINAL GBT

First, the common genetic context was verified in each sample trio, constituted by individual GBT and the derived cultures in *Neurosphere* and *Monolayer* conditions. In particular, the key GBM alterations analyzed in each sample trio were the molecular signature class, MGMT promoter methylation status and copy number aberration of specific genes. These analysis were performed to assess whether cells maintained *in-vitro* were able to retain the same GBT original alterations, and whether DGC and GICs were characterized by the same genetic background, in order to empower the side-by-side comparison between the two compartments.

2.1.1 ESTABLISHED GBT AND DERIVED NEUROSPHERE CULTURES EXHIBIT A STRONG MES SIGNATURE

In the last decade, deep molecular analyses of primary GBMs allowed to classify them into four subtypes: proneural (PN), mesenchymal (Mes), classical (CL), and neural (NL) (Phillips et al., 2006; Verhaak et al., 2010; Brennan et al., 2013). In particular, these subclasses can be associated with canonical GBM mutations such as PDGFRA amplification in PN, loss of NF1 in Mes, and amplification of EGFR in CL. Among them, two subtypes appear to be well characterized, robust and generally consistent: the Mes and PN. Especially these two subtypes were demonstrated to have a prognostic value, as the patients with a Mes signature belong to the poor prognosis subclass and are mostly resistant to current standard of care (Bhat et al., 2013; Patel et al., 2014). In addition, it has been confirmed that PN tumors can recur with a signature class shift toward the Mes state (Halliday et al., 2014; Phillips et al., 2006).

To first determine the GBM molecular subtype of established samples, the expression of a set of genes was analyzed in GBT specimens and derived *Neurosphere* cultures by qPCR. The mRNA of four PN (*SOX9*, *OLIG2*, *SOX2* and *CD133*) and Mes (*FN1*, *YLK-40*, *CD44* and *CTGF*) genes was quantified (Figure R3). Samples with strong PN and Mes signature, kindly provided by Dra. de la Iglesia, were included in the analysis as internal controls (Figure R4).

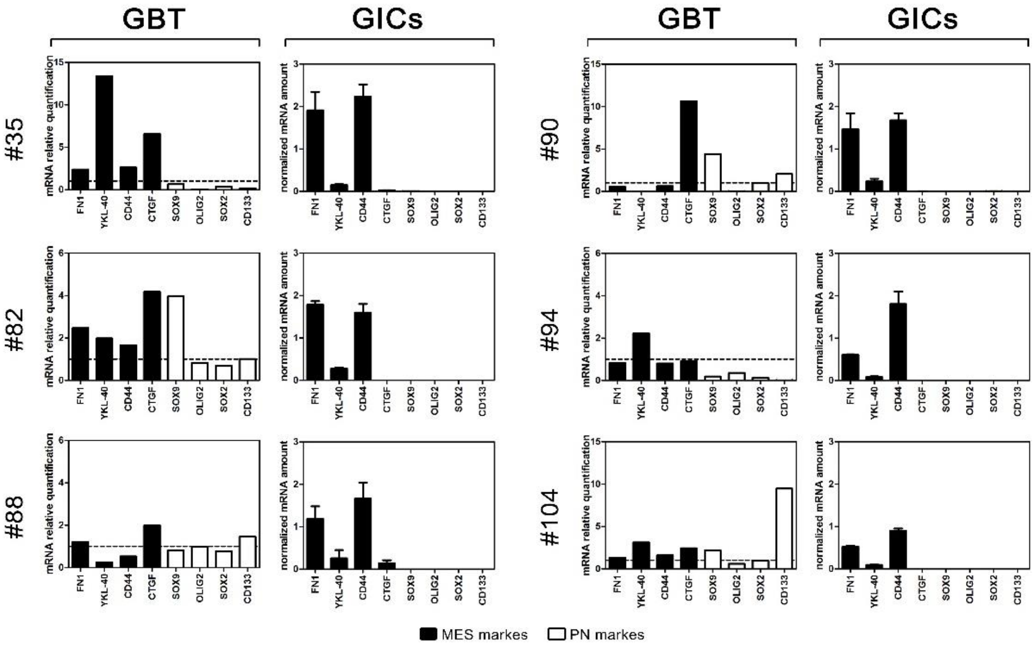

Figure R3: Evaluation of molecular signature from established GBT

Detection of Mesenchymal (black bars) and Proneural (white bars) markers through qPCR analysis. Tumoral tissue sample (GBT) mRNA expression levels were calculated from a unique post-surgical specimen according to ΔΔCt method. Ct were normalized with *TBP* and *IPO8* levels and each gene was referred to its level detected in white matter of healthy donor brain (dashed line). Conversely, GICs mRNA expression levels were obtained after normalization with *GAPDH* and *GUSB* levels. Data are presented as mean ± SEM (n=3).

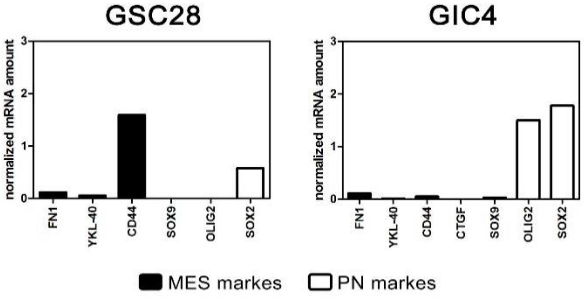

Figure R4: Internal control samples with strong PN and Mes signature

Detection of Mesenchymal (black bars) and Proneural (white bars) genes through qPCR analysis. Plotted mRNA expression levels were obtained from only one replica, after normalization with GAPDH and GUSB levels.

A comparative heatmap was generated from samples' composite metagene score (Figure R5-A). Using this approach, each sample could be ranked according to calculated metagene score as being predominantly PN or predominantly Mes. All GBT established *in-vitro* exhibited a strong Mes metagene score, which was maintained in the corresponding *Neurosphere* conditions. This data in particular indicated that GICs retained the molecular signature class from the original tumor tissue. Furthermore, those GBTs unable to grow *in-vitro* were analyzed employing the same metagene approach (Figure R5-B). According to the metagene score obtained, three proneural GBT were detected, accounting to 23% of processed post-surgical specimens and to 43% of not growing GBT. Interestingly, no GBT belonging to proneural subtype was able to grow *in-vitro* under the selected growth condition.

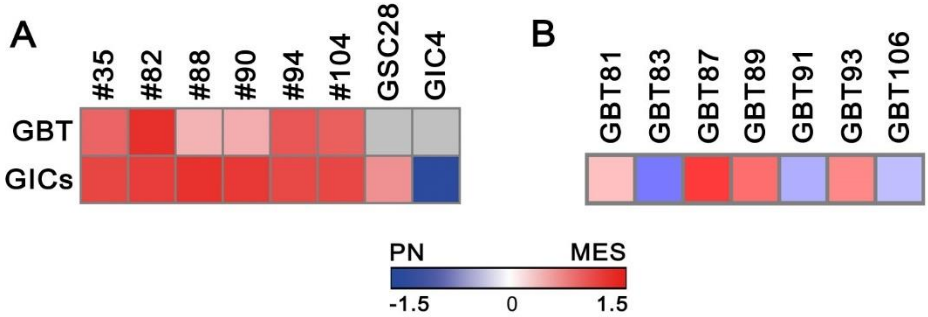

Figure R5: Comparative heatmap of GBM molecular subtypes

Metagene score was calculated for each sample and then compared to each other after Z-score correction. Blue shades represent a predominant PN signature, red a MES one, and white a relatively balanced expression of both, as indicated in figure legend. Grey shade indicates undetermined data. (A) Comparative heatmap of established samples. The metagene scores of internal control samples were indicated as well (GSC28 and GIC4). (B) Comparative heatmap of GBT not growing *in-vitro*.

Additionally, GBT82 derived cultures were tested via immunofluorescence for the expression of vimentin, a classic marker of mesenchymal tissues (Phillips et al., 2006). Both GICs and DGC were homogeneously positive for the expression of this marker, thus supporting their association with a Mes signature (Figure R6).

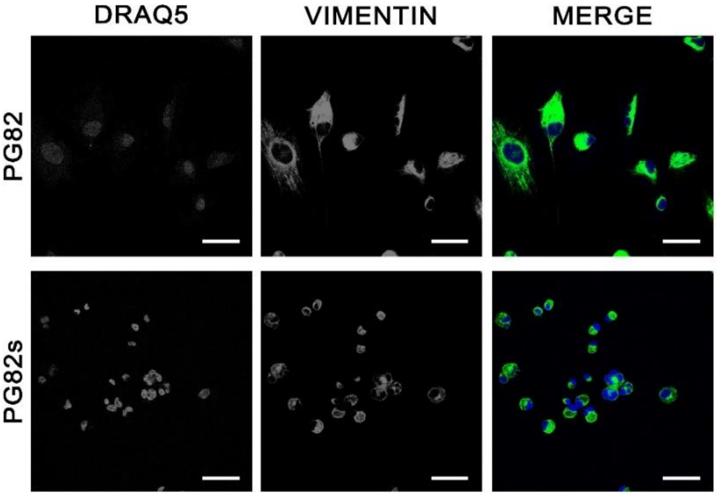

Figure R6: Vimentin IF staining

Representative picture of vimentin immunofluorescence detection. Vimentin is reported with Alexa-488. Nuclei are stained with Draq5. Scale bar of 50 µm.

2.1.2 ESTABLISHED PATIENT-DERIVED CULTURES RETAIN MGMT PROMOTER STATUS AND MAJOR GENOMIC ALTERATIONS FROM THEIR MATCHING POST-SURGICAL SPECIMEN

The MGMT promoter methylation status was then analyzed in GBT samples and the corresponding primary culture pairs by bisulfite treatment coupled with MSP (Methylation-Specific PCR). Samples presenting no PCR product in the methylation specific reaction, but demonstrating presence of unmethylated product, similar to the unmethylated control, were designated as unmethylated. On the contrary, samples that contained a clearly visible methylated product, with or without an additional unmethylated signal, were interpreted as positive for the MGMT promoter methylation (Brell et al., 2005; Cankovic et al., 2007; Smith-Sorensen et al., 2002). In fact, the presence of both products within the same sample could indicate heterogeneity in the patterns of methylation in the tumor itself as well as infiltrating normal cells with unmethylated *MGMT* promoter (Esteller et al., 1999).

All GBT specimens likewise their derived cultures exhibited promoter methylation even if with various grades (Figure R7). In primary tumors, hypermethylation of *MGMT* promoter was always accompanied by amplification of the unmethylated specific PCR reaction. On the contrary, *Neurospheres* counterpart showed exclusively the methylated product. *Monolayer* cultures exhibit variable pattern between the two tendencies above described.

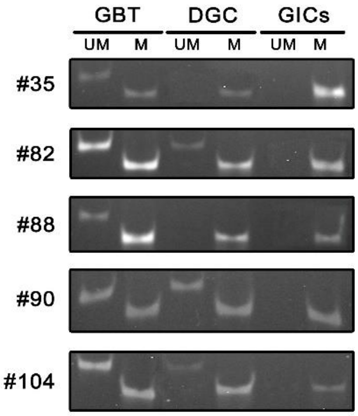

Figure R7: Detection of MGMT promoter Methylation status by MSP

PCR products of nested-MSP visualized in Acrylamide gel under UV light. Samples analyzed for each trio were post-surgical (GBT) and *in-vitro* derived cultures under *Neurosphere* (GICs) and *Monolayer* (DGC) conditions. The presence of a PCR product in lane UM indicates unmethylated status of *MGMT* promoter; the presence of product in lane M indicates methylated status of *MGMT* promoter. Unmethylated product size is 90 bp, whereas methylated is 80 bp.

Key genetic copy number alteration commonly found in GBM were then investigated in each sample trio by means of MLPA-based technique. The major alterations found in primary tumor tissues and the matching patient-derived cultures were EGFR amplification and loss of PTEN locus (Figure R8). Clear amplification of *EGFR* was detected in GBT82 and GBT104, whereas the other samples exhibited a marked tendency that should be validated using a more sensitive technique (i.e. Fluorescence in situ hybridization, FISH). *TP53* and *CDK4* exhibited no alternation in gene copy number in any of the analyzed samples. The others genes analyzed gave inconsistent results among triplicates probably due to unsolved technical problems.

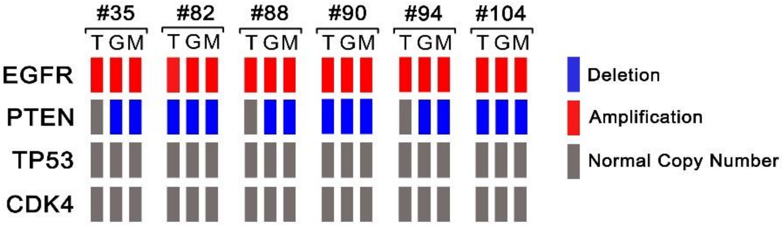

Figure R8: MLPA-based analysis of genomic alteration

Samples analyzed for each trio were post-surgical GBT (T) and *in-vitro* derived cultures under *Neurosphere* (G) and *Monolayer* (M) conditions (n = 3). Copy number data of post-surgical specimens (T) were obtained from one-single tissue piece.

2.2 PRIMARY CULTURES SELECTED UNDER NEUROSPHERE CONDITION EXHIBIT FUNCTIONAL CSCs FEATURES

CSCs own the capacity to extensively proliferate, self-renew, differentiate along the main lineages of the tissue they belong to and recapitulate the original tumors from a limited number of cells when injected orthotopically in nude mice (Vescovi et al., 2006). In order to verify the stemness of cells maintained in *Neurosphere* condition, the CSCs cardinal features were investigated in the established cultures. Most of experiments were carried out in DGC counterpart as well as internal control, therefore allowing a side-by-side comparison within the same genetic background.

2.2.1 GICS CULTURES DISPLAY A GREATER COLONY FORMATION CAPACITY COMPARED TO DGC

First, established cultures were tested for their capacity to proliferate extensively *in-vitro*. Cells were able to proliferate for at least 25 passages with a growth rate comparable to others GICs described in literature (Reynolds & Vescovi, 2009). In particular, cells were sub-cultured with a ratio of 50 times per year. Colony Formation Capacity (CFC) was then assessed by means of Plating Efficiency (PE) and Soft Agar assay. GICs cultures, when analyzed for PE, showed a great capacity to form colonies (Figure R9). In particular, GICs average growth efficiency was more than 10-fold higher than their monolayer counterpart (81.78 ± 8.50 % vs 7.55 ± 0.68 %, respectively; $P < .001$).

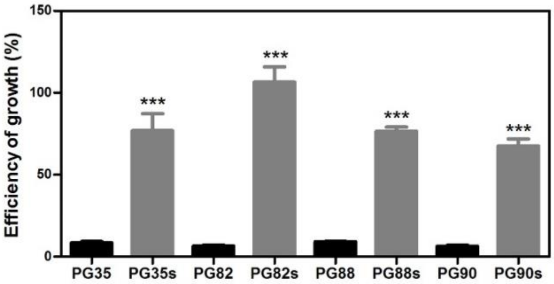

Figure R9: CFC of established cultures analyzed by means of PE assay

Data are plotted as mean growth ratio as either colonies or spheres in reference to cell seeded (n=4 at the least; *** $P < .001$, with Mann-Whitney test in comparison to DGC counterpart). Error bars represent SEM.

Data obtained with Soft Agar assay, where cells are cultured in an anchorage-independent condition, confirmed the same findings. Established GICs were more capable to grow and proliferate at low cell density than their monolayer counterpart (Figure R10-A). CFC ratio (GICs number of colonies/DGC number of colonies) proved again that GICs cultures owned a higher Colony Forming Capacity in comparison to DGC compartment (CFC ratio: 12.71 ± 0.51). Interestingly, only when DGC were seeded at extremely high concentration (i.e. 2x10^4) a proper colony growth was appreciated, but still colonies generated by GICs culture were substantially bigger (Figure R10-B).

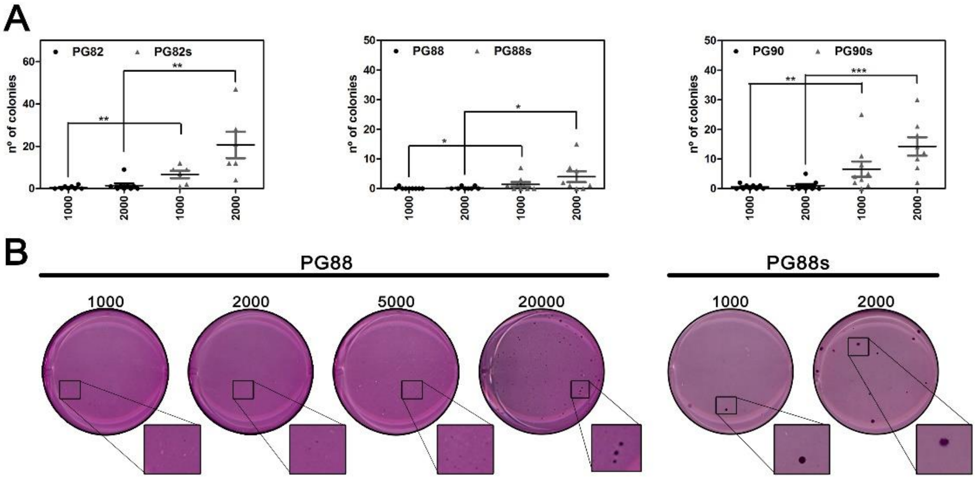

Figure R10: Soft Agar Assay of established cultures

(A) Soft Agar assay of primaries PG82, PG88 and PG90 in both culture conditions. The number of colonies scored after 21 days was plotted per concentration of cell seeded (1000 and 2000); * *P* < .05, ** *P* < .01, *** *P* < .001, with Mann-Whitney test; n = 9 for all groups. (B) Representative picture of Soft Agar Assay carried out for PG88 and PG88s after MTT staining. Cell seeded for each well is reported.

2.2.2 GICs CULTURES ARE ABLE TO SELF-RENEW AND TO DIFFERENTIATE ALONG CNS LINEAGES

GICs were tested for self-renewal capacity through a single-cell proliferation assay (Figure R11). More than 50% of cells from GICs cultures exhibited the capacity to proliferate from a single-cell unit (PG35s: 49.5 %; PG82s: 49.5 %; PG88s: 63.5 %; PG90s: 56.00 %). This data suggested that GICs cultures presented a high frequency of stem-like cells capable of self-renew independently from both cell-to-cell interactions and any paracrine stimuli.

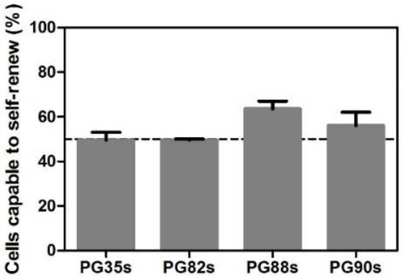

Figure R11: Single-cell proliferation assay of GICs cultures

Data are plotted as percentage mean of cells capable to growth as sphere bigger than 100 µm from a single-cell. Error bars represent SEM. Dashed line represent 50%.

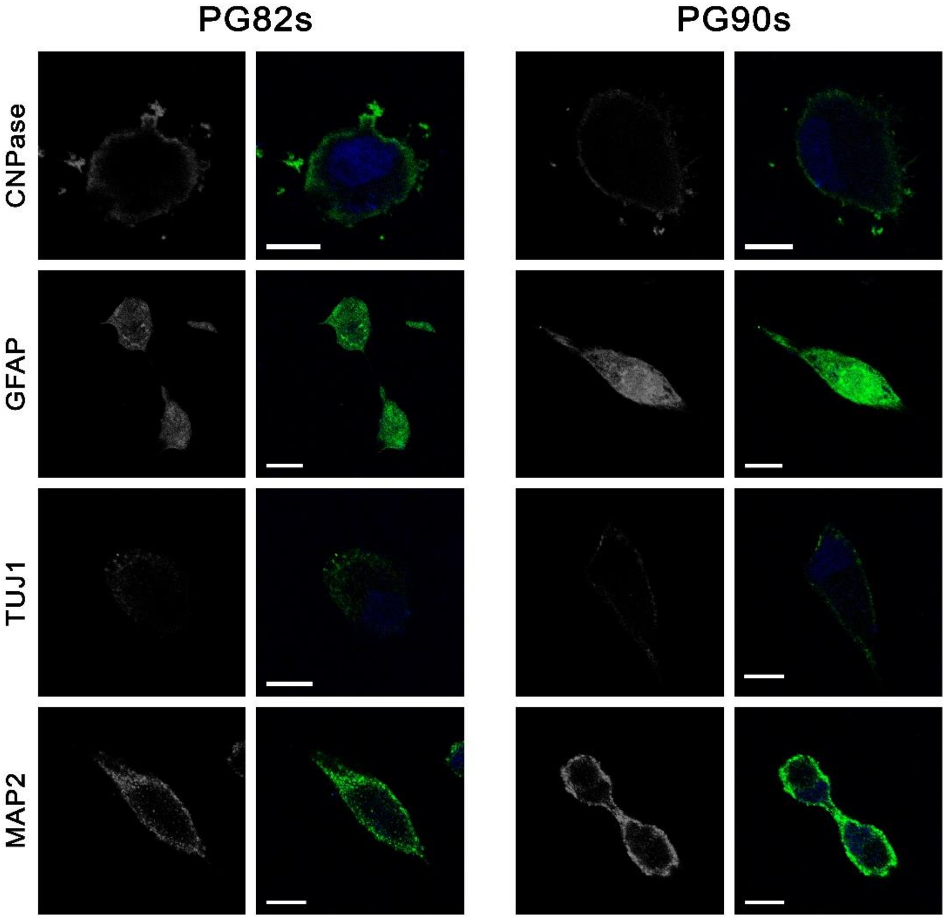

Figure R12: Differentiation of GICs along major CNS lineages

Immunofluorescence of differentiated PG82s and PG90s for neuronal markers (MAP2 and TUJ1), astrocytic marker (GFAP) and oligodendroglial marker (CNPase). Nuclei are counterstained with Draq5. Scale bar of 10 µm.

GICs were then analyzed for their capacity to differentiate under the appropriate stimuli along the major CNS lineages: astrocytic, oligodendrocytic and neuronal. Cells were cultured in 10% FBS media for 14 days. Expression of GFAP, CNPase and MAP2-TUJ1 was assessed by immunofluorescence as markers of astrocytes, oligodendrocytes and neurons, respectively. As indicated in Figure R12, GICs cultures demonstrated capability to differentiate toward all lineages mentioned.

2.2.3 GICS CULTURES GENERATE TUMORS WITH GBM HISTOLOGICAL FEATURES

Finally, in order to assess whether GICs cultures owned cancer-initiating capacity, a series of athymic mice were inoculated in the forebrain with 10^5 cells, five mice each for PG82s and PG90s. By 7 weeks, some of them started to show clinical impairment. Therefore, mice were sacrificed and brains collected. Samples were then formalin-fixed and paraffin-embedded for histological analysis. Slices were stained with Hematoxylin/Eosin and immunostained for GFAP, CD44 and Vimentin detection. Sections from patients' tumor were processed alongside. Tumors arose in three out of five mice for both GICs inoculated. Histological analysis of grafts revealed typical GBM histological features comparable to lesions found in corresponding patients (Figure R13). Moreover, grafts demonstrated a good correspondence with the expression pattern of the analyzed proteins in original tumor. In addition, grafts displayed diffuse borders between tumor and mouse brain with elongated tumorigenic cells infiltrating into brain parenchyma.

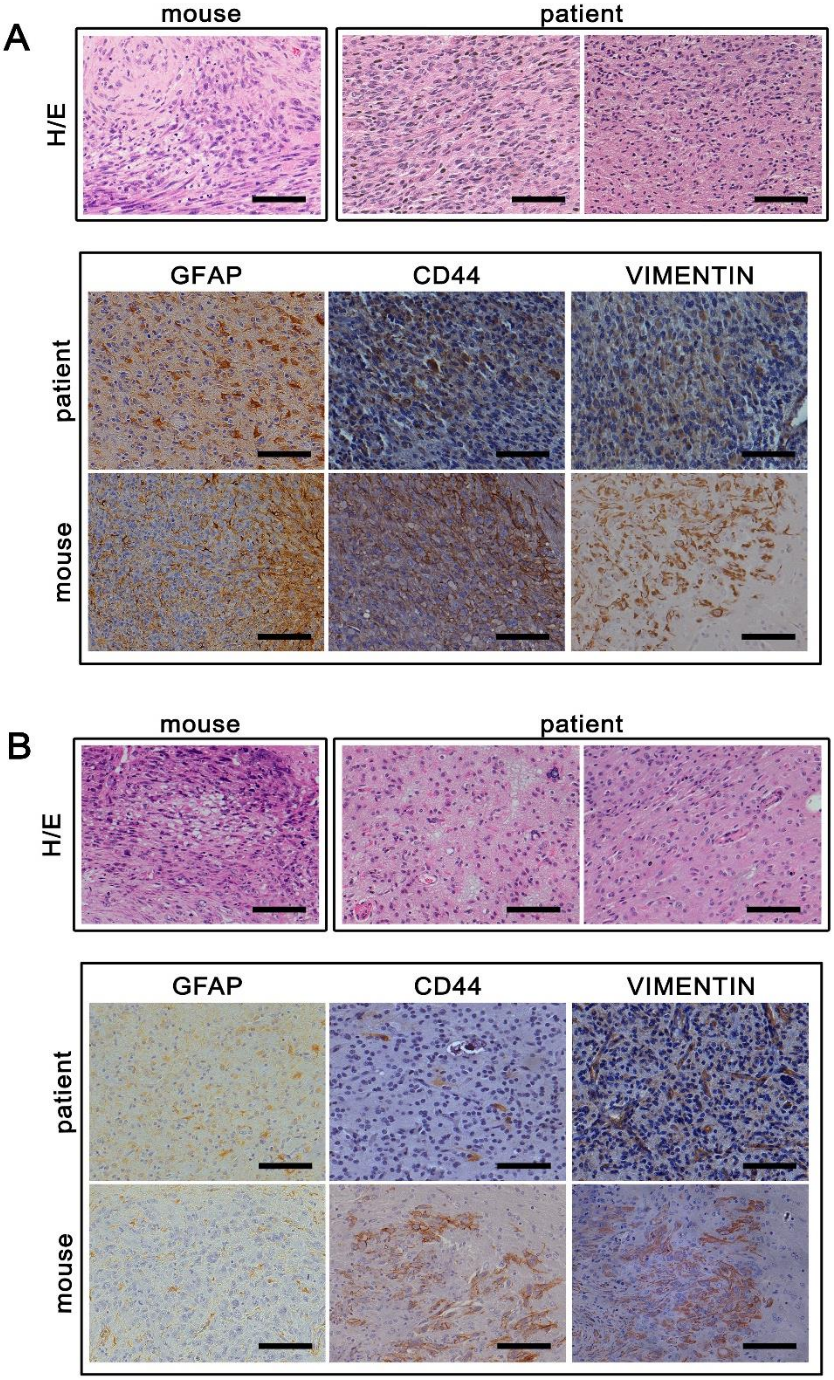

Figure R13: Histological analysis of xenografts and related patients' tumor

Stains depicted are hematoxylin and eosin (H/E) and immunohistochemistry for GFAP, CD44 and Vimentin. Samples analyzed were PG82s (A) and PG90s (B) and associated patient surgical biopsies. Scale bar of 100 µm.

2.3 GICS CULTURES DEMONSTRATE HIGH EXPRESSION OF STEM RELATED MARKERS

In addition to the mandatory assessment of GICs functional characteristics, the expression of specific markers associated to a more undifferentiated state should be verified as well (Heddleston et al., 2011; Vescovi et al., 2006). First, a panel of genes were chosen among ESCs markers and genes enriched more specifically in GICs. The expression of the selected markers was then screened for a quick presence/absence test using the semi-quantitative technique of RT-PCR (Figure R14). According to data obtained, mRNA of *CD133* and *L1CAM* could be detected exclusively in GICs cultures. On the contrary, *CD44* and *CD15* along with markers specific of ESCs, were found in both culture conditions. Taking into account that relative gene expression levels could not be calculated on RT-PCR results, to quantify the relative mRNA amount of genes, samples were then analyzed by means of qPCR.

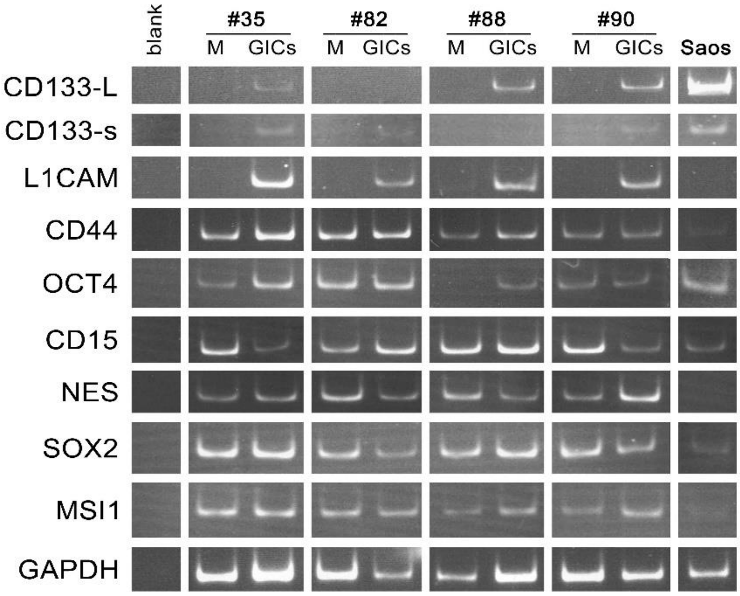

Figure R14: RT-PCR detection of genes related to an undifferentiated state

Four culture pairs were screened in both GICs and *Monolayer* (M) conditions. *GAPDH* was included in the panel as loading control. Due the complexity of the detection of *CD133* template, Saos-2 mRNA was added to the analysis as positive control. *CD133* expression was detected through two different couple of primers, one amplifying a long product of 337 bp (CD133-L) and the other a shorter product of 83 bp (CD133-s).

Given the increasing concern on markers specific of GICs, exclusively *CD133* (Bao et al., 2006), *CD44* (Anido et al., 2010), and *L1CAM* (Cheng et al., 2011) were detected using qPCR technique. Taking into account recent findings, *ITGA6* was included in the study (Lathia et al., 2010). Detection of *CD133*, *L1CAM* and *ITGA6* mRNA amount reported different expression levels between GICs and DGC cultures, being genes almost undetectable in *Monolayer* counterpart (Figure R15). The same difference was not found when analyzing *CD44* expression. It is important to note that among all markers *CD133* is the least transcribed, although the difference detected between GICs and DGC cultures is still significant.

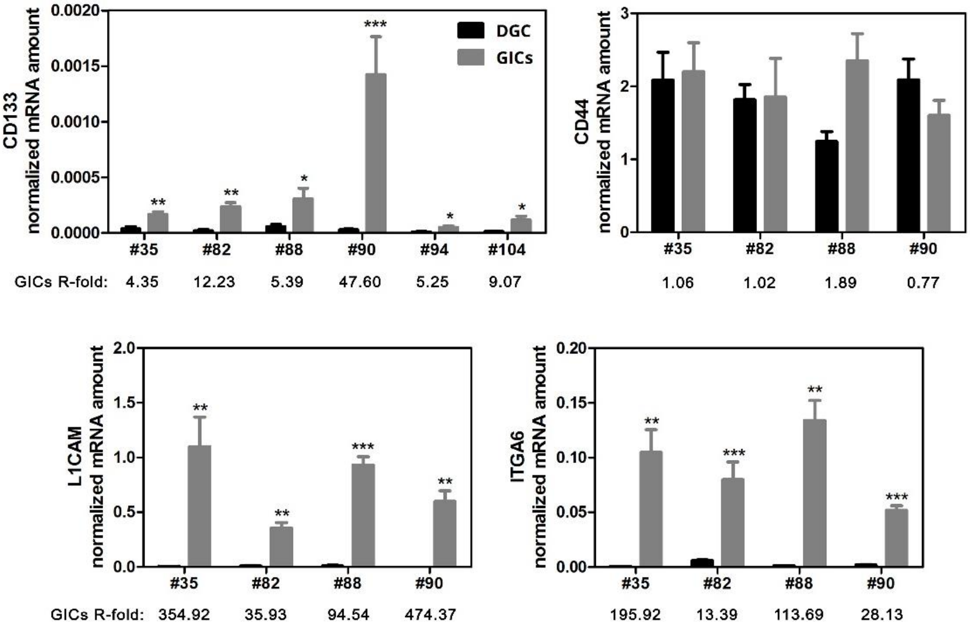

Figure R15: Quantification of GICs markers mRNA in cultures

Expression of *CD133*, *CD44*, *L1CAM* and *ITGA6* genes. mRNA levels were normalized by *GAPDH* - *GUSB* expression and plotted as mean ± SEM (n=3 at least); **P* < .05, ** *P* < .01, *** *P* < .001, with unpaired t-test in comparison to DGC counterpart. GICs R-fold were reported below each plot. R-fold was obtained from the same data subjected to the ΔΔCt method using DGC mean expression level within each culture pair as internal control.

The differential expression of selected genes was then confirmed at protein level using western blot technique (Figure R16). In order to avoid false-negative signals, being all markers surface proteins, DGC were recollected without trypsin digestion using scrapers. Data obtained were consistent with mRNA analysis. L1CAM and ITGA6 protein amount in GICs culture was statistically higher when compared to DGC counterpart. The same difference in protein amount was observed for CD44 as well, suggesting protein stabilization. This increase was statistically significant in most of the established GICs cultures. The high level of different glycosylation states of CD133 and its limited amount in samples, made difficult its immunoblotting detection (Kemper et al., 2010). Therefore, CD133 expression was exclusively evaluated through mRNA analysis.

Taken together, all data collected concerning functional features and markers expression, established GICs were considered from now on as effectively enriched in Glioblastoma Initiating Cells.

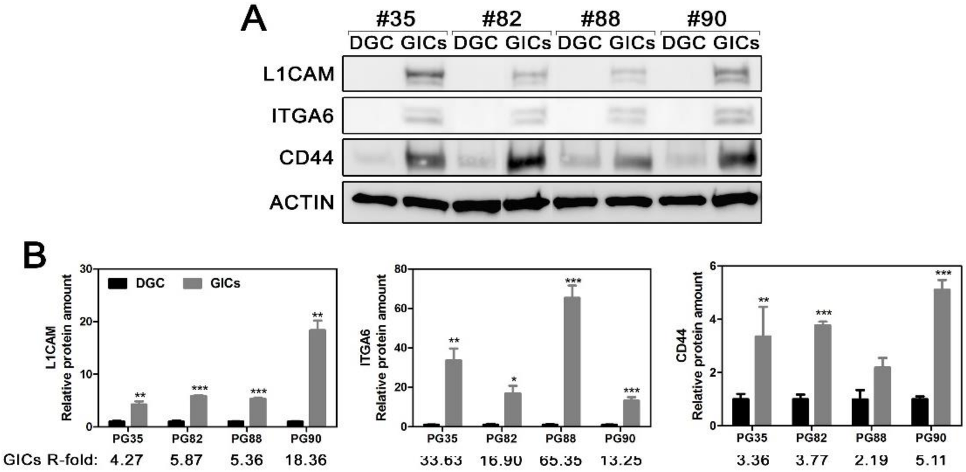

Figure R16: Quantification of GICs markers at protein level in cultures

(A) Representative Western Blot analysis of CD44, ITGA6 and L1CAM. (B) Western blot quantification of CD44, ITGA6 and L1CAM amount through densitometric analysis. Data are normalized to β-actin and plotted as mean ± SEM from at least 3 independent samples. * $P < .05$, ** $P < .01$, *** $P < .001$, with unpaired t-test in comparison to DGC counterpart. GICs R-fold indicates the relative fold difference between GICs culture and the relative DGC.

2.3.1 INDUCED DIFFERENTIATION CORRELATES WITH REDUCED EXPRESSION OF STEM-RELATED MARKERS

In order to assess the specificity of stem-related gene expression in the *neurosphere* condition, GICs were cultured in 10% FBS containing media for 7 days to promote differentiation. Expression levels of ESCs markers *NES* and *MSI1* along with GICs markers *ITGA6*, *L1CAM* and *CD44* were then quantified by qPCR technique. As indicated in Figure R17, cells under differentiating stimuli expressed significantly less selected genes. These data confirmed that the expression of stem-related markers is the result of the *Neurosphere* media selective pressure on culture that select away differentiated cells. Once this pressure is removed, cells started to differentiate and to generate culture where GICs are progressively disappearing.

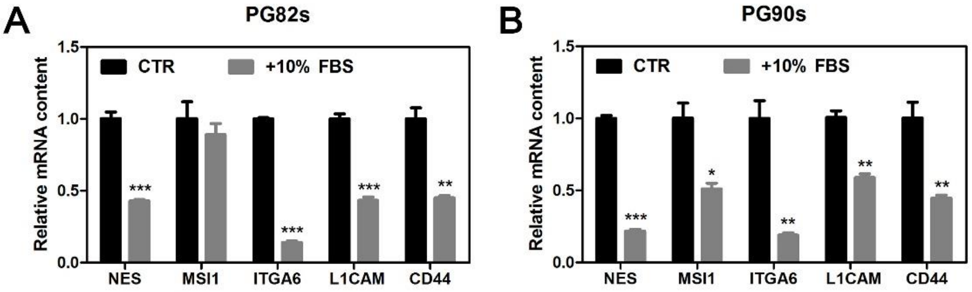

Figure R17: Expression of stem-related markers under differentiation stimuli

Expression of *NES*, *MSI1*, *ITGA6*, *L1CAM* and *CD44* after 7 days in cultures with media supplemented by 10% FBS. Cells were subcultured following the cell proliferation rate. Relative mRNA levels were normalized by *GUSB* expression and plotted according to the ΔΔCt method as mean ± SEM (n=3); * $P < .05$, ** $P < .01$, *** $P < .001$, with unpaired t-test in comparison to undifferentiated counterpart.

2.4 GICS BELONG TO HIGHLY HETEROGENEOUS CULTURES

In order to investigate the expression pattern of selected markers, the protein distribution among cells in cultures was analyzed. The concurrent localization of ITGA6-L1CAM and ITGA6-CD44 was assessed by means of immunofluorescence staining (Figure R18). Confocal images were taken with same acquisition settings in order to allow an effective comparison of fluorescence intensity between cultures. Consistently with previous findings, fluorescence signal of ITGA6 and L1CAM was almost undetectable in DGC whereas GICs exhibited a clear and intense staining. Fluorescence detected in DGC for L1CAM was weaker and diffuse along cytoplasm and nuclei but not on cell membrane, suggesting an unspecific staining. As observed previously, CD44 was expressed under both culturing conditions, although a difference of fluorescence intensity could be noticed, being higher in GICs than in DGC. In addition, a clear heterogeneity of markers distribution was observed within GICs cultures. Cultures showed multiple clones expressing a various combination of markers or none of them, being cell expressing all of them the minority.

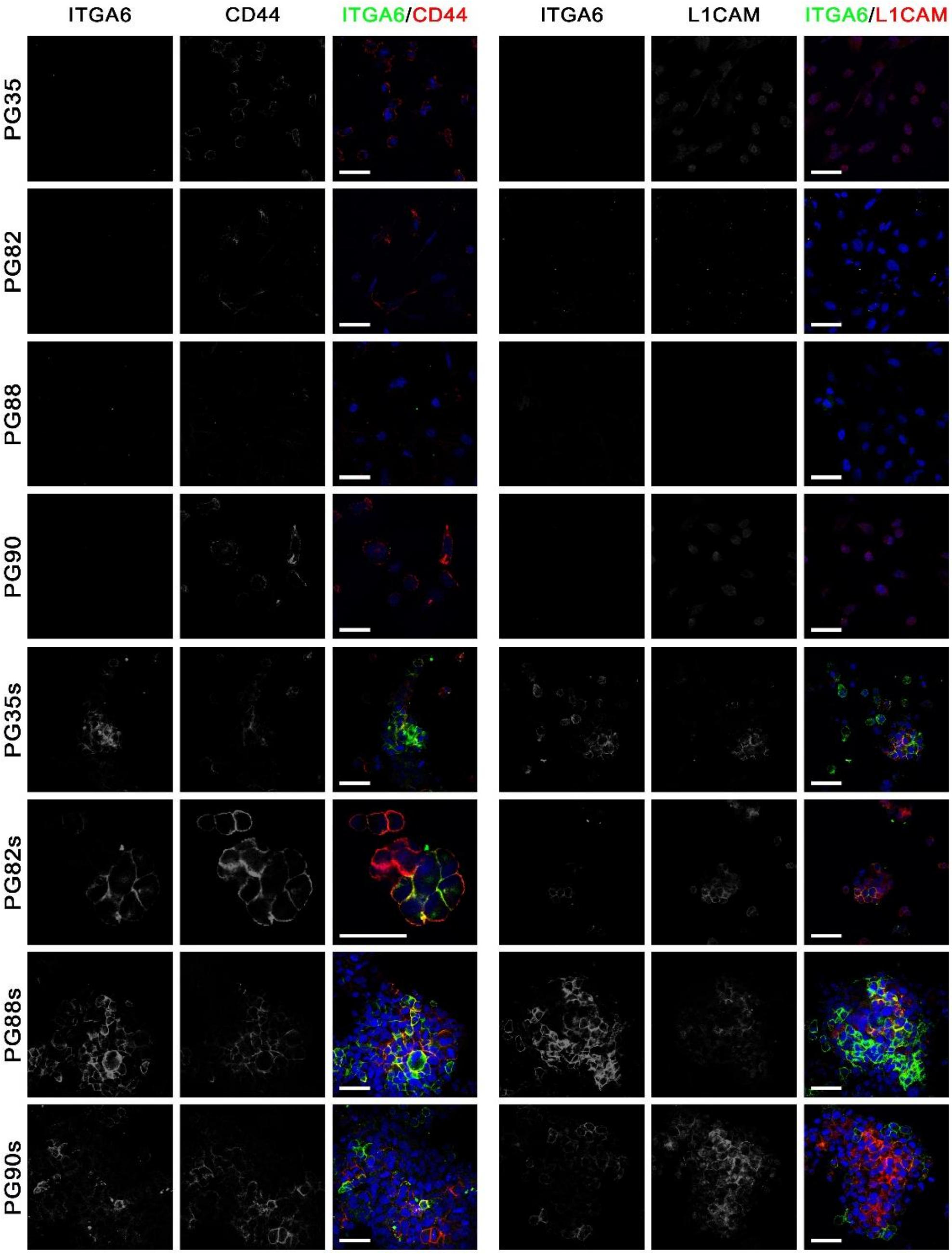

Figure R18: GICs markers distribution within cultures

Confocal images of ITGA6 (Alexa-488, green), CD44 (Alexa-555, red) and nuclei (DRAQ5, blue). Scale bar of 50 µm.

2.5 GICS RELY MORE ON OXIDATIVE METABOLISM THAN THEIR DIFFERENTIATED COUNTERPART

In order to assess the metabolic state of established cultures, the consumption of glucose and oxygen along with the production of lactate were evaluated. Metabolites were quantified after 4 days in standard culture conditions from the same number of seeding cells. Data obtained were further normalized to the number of cells counted at the end-point.

According to data obtained, GICs showed significantly lower consumption of glucose compared to DGC (*P* < .001; Figure R19-A), even though the production and extracellular accumulation of lactate was equal between both culturing conditions (Figure R19-B). Quantification of the oxygen consumption rate (OCR) revealed that GICs consumed significantly more oxygen than DGC (*P* < .01; Figure R19-C).

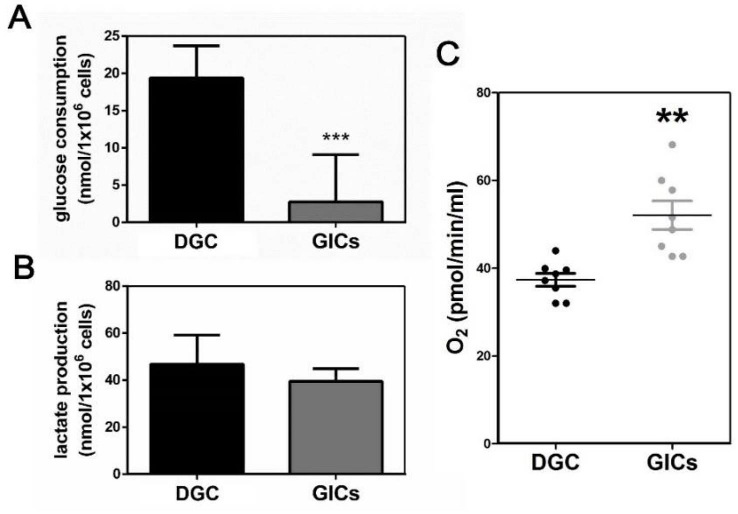

Figure R19: Analysis of metabolic profile of established cultures

Quantification of glucose (A) and lactic acid (B) in media after 4 days of culture. Dot plot of OCR values in standard proliferation condition (C). Data were plotted as mean ± SEM from analysis carried out on #82, #88 and #90 culture pairs; ** *P* < .01, *** *P* < .001, with unpaired t-test in comparison to DGC counterpart.

Moreover, to investigate the molecular basis of the observed metabolic preferences, the levels and activation state of key metabolic pathways were evaluated. Constitutive PI3K/AKT activation, a hallmark of several tumors, stimulates glucose uptake and utilization through AKT phosphorylation (Buzzai et al., 2005; Elstrom et al., 2004; Heiden et al., 2009). At the branching point between glycolysis and oxidative metabolism, the mitochondrial complex Pyruvate dehydrogenase (PDH) regulates the irreversible oxidative decarboxylation of pyruvate to acetyl-CoA to enter the TCA cycle. Serine phosphorylation of PDHE1α subunit (phosphorylation sites in Ser264; Ser271; Ser203) results in inhibition of enzyme activity. Blockade of carbon flux through PDH shunt pyruvate away from the TCA cycle toward glycolysis and impair OXPHOS (Korotchkina & Patel, 2001; Rardin et al., 2009; Wolf et al., 2010; Yeaman et al., 1978). In addition, mitochondrial isoenzyme of phosphoenolpyruvate carboxykinase (PEPCK-M) catalyzes the conversion of oxaloacetate to phosphoenolpyruvate (PEP). PEPCK-M is the only enzyme able to connect mitochondrial intermediates via oxaloacetate with the glycolytic intermediary pool above PEP (Méndez-Lucas et al., 2014). Expression of mitochondrial PEPCK correlates with glycolysis-TCA crosstalk and activation of gluconeogenetic/glyceroneogenesis pathways.

The phosphorylation of AKT (Ser473) and PDH (Ser293) along with the expression of PEPCK mitochondrial isoenzyme (PEPCK-M) were detected by western blot (Figure R20).

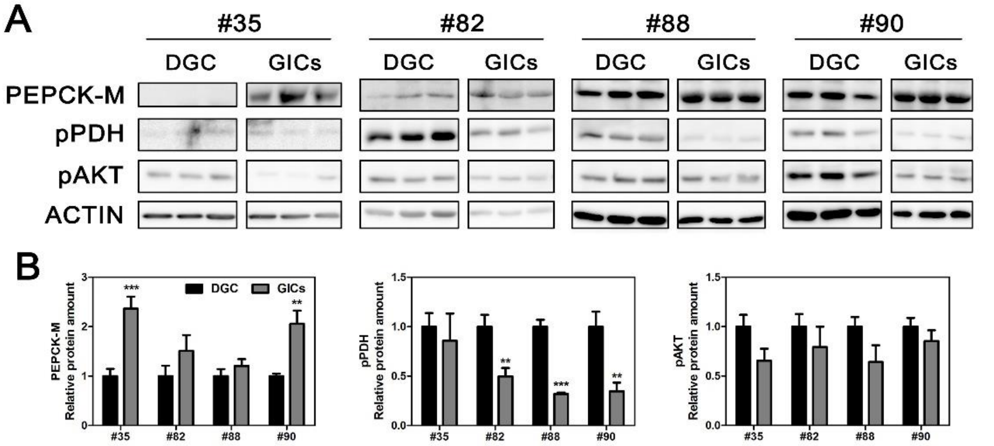

Figure R20: Analysis of metabolic enzymes

(A) Representative Western Blot analysis of metabolic enzymes PEPCK-M, pPDH and pAKT in four different cultures pairs. Matching DGC and GICs were blotted on the same membrane. (B) Western blot quantification of pPDH, PCK2 and pAKT amount through densitometric analysis. Data are normalized to β-actin and plotted as mean ± SEM from at least 2 independent experiments. ** *P* < .01, *** *P* < .001, with unpaired t-test in comparison to DGC counterpart.

A common pattern of PI3K/AKT pathway activation and PDH blockade was revealed in DGC cultures. The arrangement was consistent with previous results and confirmed a more glycolytic state. Conversely, reduced phosphorylation of PDH enzyme together with higher OCR suggested robust mitochondrial respiration and higher activity of

TCA cycle in GICs. Moreover, higher PEPCK-M expression was detected in GICs. Together with observed reduced glucose uptake, PEPCK-M could point to a different source of carbon for energy production and anabolic processes in GICs.

3 RADIOTHERAPY RESPONSE STUDY

3.1 GICS CULTURES EXHIBIT A RADIORESISTANT PHENOTYPE

In the last decade, experimental findings progressively support the pivotal role of CSC in tumor resistance to common therapies (Clevers, 2011; Dick, 2008). In GBM several noteworthy data support the involvement of CSC in tumor progression and recurrence after treatment (Bao et al., 2006). Following the common belief that tumor recurrence is essentially due to marked radioresistance (Cheng et al., 2011), established cultures were investigated in order to identify a radioresistant phenotype.

3.1.1 GICS CULTURES ARE MORE RADIORESISTANT THAN THEIR DIFFERENTIATED COUNTERPART

First, in order to determine established cultures' sensitivity to RT, irradiated cells were analyzed employing clonogenic assay, the gold standard technique to investigate long-term effects of ionizing radiation on cultures (Franken et al., 2006). Cultures were tested in their standard culture conditions and four different doses were evaluated (2, 4, 6 and 8 Gy) and compared with unirradiated samples (0 Gy). Treatment doses were given fractionated at daily dose of 2 Gy. In the case of GICs, traditional clonogenic assay was adapted to fit with the free-floating spheres condition. Surviving fraction at each dose was calculated and the obtained survival curves were represented in a logarithmic scale (Figure R21). According to the obtained survival curve parameters (SF2; SF8; AUC; Figure R22), in three out of four cases analyzed, GICs-enriched compartment exhibited a more radioresistant phenotype compared to DGC (#82; #88; #90; two-way ANOVA $P < .001$). SF2 and SF8 were in all primaries significantly higher in GICs than in their DGC counterparts (SF2 $P < .0001$ for #82 and #90, $P < .01$ for #88; SF8 $P < .0001$ for #88 and #90, $P < .01$ for #82). GICs compartment of #35 reported a more radiosensitive curve (two-way ANOVA $P < .01$) with no substantial difference between GICs and DGC at 2 Gy ($P = .8$).

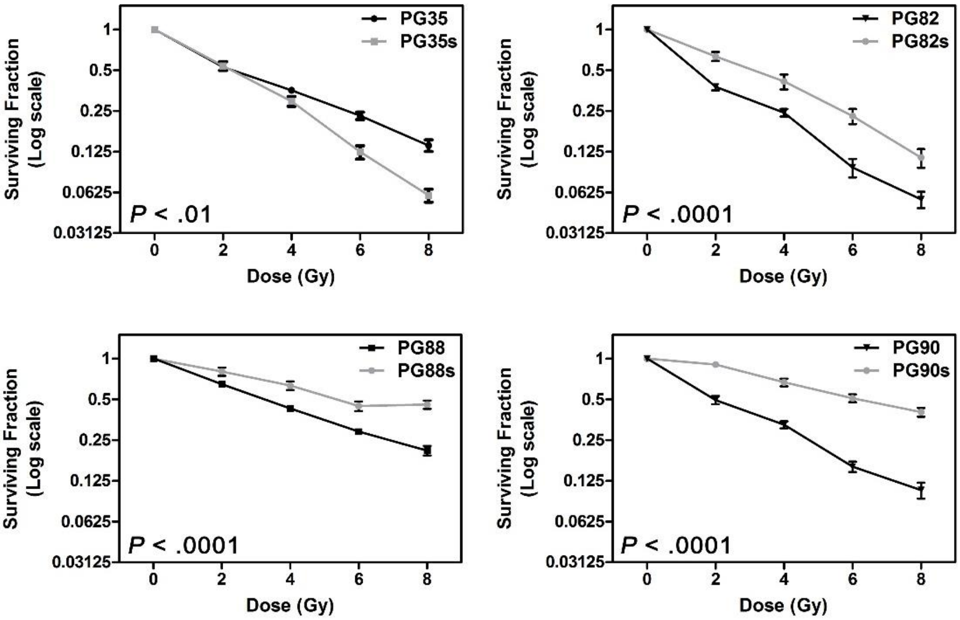

Figure R21: Survival curves after RT in fractionated doses

Curves were obtained through the clonogenic assay from at least 4 independent experiments. Indicated *P*-values were calculated by two-way ANOVA comparing GICs with DGC curves. Data are plotted in Log(2) scale as mean ± SEM.

Proliferation impairment of cultures was then modeled according to the Linear Quadratic Model (LQM; Astrahan, 2008; Fowler, 2006; Franken et al., 2006). The LQM is used to fit the survival curves obtained from RT dose-response experiments into a mathematical model. This model is the most popular approach to predict dose/fraction dependencies and to explain the biological effect of fractionated dose. In order to quantify the biological response and to allow comparison among cultures α- and β-component at 2 Gy were calculated (Figure R22). The smaller the two radiobiological components are the less RT impairs cellular proliferation. With exception of PG35s, all GICs-enriched compartments were characterized by lower α- and β- values indicating higher intrinsic radioresistance and better repair of sublethal DNA damage respectively (Fowler, 2006). The third informative radiobiological parameter calculated was α/β ratio, associated to fractionation sensitivity. In PG82s, PG88s and PG90s, α/β ratio was significantly higher compared to DGC counterpart, suggesting a reduced sensitivity to fractionated doses. A minor sensitivity to fractionation implies higher cumulative dose (D > α/β) needed to achieve an exponential (quadratic) correlation between the dose and the cellular requirement to repair damage (Emami et al., 2015). Consequently, higher doses are necessary to increase responsiveness to fractionation and to impair cell resilience. Finally, a substantial variability among GICs cultures was detected with respect to radiosensitivity. As indicated by α values, PG90s was the most radioresistant with the lowest α and PG35s the most radiosensitive, with the highest α.

		Survival Curves parameters			Linear Quadratic Model values				
		SF2	SF8	AUC	α (Gy^{-1})	β (Gy^{-2})	α/β (Gy)	GICs Intrinsic Radioresistance[1]	GICs Repair Capacity[2]
#35	DGC	0.53 ± 0,02	0.14 ± 0,01	3.37	0.2360	0.0417	5.66	1.02	1.08
	GICs	0.54 ± 0.04	0.06 ± 0.01	2.97	0.2306	0.0393	5.87		
#82	DGC	0.38 ± 0.02	0.05 ± 0.01	2.48	0.3118	0.0884	3.53	1.70	3.83
	GICs	0.63 ± 0.05	0.11 ± 0.02	3.66	0.1833	0.0225	8.14		
#88	DGC	0.65 ± 0.02	0.21 ± 0.02	3.99	0.1762	0.0205	8.59	1.80	3.50
	GICs	0.80 ± 0.06	0.46 ± 0.03	5.22	0.0985	0.0056	17.59		
#90	DGC	0.49 ± 0.03	0.11 ± 0.01	2.83	0.2529	0.0498	5.08	5.27	50.00
	GICs	0.90 ± 0.04	0.40 ± 0.03	5.57	0.0480	0.0012	38.93		

Figure R22: Survival curves parameters and values obtained from the LQ modeling

Table indicates parameters defining DGC and GICs radiation sensitivity. Data obtained from survival curves: Surviving Fraction at 2 Gy (SF2) and 8 Gy (SF8); Area Under the Curve (AUC). SF2 and SF8 are indicated as mean ± SEM. Values obtained following the LQM interpretation of the curves: α- and β-value. Obtained parameters were subsequently processed to calculate the α/β ratio, the Intrinsic Radioresistance and the Repair Capacity. (1) Calculated comparing cultures derived from the same patient: α-DGC/α-GICs. (2) Calculated comparing cultures derived from the same patient: β-DGC/β-GICs. (1) and (2) calculated according to bibliography (Fowler, 2006; Franken et al., 2002).

3.1.2 GICs' INTRINSIC RADIOSENSITIVITY PREDICTS CLINICAL RESPONSE TO TREATMENT

In order to evaluate the association between observed *in-vitro* radiobiological response and effective clinical evolution, obtained LQ parameters were compared to patient Disease-Free Survival (DFS) and Overall Survival (OS) and clinical response to treatment (see Figure R23-A). All patients analyzed were treated with Stupp chemo-radiotherapy regimen (Stupp et al., 2005). A correlation was observed primarily between LQ parameters obtained from GICs cultures and patients' DFS. In particular, the smaller the α- and β-value, the shorter the patient's DFS (Figure R23-B). The same tendency was found between GICs LQ parameters and OS, even if with a weaker association. Importantly, the same correlation was not found between clinical parameters and the obtained LQ values of DGCs compartment. Collectively, these findings suggest that patients clinical outcome may be preferentially determined by GICs intrinsic sensitivity to fractionated RT, while the radiosensitivity grade of the bulk of the tumor has only a marginal role. Moreover, the characterization of GICs' intrinsic radiosensitivity could be employed as a powerful tool to predict clinical response to standard therapy based on ionizing radiation.

A **Clinical data**

	DFS	OS	Response
#35	11 m	26 m	complete
#82	4 m	32 m	progression
#88	3 m	9 m	progression
#90	2.5 m	6.5 m	progression

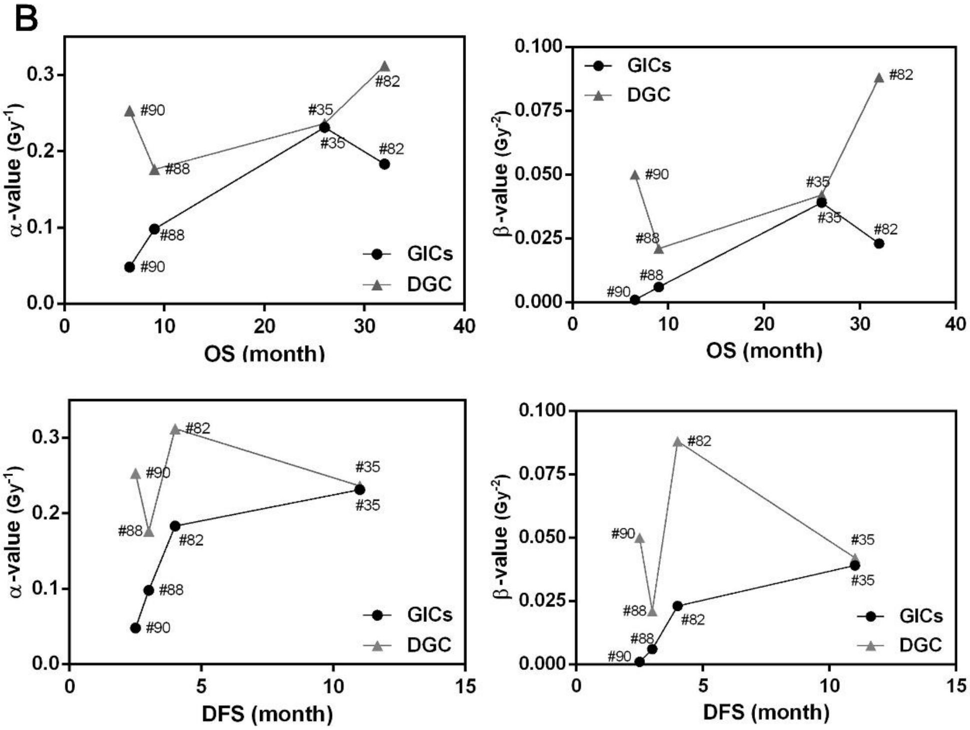

Figure R23: Clinical data of analyzed patients

(A) For each patient it is indicated the Disease-Free Survival (DFS) and the Overall Survival (OS) in month (m). In addition, response to treatment as either complete response or progression of the disease is displayed. (B) In order to visualize better the association between LQ parameters and patient clinical data, calculated α- and β-value were plot along with patients' OS and DFS.

3.1.3 HIGHLY RESISTANT GICS SHOWED BIGGER SPHERE SIZE

The adapted clonogenic assay protocol for GICs cultures allowed the additional and accurate evaluation of spheres dimension when scored at the end-point. Sphere size is connected to proliferative capacity in culture. Data collected were represented in Figure R24. As expected, the sphere dimension was significantly reduced after treatment in a manner proportional to the dose received. Interestingly, those GICs displaying higher resistance to radiation (PG88s and PG90S) generated bigger spheres in both control and post-radiation conditions.

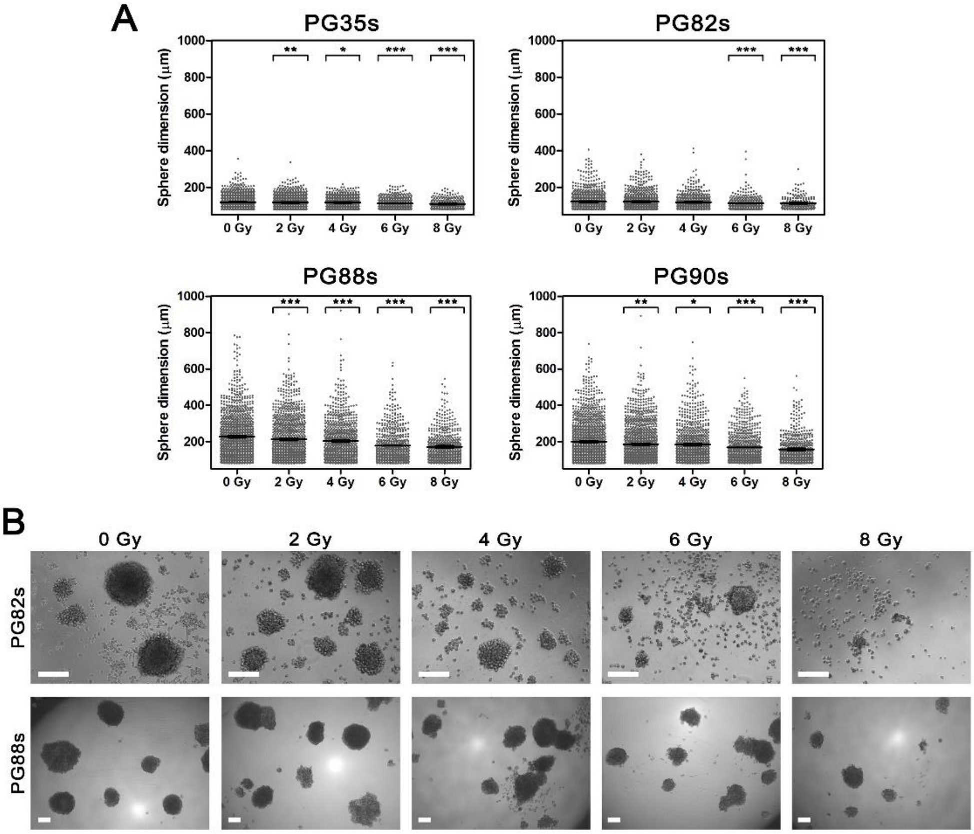

Figure R24: Sphere dimension analysis after RT

(A) Scatter plot of GICs spheres sizes after 14 days in culture at control and treated condition; * P < .05, ** P < .01, *** P < .001, with Mann-Whitney test in comparison to control sample (0 Gy). (B) Representative picture of PG82s and PG88s spheres at every condition. Scale bars of 200 μm.

3.2 REPEATED RADIATION CYCLES PROVOKE A GICS' SWITCH TOWARD A MORE RADIORESISTANT PHENOTYPE

According to data obtained from clonogenic assay, #35 was the unique culture pair that did not adhere to the common belief of GICs being more resistant to therapies. In order to examine in depth the radiosensitivity of #35 culture pair, the response to repeated cycles of RT was studied. Cultures were exposed to standard 4-days cycles of fractionated doses (2 Gy per fraction) scheduled every 3 weeks according to the regimen displayed in Figure R25-A. The recovery period within two consecutive cycles was calculated according to data obtained from Doubling Time evaluation (Figure R25-B) in order to allow the complete cell cycle restoration. After 21 days from the beginning of the experiment both cultures maintained in standard growing conditions reached their initial proliferation rate. Following the recovery period, cultures were named PG35R and PG35sR where R stands for one completed cycle of radiation and recovery. Subsequently, PG35R and PG35sR underwent a second cycle of radiation and cell viability was tested using the clonogenic assay. After an additional recovery period, cultures were then named PG35RR and PG35sRR and were treated with a third cycle of fractioned RT. Thereafter, the cell proliferation impairment was again assessed by means of clonogenic assay.

Interestingly, the survival curve obtained from PG35sR revealed a significant switch toward a more radioresistant phenotype (Figure R25-C). When compared to PG35s, PG35sR displayed significantly higher SF2 and SF8 ($P < .0001$) and an overall statistical difference between the two curves (two-way ANOVA $P < .0001$). Moreover, PG35sR curve showed an important reduction of α- and β-values at 2 Gy indicating an increased intrinsic radioresistance and higher repair capacity, respectively (Figure R25-E). On the contrary, PG35R showed a weak radiosensitization compared to PG35 (two-way ANOVA $P < .05$) but no statistical variation of SF2 and SF8 ($P = .5$ and $P = .1$ respectively). Comprehensively, the curves obtained from PG35R and PG35sR diverged statistically being PG35sR significantly more radioresistant than PG35R (two-way ANOVA $P < .0001$).

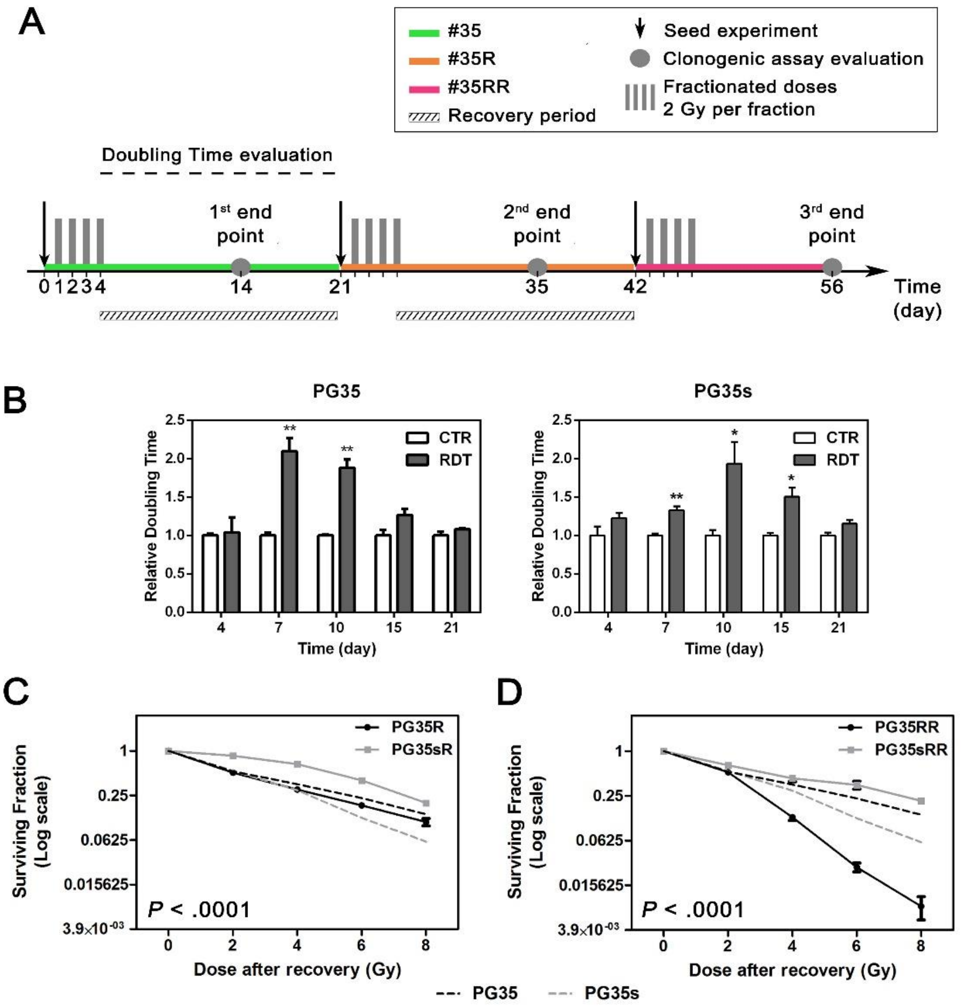

E

	SF2	SF8	AUC	α (Gy⁻¹)	β (Gy⁻²)	α/β (Gy)
PG35R	0.51 ± 0.02	0.110 ± 0.012	3.10	0.2461	0.0454	5.42
PG35sR	0.86 ± 0.04	0.198 ± 0.014	5.05	0.0689	0.0026	26.33
PG35RR	0.45 ± 0.03	0.008 ± 0.003	2.07	0.2399	0.0434	5.52
PG35sRR	0.65 ± 0.05	0.214 ± 0.016	4.07	0.1766	0.0206	8.56

Figure R25: PG35s switched toward a more radioresistant phenotype

(A) Design of the repeated cycles of fractioned RT carried out on #35 culture pair. (B) Doubling Time data after 8 Gy exposure (RDT) of PG35 and PG35s referred to the unirradiated control (CTR). Data were plotted as mean ± SEM; * P < .05, ** P < .01, with unpaired t-test in comparison to control sample. (C) Clonogenic assay survival curves after second and third radiation schedule (n=4 at the least; two-way ANOVA P calculated comparing PG35R with PG35sR and PG35RR with PG35sRR).

(legend continued on next page)

Data are plotted in Log(2) scale as mean ± SEM. Black and grey dashed lines represented respectively PG35 and PG35s survival curves and were indicated as internal reference. (D) Table indicate measures of DGC and GICs radiation sensitivity obtained from the survival curves: cell Surviving Fraction at 2 (SF2) and 8 Gy (SF8) and Area Under the Curve (AUC). SF2 and SF8 are plotted as mean ± SEM. In addition, measure of DGC and GICs radiosensitivity according to the LQM were indicated: α- and β-value at 2 Gy and their ratio.

Finally after the third radiation cycle, PG35RR reported a dramatic radiosensitization (two-way ANOVA $P < .0001$) with a striking drop in SF8 ($P < .0001$) compared to PG35R (Figure R25-D). Concurrently, PG35sRR showed a slight increase in α- and β- values when compared to PG35sR, but importantly SF8 reported no significant variation ($P = .67$) and PG35sRR maintained a more radioresistant phenotype compared to PG35s.
In conclusion, repeated cycles of fractioned RT induced in PG35 and PG35s opposite responses based on the acquisition of different grades of radiosensitivity.

3.3 ALAMARBLUE REDUCTION RATE POSITIVELY CORRELATES WITH GICS SURVIVAL FRACTION

Viability of neurospheres was also determined using AlamarBlue™ (AB, Invitrogen) reagent after 14 days of radiation treatment. The assay allows to evaluate repeatedly the reducing power of cells in real-time schedule with no need of serial washes and sample transfer. These characteristics made AlamarBlue™ reliable for neurospheres cultures viability detection post RT. The fluorescence intensity was found to be linear from 1 to 4 hours of AB incubation (Figure M6: AlamarBlue® incubation time optimization). AB reduction rate of clonogenic assay plates was detected by fluorescence every hour from 1 to 4 hours and the mean fluorescence from all lectures was calculated for each plate (Figure R26). The correlation coefficient between calculated GICs surviving fraction and the reagent reduction rate was >0.9 for most of the tested primaries, with exception of PG88s ($r^2 = 0.51$). Values of r-squared greater than 0.9 indicate a good correlation and prove that 90% of the variance in AB reduction can be explained by variation in the number of neurospheres. The verified correlation suggested that AB reduction could be effectively used to predict quickly neurosphere surviving fraction after radiotherapy with a good fit.

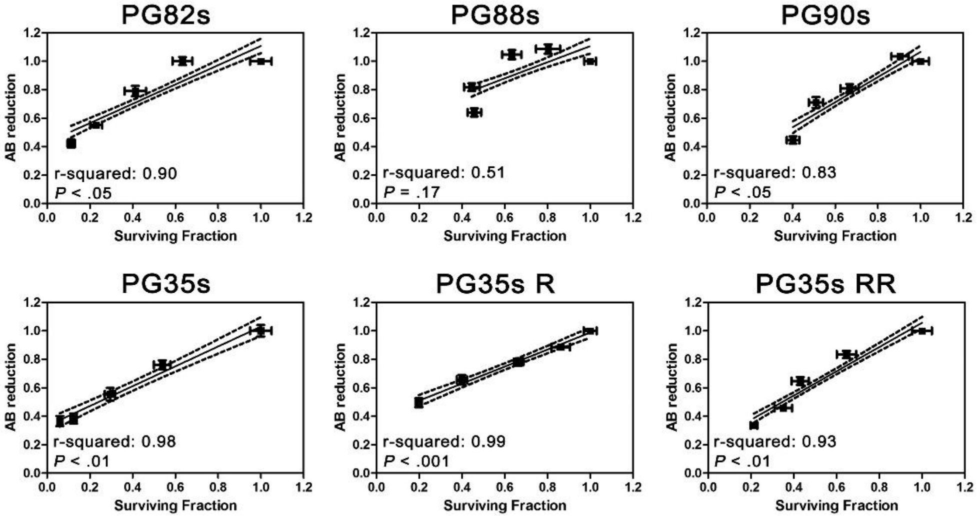

Figure R26: Correlation between GICs survival curves and AlamarBlue reduction rate

Data are plotted as mean ± SEM for both axis. The coefficient r-squared was calculated from the Pearson correlation coefficient using GraphPad Prism (v 5.0; GraphPad Software). The significance of correlation is indicated by p-values displayed for each plot.

3.4 TRANSCRIPTOME OF IRRADIATED CULTURES DEFINES INFLAMMATORY AND EMT-RELATED PATHWAYS AS KEY RESPONSES OF GICS

3.4.1 IRRADIATED GBT35-DERIVED CULTURES DO NO CONSIDERABLY DIFFER FROM UNIRRADIATED SAMPLES

In order to identify mechanisms mediating GBM radioresistance, the molecular basis driving GICs and DGC different RT response were analyzed by genome-wide microarray analysis. To this end, repeated RT cycles on #35 culture pair was considered to provide a good platform to define determinants and regulators driving GICs radioresistance. Transcriptome of fourteen samples representing five different #35 experimental conditions were analyzed (conditions are indicated in Figure R27-A). Control condition samples were collected together with IR samples one hour after the last 2 Gy fraction treatment. Irradiated PG35sR was included to the analysis as it represents the condition of the peculiar radioresistant switch. Gene expression profiles were measured using Human Gene 1.0 ST Array (Affymetrix).

First, to visualize the overall transcriptome status of analyzed conditions, unsupervised principal component analysis (PCA) of microarray data was conducted (Figure R27-B).

Two major clusters were identified: control samples grouped with their corresponding first-cycle 8 Gy-treated condition, while a clear separation was observed between differentiated (cluster 1) and GICs-enriched samples (cluster 2). Interestingly, irradiated PG35sR displayed a strong segregation from the above-mentioned clusters, thus defining a third cluster.

A dedicated chapter was realized to investigate the diverse molecular basis of DGC and GICs clusters in control condition (Chapter 3.5).

A

SAMPLE NAME	DESCRIPTION
PG35 CT	#35 DGC unirradiated
PG35 IR	#35 DGC after 8 Gy (2 Gy per fraction)
PG35s CT	#35 GICs unirradiated
PG35s IR	#35 GICs after 8 Gy (2 Gy per fraction)
PG35sR IR	PG35sR after 8 Gy (2 Gy per fraction)

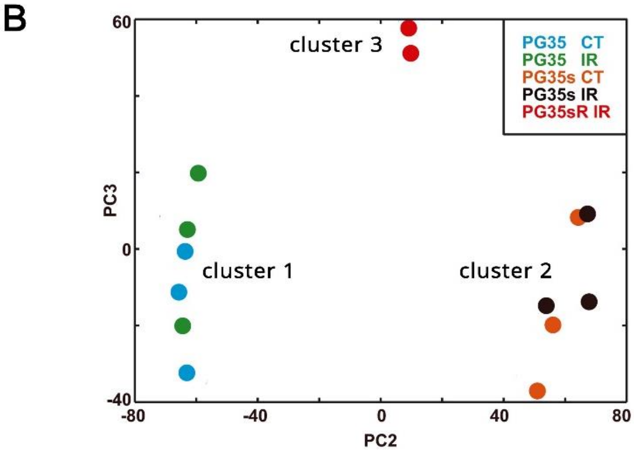

Figure R27: Transcriptomic analysis of irradiated #35 cultures

(A) Analyzed cultures were PG35 and PG35s 8 Gy irradiated and control condition plus PG35sR following a second cycle of fractioned RT. PG35sR stands for PG35s after a complete cycle of RT and subsequent recovery (Figure R25-A). (B) Genome-wide transcriptomic analysis of microarray data using unsupervised PCA plot of microarray data.

As expected from the reduced segregation between CT and IR groups observed in the PCA plot, comparative analysis of the transcriptomes was unable to identify genes significantly upregulated or downregulated (level of significance: FDR < 0.05).

To investigate the biological significance of microarray data, a Gene Set Enrichment Analysis (GSEA, Broad Institute; Mootha et al., 2003; Subramanian et al., 2005) was performed. This approach favors an overall insight of the obtained data through the identification of changes in canonical signaling pathways or co-regulated gene sets. GSEA allows highlighting even subtle changes that might remain undetected when analyzing individual genes. In order to identify gene sets positively or negatively enriched following RT, first-cycle treated groups were compared to their corresponding control conditions and three different pathway databases were interrogated for gene set enrichment (BioCarta, KEGG and Reactome). According to data obtained, few gene sets recorded a significant enrichment (FDR < 0.05; Figure R28 and Figure R29).

Both DGC and GICs showed a mild positive enrichment in inflammatory pathway after IR as indicated by BioCarta LAIR_PATHWAY, IL1R_PATHWAY and IL10_PATHWAY for DGC and BioCarta IL6_PATHWAY for GICs (Figure R28) with *IL6* and *IL8* genes contributing the most to enrich the indicated gene sets.

DATABASE	GENE SET NAME	NES	FDR *q*-value	GENE SET BRIEF DESCRIPTION
Pathways positively enriched in PG35 after IR				
Reactome	GENERIC_TRANSCRIPTION_PATHWAY	2.53	0.000	*Genes involved in Generic Transcription Pathway*
KEGG	BLADDER_CANCER	2.03	0.000	*Alterated pathways in BC (RTK/Ras, p53/Rb, E-cad, MMPs and VEGF)*
BioCarta	LAIR_PATHWAY	1.97	0.038	*Cells and Molecules involved in local acute inflammatory response*
Reactome	NEGATIVE_REGULATORS_OF_RIG_I_MDA5_SIGNALING	1.95	0.039	*Genes involved in Negative regulators of RIG-I/MDA5 signaling*
KEGG	SMALL_CELL_LUNG_CANCER	1.90	0.016	*Molecular mechanisms altered in SCLC (MYC, p53, PTEN, RB, and FHIT)*
BioCarta	IL1R_PATHWAY	1.90	0.046	*Signal transduction through IL1R*
BioCarta	IL10_PATHWAY	1.87	0.044	*IL-10 Anti-inflammatory Signaling Pathway*
KEGG	EPITHELIAL_CELL_SIGNALING_IN_HELICOBACTER_PYLORI_INFECTION	1.80	0.040	*Epithelial cell signaling in Helicobacter pylori infection*
Pathways positively enriched in PG35s after IR				
Reactome	GENERIC_TRANSCRIPTION_PATHWAY	2.36	0.000	*Genes involved in Generic Transcription Pathway*
BioCarta	IL6_PATHWAY	2.10	0.005	*IL 6 signaling pathway*
KEGG	SPLICEOSOME	1.94	0.030	*Spliceosome*
Biocarta	TEL_PATHWAY	1.94	0.045	*Telomeres, Telomerase, Cellular Aging, and Immortality*

Figure R28: GSEA gene sets positively enriched after IR in PG35 and PG35s samples

List of gene sets significantly enriched after IR in PG35 and PG35s contexts. Gene sets were obtained interrogating three different databases (Reactome, KEGG and BioCarta) through GSEA. Gene sets were indicated following GSEA nomenclature and were ranked according to Normalized Enrichment Score (NES). GSEA FDR *q*-values were indicated for each gene set (FDR < 0.05).

In addition, both DGC and GICs displayed after IR weak enhancement of transcriptional process, enrichment mediated mostly by a number of different Zinc Finger Proteins. Curiously, several negatively enriched gene sets in DGC after IR reported inhibition of transcription, DNA replication, overall maintenance of chromosomes, mitotic process and as well meiosis (Figure R29). An inspection of the leading edge of the bizarre meiotic-related gene sets revealed that their significance is driven largely by down-regulation of core histones (*H2A*, *H2B*, *H3*, and *H4*) superfamilies. The same alterations contributed to the majority of negatively enriched gene sets: AMYLOIDS, transcription-related pathways, telomeres maintenance and centromeres formation. In addition, centromeres formation negative enrichment was driven by *CENPA* and others centromere-associated network protein. A more complex pool of genes contributed to negatively enrich DNA replication and mitotic-related process, including kinesin-like protein family, a group of microtubule-dependent motor proteins that transport organelles and move chromosomes during cell division. Altogether down-regulated genes suggested an important deregulation of cell-cycle and loss of chromosomal stability.

Interestingly, any of the differentially expressed gene sets was negatively enriched after IR in GICs compartment with FDR < 0.05.

DATABASE	GENE SET NAME	NES	FDR *q*-value	GENE SET BRIEF DESCRIPTION
Pathways negatively enriched in PG35 after IR				
Reactome	AMYLOIDS	-3.03	0.000	*Genes involved in Amyloids*
Reactome	RNA_POL_I_PROMOTER_OPENING	-3.03	0.000	*Genes involved in RNA Polymerase I Promoter Opening*
Reactome	MEIOTIC_RECOMBINATION	-2.96	0.000	*Genes involved in Meiotic Recombination*
Reactome	RNA_POL_I_TRANSCRIPTION	-2.89	0.000	*Genes involved in RNA Polymerase I Transcription*
Reactome	MEIOSIS	-2.87	0.000	*Genes involved in Meiosis*
Reactome	DEPOSITION_OF_NEW_CENPA_CONTAINING _NUCLEOSOMES_AT_THE_CENTROMERE	-2.77	0.000	*Genes involved in Deposition of New CENPA-containing Nucleosomes at the Centromere (late telophase/early G1)*
Reactome	RNA_POL_I_RNA_POL_III_AND_MITOCHONDRIAL _TRANSCRIPTION	-2.76	0.000	*Genes involved in RNA Polymerase I, RNA Polymerase III, and Mitochondrial Transcription*
Reactome	CHROMOSOME_MAINTENANCE	-2.69	0.000	*Genes involved in Chromosome Maintenance (Telomeres maintenance and nucleosome assembly included)*
Reactome	MEIOTIC_SYNAPSIS	-2.67	0.000	*Stable physical pairing of homologous chromosomes*
Reactome	PACKAGING_OF_TELOMERE_ENDS	-2.62	0.000	*Processing and maintainance the Telomeres*
Reactome	TELOMERE_MAINTENANCE	-2.60	0.000	*Genes involved in Telomere Maintenance*
Reactome	MITOTIC_PROMETAPHASE	-2.48	0.000	*Genes involved in Mitotic Prometaphase (dissolution of nuclear membrane, Kinetochores creation, Microtubules attachment)*
Reactome	TRANSCRIPTION	-2.35	0.000	*Genes involved in Transcription*
Reactome	REGULATION_OF_BETA_CELL_DEVELOPMENT	-2.15	0.000	*Genes involved in Regulation of β-cell development*
Reactome	CELL_CYCLE	-2.05	0.002	*Genes involved in Cell Cycle regulation*
Reactome	REGULATION_OF_GENE_EXPRESSION_IN_BETA_CELLS	-1.99	0.004	*Genes involved in Regulation of gene expression in β-cells*
Reactome	KINESINS	-1.93	0.006	*Genes involved in Kinesins (motor proteins)*
Reactome	MITOTIC_M_M_G1_PHASES	-1.92	0.007	*Genes involved in Mitotic M-M/G1 phases*
Reactome	DNA_REPLICATION	-1.88	0.009	*Genes involved in DNA Replication*
Reactome	CHYLOMICRON_MEDIATED_LIPID_TRANSPORT	-1.79	0.021	*Genes involved in Chylomicron-mediated lipid transport*
Reactome	MUSCLE_CONTRACTION	-1.76	0.028	*Genes involved in Muscle contraction*
Reactome	DNA_STRAND_ELONGATION	-1.74	0.030	*DNA strand elongation at the DNA replication fork*
Reactome	RESOLUTION_OF_AP_SITES_VIA_THE_MULTIPLE _NUCLEOTIDE_PATCH_REPLACEMENT_PATHWAY	-1.70	0.039	*Genes involved in an alternative pathway of Base Excision Repair (BER)*
Reactome	EXTENSION_OF_TELOMERES	-1.68	0.045	*Genes involved in Telomeres Extension*

Figure R29: GSEA gene sets negatively enriched after IR in PG35

List of gene sets significantly downregulated after IR in PG35 context. Gene sets were obtained interrogating three different databases (Reactome, KEGG and BioCarta) through GSEA. Gene sets were indicated following GSEA nomenclature and were ranked according to Normalized Enrichment Score (NES). GSEA FDR *q*-values were indicated for each gene set (FDR < 0.05).

3.4.2 IRRADIATED PG35SR EXHIBIT SIGNIFICANT ENRICHMENT OF PATHWAYS ASSOCIATED WITH EMT, INFLAMMATION AND MIGRATION

To identify determinants of the radioresistant switch, double-treated GICs (cluster 3) were compared to samples composing cluster 2. GSEA analysis revealed significant positive enrichment of several gene sets (Figure R30). When BioCarta database was interrogated, inflammation-related processes were the pathways predominantly enriched, as indicated by STEM_PATHWAY, INFLAM_PATHWAY, IL1R_PATHWAY, LAIR_PATHWAY, ERYTH_PATHWAY, IL17_PATHWAY and IL10_PATHWAY. Interestingly, *IL6*, *IL8* and *CSF3* genes contributed the most to those gene sets upregulation. At the same time, KEGG and Reactome databases highlighted the enrichment of pathways regulating Extracellular Matrix (ECM) remodeling and cell-to-cell or cell-to-ECM interaction. Surprisingly, no significant downregulation of gene sets was detected when interrogating the three databases.

Then, in order to associate the observed transcriptomic differences with biological functions, the GOrilla web application tool (http://cbl-gorilla.cs.technion.ac.il/; Eden et al., 2009) was interrogated. A total of 506 genes showing more than 2-fold higher expression in cluster 3 compared to cluster 2 (FDR < 0.05) were run against the complete background list of genes composing the microarray. With a fixed *P*-value threshold of 10^{-09}, the analysis identified 20 gene ontology (GO) terms ''biological process'' enriched in cluster 3. Among them, 6 GO categories (30%) correlated positively with cell migration and cell-to-cell communication (Figure R31).

Moreover, to identify specific biological states or processes, GSEA was interrogated through the Hallmark collection (H). Interestingly, hallmarks associated with Epithelial/Mesenchymal Transition (EMT), activation of IL6/JAK/STAT3 axis, and inflammatory response were significantly enriched in radiated PG35sR (Figure R32). Of note, the most enriched inflammatory pathways were associated with TNF-α, IFN-γ, IFN-α and IL6-family signaling response.

Next, to identify which Transcription Factors (TFs) might be responsible for the observed transcriptional changes in GICs after radioresistant shift, a GSEA using the TF targets (TFT) gene sets was performed. TFT collection allow to identify TF whose binding motifs were most commonly found in the promoters of genes differentially expressed. Interestingly the most significantly enriched TF in cluster 3 compared with cluster 2 was STAT3 (Figure R33).

GENE SET NAME	GENE SET BRIEF DESCRIPTION	NES	FDR *q*-value
BioCarta			
STEM_PATHWAY	*Regulation of hematopoiesis by cytokines*	2.21	0.001
EDG1_PATHWAY	*Phospholipids as signalling intermediaries*	2.16	0.001
INFLAM_PATHWAY	*Cytokines and Inflammatory Response*	2.15	0.001
IL1R_PATHWAY	*Signal transduction through IL1R (IL1 pro-inflammatory cytokine)*	2.13	0.001
LAIR_PATHWAY	*Cells and Molecules involved in local acute inflammatory response*	2.12	0.001
ERYTH_PATHWAY	*Erythrocyte Differentiation Pathway*	2.11	0.002
IL17_PATHWAY	*IL 17 Signaling Pathway (Inflammatory response)*	2.00	0.006
IL10_PATHWAY	*IL-10 Anti-inflammatory Signaling Pathway*	1.91	0.018
GSK3_PATHWAY	*Inactivation of Gsk3 by AKT*	1.89	0.022
NTHI_PATHWAY	*NFkB activation by Nontypeable Hemophilus influenzae*	1.86	0.027
SPPA_PATHWAY	*Aspirin Blocks Signaling Pathway Involved in Platelet Activation*	1.85	0.028
GPCR_PATHWAY	*Signaling Pathway from G-Protein Families*	1.84	0.031
P38MAPK_PATHWAY	*p38/MAPK Signaling Pathway*	1.83	0.030
MAPK_PATHWAY	*MAPKinase Signaling Pathway*	1.83	0.028
AT1R_PATHWAY	*Angiotensin II mediated activation of JNK Pathway via Pyk2 dependent signaling*	1.80	0.037
CARM_ER_PATHWAY	*CARM1 and Regulation of the Estrogen Receptor*	1.80	0.035
PPARA_PATHWAY	*Mechanism of Gene Regulation by Peroxisome Proliferators via PPARa(alpha)*	1.77	0.044
SHH_PATHWAY	*Sonic Hedgehog (Shh) Pathway*	1.77	0.042
VIP_PATHWAY	*Neuropeptides VIP and PACAP inhibit the apoptosis of activated T cells*	1.76	0.045
KEGG			
GLYCOSAMINOGLYCAN_BIOSYNTHESIS_KERATAN_SULFATE	*Glycosaminoglycan biosynthesis - keratan sulfate*	2.17	0.001
ECM_RECEPTOR_INTERACTION	*ECM-receptor interaction*	2.04	0.006
GLYCOSAMINOGLYCAN_BIOSYNTHESIS_CHONDROITIN_SULFATE	*Glycosaminoglycan biosynthesis - chondroitin sulfate*	2.00	0.006
HYPERTROPHIC_CARDIOMYOPATHY_HCM	*Hypertrophic cardiomyopathy (HCM)*	1.90	0.021
LEISHMANIA_INFECTION	*Leishmania infection*	1.87	0.023
SMALL_CELL_LUNG_CANCER	*Molecular mechanisms altered in SCLC (MYC, p53, PTEN, RB, and FHIT)*	1.78	0.049
PANCREATIC_CANCER	*Pathways activated in pancreatic cancer*	1.76	0.048
FOCAL_ADHESION	*Cell-matrix adhesions molecule (Integrin signaling)*	1.74	0.049
Reactome			
INTERFERON_ALPHA_BETA_SIGNALING	*Genes involved in Interferon alpha/beta signaling*	2.26	0.000
CHONDROITIN_SULFATE_DERMATAN_SULFATE_METABOLISM	*Chondroitin sulfate/dermatan sulfate metabolism*	2.13	0.003
A_TETRASACCHARIDE_LINKER_SEQUENCE_IS_REQUIRED_FOR_GAG_SYNTHESIS	*Genes involved in A tetrasaccharide linker sequence is required for GAG synthesis*	2.13	0.002
COLLAGEN_FORMATION	*Genes involved in Collagen formation*	2.05	0.009
INTEGRIN_CELL_SURFACE_INTERACTIONS	*Genes involved in Integrin cell surface interactions*	2.02	0.010
SIGNALING_BY_ROBO_RECEPTOR	*Genes involved in Signaling by Robo receptor*	2.02	0.009
GLYCOSAMINOGLYCAN_METABOLISM	*Genes involved in Glycosaminoglycan metabolism*	2.02	0.008
INTERFERON_GAMMA_SIGNALING	*Genes involved in Interferon gamma signaling*	2.01	0.008
KERATAN_SULFATE_KERATIN_METABOLISM	*Genes involved in Keratan sulfate biosynthesis*	1.98	0.012
MYOGENESIS	*Genes involved in Myogenesis*	1.97	0.012
KERATAN_SULFATE_BIOSYNTHESIS	*Genes involved in Keratan sulfate/keratin metabolism*	1.95	0.013
EXTRACELLULAR_MATRIX_ORGANIZATION	*Genes involved in Extracellular matrix organization*	1.95	0.012
INTERFERON_SIGNALING	*Genes involved in Interferon Signaling*	1.95	0.012
CIRCADIAN_CLOCK	*Genes involved in Circadian Clock*	1.91	0.019
RORA_ACTIVATES_CIRCADIAN_EXPRESSION	*Genes involved in RORA Activates Circadian Expression*	1.90	0.021
INSULIN_SYNTHESIS_AND_PROCESSING	*Genes involved in Insulin Synthesis and Processing*	1.84	0.039
ACTIVATION_OF_CHAPERONE_GENES_BY_XBP1S	*Genes involved in Activation of Chaperone Genes by XBP1(S)*	1.83	0.040
BMAL1_CLOCK_NPAS2_ACTIVATES_CIRCADIAN_EXPRESSION	*Genes involved in BMAL1:CLOCK/NPAS2 Activates Circadian Expression*	1.83	0.039
HEPARAN_SULFATE_HEPARIN_HS_GAG_METABOLISM	*Genes involved in Heparan sulfate/heparin (HS-GAG) metabolism*	1.83	0.038
SIGNALING_BY_PDGF	*Genes involved in Signaling by PDGF*	1.83	0.036
NRAGE_SIGNALS_DEATH_THROUGH_JNK	*Genes involved in NRAGE signals death through JNK*	1.81	0.043
CIRCADIAN_REPRESSION_OF_EXPRESSION_BY_REV_ERBA	*Genes involved in Circadian Repression of Expression by REV-ERBA*	1.80	0.045
HS_GAG_DEGRADATION	*Genes involved in HS-GAG degradation*	1.78	0.049

Figure R30: GSEA gene sets positively enriched in cluster 3 compared to cluster 2

List of gene sets significantly enriched in cluster 3 compared to cluster 2. GSEA databases (Reactome, KEGG and BioCarta) were interrogated. Gene sets were ranked according to Normalized Enrichment Score (NES). GSEA FDR *q*-values were indicated (FDR < 0.05).

A

GO term	DESCRIPTION	ES	FDR *q*-value
GO:0030334	Regulation of cell migration	2.85	2.98E-08
GO:2000145	Regulation of cell motility	2.66	1.70E-07
GO:0051270	Regulation of cellular component movement	2.65	4.41E-08
GO:0022603	Regulation of anatomical structure morphogenesis	2.52	7.05E-09
GO:0007155	Cell adhesion	2.45	3.39E-08
GO:0022610	Biological adhesion	2.44	3.89E-08
GO:0051094	Positive regulation of developmental process	2.21	2.67E-07
GO:0051240	Positive regulation of multicellular organismal process	2.16	3.22E-08
GO:0045595	Regulation of cell differentiation	2.10	4.67E-08
GO:2000026	Regulation of multicellular organismal development	1.94	5.76E-07
GO:0010033	Response to organic substance	1.91	3.13E-07
GO:0050793	Regulation of developmental process	1.88	3.68E-08
GO:0051239	Regulation of multicellular organismal process	1.83	7.38E-09
GO:0009966	Regulation of signal transduction	1.77	3.46E-08
GO:0023051	Regulation of signaling	1.75	6.98E-09
GO:0010646	Regulation of cell communication	1.71	3.32E-08
GO:0048583	Regulation of response to stimulus	1.67	1.40E-08
GO:0048856	Anatomical structure development	1.66	1.25E-07
GO:0044767	Single-organism developmental process	1.52	2.78E-07
GO:0032502	Developmental process	1.48	2.66E-07

B

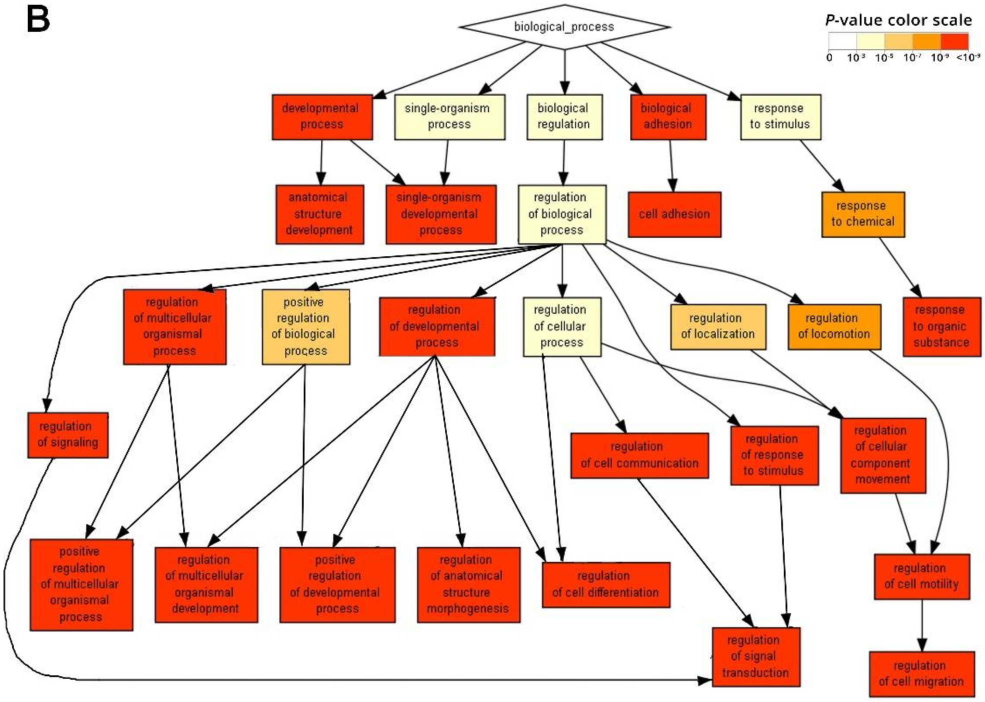

Figure R31: GO biological process enriched in cluster 3 compared to cluster 2

(A) List of biological processes identified as GO categories ranked according to Enrichment Score (ES) using *P*-value threshold of 10^{-09} (GOrilla web tool). *(legend continued on next page)*

(B) GOrilla output with enriched GO terms, color code indicates the significance (see legend).

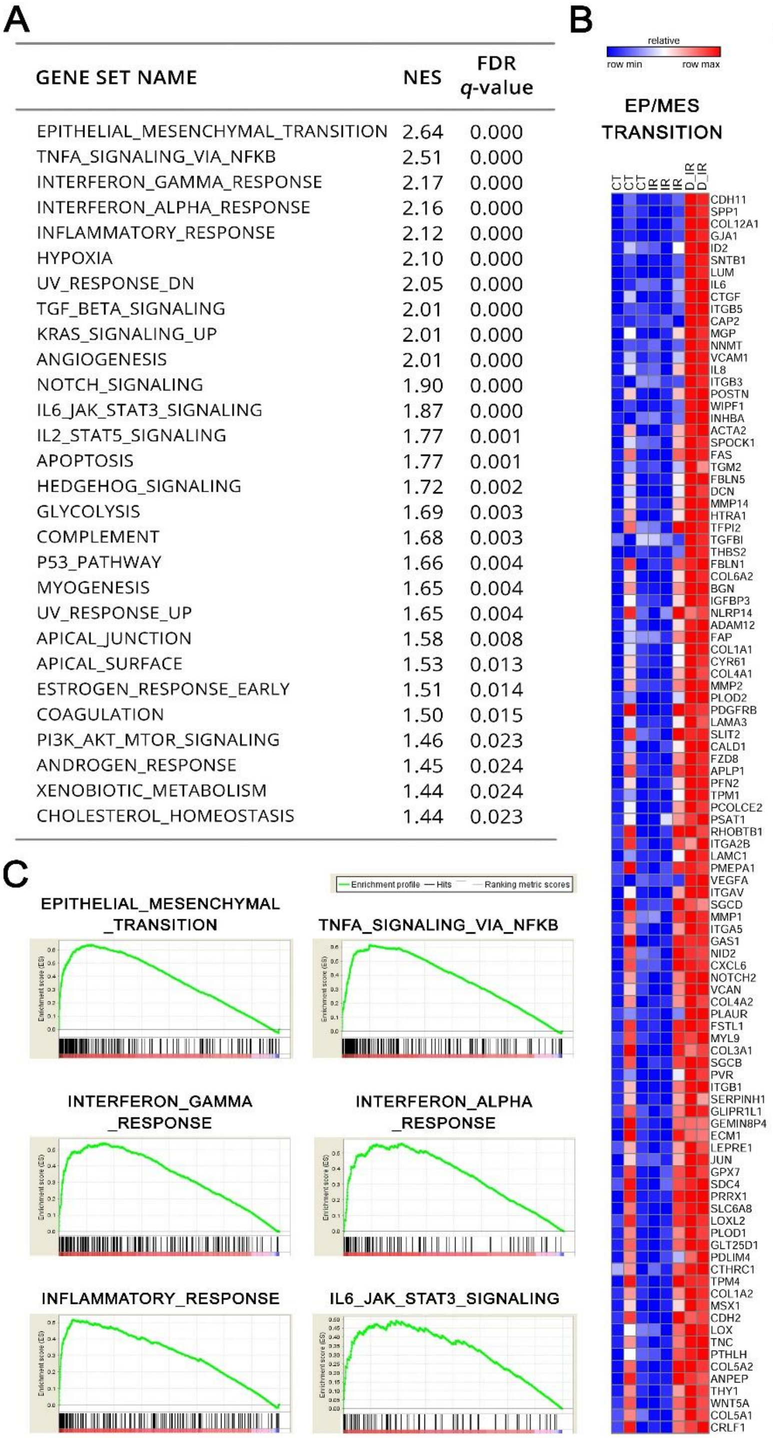

GENE SET NAME	NES	FDR *q*-value
EPITHELIAL_MESENCHYMAL_TRANSITION	2.64	0.000
TNFA_SIGNALING_VIA_NFKB	2.51	0.000
INTERFERON_GAMMA_RESPONSE	2.17	0.000
INTERFERON_ALPHA_RESPONSE	2.16	0.000
INFLAMMATORY_RESPONSE	2.12	0.000
HYPOXIA	2.10	0.000
UV_RESPONSE_DN	2.05	0.000
TGF_BETA_SIGNALING	2.01	0.000
KRAS_SIGNALING_UP	2.01	0.000
ANGIOGENESIS	2.01	0.000
NOTCH_SIGNALING	1.90	0.000
IL6_JAK_STAT3_SIGNALING	1.87	0.000
IL2_STAT5_SIGNALING	1.77	0.001
APOPTOSIS	1.77	0.001
HEDGEHOG_SIGNALING	1.72	0.002
GLYCOLYSIS	1.69	0.003
COMPLEMENT	1.68	0.003
P53_PATHWAY	1.66	0.004
MYOGENESIS	1.65	0.004
UV_RESPONSE_UP	1.65	0.004
APICAL_JUNCTION	1.58	0.008
APICAL_SURFACE	1.53	0.013
ESTROGEN_RESPONSE_EARLY	1.51	0.014
COAGULATION	1.50	0.015
PI3K_AKT_MTOR_SIGNALING	1.46	0.023
ANDROGEN_RESPONSE	1.45	0.024
XENOBIOTIC_METABOLISM	1.44	0.024
CHOLESTEROL_HOMEOSTASIS	1.44	0.023

Figure R32: GSEA Hallmarks significantly enriched in cluster 3 compared with cluster 2 *(legend continued from previous page)* (A) GSEA list of Hallmark gene sets significantly enriched in cluster 3 compared to cluster 2. Gene sets were ranked according to NES. GSEA significance level: FDR < 0.05. (B) Comparative heat-plot indicating genes that contributed to enrichment of selected pathways. Plot was performed using individual genes expression levels in samples composing custer 1 (CT and IR) and cluster 3 (D_IR). (C) GSEA enrichment plot of indicated gene sets.

Taking into consideration that the TF STAT3 has been described together with C/EBPβ as potential driver of mesenchymal transition in GBM (Carro et al., 2010), the activation of C/EBPβ by IR was verified within enriched GSEA-TFT gene sets as well (Figure R33-C). Different C/EBPβ recognizing region were significantly enriched in cluster 3: V$CEBPB_02 (position #31), TTGCWCAAY_V$CEBPB_02 (position #44) and V$CEBPB_01 (position #184). Interestingly, the TNF-α signaling pathway via NF-κB that stands in the second position among hallmark significantly enriched after IR (), was recently described in PN-GICs as potent driver of PN/MES transition (Bhat et al., 2013). Of note, among the top-twenty TF, NF-κB reported a significant activation (Figure R33-A and Figure R33-B). In addition, one of the classical EMT inducers, *SNAIL1* reported significant upregulation in cluster 3 compared to cluster 2 (R-fold: 3.50; FDR = 0.0005). Finally, to determine whether repeated radiation cycles induced in PG35s a global shift toward a more Mes transcriptome, a GSEA on proneural and mesenchymal gene signatures from Verhaak work (Verhaak et al., 2010) was performed. Cluster 3 when compared to cluster 2 effectively exhibited highly significant enrichment of genes in the mesenchymal gene signature (FDR = 0.000), while the opposite PN signature did not display a significant expression change (FDR = 0.936; Figure R33-D).

In order to validate the activation of STAT3 mediated by IR, its phosphorylation status after IR was investigated in a bigger panel of primary GICs (Figure R34). The canonical STAT3 phosphorylation site Tyr705 (Y705) responding to IL6-family signaling was investigated concomitantly with the alternative site Ser727 (S727) which relevancy in GBM cell lines and patients has been recently described (Lin et al., 2014; Ouédraogo et al., 2015). Three different patient-derived GICs (PG82s, PG88s and PG90s) were analyzed at protein level. Samples were irradiated following the standard fractionated schedule until 8 Gy. Then, one hour after the last fraction, samples were collected and analyzed. According to data obtained the highly radioresistant GICs PG88s and PG90s showed a significant phosphorylation at Y705 but not at S727 compared to unirradiated samples (Figure R34). Of note, the two bands observed when analyzing protein blotting likely corresponds to the two major isoforms of STAT3 (α: 89 kDa and β: 80 kDa) generated by alternative splicing (Qi & Yang, 2014).

A

GENE SET NAME	NES	FDR *q*-value
V$STAT3_01	2.08	0.003
V$HOX13_01	2.02	0.002
V$FOX_Q2	1.90	0.004
GGGNNTTTCC_V$NFKB_Q6_01	1.89	0.004
V$EN1_01	1.88	0.004
V$HEN1_02	1.88	0.003
V$AP1_Q4_01	1.87	0.003
V$FREAC4_01	1.82	0.004
V$CDP_02	1.82	0.004
RTTTNNNYTGGM_UNKNOWN	1.82	0.004
V$CEBPA_01	1.80	0.004
V$FOXO1_02	1.79	0.004
V$TEF1_Q6	1.79	0.005
V$AP1_Q6	1.78	0.005
V$NFE2_01	1.78	0.005
V$NFKB_Q6	1.77	0.005
YYCATTCAWW_UNKNOWN	1.77	0.005
YTAATTAA_V$LHX3_01	1.76	0.005
V$FOXJ2_01	1.76	0.005
V$HIF1_Q5	1.76	0.004

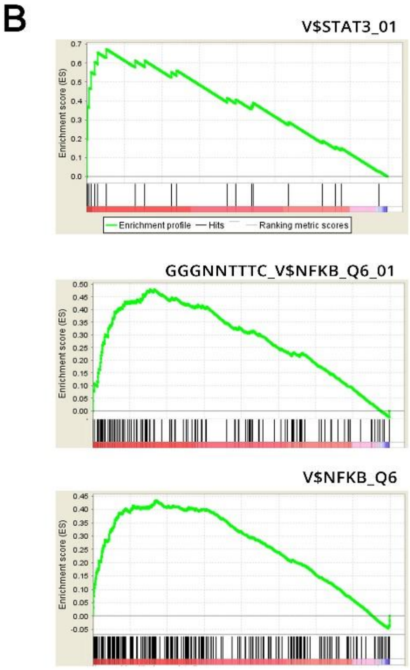

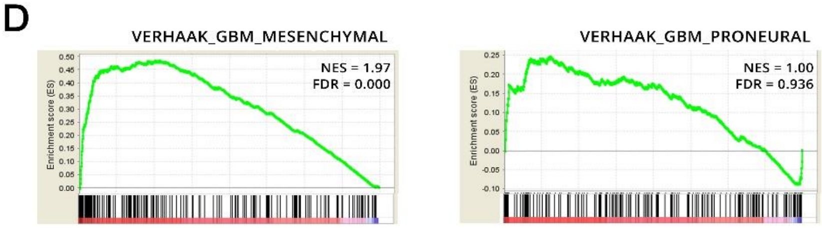

Figure R33: TF activated in cluster 3 compared to cluster 2

(A) Top twenty TFT gene sets that correlates with radiated PG35sR when compared with PG35s CT and IR. Gene sets were ranked according to NES. GSEA FDR *q*-values were indicated (FDR < 0.05). (B) GSEA enrichment plot of indicated STAT3 and NF-κB gene sets (C) GSEA enrichment plot of indicated C/EBP gene sets. As C/EBP gene sets were not included within the top twenty mostly enriched TF, their individual NES and FDR were reported. (D) GSEA enrichment plot of Verhaak signatures for Mes and PN traits.

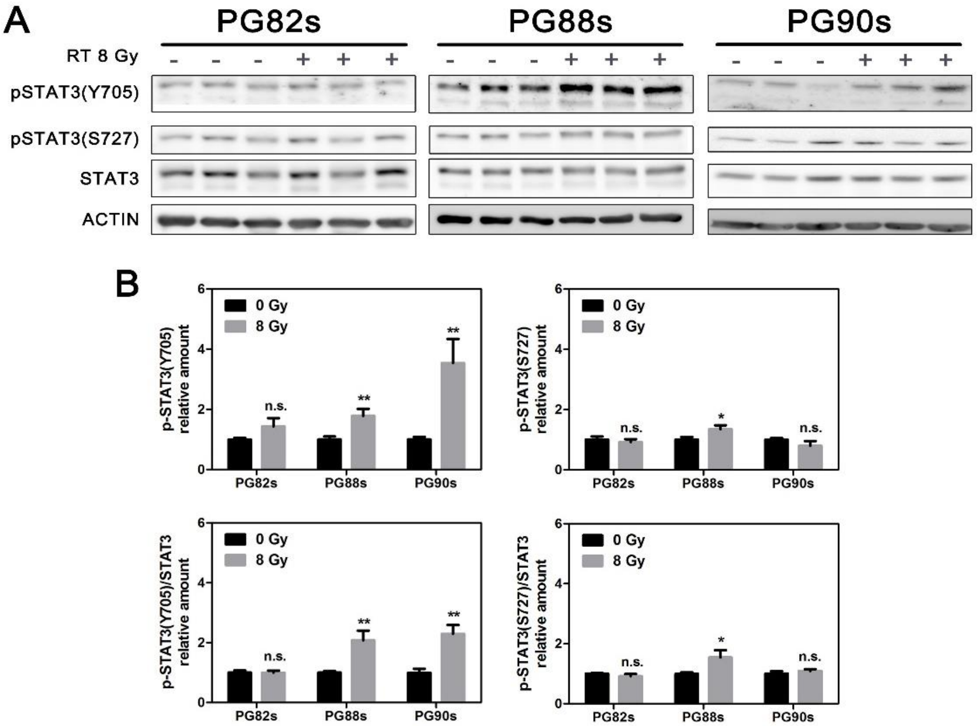

Figure R34: Irradiated GICs showed STAT3 activation via Tyr705 phosphorylation

(A) Representative Western Blot analysis of STAT3 phosphorylation status in three different GICs cultures. (B) WB quantification of pSTAT3(Y705), pSTAT3(S727) and STAT3 through densitometric analysis. Data are normalized to either β-actin or total STAT3 and plotted as mean ± SEM from at least 3 independent experiments. * *P* < .05; ** *P* < .01; with unpaired t-test in comparison to unirradiated samples.

As the last investigation on microarray samples, global transcriptomic data from cluster 2 and cluster 3 were compared in order to identify specific genes. The comparison revealed 955 differentially expressed genes with FDR < 0.05. In particular, expression level of 161 genes was more than four-fold higher in cluster 3, while 9 genes were downregulated below 0.25 R-fold (Figure R35-A; for more details and the complete list see Annex 1). Among them, various growth factor and cytokines were significantly upregulated (*CTGF, CSF3, LIF*, *IL6*, *IL1B*, *IL1F8* and *IL8*). In addition, *CHI3L1* (also known as YLK40) as well as *CTGF*, among the most well described indicators of Mes signature in GBM (Bhat et al., 2013), displayed increased expression. Of note, also *HES1* gene, a Notch downstream target required for the maintenance of the self-renewing ability of CNS progenitors and for the inhibition of the commitment to a neuronal fate (Nakamura et al., 2000; Solecki et al., 2001), reported significant upregulation.

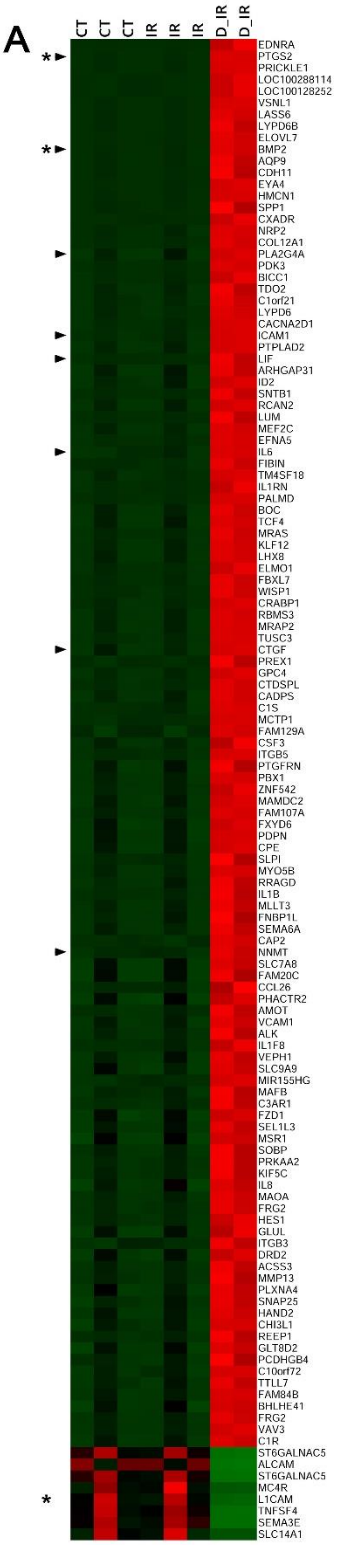

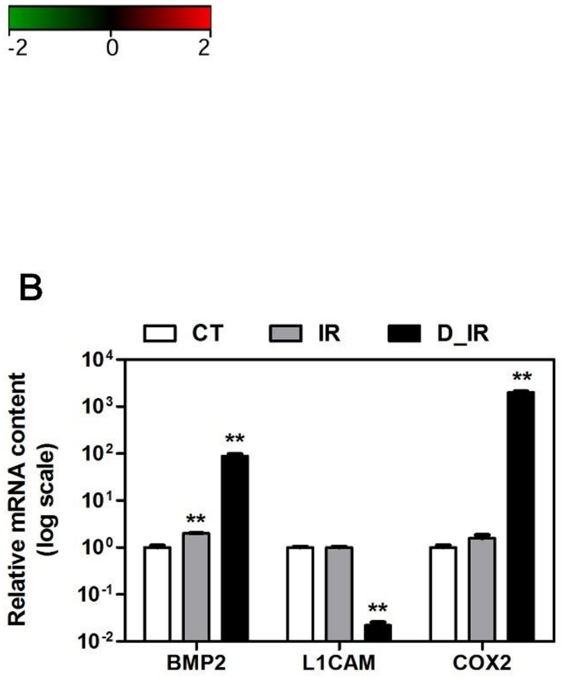

Figure R35: Genes differentially expressed in cluster 3 versus cluster 2

(A) List of genes significantly upregulated by more than five-fold and genes significantly downregulated below 0.20 R-fold after the second cycle of RT (D_IR) compared to unirradiated (CT) and single irradiated samples (IR). Significance level: FDR < 0.05. Genes were ranked according to R-fold; heat-plot was realized upon z-score corrected R-fold. The complete list of genes differentially expressed with FDR < 0.05 can be found in Annex 1. (B) Preliminary confirmation of microarray finding of a small set of genes that showed great fold changes after two IR cycles (D_IR). Selected genes were indicated with * in the heat-plot. ** *P* < .01; with unpaired t-test in comparison to unirradiated samples (CT).

In order to validate microarray results, expression of three genes among the most differentially expressed were analyzed using qPCR (Figure R35-B). Upregulation of *BPM2* and *COX2* together with downregulation of *L1CAM* were confirmed with a good level of significance (*P* < .01).

3.4.3 A DEFINED PANEL OF GENES EXHIBITS PREFERENTIAL UPREGULATION IN GICS CONTEXT AFTER IR

To complete the picture and to validate the reliability of array findings, q-PCR was performed in all established cultures on a small subset of genes (Figure R36). The selected gene set was compiled among the mostly upregulated genes with FDR < 0.05 and taking into consideration the genes contributing to enrich EMT, inflammatory pathways (flagged with a black triangle in Figure R35-A).

GENE SYMBOL	GENE NAME	R-fold	NOM *p*-value	CONTRIBUTING H-GENE SET
COX2 (PTGS2)	*Prostaglandin-endoperoxide synthase 2*	49.15	3.05E-06	TNF-α(2); IFN-γ(3)
BMP2	*Bone morphogenetic protein 2*	21.50	1.70E-06	TNF-α(2)
PLA2G4A	*Phospholipase A2, group IVA*	16.55	3.70E-04	IFN-γ(3)
ICAM1	*Intercellular adhesion molecule 1*	14.51	6.59E-06	TNF-α(2); IFN-γ(3); Inflammatory(4)
LIF	*Leukemia inhibitory factor*	13.84	2.05E-04	TNF-α(2); Inflammatory(4)
IL6	*Interleukin 6*	12.25	2.14E-05	EMT(1); TNF-α(2); IFN-γ(3); Inflammatory(4); IL6(5)
CTGF	*Connective tissue growth factor*	9.67	6.96E-05	EMT(1)
NNMT	*Nicotinamide N-methyltransferase*	6.70	2.02E-06	EMT(1)

Figure R36: Selected subset of genes to validate microarray data

List of genes further investigated in other patient-derived cultures to validate microarray data. Genes are ranked according to R-fold and all reported significative upregulation in cluster 3 compared to cluster 2 (FDR < 0.05). Hallmark (H) GSEA geneset that those gene contributed to enrich were indicated: (1) EPITHELIAL_MESENCHYMAL_TRANSITION; (2) TNFA_SIGNALING_VIA_NFKB; (3) INTERFERON_GAMMA_RESPONSE; (4) INFLAMMATORY_RESPONSE and (5) IL6_JAK_STAT3_SIGNALING.

Upregulation of the defined gene set was first confirmed by qPCR in #35 culture pair treated according to the previously described protocol (Figure R25) following the standard fractionated protocol. Samples were collected one hour after the last fraction of the first (PG35/PG35s) and second (PG35R/PG35sR) IR cycle, corresponding respectively to 8 Gy and 16 Gy of total dose. The whole set of genes, with exception of *BMP2,* showed after the second IR cycle significant upregulation in GICs compartment (Figure R37). Of note, *ICAM1*, *NNMT* and *IL6* exhibited significant upregulation already after the first treatment cycle. Conversely, irradiated DGC samples reported either significant downregulation or no variation in all the genes analyzed.

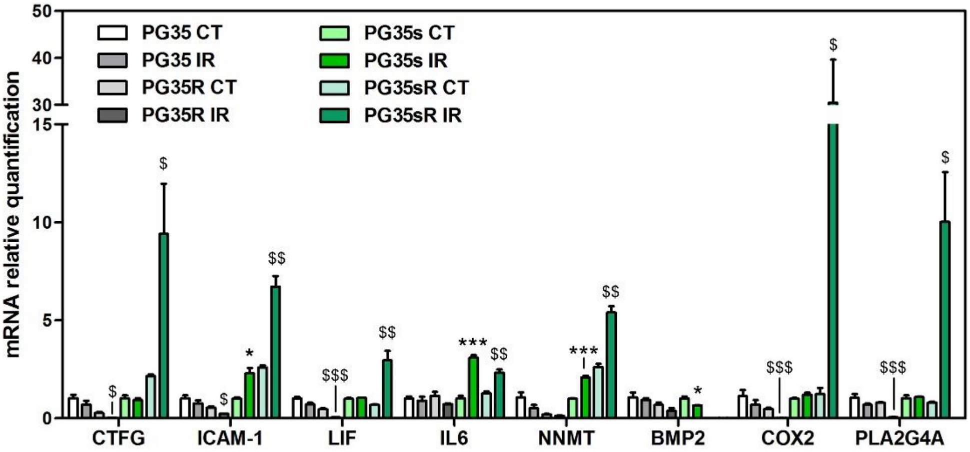

Figure R37: Expression modulation of the defined panel of genes in #35 culture pair after radiotherapy

Expression of the previously defined gene set one hour after treatment finalization of 8 Gy (#35 IR), 16 Gy (#35R IR) and in control condition (CT). mRNA levels were normalized by *GAPDH* - *GUSB* expression and the relative amounts were calculated using the ΔΔCt method referred to control sample (either PG35 CT or PG35s CT). Data were plotted as mean ± SEM (n=3 at least); **P* < .05, ** *P* < .01, *** *P* < .001, with unpaired t-test in comparison to unirradiated control (#35 CT); $^{\$}$ *P* < .05, $^{\$\$}$ *P* < .01, $^{\$\$\$}$ *P* < .001, with unpaired t-test in comparison to samples recovered completely after the first IR cycle and non-treated with the second cycle (#35R).

Next, the expression alteration of the gene set mediated by IR was investigated in the remaining established patient-derived culture pairs. According to LQM parameters obtained from clonogenic assay survival curves, the cultures enriched in GICs exhibited great radioresistance compared to DGC, already after a single 8 Gy cycle. Consequently, the analysis was carried out directly one hour after the last fraction of the 8 Gy schedule. In all culture pairs analyzed, the panel showed significant higher upregulation in GICs cultures after RT compared to DGC (Figure R38).

In addition, unsupervised hierarchical clustering of the obtained mRNA expression levels, placed together the majority of irradiated GICs samples, indicating the influence of those genes in shaping specifically the overall radiation response of GICs-enriched cultures (Figure R39), the most radioresistant compartment of tumoral cells in GBM.

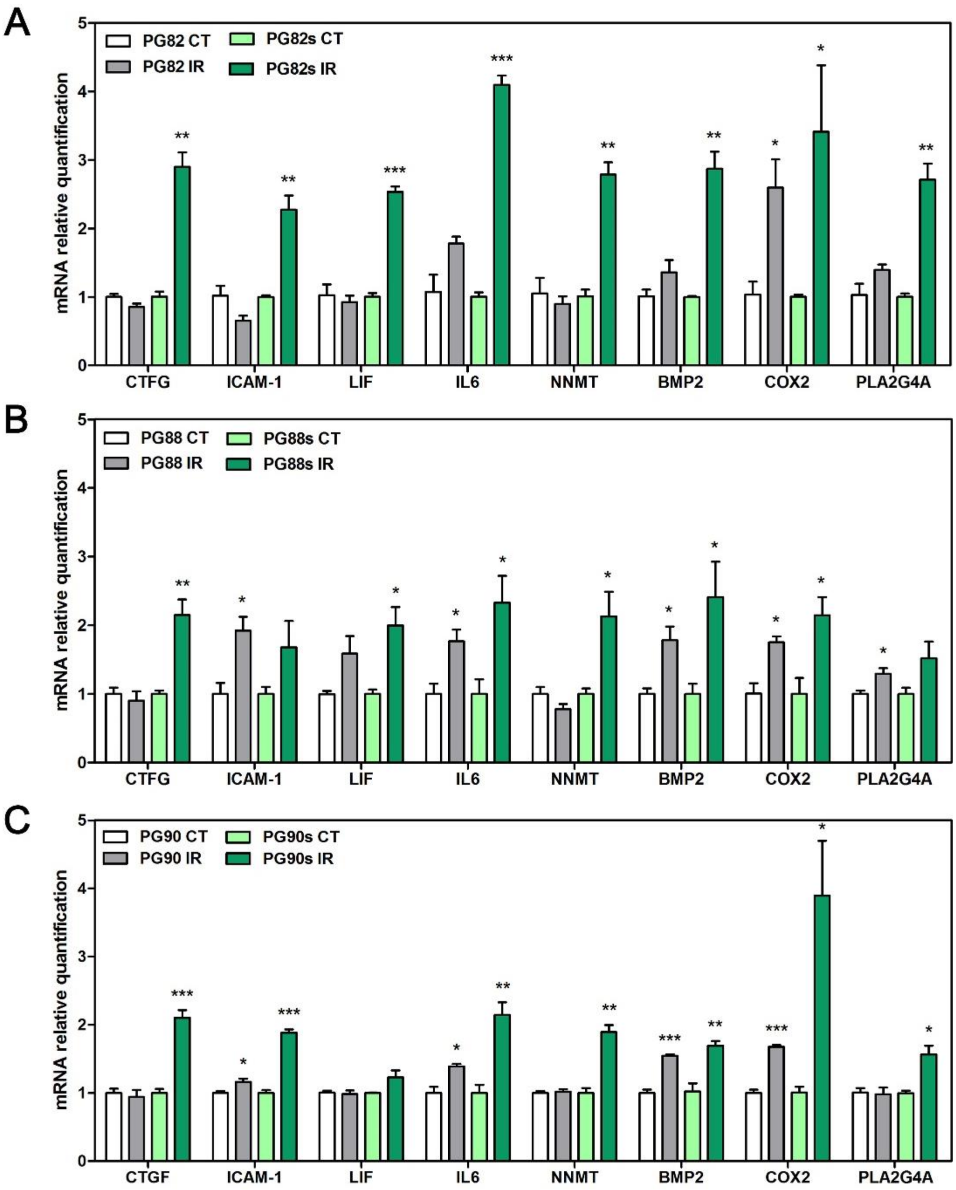

Figure R38: Expression modulation of the defined panel of genes in #82, #88 and #90 culture pairs after radiotherapy

(A-C) Expression of the gene set one hour after 8 Gy treatment finalization (IR) and in control condition (CT). Culture pairs analyzed were #82 (A), #88 (B) and #90 (C). mRNA levels were normalized by *GAPDH* - *GUSB* expression and the relative amounts were calculated using the ΔΔCt method referred to control sample. Data were plotted as mean ± SEM (n=3 at least); **P* < .05, ** *P* < .01, *** *P* < .001, with unpaired t-test in comparison to unirradiated control.

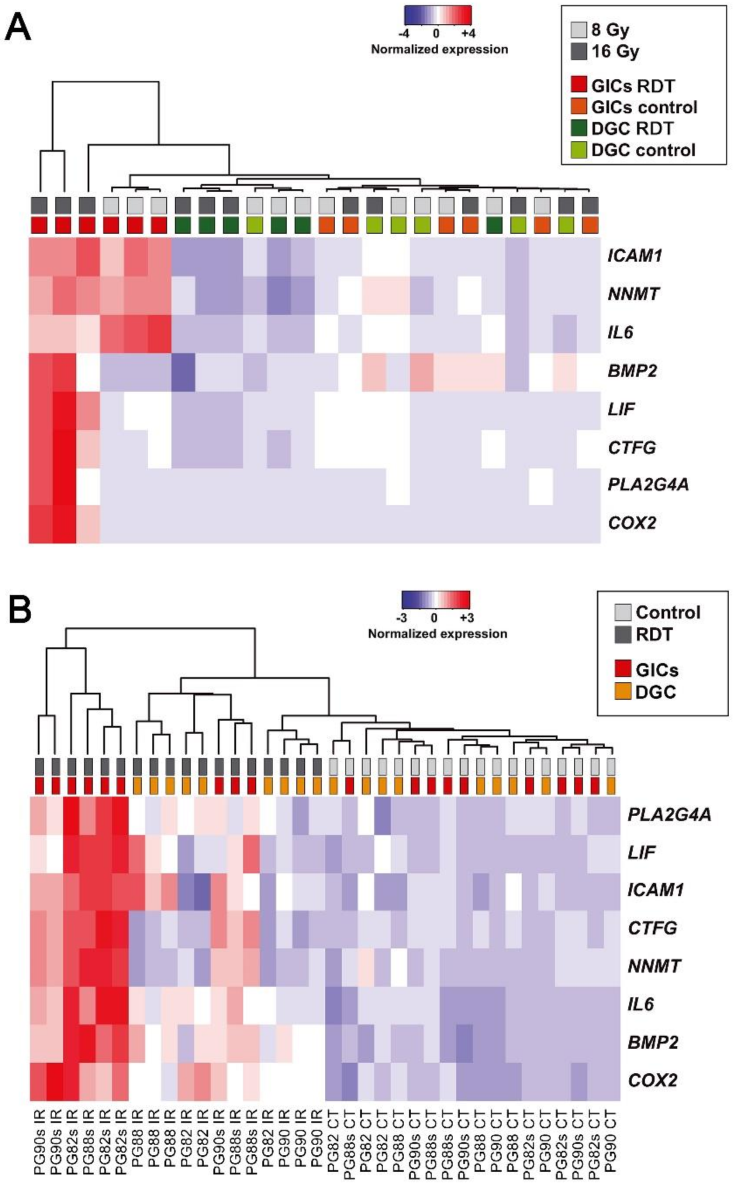

Figure R39: Unsupervised hierarchical clustering of gene set expression levels

(A-B) Unsupervised cluster of normalized and Z-score corrected mRNA expression levels of indicated genes obtained by means of qPCR. Data analyzed correspond to #35-Figure R37 (A) and #82, #88, #90-Figure R38 (B).

In order to explore IL6/STAT3-related pathway, the receptor IL6Rα was quantified at mRNA level in primary cultures one hour after fractionated 8 Gy exposure and in control condition (Figure R40). Interestingly, the majority of GICs reported in unirradiated condition statistically higher expression level of *IL6R* when compared with matching differentiated cultures (#35; #35R; #82; #90). Strikingly, although culture pair #88 did not exhibit remarkable difference in *IL6R* amount in control condition, IR induced significantly its expression exclusively in GICs cultures. These data collectively indicate an increased responsiveness of GICs-enriched cultures to IL6 ligand in both basal and irradiated states.

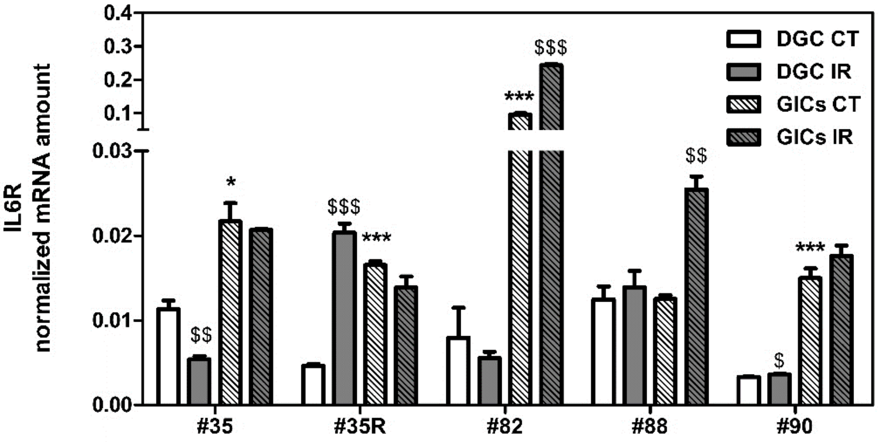

Figure R40: IL6R expression in primary cultures

Primary culture pairs were analyzed one hour after the last dose of fractionated 8 Gy (IR) and in control conditions (CT). Cellular amount of *IL6R* mRNA normalized by *GAPDH* and *GUSB* expression. Analyzed primary cultures were #35, #35R, #82, #88 and #90. Data are plotted as mean ± SEM (n=3). **P* < .05, *** *P* < .001, with unpaired t-test in comparison to unirradiated DGC (DGC CT). $^{\$}$ *P* < .05, $^{\$\$}$ *P* < .01, $^{\$\$\$}$ *P* < .001, with unpaired t-test in comparison to corresponding unirradiated control.

Then, to investigate the clinical impact of the defined gene set in GBM patients, the expression levels of the selected gene set were investigated in using an *in silico* approach. Data were extracted from dataset collected by The Cancer Genome Atlas (TCGA) using the TCGA cancer browser (extracted array: AgilentG4502A_07_2). The unsupervised hierarchical clustering of TCGA data revealed a significant association between basal expression of the selected panel and GBM Mes subtype (Figure R41). Particularly, the mRNA level of a selected group of genes revealed a significantly higher expression in Mes subtype (Figure R42), defining a subgroup of genes named

RT-induced Mes genes (RT-Mes genes: *COX2*, *LIF*, *ICAM1*, *IL6, CTGF* and *NNMT*). These findings supported a higher basal expression of RT-Mes genes in the more aggressive GBM subtype, thus indicating a potential association between their expression and a worst response to therapies and eventually poor prognosis.

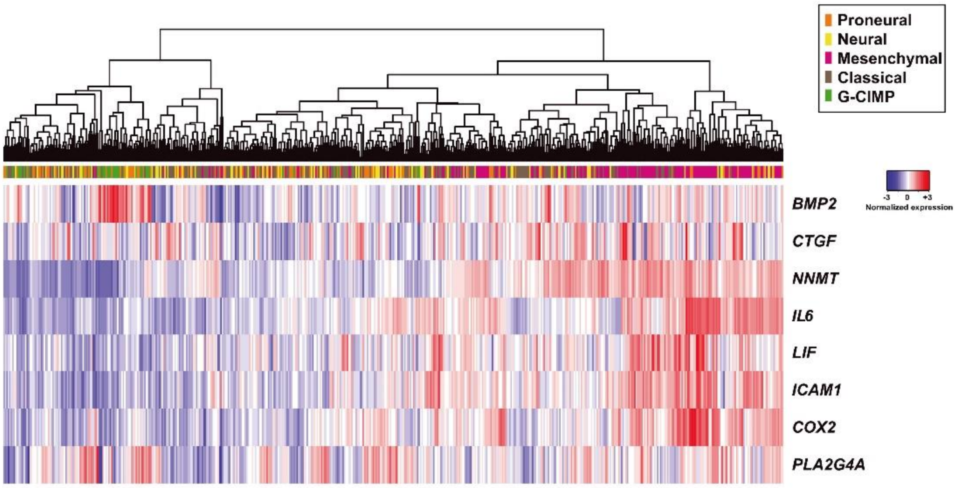

Figure R41: Unsupervised hierarchical clustering of gene set expression levels within a TCGA dataset

Unsupervised clustering of the panel expression levels in GBM patients according to the TCGA array platform AgilentG4502A_07_2 extracted from the TCGA cancer browser. For each patient's specimen the GBM molecular subtype was indicated as defined by the TCGA consortium.

The correlation between higher expression of RT-Mes genes and patient prognosis was investigated using TCGA data extracted from cBioPortal (http://www.cbioportal.org/). 607 samples with mRNA data available were included in the study. Basal upregulation of individual *LIF*, *ICAM1*, *IL6, CTGF* and *NNMT* genes was detected in 27 cases (5%; Figure R43-A) whereas no cases were found with *COX2* expression alteration. Low expression of the RT-Mes genes was significantly associated with longer progression free survival and overall survival. Median PFS was 4.07 months for patients with high expression of the gene set, whereas 7.62 months for those with low expression (*P* < .001; Figure R43-B). in addition, median OS was 11.83 and 14.62 months for patients with high and low expression of the selected group of genes, respectively (*P* < .05; Figure R43-C). Taken together, the results suggest a potential involvement of *COX2, LIF, ICAM1, IL6, CTGF* and *NNMT* genes in GBM treatment response and outcome of GBM patients.

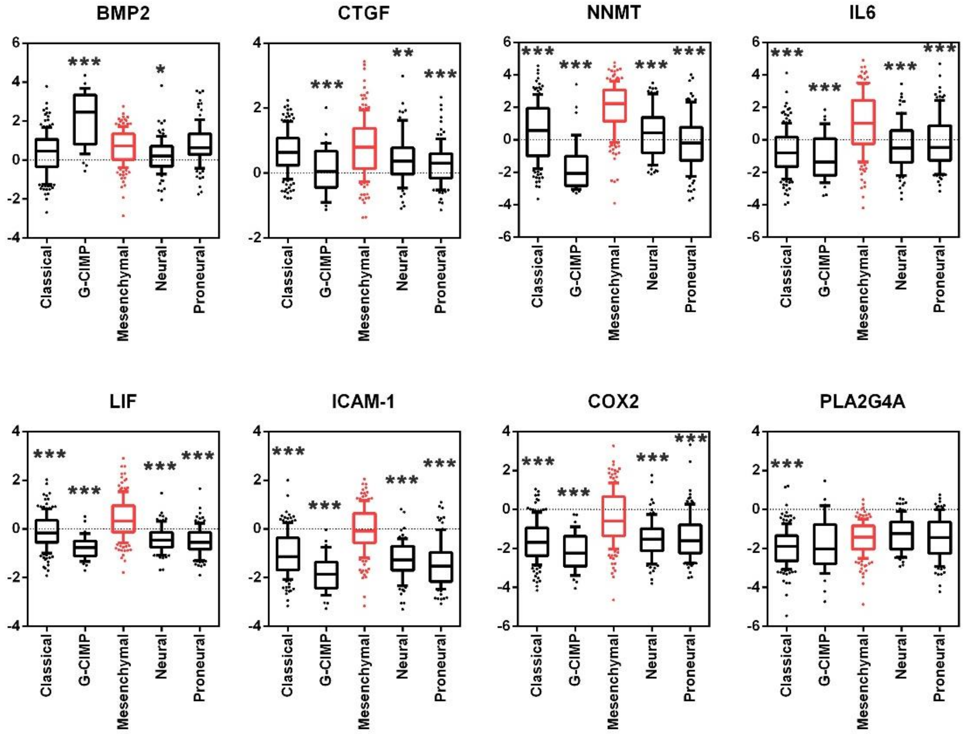

Figure R42: Expression of COX2, LIF, ICAM1, IL6 and NNMT genes showed significant upregulation in GBM Mes subtype

Box-plot diagram showing the expression of the indicated genes across the different molecular subtypes of GBM. Data were obtained from the TCGA array platform (AgilentG4502A_07_2) extracted from the TCGA cancer browser. *$P < .05$, ** $P < .01$, *** $P < .001$, with ANOVA test in comparison to expression in Mes subtype.

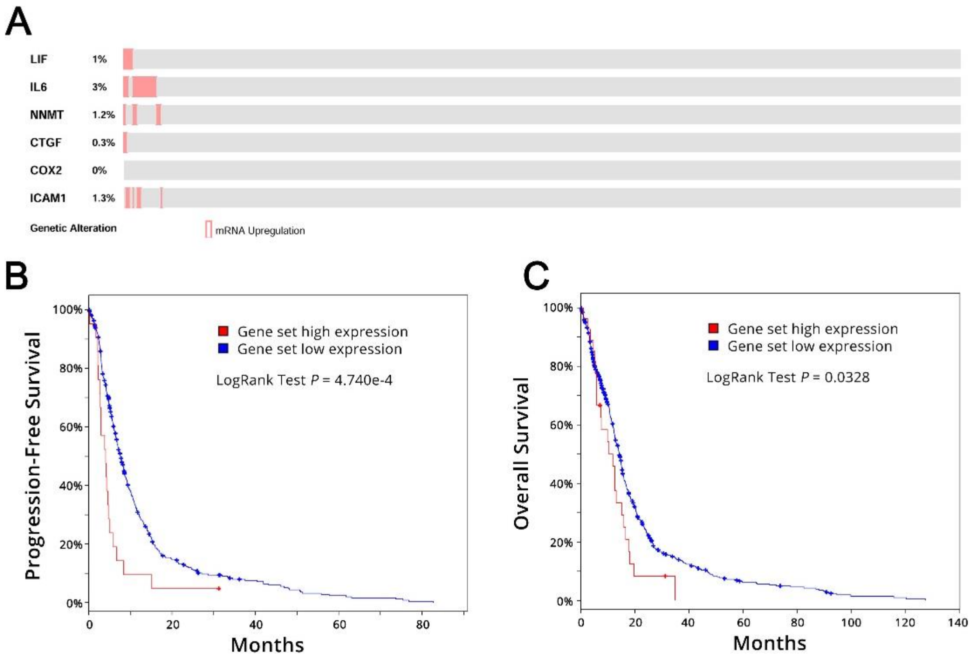

Figure R43: Expression of COX2, LIF, ICAM1, IL6, CTGF and NNMT genes reported significant correlation with GBM patients' poor OS and PFS

(A) Oncoprint of cBioPortal study for the selected genes. (B-C) Kaplan Meier curves showing Progression-Free Survival (B) and Overall Survival (C) of GBM specimens with upregulation of the gene set *versus* GBM with no expression alteration of these genes.

3.5 BRIEF DIGRESSION ON UNIRRADIATED SAMPLES' MICROARRAY DATA

Microarray data were further exploited in order to deepen the molecular differences between unirradiated PG35 and PG35s. Again, a GSEA was executed to define which gene sets were positively or negatively enriched in GICs context compared to DGC. Leading pathways with FDR < 0.05 were identified interrogating previously mentioned databases (KEGG, BioCarta and Reactome). The majority of significant pathways were connected with genes upregulated in GICs context (Figure R44-A). Analysis with KEGG and Reactome databases revealed significant upregulation of pathways associated with immune response, lipid and purine-pyrimidine metabolism. Of note, enrichment of CAMs-related pathway confirmed significant upregulation of well-known GICs markers: ITGA6 and L1CAM (Figure R44-B and Figure R45). Any of BioCarta gene sets were significantly enriched, either positively or negatively. Furthermore, 138 genes reported significantly different expression within GICs and DGC context ($P < .05$).

Particularly, 116 genes showed upregulation in GICs context with an R-fold higher than 4, whereas 22 were downregulated below 0.20 in compare to DGC (Annex 2). The genes that contributed the most to enrich indicated GSEA pathways were reported in Figure R45 grouped by biological function.

A

GENESET NAME	NES	FDR q-value
Pathways positively enriched in PG35s		
KEGG		
ANTIGEN_PROCESSING_AND_PRESENTATION	2.11	0.000
AUTOIMMUNE_THYROID_DISEASE	2.06	0.000
ASTHMA	2.04	0.000
GRAFT_VERSUS_HOST_DISEASE	1.99	0.000
ALLOGRAFT_REJECTION	1.99	0.000
STEROID_HORMONE_BIOSYNTHESIS	1.90	0.001
FATTY_ACID_METABOLISM	1.77	0.017
PYRIMIDINE_METABOLISM	1.74	0.021
TYPE_I_DIABETES_MELLITUS	1.71	0.031
STEROID_BIOSYNTHESIS	1.69	0.037
CELL_ADHESION_MOLECULES_CAMS	1.68	0.037
METABOLISM_OF_XENOBIOTICS_BY_CYTOCHROME_P450	1.68	0.035
INTESTINAL_IMMUNE_NETWORK_FOR_IGA_PRODUCTION	1.67	0.033
Reactome		
METABOLISM_OF_NUCLEOTIDES	1.99	0.002
PURINE_METABOLISM	1.97	0.002
CHOLESTEROL_BIOSYNTHESIS	1.88	0.017
PD1_SIGNALING	1.82	0.044
Pathways negatively enriched in PG35s		
Reactome		
MYOGENESIS	-1.93	0.008
COLLAGEN_FORMATION	-1.90	0.014
LIGAND_GATED_ION_CHANNEL_TRANSPORT	-1.88	0.017
MUSCLE_CONTRACTION	-1.86	0.017
SMOOTH_MUSCLE_CONTRACTION	-1.86	0.014

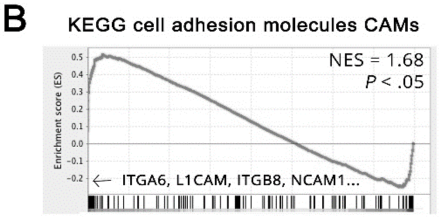

Figure R44: GSEA pathways differentially enriched in PG35s CT versus PG35 CT

(A) GSEA analysis using pathways annotation from KEGG and Reactome databases. Indicated gene sets were ranked according to Normalized Enrichment Score (NES). Listed gene sets were selected using FDR < 0.05. (B) GSEA enrichment plots of KEGG pathway Cell Adhesion Molecules (CAMs). The NES and the p-value are shown.

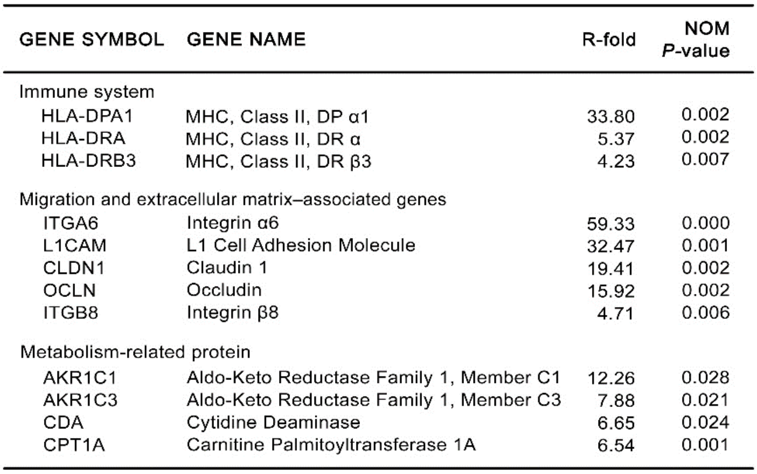

GENE SYMBOL	GENE NAME	R-fold	NOM *P*-value
Immune system			
HLA-DPA1	MHC, Class II, DP α1	33.80	0.002
HLA-DRA	MHC, Class II, DR α	5.37	0.002
HLA-DRB3	MHC, Class II, DR β3	4.23	0.007
Migration and extracellular matrix–associated genes			
ITGA6	Integrin α6	59.33	0.000
L1CAM	L1 Cell Adhesion Molecule	32.47	0.001
CLDN1	Claudin 1	19.41	0.002
OCLN	Occludin	15.92	0.002
ITGB8	Integrin β8	4.71	0.006
Metabolism-related protein			
AKR1C1	Aldo-Keto Reductase Family 1, Member C1	12.26	0.028
AKR1C3	Aldo-Keto Reductase Family 1, Member C3	7.88	0.021
CDA	Cytidine Deaminase	6.65	0.024
CPT1A	Carnitine Palmitoyltransferase 1A	6.54	0.001

Figure R45: Selection of genes highly upregulated in PG35s versus PG35

Listed genes were the one that mostly enriched KEGG annotated pathways. Selected genes has R-fold > 4.00 (*P* < .05).

4 INTEGRIN α6

The Integrin subunit α6 (ITGA6; also known as CD49f) was described in 2010 as a functional marker of GBM CSC capable to enrich GICs population alone or in combination with CD133 (Lathia et al., 2010). At the present time, the implication of ITGA6 expression in cell response to radiation therapy has not been investigated yet. Given the high expression of this marker in established GICs-enriched cultures, the potential role of ITGA6 in response to RT was examined.

4.1 ITGA6 IS HIGHLY EXPRESSED IN NON G-CIMP GBM SPECIMENS

First, the mRNA expression of *ITGA6* was analyzed in brain tumors specimens with an *in-silico* approach from a number of databases using The Cancer Genome Atlas (TCGA) data. According to data extracted from cBioPortal (http://www.cbioportal.org/), the *ITGA6* mRNA level is significantly higher in GBM tissue (n = 166) compared to low grade Glioma (n = 530; $P < .01$; Figure R46-A). This difference was consistent with previous studies (Bredel et al., 2005) whose data were implemented in Oncomine database (www.oncomine.org; Figure R46-B). Moreover, additional analysis on TCGA data displayed from Oncomine revealed significantly higher *ITGA6* mRNA expression in GBM (n = 542) when compared with healthy brain specimens (n = 10; $P < .001$; Figure R46-C). Finally, GBM data extracted from two distinct datasets of TCGA Cancer Browser (Affymetrix U133A and AgilentG4502A_07_2 array) were grouped according to molecular subtypes and *ITGA6* mRNA level was compared between groups. Both analysis reported a significant lower expression of *ITGA6* in G-CIMP GBM (Figure R46-D and Figure R46-E) when compared with others subtypes. Interestingly, data extracted from AgilentG4502A_07_2 array reported a significant *ITGA6* higher expression in Mes compared to PN subtype ($P < .01$). These data suggested that ITGA6 in the context of cerebral tissue might be associated to primary brain tumors and particularly to the most aggressive subtype of GBM.

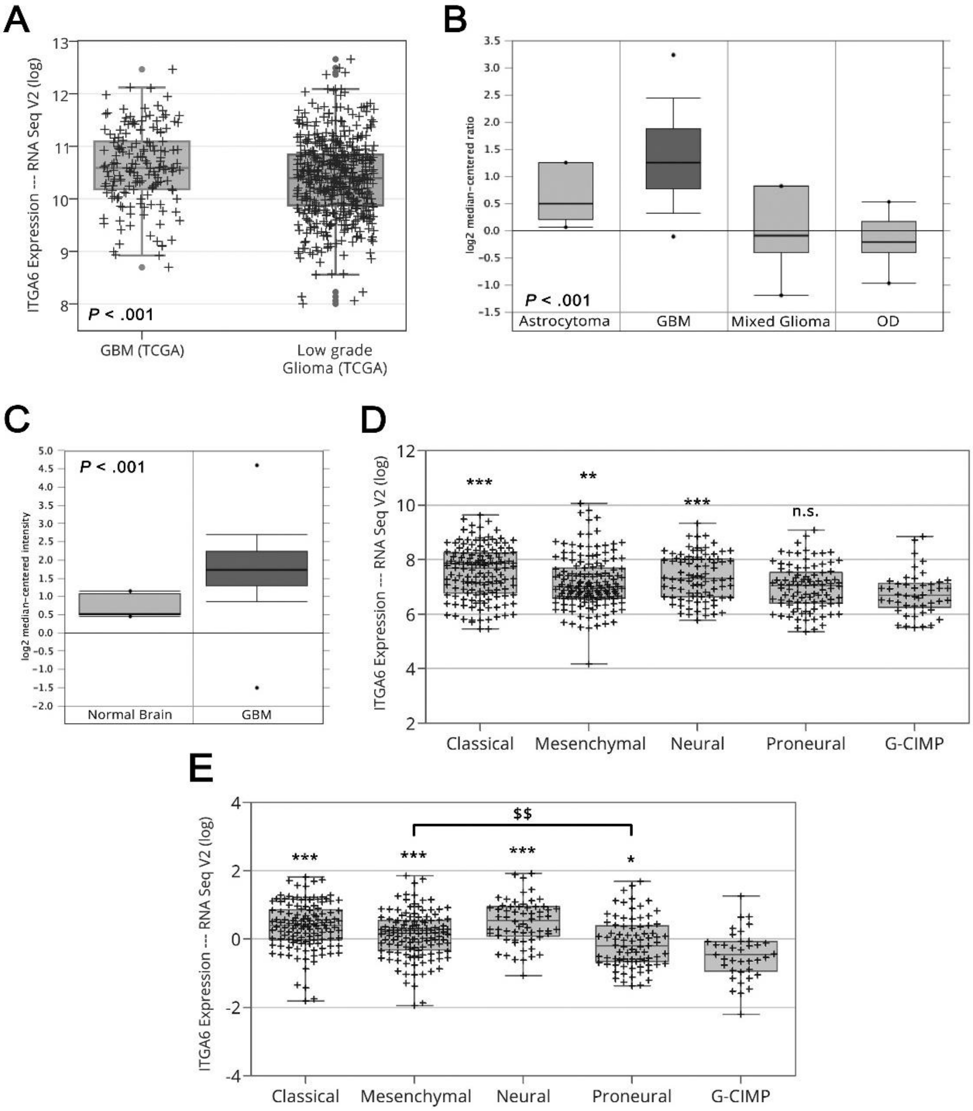

Figure R46: ITGA6 mRNA expression in Gliomas

(A) Box-plot diagram showing *ITGA6* mRNA expression in GBM and low grade Gliomas. Picture modified from cBioPortal database using Plotly software (https://plot.ly/). Reported p-value calculated with Mann-Whitney test. (B) Diagram showing Oncomine data (from Bredel et al., 2005) displaying *ITGA6* mRNA expression levels in Astrocytomas (*n* = 4), GBM (*n* = 31), Mixed Glioma (*n* = 6) and Oligodendroglial tumors (OD; *n* = 8). Displayed p-value is calculated from Oncomine. (C) Diagram showing TCGA data (Affymetrix U133A platform) displaying *ITGA6* mRNA expression levels in normal brain (*n* = 10) and GBM (*n* = 542). Displayed p-value is calculated from Oncomine. (D-E) *ITGA6* mRNA level in the different GBM molecular subtypes. (D) Data extracted from Affymetrix U133A platform. Displayed p-values were calculated with Mann-Whitney test compared to G-CIMP mRNA levels *(legend continued on next page)* (n.s. = not significant; ** *P* < .01, *** *P* < .001). (E) Data extracted from AgilentG4502A_07_2 dataset. Displayed p-values were calculated with Mann-Whitney test; * obtained comparing G-CIMP to other subtypes (* *P* < .05, *** *P* < .001); $ obtained comparing PN and Mes mRNA levels ($$ *P* = .007).

4.2 GICS EXPRESSING HIGHER LEVELS OF ITGA6 ARE MORE RADIORESISTANT

Given the strong Mes molecular signature of established cultures and ITGA6 greater expression in GBM non-G-CIMP and non-PN subtypes, established GICs were expected to provide an attractive insight into ITGA6 role in GBM biology. Particularly, GICs cultures were employed to investigate the implication of ITGA6 expression in radioresistance-related mechanisms.

First, three GICs cultures were sorted by means of fluorescence-activated cell sorting (FACS) according to ITGA6 expression (Figure R47-A). Two distinct subpopulations were obtained per GICs culture: one enriched in cells expressing high levels of ITGA6 (ITGA6^{HI}), the other containing cells expressing low levels of ITGA6 (ITGA6^{LO}). To set fluorescence intensity gates HI and LO, DGC cultures were employed. Fluorescence level of HI gate was assumed to exclude the majority of DGC cells, whereas LO gate was set to include the greatest part of DGC (Figure R47-B). Sorted cells were immediately plated under *Neurosphere* culture condition and ITGA6 differential expression was validated at protein level (Figure R47-C). According to protein analysis, ITGA6^{LO} cells derived from PG90s culture revealed almost undetectable levels of ITGA6. Consequently, sorted PG90s were employed in following studies.

In order to investigate the role of ITGA6 in RT response, the radiosensitivity of PG90s ITGA6^{HI} and ITGA6^{LO} was compared. Cultures were treated at 2 and 4 Gy in their standard culture conditions following the standard schedule of fractionated doses (2 Gy per fraction). Surviving fractions were calculated based on plating efficiency of relative unirradiated control samples (Figure R48-A). According to obtained curves and SF2, SF4 and AUC parameters (Figure R48-B) ITGA6^{HI} reported a more radioresistant phenotype compared to ITGA6^{LO} (two-way ANOVA *P* < .0001). Interestingly, PG90s ITGA6^{HI} survival curve did not differ statistically from PG90s curve (two-way ANOVA *P* < .7; Figure R22). The LQM parameters showed lower α- and β-values for ITGA6^{HI} indicating respectively higher intrinsic radioresistance and better repair of sublethal DNA damage compared to ITGA6^{LO}. In addition, ITGA6^{HI} α/β ratio was significantly higher suggesting a reduced sensitivity to fractionated doses.

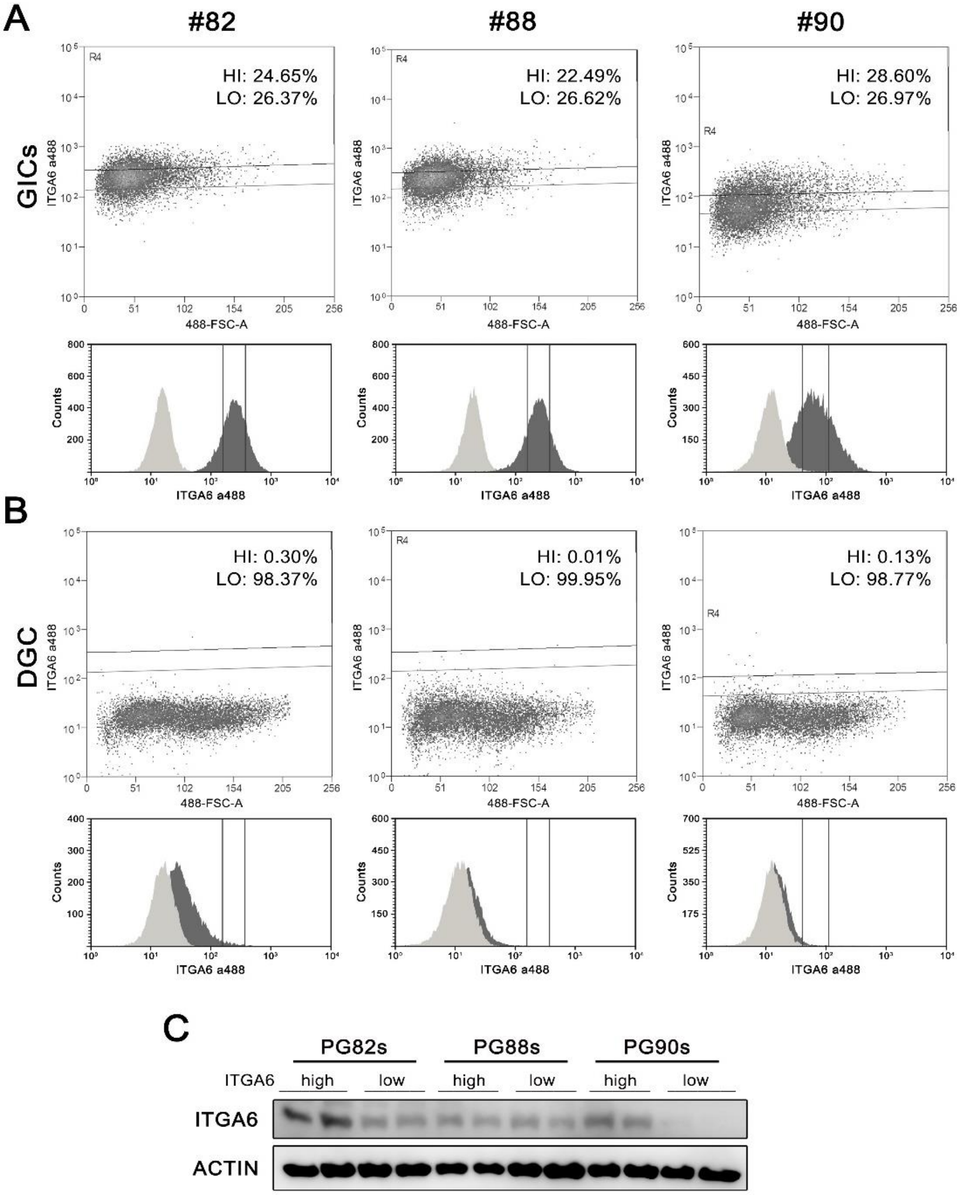

Figure R47: Isolation of ITGA6^{HI} and ITGA6^{LO} cells from three GICs-enriched cultures

(A) ITGA6^{HI} and ITGA6^{LO} cells were isolated from GICs culture using FACS analysis. Percentages of sorted cells are indicated respectively as HI and LO. Under each FACS plot is reported the fluorescence intensity of analyzed samples (dark grey profile) compared to fluorescence of cells incubated only with secondary antibody (light grey profile). (B) ITGA6 FACS analysis performed in DGC cultures to set the gates. Percentages of cells included per gate are indicated. The fluorescence intensity of analyzed samples (dark grey profile) is compared to fluorescence of cells incubated only with secondary antibody (light grey profile). (C) ITGA6 Western Blot analysis of sorted ITGA6^{HI} and ITGA6^{LO} cells.

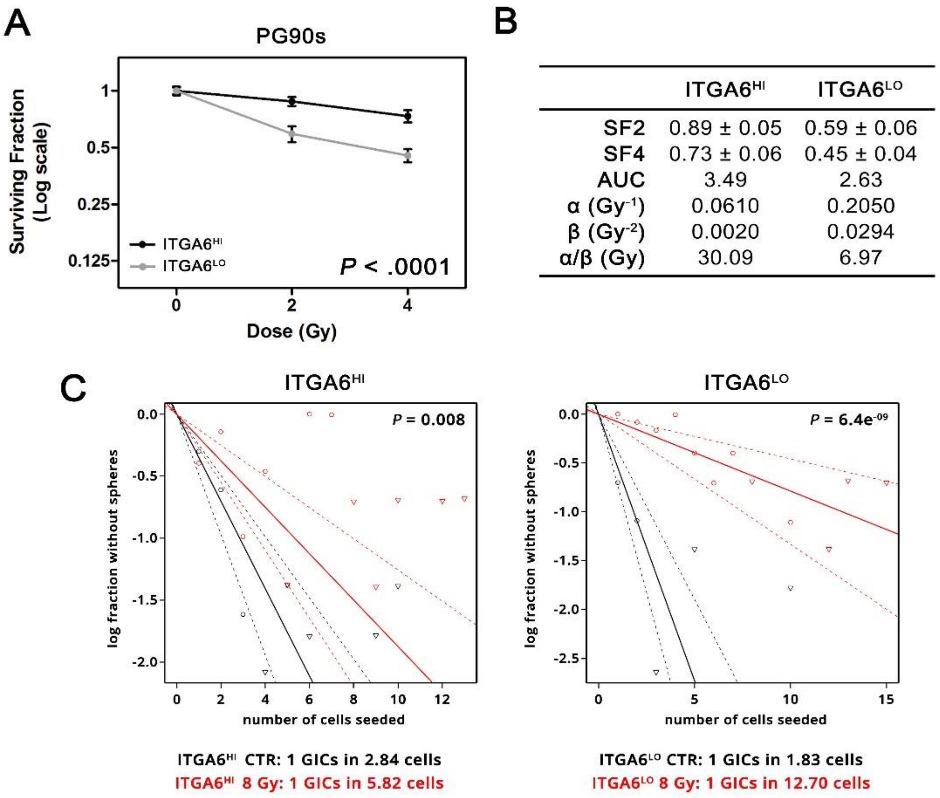

	ITGA6^{HI}	ITGA6^{LO}
SF2	0.89 ± 0.05	0.59 ± 0.06
SF4	0.73 ± 0.06	0.45 ± 0.04
AUC	3.49	2.63
α (Gy^{-1})	0.0610	0.2050
β (Gy^{-2})	0.0020	0.0294
α/β (Gy)	30.09	6.97

ITGA6^{HI} CTR: 1 GICs in 2.84 cells
ITGA6^{HI} 8 Gy: 1 GICs in 5.82 cells

ITGA6^{LO} CTR: 1 GICs in 1.83 cells
ITGA6^{LO} 8 Gy: 1 GICs in 12.70 cells

Figure R48: PG90s ITGA6^{HI} and ITGA6^{LO} reported different sensitivity to RT

(A) Survival curves obtained through the clonogenic assay from 4 independent experiments. Indicated P-values were calculated by two-way ANOVA comparing PG90s ITGA6^{HI} and ITGA6^{LO} curves. Data are plotted in Log(2) scale as mean ± SEM. (B) Cell radiation sensitivity quantified by survival curves parameters (SF2; SF4 and AUC) and values obtained from the LQ modeling (α, β and α/β). Surviving Fraction at 2 Gy (SF2) and 4 Gy (SF4); Area Under the Curve (AUC). SF2 and SF4 are indicated as mean ± SEM. (C) Extreme limiting dilution assay plot as obtained from ELDA web tool. Data are plotted as the log proportion of not dividing cells vs. the number of cells seeded. The trend line represents the estimated active cell frequency. The dotted lines give the 95% confidence interval. Estimated GICs frequency within each population analyzed is indicated at the bottom of the plot. Reported p-values were calculated from ELDA tool.

Then, to compare GICs frequency within ITGA6^{HI} and ITGA6^{LO} after IR, the Extreme Limiting Dilution Assay (ELDA) was performed (Figure R48-C). Cells were seeded at extremely low density in their standard growing condition and were treated with 8 Gy using standard fractionated schedule (2 Gy per fraction). After 14 days their capacity to form colonies was scored and data were processed employing ELDA web-based tool (http://bioinf.wehi.edu.au/software/elda/; Hu & Smyth, 2009). The estimation for stem cell frequency after IR in ITGA6^{HI} reported a 2-fold reduction compared to corresponding unirradiated sample ($P < .01$), whereas ITGA6^{LO} showed a dramatic drop down of 7-fold ($P < .0001$). Of note, the calculated GICs frequency in unirradiated ITGA6^{HI} and ITGA6^{LO} did not differ significantly ($P = .09$), whereas when IR samples were compared the difference was statistically significant ($P = .02$). These data suggested that GICs expressing higher levels of ITGA6 display a more radioresistant phenotype.

4.3 LENTIVIRAL INHIBITION OF ITGA6 EXPRESSION TRIGGERS GICS RADIOSENSITIZATION

To investigate thoroughly the molecular mechanism supporting ITGA6 involvement into radioresistance, a loss-of-function study was performed. ITGA6 was knocked-down using lentiviral-based shRNA. Sequences of shRNA was mapping in the shared region of the most frequent ITGA6 splicing variants (ITGA6A and ITGA6B; Figure R49). First, three different shRNA sequences against ITGA6 were tested and knockdown verified by qPCR (Figure R50-A). according to data obtained, shRNA_3 was the shRNA that most efficiently knocked down ITGA6 transcript.

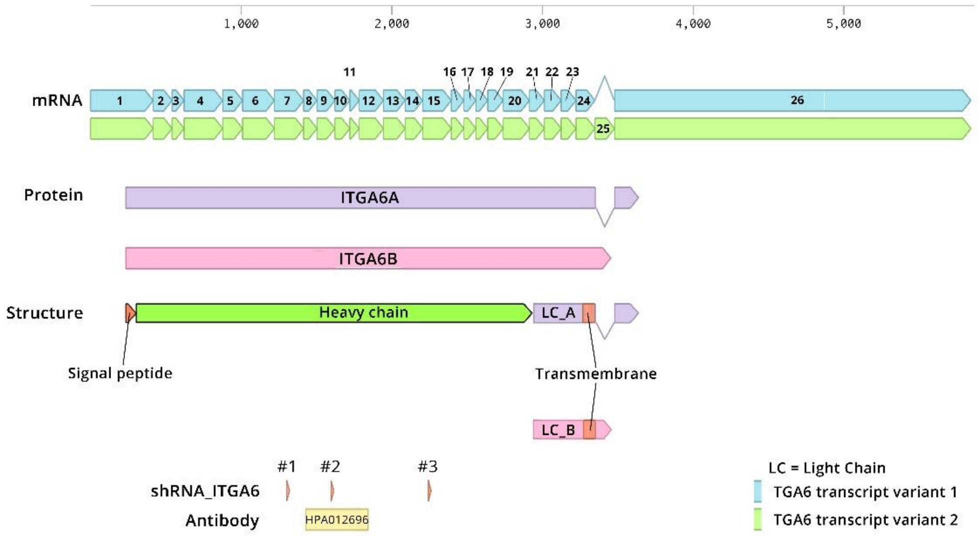

Figure R49: ITGA6 splicing variants A and B

Picture executed according to ITGA6 GenBank sequences (NM_001079818.2 and NM_000210.3) and UniProt data (P23229). Image was edited with Benchling Web Platfrom (https://benchling.com/; Galdzicki et al., 2014).

(legend continued on next page)

Localization of shRNA sequences was displayed as orange triangles. The amino acid sequence recognized by the WB antibody (HPA012696) was included. ITGA6 variant 1 represents the shorter transcript and encodes the longer isoform (A). Transcript variant 2 contains an alternate coding exon (exon 25) compared to variant 1, which results in a frameshift. The resulting isoform (B) is shorter and has a distinct C-terminus compared to isoform A.

Next, three different GICs cultures (PG82s, PG88s and PG90s) were infected with shRNA_3 particle and ITGA6 knockdown was confirmed by western blot and qPCR analysis (Figure R50-B, Figure R50-C and Figure R50-D). Importantly, shRNA_3 significantly reduced the amount of ITGA6 in all GICs cultures tested. Of note, the observed inhibition was significant for both ITGA6 fragment detected at protein level, usually interpreted as the integrin heavy chain (120 kDa) and the entire un-cleaved protein (150 kDa).

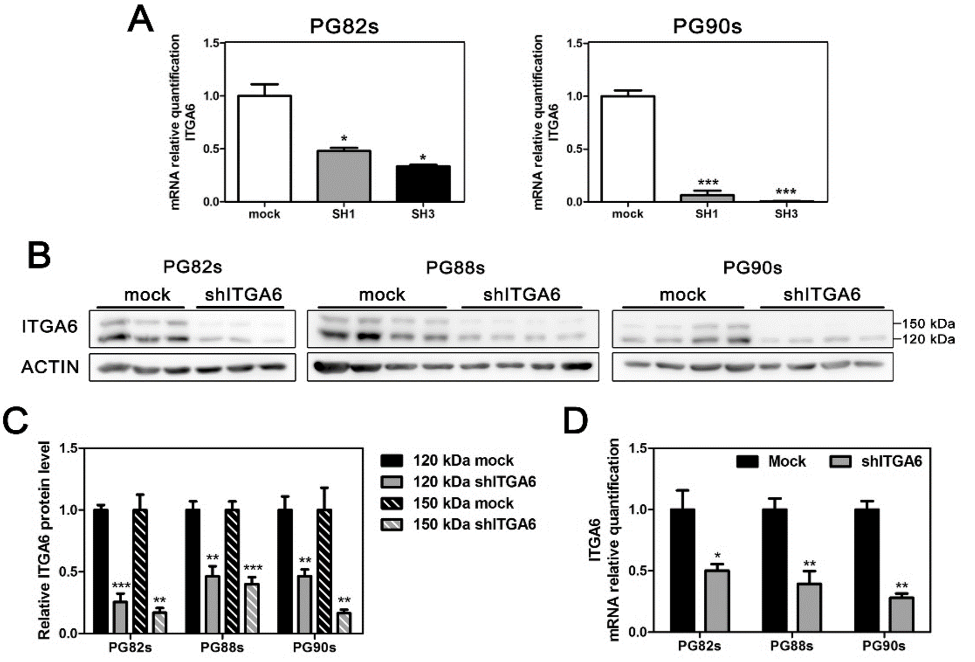

Figure R50: ITGA6 knockdown after transfection with lentiviral particles.

(A) Screening of different shRNA in PG82s and PG90s by qPCR. Expression levels were calculated after normalization to *GAPDH* and *GUSB*. (B) Western Blot analysis of ITGA6 amount following shRNA_3 knockdown in GICs cultures. (C) ITGA6 protein quantification through densitometric analysis. Data are normalized to β-actin protein level (at least n=3). (D) qPCR analysis of *ITGA6* level after transfection. mRNA levels were plotted normalized by *GAPDH* and *GUSB* expression (n=3). All data are presented as mean ± SEM; * *P* < .05; ** *P* < .01; *** *P* < .001; with unpaired t-test in comparison to mock sample.

The radiosensitivity of transfected cultures was evaluated by means of clonogenic assay and ELDA estimation of GICs frequency. In line with our previous results, loss of ITGA6 in GICs enhances radiosensitivity in all cultures tested (Figure R51). In order to define cultures survival following RT, cells were plated for clonogenic assay in standard culture conditions and treated with established IR schedule of fractioned doses at 2 and 4 Gy (Figure R51-A). Surviving fractions at each dose were calculated along with AUC and LQM parameters at 2 Gy (Figure R51-B). In all cultures mock samples showed a more radioresistant phenotype compared to shITGA6 (two-way ANOVA *P* < .01) as indicated by higher values of SF2, SF4 and AUC. Moreover, according to calculated LQM parameters, shITGA6 samples reported higher α- and β- values indicating an increased RT radiosensitivity and an impaired capacity to repair sublethal DNA damage. In addition, lower α/β ratio of shITGA6 suggested an enhanced sensitivity to fractionated doses.

Subsequently, the capacity of GICs to overcome treatment was assessed in shITGA6 and mock cultures by means of ELDA. Cells were treated at 8 Gy with standard fractionated schedule and neurosphere growth was scored after 14 days. The estimation for stem cell frequency reported an increased capacity to retain stemness after treatment in mock samples when compared to samples with ITGA6 knockdown (Figure R51-C). The reduction of GICs frequency was in all tested cultures statistically more significant in shITGA6 cultures.

Finally, the capability to repair double strand breaks (DSB) in a time-dependent manner was investigated through quantification of γ-H2AX foci/cell. Foci formation and decay were analyzed by means of immunofluorescence after 4 Gy delivered in unique fraction. The standard RT treatment of 8 Gy in fractionated doses was changed to 4 Gy schedule given the peculiar sensitivity of the technique employed. As pointed out by other groups, foci detection through confocal microsections is able to discriminate foci with a good sensitivity at low IR doses, up to 4 or 6 Gy (Bulat et al., 2016). On the contrary, if foci detection is needed after higher IR doses, immunoblotting techniques should be employed. The data obtained in PG82s reported a significantly higher γ-H2AX foci decay ratio in mock samples after 4 and 24 hours from IR exposure, thus indicating that ITGA6 knockdown impaired the DNA damage repair (Figure R52). Preliminary data obtained from PG90s culture exhibited comparable impairment of γ-H2AX foci decay in samples with ITGA6 knockdown (Figure R52).

Taken together, all these data suggest that ITGA6 may play a role in GICs radioresistance, and consequently ITGA6 could be considered as a putative therapeutic candidate to radiosensitize GBM GICs.

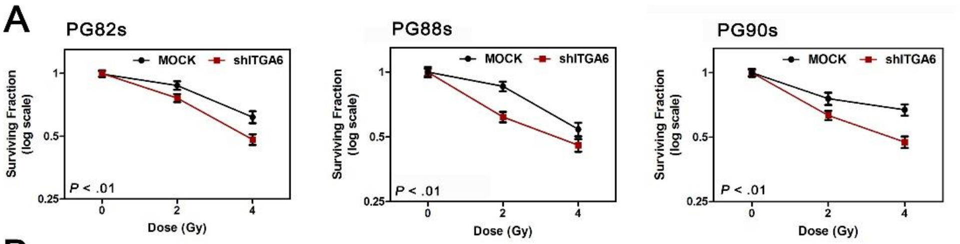

B

	PG82s mock	PG82s shITGA6	PG88s mock	PG88s shITGA6	PG90s mock	PG90s shITGA6
SF2	0.88 ± 0.04	0.76 ± 0.03	0.86 ± 0.04	0.62 ± 0.03	0.76 ± 0.05	0.63 ± 0.03
SF4	0.62 ± 0.04	0.48 ± 0.03	0.54 ± 0.04	0.46 ± 0.03	0.67 ± 0.04	0.47 ± 0.03
AUC	3.36	3.00	3.26	2.67	3.19	2.74
α (Gy^{-1})	0.0625	0.1195	0.0707	0.1906	0.1215	0.1835
β (Gy^{-2})	0.0021	0.0085	0.0028	0.0247	0.0088	0.0226
α/β (Gy)	29.76	14.01	25.61	7.72	13.73	8.13

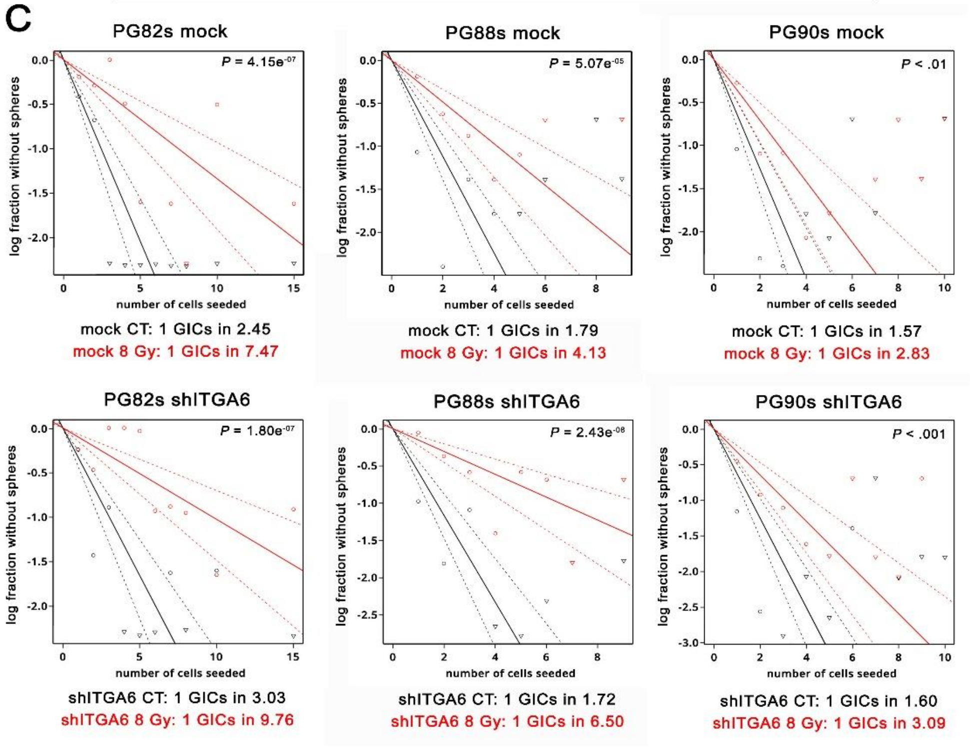

Figure R51: Lentiviral-based knockdown of ITGA6 enhance GICs radiosensitivity

(A) Survival curves obtained through the clonogenic assay from 4 independent experiments. Data are plotted in Log(2) scale as mean ± SEM. Indicated P-values were calculated by two-way ANOVA comparing matching mock and shITGA6 curves. *(legend continued on next page)*

(B) Cell radiation sensitivity quantified by survival curves parameters (SF2; SF4 and AUC) and values obtained from the LQ modeling (α, β and α/β). Surviving Fraction at 2 Gy (SF2) and 4 Gy (SF4); Area Under the Curve (AUC). SF2 and SF4 are indicated as mean ± SEM. (C) Extreme limiting dilution assay plot as obtained from ELDA web tool. In each plot the calculated log of active cell frequency after 8 Gy was compared with the control unirradiated condition (0 Gy). The dotted lines give the 95% confidence interval. Estimated GICs frequency within each population analyzed is indicated at the bottom of the plot. Reported p-values were calculated from ELDA tool.

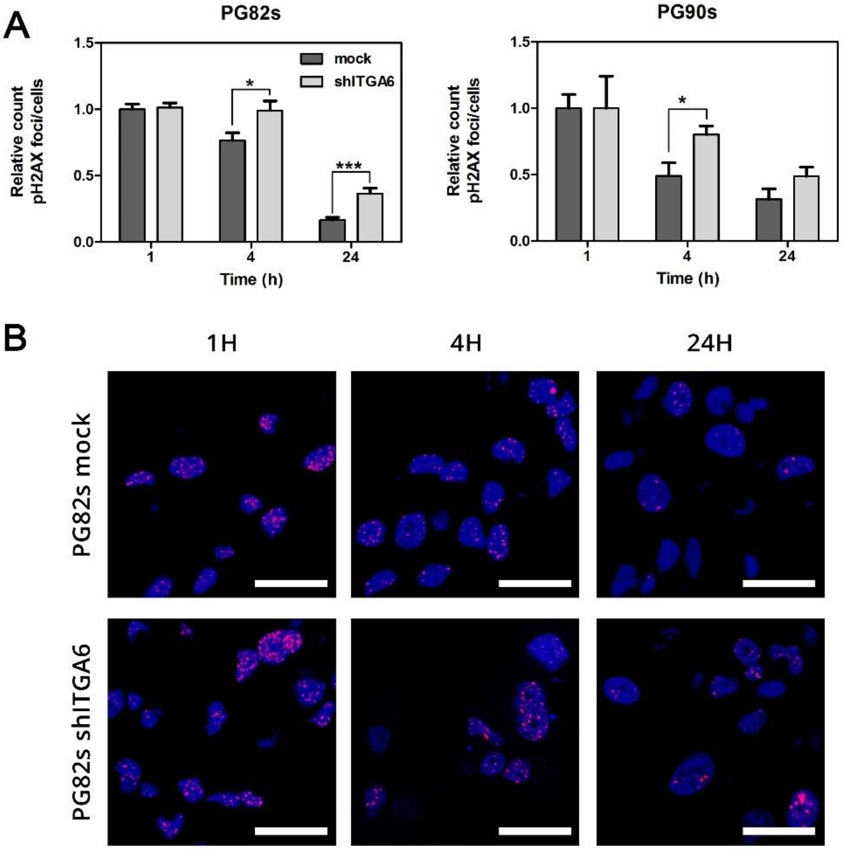

Figure R52: γH2AX decay after ITGA6 knockdown

(A) Time-course of γH2AX foci after single-fraction of 4 Gy. Two GICs-enriched cultures were tested: PG82s (n=3) and PG90s (n=1). All data are presented as mean ± SEM; * *P* < .05; *** *P* < .001 with unpaired t-test in comparison to mock sample. (B) Representative microsections of the time-course detection of γH2AX in PG82s following 4 Gy. γH2AX foci are stained in red, nuclei are counterstained with DRAQ5. Scale bar of 25 µm.

DISCUSSION

"When I came into the field as a hospital physicist in September 1950, I was told "don't go into 'radiotherapy'—that subject will soon be considered a crude old method—cancer will be cured by 'a spot of the jabs'." (They were talking about immunotherapy then.) But just look at radiation oncology now." JACK F FOWLER – *Development of radiobiology for oncology - a personal view* (2006)

1 PRIMARY CULTURES ESTABLISHMENT AND CHARACTERIZATION

Glioblastoma Multiforme remains an incurable disease despite aggressive and multimodal advanced treatment. GBM progression and recurrence are believed to be mainly driven by a marked invasiveness and resistance to treatment, thus pointing out the exclusive palliative role of current therapies (Gilbertson & Rich, 2007). Following comparison between serial CT scans and correlative autopsy data, it was reported that GBM in 90% of cases recurs in the field of high-dose irradiation, within 2-3 cm from the resection cavity (Hochberg & Pruitt, 1980; Lee et al., 1999). In addition, a recent study on low grade glioma indicates that GBM recurrences originate from cancer cells present in the original lesion, but that are not necessarily sharing the full set of parental mutations (Johnson et al., 2014). Considering the spatial recurrence pattern and the clonal phylogeny of tumor relapse elucidated in up-mentioned works, it is reasonable to think about recurrence as originated from pre-existing clones that after treatment acquire a proliferation advantage over the bulk of the tumor. Given the intratumoral heterogeneity and the increasing relevance of GBM cancer stem cells in tumor recurrence, we ought to develop an *in-vitro* model to investigate molecular mechanisms underlying GBM radioresistance based on two major cornerstones: (i) the key duality between GICs and cells of the bulk tumor; and (ii) the intratumoral heterogeneity.

First, we conceived a paired model where both GICs and differentiated GBM cells depicting the bulk of the tumor were represented. Both culture models were derived from the same GBM post-surgical specimen, but were established and maintained in different culturing conditions. In this way, we were able to analyze both GICs-enriched population and differentiated cells from the same sample, and to compare cell-behavior and cell-response of matching cultures sharing the same major genomic alterations. Of note, in order to uncover clinically relevant findings, several studies recommend to work with primary cultures instead of cell lines, as their transcriptomic environment is closer to patient tumor than standardized GBM cell lines (Lee et al., 2006; Li et al., 2008).

Secondly, we aimed to design a model that could preserve as much as possible the intratumoral heterogeneity of GBM, within the known limits of *in-vitro* cultures. Consequently, cultures obtained from GBM specimens were not sorted for expression of putative cancer stem-cell markers. To this end, GICs-enriched cultures were established using the neurosphere culture method (Galli et al., 2004; Lee et al., 2006; Svendsen et al., 1998) and stemness was validated based on functional characteristics (Heddleston et al., 2011; Vescovi et al., 2006).

Beyond the up mentioned purpose, the choice of working with unsorted cultures arose from the remarkable detection of ambiguous literature related on cancer stem cell markers, especially concerning CD133 (Campos & Herold-Mende, 2011). Controversial findings in literature warn against the over-reliance on "markers" for the isolation of the tumor-initiating cell population. In fact, a unique marker or a combination of them, able to solely and entirely isolate the small fraction of GICs subpopulation within the bulk of the tumor has not been identified yet (Gerweck & Wakimoto, 2016). CD133 (also known as Prominin-1), a transmembrane protein with still unknown biological function, was initially described as an efficient marker for isolation of hematopoietic stem cells (Miraglia et al., 1997). Its application has been extended to the isolation of CSCs and in 2003 CD133 was first described as useful marker to enrich CSCs with tumor-initiating capacity from different types of brain tumors (Singh et al., 2003, 2004). However, the use of CD133 faces limitations as it was reported later that also CD133-negative cells can generate tumor in nude mice (Beier et al., 2007) and that those tumors unexpectedly contained fractions of CD133$^+$ cells (Wang et al., 2008). In addition, intriguing works uncovered similarities between CD133$^+$ GICs and the PN subtype, whereas CD133$^-$ CSC exhibited a marked association with the Mes one (Joo et al., 2008; Lottaz et al., 2010). Finally, it was proposed that different expression levels of CD133 in GICs may reflect different stages of differentiation, where CD133$^-$ FABP7$^+$/NESTIN$^+$ are progenitor clones, CD133$^+$ cells have less stem potential and finally CD133$^-$ TBR2$^+$/DLX2$^+$ cells are markedly more differentiated (Chen et al., 2010). Consequently, CD133 seems to be insufficiently informative in segregating GICs and considerable disagreement arose over the reproducibility and usefulness of this marker.

In this PhD thesis, six different GBM patients' samples were processed and successfully established as both Differentiated Glial Cells (DGC) and Glioblastoma Initiating Cells (GICs). For chronological reasons only four of them were subjected to the full body of experimental analysis.

First, in order to verify the common genetic context of established cultures and parental tumors we investigated their transcriptomic subtype, the MGMT promoter state and the presence of copy number alteration in core pathways. These analyses confirmed that established cultures retained most of primary tumors alterations, bearing Mes trait, *MGMT* promoter methylation and *PTEN* deletion.

To define the transcriptomic subtype, we focused exclusively on Mes-PN, as among the GBM subclasses these subtypes represent the more robust and generally consistent ones. Moreover, recent works identified in GICs subpopulations exclusively Mes and PN molecular signatures (Bhat et al., 2013; Halliday et al., 2014). According to data obtained in the present study, all established tumor samples displayed mixed transcriptional subtypes, with Mes being the predominant one. The detection of non-pure signature is consistent with the GBM heterogeneous nature, described even at single-cell level, and with the presence of a small fraction of cells displaying PN trait in all GBM (Patel et al., 2014). Surprisingly, we found in all established GICs a pure Mes profile, suggesting a potential proliferative advantage of Mes cells for growing under the selected *Stem* media conditions. On the contrary, Bhat and colleagues found that GICs isolated from MES tumors had lost MES trait *in-vitro* and exhibited a marked PN signature (Bhat et al., 2013). Of note, to establish GICs cultures, Bhat and colleagues used DMEM/F12 supplemented with B27, EGF and bFGF. B27 is an optimized serum-free supplement developed to support long-term cultures of hippocampal and cortical neurons (Brewer et al., 1993). However, researchers had expanded its application to other type of cells, including glial cells and NSC. The *Stem* media employed in this thesis to maintain GICs was developed to sustain *in vitro* Stem Cells isolated from adult murine striatum (Gritti et al., 1996). All the components supplemented to DMEM/F12 in *Stem* media are included without exceptions in B27, although B27 contains, in addition, high levels of different antioxidants. It is likely that within the heterogeneous pool of cells predominantly expressing a Mes signature in a GBM specimen, B27 primarily enables the isolation of those GICs bearing a marked neuronal trait, fitting with the PN profile, whereas *Stem* media facilitates the proliferation of Mes-GICs. Taking into account that the authors reported the expression of PN signature at very early passages, they themselves hypothesized a selective enrichment of PN GICs under *in vitro* proliferating condition. Interestingly, the totality of tumor samples displaying PN predominant signature were unable to grow in our culturing condition, endorsing the hypothesis that *Stem* media primarily enable the proliferation of cells bearing Mes trait. In conclusion, we cannot exclude that different culture media may lead to an enrichment of GICs bearing distinct phenotype.

Regarding detection of aberrant copy number alterations, established cultures displayed clear *PTEN* deficiency, even if in few cases parental tumors did not show PTEN deletion. A possible explanation could be found in GBM spatial heterogeneity. To this end it is important to specify that different specimens of the same patient were used for genomic analyses and for culture establishment. In fact, spatial intratumoral GBM heterogeneity leaded researchers to underline the criticism of using single biopsy for diagnostic purposes, as a unique specimen is unlikely to represent the full set of patient's mutations (Sottoriva et al., 2013). Curiously, PTEN deficiency has been described as the sole genomic alteration required for the successful neurosphere propagation in cultures. On the contrary, molecular subtype, *MGMT* methylation status, *TP53* mutation, *CDKN2A* deletion, *PDGFR* amplification, and *EGFR* amplification have not shown a significant correlation with *in-vitro* neurosphere growth (Chen et al., 2010). Of note, loss of heterozygosity of chromosome 10q, which include *PTEN* locus, has been used to discard the hypothesis of non-neoplastic cells growing in established GBM cultures (Bhat et al., 2013). Consequently, given the observed *PTEN* deletion in all established cultures we could infer with a good confidence their neoplastic origin. Importantly, according to data obtained on patient's sample concerning the alteration in core pathways, we can not rule out the presence of cells with classical traits. In fact, given the *EGFR* and *PTEN* status, a mixed signature with CL subtype could be possible (Brennan et al., 2013). To obtain a more detailed classification, further investigations would be required.

After these preliminary analyses, we investigated cultures' functional features to validate *stemness* of established neurospheres. To this end, DGC provided a valuable internal control of differentiated cells sharing the same GICs genetic aberrations. Established cultures were tested with regards to proliferation, self-renewal capacity, clonogenic capacity, multipotency, tumor initiating capability and CSCs markers expression eventually. According to data obtained, exclusively the neurosphere cultures displayed the full CSCs phenotype and resembled GICs already described in literature (Vescovi et al., 2006). Importantly, GICs cultures exhibited high expression levels of CD44, L1CAM and ITGA6 GICs markers in a heterogeneous manner. Taken together, these observations demonstrate that established neurosphere cultures are enriched in GICs, while monolayer cultures are not, as indicated by their poor clonogenic capacity and absent CSCs markers expression. Interestingly, the lack of a homogeneous pattern of CSCs markers expression in GICs cultures highlighted the GICs heterogeneous nature.

Concerning metabolic study, it is a common misunderstanding that tumor cells are strictly dependent on glucose catabolism for energy production and various anaplerotic reactions. Since early 1920s, when Otto Warburg published his studies on the marked increase of glucose uptake and lactate production in tumor cells, the energy metabolism reprogramming of cancer cells is achieving global agreement (Warburg, 1925; Warburg et al., 1927). His theory, known as the Warburg Effect, states that malignant transformation of cells shifts glucose metabolism away from efficient mitochondria energy-production towards a less efficient metabolic platform, in which glycolysis is the major source of energy (Liberti & Locasale, 2016; Warburg, 1956). Transformed cell lines display excess of glycolysis with high rate of lactate production even in the presence of oxygen (Heiden et al., 2009; Liberti & Locasale, 2016; Warburg, 1956) with a minor contribution of TCA coupled with oxidative phosphorylation (oxphos) for the oxidation of pyruvate. This feature is exploited for the Positron Emission Tomography imaging of solid cancers (PET) based on the avidity of cancer cell for 2-[^{18}F]fluoro-2-deoxy-D-glucose, a glucose analog. However, it is now well established that tumors rely on a more complex metabolic pattern. In order to define the metabolic state of established cultures, we evaluated the oxygen consumption rate, lactate production and glucose uptake. Data obtained suggested that GICs rely more on TCA and oxphos than their differentiated counterpart. In particular, DGC metabolism corresponded fully to anaerobic glycolysis, a profile traditionally attributed to highly cycling cancer cells and described by the Warburg effect. Moreover, the use of a not uniform source of energy production was hypothesized between the two culturing conditions. GICs higher amounts of PEPCK-M and reduced glucose consumption, along with equal lactate production, could point to a higher consumption of alternative carbon sources in neurosphere cultures different from glucose (i.e., glutamine). Data obtained from *in-vitro* analysis always require caution, as cells adapted to culture conditions could acquire extensive genomic and gene expression changes (Lee et al., 2006). This phenomenon should be especially taken into account when evaluating cell metabolic state, since culture lose interaction with their native surrounding *niche* which for sure influence and support metabolism of tumor cells. Even though, data collected from our cultures are consistent with findings obtained *in-vitro* from neurosphere cultures (Vlashi et al., 2011), and *in-vivo* from GBM mice xenografts (Marin-Valencia et al., 2012) and in human GBM patients (Maher et al., 2012).

2 RADIOTHERAPY RESPONSE STUDY

Radiotherapy alone has been the unique standardized GBM therapy for decades until 2005, with an unquestionable major survival benefit (Laperriere et al., 2002). Dose studies dating back to late 1970s ended up defining a RT treatment that conferred a significant survival advantage with acceptable toxicity (Walker et al., 1978, 1979). Since then and until 2005, the standard RT dose for patient aged up to 70 years and in good general and neurological condition consists of fractionated focal irradiation in daily standard fractions of 1.8-2 Gy given 5 days per week over a period of 6 weeks, for a total dose of 50-60 Gy. The implementation of RT after surgery increased GBM patients' survival from a range of 3 to 4 months to a range of 7 to 12 months (Delgado-López & Corrales-García, 2016; Wen & Kesari, 2008). In 2005, a milestone study proposed a new therapeutic strategy based on the combination of RT with TMZ a concomitant and adjuvant chemotherapeutic agent (Stupp et al., 2005). Nowadays, after the decisive improvement of surgical procedures (Eljamel, 2015) and the introduction of TMZ, median patients' survival was extended from 12.1 months to 14.6 months (Stupp et al., 2005, 2009). Currently, although many GBM initially respond, they essentially all recur and 90% of them relapse at the original site (Hochberg & Pruitt, 1980; Lee et al., 1999). The inability of conventional therapies to achieve durable remissions makes GBM an incurable disease (Aldape et al., 2015), and still the exact molecular mechanisms driving GBM resistance are unknown.

In the last decade, increasing evidence reinforced the hypothesis of CSCs having unique biologic properties leading to a phenotype more resistant to conventional therapies compared to the bulk of the tumor (Dick, 2008; Diehn et al., 2009; Visvader & Lindeman, 2008). In the context of GBM, most of the literature bases the evaluation of cultures and tumors radiosensitivity on the different expression level of CD133 as marker of GICs. Several studies supported a significant association of cancer stem cell markers' expression, *CD133* and *Nestin*, with poor outcome (Pallini et al., 2008; Strojnik et al., 2007; Zeppernick et al., 2008). Coupled analysis, before and after radiation therapy, pointed out an increased amount of CD133$^+$ cells in GBM patients (Pallini et al., 2011; Tamura et al., 2013) and in orthotopic xenografts (Jamal et al., 2012) after RT. Finally, the landmark paper from J. Rich's lab proved that CD133$^+$ Glioblastoma Initiating Cells were more radioresistant than CD133$^-$ cells (Bao et al., 2006). Nonetheless, the majority of following works revealed that not all CD133$^+$ cells were radioresistant compared to CD133$^-$ (Jamal et al., 2012; McCord et al., 2009;

Ropolo et al., 2009) and reluctantly concluded that GICs RT response do not significantly differ *in-vitro* from the one of non-GICs. Yet, the forced association between non-GICs and cells non-expressing CD133 marker could lead to misinterpretations. To this end, it is important to consider that in most of the above-mentioned studies CD133$^-$ cells were maintained under non-differentiating conditions, as well as CD133$^+$ cells. Moreover, a significant association between CD133$^-$ GICs and Mes trait (Joo et al., 2008; Lottaz et al., 2010), itself characterized by an aggressive and radio-resistant phenotype (Bhat et al., 2013), was observed. Thus, the unexpected picture could be explained by the over-reliance on a unique and problematic marker for the selection of GICs. Consequently, we considered that a new and more updated investigation was needed.

By means of clonogenic assay, we investigated the radiation sensitivity of four culture pairs. Again, DGC and GICs deriving from the same patient were compared side-by-side. Cells were treated with fractionated doses of ionizing radiation up to 8 Gy using 2 Gy per fraction. Radiation schedule was defined in order to closely mimic the clinical fractionated treatment. Interestingly, GICs cultures exhibited among them a marked diversification with respect to radiosensitivity. In addition, three out of four GICs-enriched culture displayed a clear radioresistant phenotype when compared to matching DGC, as indicated by smaller GICs' α- and β- values. Concerning #35 culture pair, GICs reported initially a higher sensitivity to radiation than PG35 counterpart. Given this unexpected result, we decided to explore the effect of longer RT schedule on #35. To this end, we evaluated the response to a second and third full cycle of IR. Analyzing the effect of repeated RT by means of clonogenic assay, opposite responses were detected. While PG35 exhibited enhanced responsiveness to treatment, PG35s displayed increased radioresistance. According to data collected, it was not possible to establish whether the variation in PG35s response was due to an acquisition of better DSB repair capacity plus a reduced radiosensitivity or to a selection of a preexisting radio-resistant clone. Taken together, these data demonstrate that all established unsorted GICs-enriched cultures ended up being more radioresistant than their differentiated counterparts.

To our knowledge, these data represent the first rigorous study of *in-vitro* radiation response carried out on unsorted-unselected GICs and matched monolayer counterparts. Other groups investigated RT response on similar paired culture systems, composed by unsorted GICs and differentiated counterpart (Fouse et al., 2014; Schneider et al., 2016). Both studies reported no significant differences in response (Schneider et al., 2016), or even enhanced sensitivity (Fouse et al., 2014) of GICs cultures when compared to matched non-GICs cultures. However, in both cases RT response was evaluated shortly after treatment (from 24 hours to 5 days) which might be an insufficient time period to appreciate RT effects. Moreover, radiosensitivity was inferred from unconventional cytometry-based analysis, probably not enough sensitive to evaluate proliferative impairment triggered by IR. In fact, proliferation impairment induced by IR is a long-term effect and direct activation of death pathways is unlikely to be observed within the first 48 hours from the IR exposure (Fowler, 2006).

Several works demonstrated that *in-vitro* findings scarcely recapitulate *in-vivo* data especially due to the lack of microenvironmental stimuli and crosstalk among different cell types (Jamal et al., 2012). Nevertheless, we verified whether cultures response to RT had a clinical relevance by comparing patient's clinical data to matching cultures radiosensitivity. Strikingly, the LQM parameters obtained from irradiated GICs, but not from DGC, correlates with patient's outcome. In particular, the smaller the α- and β-values, the shorter the patient disease free survival and overall survival. Obtained data collectively supported the GICs leading role in defining patient treatment response. In particular, GICs intrinsic radiosensitivity was found to likely influence patient clinical outcome, whereas the radiosensitive grade of the bulk of the tumor had only a marginal role. Similarly, Gerweck and Wakimoto demonstrated in spontaneous murine tumors that the radiation sensitivity of mouse-derived GICs cultures predicts the radiocurability of the corresponding parental tumors (Gerweck & Wakimoto, 2016). These findings confirmed that unsorted GICs do represent a suitable subpopulation to estimate and eventually target the radiation sensitivity of parental tumor. Surely, a bigger collection of biopsies from each patient would cover better the spatial heterogeneity and provide an even more objective prediction of clinical outcome. In addition, an extended cohort of analyzed samples is needed to achieve more convincing results.

In conclusion, we propose a quick and affordable method to faithfully determine cancer cells' treatment response and potentially predict patient outcome based on empirical data. This strategy could help drive therapeutic decisions and might allow rapid screen for second line drugs, thus moving closer to the attractive "personalized medicine". Notably, this approach allows researchers to investigate in respect of *Replacement* concept presented in 3R principle concerning the protection of animals (Russell & Burch, 1959).

Given the peculiar radioresistant shift of PG35s culture after multiple radiation cycles, we performed a whole transcriptomic analysis on irradiated and re-irradiated samples to identify the molecular determinants that were driving the observed acquisition of resistance.

It was reported that gene expression alteration in response to RT occurs primarily through the regulation of translation, while minor role is left to transcription (Lü et al., 2006). Even though, other works specified that post-IR pivotal regulation of protein synthesis may be specific of non-transformed cells exclusively (Braunstein et al., 2009). Consequently, to avoid loss of data, we decided to perform transcriptional analysis on the total pools of mRNA extracted. More recently, new findings supported the limited effect of the translation on gene expression modulation after RT (Halliday et al., 2014). Importantly, given the therapy-induced re-organization and phenotypic transformation of cancer cells (Liu et al., 2006; Phillips et al., 2006), the characterization of pathways in conventional untreated cancer cells might miss the focus on real molecular determinants of the GBM post-therapeutic recurrence (Nakano, 2014).

By means of transcriptomic analysis, we detected in both 8 Gy irradiated DGC and GICs contexts little variations of expression, with no genes displaying significant changes. Even though, we performed GSEA in order to identify coordinated changes in gene expression that could be related to known pathways or biological functions. Both components displayed subtle enhancement of inflammatory pathway, but interestingly only DGC exhibited significant mitotic blockade, disruption of chromosomal integrity and of DNA replication. The latter observations are consistent with *in vivo* studies carried out on a GBM mouse model PDGF-driven Ink4A/Arf$^{-/-}$ PTEN$^{-/-}$ (Halliday et al., 2014). In his work Halliday described negative regulation of mitosis, RNA processing and DNA replication after a single-dose of 10 Gy. This finding mirrored our data on DGC culture, thus supporting our hypothesis that DGC are closely mimicking of the bulk of the tumor.

According to data obtained from PCA plot, the re-irradiated GICs clearly segregated from their initial transcriptomic identity and acquired a new phenotype. Different analyses carried out using GSEA and GOrilla tools highlighted marked activation of inflammatory-related pathways, ECM remodeling, cell migration and intercellular crosstalk. Importantly, any gene set reported a significant downregulation, similarly to previous studies (Halliday et al., 2014). Strikingly, a number of gene-sets pointed to epithelial/mesenchymal transition processes, operated via IL6/JAK/STAT3 and TNF-α/NF-κB pathways. Notably, both of them have been reported to drive, in collaboration with others TFs (C/EBPβ and TAZ), the malignant shift from PN to Mes signature in GBM samples both *in-vitro* and *in-vivo* (Bhat et al., 2013; Carro et al., 2010; Halliday et al., 2014). The analysis of the TFs that were more consistently driving the observed transcriptional changes highlighted among others STAT3, NF-κB and C/EBPβ. Moreover, as already described on PN or CL GBM tumors (Halliday et al., 2014; Phillips et al., 2006), we detected a significant enhancement of the Mes signature following the double-cycle of RT. Of note, unirradiated GICs were already classified as Mes based on metagene score analysis. However, taking into account that the signature analysis was not complete, as it did not include CL and N gene sets, we can not discard that established GICs belong to a mixed Mes/CL subtype and that IR enhanced the Mes trait.

Previous work described that single 10-Gy fraction on PN PDGFR-driven tumors in mouse model induced a transient p53-dependent cell cycle arrest and partial apoptosis, beyond the PN/Mes shift mediated by STAT3 and C/EBPβ (Halliday et al., 2014). None of the cell-cycle and death-related pathways were found transcriptionally activated following double-IR exposure in our established Mes GICs. These findings are consistent with previous works suggesting that G2/M phase arrest and profound apoptosis are exclusive features of post-irradiated PN GBM (Bhat et al., 2013).

Given the key role of STAT3 TF in PN/Mes transition, we verified its phosphorylation status after IR treatment in three different GICs. Taking into account the complexity of a proper time course evaluation after fractionated doses, STAT3 phosphorylation was investigated one hour after the last fraction. At this point, we detected a slight but still significant gain of phosphorylation of STAT3 on residues Y705 in those GICs displaying a more radioresistant phenotype (PG88s and PG90s). Similarly, Halliday and colleagues reported analogous enhancement of phosphorylation at 6 and 24 hours after single 10-Gy fraction in PN mouse models (Halliday et al., 2014). According to our data, the observed radiotherapy-induced activation of STAT3 concern mainly the Y705 residues, as p-STAT3(S727) did not exhibit significant enhancement. Importantly, the two phosphorylation sites commonly respond to distinct stimuli. The canonical activation of STAT3 mediated by phosphorylation in Y705 responds to the IL6-family cytokines (IL-6, IL-11, LIF and OSM among others), which bind to gp130 receptor and activate the downstream JAK kinases. Alternative phosphorylation of Y705 residues is mediated by other signals, including tyrosine kinases as Src (Walker et al., 2014). STAT3 once phosphorylated forms homo- or heterodimers and translocates to the nucleus, where it regulates genes expression to promote proliferation, survival, pluripotency, and motility. Phosphorylation on S727 corresponds to an alternative activation of STAT3, independent to gp130/JAK pathway, mediated by MAPK, PKC and JNK pathways. The unconventional activation via S727 is mostly associated to recently described STAT3 mitochondrial functions (Qi & Yang, 2014). Of note, S727 phosphorylation was recently described to correlates with GBM cell lines intrinsic radioresistance (Ouédraogo et al., 2015). Interestingly, it has been reported in mouse Embryonic Stem Cells (mESC) that STAT3 Y705 activated by LIF/JAK maintains pluripotency and self-renewal, while under differentiating conditions, FGF/ERK pathways is required to phosphorylate STAT3 on S727 and thus to trigger the commitment of cells toward the neuronal differentiation (Huang et al., 2014). Taken together, our results indicate radiation-induced STAT3 activation through phosphorylation on Y705 in those GICs displaying a more radioresistant phenotype. Considering the absence of S727 phosphorylation, STAT3 activation likely responds to IL6-family or TRK signaling and triggers STAT3 nuclear translocation and activation of its TF-related functions.

Detailed analysis of gene expression changes in re-irradiated GICs uncovered 955 differentially expressed genes. Within the most upregulated genes, 161 exhibited inductions beyond four-times. Among them, we selected a small subset of genes tightly associated with inflammatory pathways and EMT (*COX2*, *BMP2*, *PLA2G4A*, *ICAM1*, *LIF*, *IL6*, *CTGF* and *NNMT*) in order to validate microarray findings in #35 culture pairs and in other established GICs-enriched cultures. Interestingly, all of them displayed enhancement at transcriptional level in irradiated cultures and reported a significant preferential upregulation in irradiated GICs. Further analysis allowed us to uncover *ICAM1, COX2*, *LIF*, *IL6, CTGF* and *NNMT* tight association with Mes signature within TCGA samples and a significant correlation with poor patient outcome, thus defining a subset of RT-induced Mes genes. Taking into account the results obtained, we can not conclude whether the RT-induced Mes-associated signature is cause or consequence of GICs radioresistance. However, given the significant association of signature with poor patient outcome, we could speculate that somehow these genes can promote radioresistance mechanisms.

ICAM1 is a membrane glycoprotein member of the immunoglobulin superfamily, involved in adhesion-dependent cellular interactions and it is typically expressed on endothelial cells and also on cells of the immune system. It also plays a key role in inflammatory processes where is involved in leukocytes adhesion to endothelial cells and extravasation (Ley et al., 2007). In GBM, ICAM1 is expressed in high levels compared to normal brain (Mäenpää et al., 1997) and matches with Mes signature (Bhat et al., 2013). ICAM1 expression becomes upregulated at sites of inflammation, especially in response to TNF-α, INF-γ, LPS and IL1 in endothelial cells (Woodfin et al., 2016), while in GBM its expression has been described after TNF-α/ NF-κB (Bhat et al., 2013) and STAT3 (Carro et al., 2010) stimulation. Importantly, enhanced expression of ICAM1 via cooperative NF-κB/STAT3 interaction has been reported following RT in GBM cell lines (Kesanakurti et al., 2013).

PLA2G4A gene encodes for the Ca^{2+}-sensitive cytosolic phospholipase A2 ($cPLA_2$) group IV family, member α. The group IV includes at least four paralogues (α, β, γ and δ), and $cPLA_2α$ is the most ubiquitously expressed enzyme. $cPLA_2α$ initiates the inflammatory response catalyzing the hydrolysis of membrane phospholipids to lysophospholipids (e.g. lysophosphatidylcholine, LPC) and arachidonic acid (AA), thus leading to lipid second messenger release. LPC production leads to the activation of the pro-survival pathways PI3K/AKT and MAP/ERK, which result in increased cell viability, proliferation, migration, growth factor production, apoptosis and expression of adhesion molecules (Schulte et al., 2011). Free AA is rapidly metabolized by either cyclooxygenases (COX) or lipoxygenases (LOX) to yield a wide spectrum of eicosanoid metabolites, particularly prostaglandin and leukotrienes respectively. Eicosanoids are lipid-based cellular hormones that regulate vascular permeability, inflammatory responses and other intracellular pathways (Linkous & Yazlovitskaya, 2010). Importantly, it has been described that clinically relevant doses of IR trigger the immediate activation of $cPLA_2$ in vascular endothelial cells promoting pro-survival effects via PI3K/AKT and MAP/ERK pathways, potentially stimulating the formation of a functional vascular network (Linkous et al., 2009; Yazlovitskaya et al., 2008). $cPLA_2$ inhibition has been reported to radiosensitize, impair angiogenesis, cell proliferation and invasion in non-small cell lung cancer (Thotala et al., 2013) and to decreases cell survival and tumor growth in irradiated ovarian cancer (Schulte et al., 2011). Importantly, heterotopic injection of glioma cell line in $cPLA_2α^{-/-}$ mice dramatically impairs tumor growth (Linkous et al., 2010). COX2 is an inducible form of cyclooxygenase and acts downstream of $cPLA_2$. COX2 expression is promoted by various stimuli, including inflammatory signals, mitogens, cytokines, and growth factors (e.g. IL1β, IL6, IL8, VEGF, TNFα; Kuwano et al., 2004). Transcription factors described to regulate *COX2* expression are NF-κB (Bhat et al., 2013) and STAT3 (Yu et al., 2014). Importantly, higher expression of COX2 has been observed in GBM, where it positively correlates with tumor grade and it is associated with aggressive phenotype, thus being a strong predictor of poor survival (Bhat et al., 2013; Shono et al., 2001). Recently, TCGA network detailed higher expression of *COX2* in Mes subtype and its significant inhibition in G-CIMP$^+$ tumors (Brennan et al., 2013). Moreover, it has been reported that COX2 increases the aggressiveness of GBM cell lines, promoting colony growth and migration/invasion (Xu et al., 2014). Interestingly, inhibition of COX2 provoked significant radiosensitization of glioblastoma cell lines and CD133+ GICs (Ma et al., 2011; Petersen et al., 2000).

NNMT (Nicotinamide N-Methyltransferase) is a cytosolic methyltransferase that plays a crucial role in the detoxification of many xenobiotic compounds, through N-methylation of nicotinamide (NAM) and pyridines. *NNMT* is predominantly expressed in liver, although high abnormal levels have been detected in various tumors, Glioblastoma included (Lal et al., 1999; Markert et al., 2001). The upregulation of this enzyme has been associated to growth, migration and metastasis in bladder cancer (Wu et al., 2008), and to radioresistance in immortalized human mesenchymal stem cells and bladder cancer cell lines (D'Andrea et al., 2011; Kassem et al., 2002). The potential role of NNMT in radiosensitizing cells has been explained by its ability to catalyze intracellular NAM. This amine has the ability to impair the maintenance on genome integrity and the repair of DNA single-stranded breaks via BER for its inhibitory effect on PARP (Kassem et al., 2002). Consequently, the decrease in concentration of intracellular NAM operated by NNMT might attenuate the inhibitory effect on PARP, leading to a more efficient SSB repair. Moreover, Colman and colleagues reported a mild association of high *NNMT* expression in GBM to poor outcome and Mes signature (Colman et al., 2010). Finally, several works reported upregulation of *NNMT* mediated by STAT3 activation (Azare et al., 2007; Tomida et al., 2008).

Following clinically relevant fractionated IR, we found a marked upregulation of *ICAM1*, *PLA2G4A*, *COX2* and *NNMT* in GICs, suggesting the preferential activation of inflammatory pathways and the improvement of SSB repair, through the removal of the inhibitory effect on PARP. Remarkably, also *IL6* and *LIF,* crucial activators of STAT3 via gp130/JAK signaling (Heinrich et al., 2003; Yu et al., 2014), were upregulated following IR in GICs-enriched cultures. Interestingly, IL-6 and STAT3 are involved in a positive regulatory loop, as IL-6 initiates STAT3 activation via the complex gp130/ IL-6Rα and activated STAT3 in turn induces *IL6* transcription and secretion (Wang et al., 2004). Consequently, *IL6* and *LIF* upregulation may potentially support, together with *CTGF* upregulation, the observed enhancement of Mes trait operated by STAT3 TF, among others. Recently, GBM resident macrophages and microglia were identified as potential inducer of Mes differentiation in GBM, via TNFα production and consequent activation of NF-κB downstream pathway in GBM cells (Bhat et al., 2013). Similarly, we could hypothesize a paracrine effect of the GICs-secreted cytokines IL6 and LIF on the cancer cell that escaped surgical ablation and are located in spatial proximity of radiated GICs. On this base, GICs might drive and orchestrate a global shift toward a Mes identity of surrounding cancer cells, pushing them to a more aggressive state. Importantly, we found that IL6 receptor (IL6Rα) is preferentially expressed in GICs compartment and that when it is not, its expression is significantly induced after IR. The difference observed, consistent with previous findings (Wang et al., 2009), potentially indicates a higher responsiveness to IL6 cytokine and an enhanced transition to Mes identity for GICs-enriched cultures. Moreover, the results suggest that an autocrine effect mediated by IL6 signaling in GICs upon RT is likely to occur. Of note, the radiation-induced mesenchymal shift, already observed in PN GBM mouse models (Halliday et al., 2014), may represent an important mechanism of resistance of GBM, given the higher radioresistance of Mes GICs compared to PN GICs (Bhat et al., 2013).

Recently, great interest has invested GICs niche, tumor microenvironment and the possible "interclonal cooperativity" (Parker et al., 2015). The complex tumor stroma, consisting of reactive astrocytes, microglial cells and immune infiltrate, is thought to cooperate to create a favorable microenvironment and to enhance tumor progression and treatment resistance via coordinated crosstalk with cancer cells. In this context, inflammatory pathway has gained a leading role (Aggarwal et al., 2014; Elinav et al., 2013; Locatelli et al., 2013; Mantovani et al., 2008).

Importantly, radiotherapy itself strongly activates the inflammatory pathway in a ROS-dependent manner. Free radical burst in irradiated cells has been shown to be tightly associated with the enhancement of an inflammatory state in targeted cells and in surrounding tissues via bystander effect (Azzam et al., 2012; Hei et al., 2008; Miao et al., 2014; Prise & O'Sullivan, 2009). Irradiated cells get affected in several signaling pathways and ended up changing the regulation of genes' expression. Numerous cytokines result induced, including IL1β, IL6, IL8, TNF-α, TGF-β and INF-γ, driving to perturbation of targeted cells' secretome and activation of key TF: NF-κB, AP-1 and STATs (Miao et al., 2014). The triggered pro-inflammatory network enhances even more the generation of inflammatory mediators and ROS in an amplificatory loop, which has its core in the TFs' activation. The activated cascades have crucial prosurvival function and promotes cancer progression, angiogenesis and invasiveness (Ivanov & Hei, 2014; Multhoff & Radons, 2012; Prise & O'Sullivan, 2009; Valerie et al., 2007).

In addition, pro-inflammatory molecules can recruit and activate various tumor-associated macrophages (TAMs) into targeted sites (Azzam et al., 2012; Miao et al., 2014; Multhoff & Radons, 2012). Activated macrophages can in turn increase the microenvironment content of reactive species and secrete cytokines that collectively may play a contrasting role. On one hand they can limit tumor growth, on the other hand they may amplify the preexisting perturbations of the GICs' niche secretome pushing it toward an enhanced tumor-promoting microenvironment. Importantly, TNF, IL-6 and IL-17 represent crucial players of those inflammatory processes mediating immune escape. Moreover, Prostaglandin E_2 (PGE_2), synthesized by COX2, has been associated in GBM context with suppression of T-cells activation and proliferation (Li & Graeber, 2012). TAMs in CNS are closely related to resident microglia and are believed to be a key components of the GBM microenvironment (Hambardzumyan & Bergers, 2015; Liebelt et al., 2016). TAMs are especially enriched in Mes subtypes and in those GBM patient with poorest outcome (Engler et al., 2012; Verhaak et al., 2010). M2-"alternatively activated" TAMs have been associated with phenomenon of immune tolerance (Quatromoni & Eruslanov, 2012; Rőszer, 2015) and in GBM have been reported to promote neovascularization and to play a supportive role in tumor progression (Frey et al., 2015; Pyonteck et al., 2013). Interestingly, in ovarian cancer and cervical carcinoma the combinations of cytokines IL-6 with LIF or PGE_2 with IL6 respectively, have been identified as crucial factors that skew blood monocytes into M2-TAM thus promoting an immune suppressive effect (Duluc et al., 2007; Heusinkveld et al., 2011).

Taking into consideration our results, the significantly higher radioresistance of GICs compared to corresponding DGC makes reasonable to assume that among cancer cells evading surgical ablation, GICs have an intrinsic survival advantage over the more differentiated cells upon RT. Moreover, considering GICs' ability to better upregulate *LIF*, *IL6*, *COX2*, *PLA2G4A* in response to IR *in-vitro*, it might be speculated that GICs can more efficiently activate the inflammatory cascade and polarize surrounding TAMs toward M2 phenotype to promote eventually prosurvival bystander effect and immune evasion, respectively. Interestingly, it has been already suggested that GICs may recruit TAMs more efficiently than their differentiated neoplastic counterparts (Yi et al., 2011). Hambardzumyan and Bergers hypothesized that the difference observed by Yi's group might be explained by a GICs higher expression of chemoattractants as VEGF, colony stimulating factor 1 (CSF1), IL6 and IL1β, which potentially will polarize macrophages and immature monocytes to an immune-suppressive phenotype (Hambardzumyan & Bergers, 2015).

To this end, considering the relevance of RT for GBM patient management, the therapy-induced acquisition of a more aggressive phenotype and the activation of prosurvival pathways observed in our GICs model could have severe implications. The proposed model may help to better understand the mechanisms driving GICs radioresistance and in the long run to improve radiation therapeutical effects in humans. In addition, our results support the relevance of targeting the pro-inflammatory signaling pathways as potential strategy for GBM radiosensitization, approach that have already reported promising results *in-vitro* and *in-vivo* (Kim et al., 2014; Multhoff & Radons, 2012; Wang et al., 2015; Yang et al., 2012).

3 INTEGRIN α6 SUBUNIT

Integrins are a family of adhesion molecules driving cell-to-cell and cell–ECM communication. These transmembrane proteins are involved in various cellular processes including cell survival, proliferation, migration, invasion, and angiogenesis and consequently their functions are expected to potentially support tumor development (Desgrosellier & Cheresh, 2010; Guo & Giancotti, 2004).

In the last years, a promising peptide, named Cilengitide, was developed to target and selectively inhibit Integrin heterodimers αvβ3 and αvβ5. Despite encouraging preclinical trials on GBM mouse models and phase I/II studies in GBM patients (Nabors et al., 2007; Reardon et al., 2008), Cilengitide did not report any significant clinical improvement when combined with standard therapies (Nabors et al., 2015; Stupp et al., 2014b). Nevertheless, to target integrins still remains an attractive goal as these adhesion molecules are implicated in crucial aspects of malignant progression. Furthermore, integrins expression patterns in neoplastic lesions differ from those of non-neoplastic tissues, thus allowing selective targeting of tumoral cells.

Integrin α6 has been described in GBM as a strong GICs marker capable to selectively enrich CSCs independently of CD133 expression and to sustain their self-renewal, proliferation and tumor initiating capacities (Lathia et al., 2010). Given the lack of information on ITGA6 role in GICs response to conventional treatment and the high expression level of this marker in established GICs cultures, we decided to explore the relevance of Integrin subunit α6 in GICs' radioresistance.

First, we detected a significantly higher *ITGA6* expression level in those GBM classified as Mes in TCGA databases. Importantly, Mes molecular trait in GBM has been associated to the most radioresistant phenotype among the other described profiles (Bhat et al., 2013; Patel et al., 2014). Given the predominant Mes signature in established GICs-enriched cultures, the obtained *in-silico* data supported the belief that our cultures could work as a promising platform to explore Integrin α6 role in GICs radioresistance.

Next, we decided to compare the RT-response of GICs pools derived from the same cultures but expressing ITGA6 at different levels. First, we analyzed the difference between populations obtained from GICs-enriched cultures by means of FACs sorting for ITGA6 (ITGA6^{HI} and ITGA6^{LO}). Then, similar evaluations were carried out on cultures knocked-down for the ITGA6 with a lentiviral-based shRNA. Cultures response to RT was evaluated by means of the well-established clonogenic assay. In addition, ELDA was performed to explore the capacity of the compared populations to retain stemness phenotype following IR. According to data obtained in both models, GICs cultures expressing lower amount of ITGA6 reported enhanced radiosensitivity, indicating a potential improvement of tumor radiocurability. Moreover, both ITGA6^{LO} and ITGA6shRNA-inhibited GICs cultures reported decreased capacity to retain stemness upon RT. In addition, quantification of γH2AX foci after IR proved that ITGA6 knockdown effectively impairs DNA damage repair. Importantly, the radiosensitizing effect was much more strong in sorted GICs compared to shRNA-inhibited cultures. This difference can be explained by the dissimilar capacity of the two models to achieve reduced ITGA6 amount in cultures. Indeed, shITGA6 reported inhibition around the 50% of the total amount, while ITGA6^{LO} reported much lower ITGA6 yield. However, the decision to move to a lentiviral-based knock-down was made on the evidence that sorted pools tended over time to an equal expression of ITGA6, suggesting a dynamic and inducible expression of this marker. Of note, a tight connection between EGF, a constitutive component of our *Stem* media, and Integrin α6/β1 level has been reported in ovarian cancer in the context of a JAK2/STAT3 mediated EMT (Colomiere et al., 2009).

Importantly, accumulating evidences across cancer types suggest the relevance of cell-ECM crosstalk in modulating the cancer response to radiotherapy (Mannino & Chalmers, 2011; Sandfort et al., 2007). In particular, Integrin β1 expression and activation were reported as significantly associated with an increased radioresistance in human glioma cell lines (Cordes et al., 2006). To our knowledge, these data correspond to the first work exploring the relevance of Integrin α6 in GICs radioresistance.

Taken together our data suggest a possible involvement of ITGA6 in GICs response at ionizing radiation and indicated that, once elucidated the ITGA6-associated mechanisms in radioresistance, ITGA6 may represent an attractive target to enhance GBM radiocurability.

To sum up, the data obtained in this doctoral thesis highlighted the crucial relevance of GICs in the radioresistance of GBM and the potential role exerted by the GICs marker, Integrin α6, in radioresistant mechanisms. Moreover, our data highlighted inflammatory response and PN to Mes transition as key features of GICs-enriched cultures following ionizing radiation. Finally, the data collected in this thesis support the strength of the proposed paired *in-vitro* model to explore GBM biology and the phenomena of radioresistance.

CONCLUSIONS

1. Established patient-derived neurosphere cultures exhibit functional CSCs phenotype with marked clonogenic and self-renewal capability, tumor formation capacity and noticeable differentiation along the central nervous system major lineages.
2. Established patient-derived neurosphere cultures express high level of CSCs-related markers CD133, L1CAM, CD44 and ITGA6.
3. The neurosphere culture method is a proper approach to isolate GICs within the GBM tumor mass, preserving GICs heterogenic nature. Selective culture conditions obviate the application of cell-sorting techniques based on a unique marker that would underestimate the GICs complexity.
4. Matching differentiated cultures exhibit negligible clonogenic capacity and do not express CD133, L1CAM and ITGA6 markers, thus indicating the absence of cells bearing CSCs features.
5. GICs-enriched cultures rely on oxidative metabolism and consumption of alternative carbon sources. Conversely, DGC metabolism correspond fully to anaerobic glycolysis as described by the Warburg effect.
6. GICs-enriched cultures report noticeable intrinsic radioresistance and capacity to repair sublethal DNA damage according to calculated α- and β-values, respectively. Importantly, DGC ended up being more radiosensitive than matching GICs cultures.
7. AlamarBlue reduction can be used to predict quickly neurosphere surviving fraction after radiotherapy with a good fit.
8. GICs-enriched cultures display different grades of radiosensitivity, which correlates with patients' DFS and OS. Thus, the *in-vitro* model proposed in this thesis is a suitable and affordable method to predict patients' outcome.
9. Genome-wide transcriptional profiling of irradiated DGC indicates an enhancement of pathways related to mitotic blockade, disruption of chromosomal integrity and DNA replication.
10. Double-irradiated GICs exhibit activation of pathways related to inflammation, ECM remodeling, cell migration and intercellular crosstalk, being IL6/JAK/STAT3 and TNFα/ NF-κB signaling, master regulators of PN to Mes transition, the most relevant.
11. Defined RT-Mes genes, *COX2*, *LIF*, *ICAM1*, *IL6*, *CTGF* and *NNMT*, display preferential upregulation in GICs after RT and are associated with Mes subtype and poor patient outcome.
12. GICs expressing ITGA6^{HIGH} exhibit higher radioresistant phenotype and greater capacity to retain stemness upon RT, when compared to ITGA6^{LOW}.
13. Observed higher α- and β- values in shITGA6 cultures indicates increased radiosensitivity and an impaired capacity to repair sublethal DNA damage, respectively. Moreover, ITGA6 knockdown compromises DNA damage repair capacity, as indicated by γH2AX immunostaining.

ANNEX

Affymetrix gene ID	Gene symbol	Gene name	R-fold	NOM *p*-value
8097692	EDNRA	*Endothelin receptor type A*	50.11	4.52E-04
7922976	PTGS2	*Prostaglandin-endoperoxide synthase 2 (COX2)*	49.15	3.05E-06
7962375	PRICKLE1	*Prickle homolog 1 (Drosophila)*	32.88	7.70E-06
8031646	LOC100128252	*Hypothetical LOC100128252*	32.03	1.95E-06
8031646	LOC100288114	*Hypothetical LOC100288114*	32.03	1.95E-06
8040430	VSNL1	*Visinin-like 1*	29.15	1.27E-06
8046086	LASS6	*LAG1 homolog, ceramide synthase 6*	28.95	8.71E-07
8045664	LYPD6B	*LY6/PLAUR domain containing 6B*	22.64	1.44E-06
8112274	ELOVL7	*Family member 7, elongation of long chain fatty acids (yeast)*	22.01	2.06E-08
8060850	BMP2	*Bone morphogenetic protein 2*	21.50	1.70E-06
7983910	AQP9	*Aquaporin 9*	21.33	2.52E-06
8001800	CDH11	*Cadherin 11, type 2, OB-cadherin (osteoblast)*	19.80	1.97E-05
8122150	EYA4	*Eyes absent homolog 4 (Drosophila)*	18.24	1.23E-07
7908204	HMCN1	*Hemicentin 1*	18.08	6.54E-07
8096301	SPP1	*Secreted phosphoprotein 1*	17.83	7.42E-04
8067955	CXADR	*Coxsackie virus and adenovirus receptor*	17.18	4.03E-05
8047738	NRP2	*Neuropilin 2*	17.15	1.22E-05
8127563	COL12A1	*Collagen, type XII, alpha 1*	16.66	6.69E-07
7908351	PLA2G4A	*Phospholipase A2, group IVA (cytosolic, calcium-dependent)*	16.55	3.70E-04
8166511	PDK3	*Pyruvate dehydrogenase kinase, isozyme 3*	16.16	3.23E-06
7927681	BICC1	*Bicaudal C homolog 1 (Drosophila)*	15.79	6.64E-07
8097991	TDO2	*Tryptophan 2,3-dioxygenase*	15.14	1.75E-05
7908161	C1orf21	*Chromosome 1 open reading frame 21*	14.83	4.43E-06
8045674	LYPD6	*LY6/PLAUR domain containing 6*	14.62	3.09E-06
8140579	CACNA2D1	*Calcium channel, voltage-dependent, alpha 2/delta subunit 1*	14.56	3.84E-06
8025601	ICAM1	*Intercellular adhesion molecule 1*	14.51	6.59E-06
8160346	PTPLAD2	*Protein tyrosine phosphatase-like A domain containing 2*	14.36	8.05E-05
8075310	LIF	*Leukemia inhibitory factor (cholinergic differentiation factor)*	13.84	2.05E-04
8081838	ARHGAP31	*Rho gtpase activating protein 31*	13.60	3.51E-04
8040103	ID2	*Inhibitor of DNA binding 2*	13.56	1.88E-04
8152606	SNTB1	*Syntrophin, beta 1*	13.31	2.02E-06
8126760	RCAN2	*Regulator of calcineurin 2*	13.14	1.36E-04
7965403	LUM	*Lumican*	12.83	5.46E-04
8113039	MEF2C	*Myocyte enhancer factor 2C*	12.41	3.55E-05
8113433	EFNA5	*Ephrin-A5*	12.36	7.96E-07
8131803	IL6	*Interleukin 6 (interferon, beta 2)*	12.25	2.14E-05
7939052	FIBIN	*Fin bud initiation factor homolog (zebrafish)*	11.96	4.26E-07
8091402	TM4SF18	*Transmembrane 4 L six family member 18*	11.76	5.02E-06
8044574	IL1RN	*Interleukin 1 receptor antagonist*	11.56	5.28E-05
7903227	PALMD	*Palmdelphin*	11.40	1.62E-07
8081686	BOC	*Boc homolog (mouse)*	11.22	5.32E-05
8023415	TCF4	*Transcription factor 4*	10.88	2.21E-04
8082965	MRAS	*Muscle RAS oncogene homolog*	10.66	1.32E-06
7972003	KLF12	*Kruppel-like factor 12*	10.65	2.81E-05
7902353	LHX8	*LIM homeobox 8*	10.49	7.50E-05
8180411	ELMO1	*Engulfment and cell motility 1*	10.41	6.92E-07
8104592	FBXL7	*F-box and leucine-rich repeat protein 7*	10.34	8.96E-07
8148435	WISP1	*WNT1 inducible signaling pathway protein 1*	10.15	5.76E-07
7985159	CRABP1	*Cellular retinoic acid binding protein 1*	10.09	5.35E-06

Annex 1: List of genes differentially expressed in cluster 3 versus cluster 2

Genes significantly upregulated by more than four-fold and genes significantly downregulated below 0.25 R-fold. Significance level: FDR < 0.05. Indicated nominal *P*-value was calculated with two-tailed unpaired t-test.

Affymetrix gene ID	Gene symbol	Gene name	R-fold	NOM *p*-value
8078330	RBMS3	*RNA binding motif, single stranded interacting protein 3*	10.06	3.09E-05
8120961	MRAP2	*Melanocortin 2 receptor accessory protein 2*	9.72	4.62E-05
8144726	TUSC3	*Tumor suppressor candidate 3*	9.67	2.90E-06
8129562	CTGF	*Connective tissue growth factor*	9.67	1.04E-02
8066848	PREX1	*PI-3,4,5-trisphosphate-dependent rac exchange factor 1*	9.49	4.27E-02
8175217	GPC4	*Glypican 4*	9.44	2.01E-03
8078650	CTDSPL	*CT domain, rna polymerase ii, polypeptide a, small phosphatase-like*	9.10	5.17E-04
8088491	CADPS	*Ca++-dependent secretion activator*	9.09	7.53E-03
7953603	C1S	*Complement component 1, s subcomponent*	9.01	1.82E-03
8113130	MCTP1	*Multiple c2 domains, transmembrane 1*	8.91	6.44E-04
7922846	FAM129A	*Family with sequence similarity 129, member a*	8.72	1.39E-02
8006999	CSF3	*Colony stimulating factor 3 (granulocyte)*	8.52	5.86E-03
8090162	ITGB5	*Integrin, beta 5*	8.46	1.28E-03
7904293	PTGFRN	*Prostaglandin f2 receptor negative regulator*	8.39	1.92E-02
7906954	PBX1	*Pre-b-cell leukemia homeobox 1*	8.22	8.32E-03
8031632	ZNF542	*Zinc finger protein 542*	8.19	4.88E-03
8155754	MAMDC2	*Mam domain containing 2*	8.02	1.82E-02
8088415	FAM107A	*Family with sequence similarity 107, member a*	7.96	5.86E-03
7951977	FXYD6	*Fxyd domain containing ion transport regulator 6*	7.94	2.76E-02
7898057	PDPN	*Podoplanin*	7.89	2.29E-02
8098204	CPE	*Carboxypeptidase e*	7.84	2.05E-02
8066493	SLPI	*Secretory leukocyte peptidase inhibitor*	7.78	3.96E-02
8023267	MYO5B	*Myosin vb*	7.73	5.05E-03
8128123	RRAGD	*Ras-related gtp binding d*	7.48	5.77E-03
8054722	IL1B	*Interleukin 1, beta*	7.41	3.94E-02
8160332	MLLT3	*Myeloid/lymphoid or mixed-lineage leukemia*	7.36	5.05E-03
7903092	FNBP1L	*Formin binding protein 1-like*	7.31	2.64E-02
8113666	SEMA6A	*Sema domain,(semaphorin) 6a*	7.22	4.52E-03
8117054	CAP2	*Cap, adenylate cyclase-associated protein, 2 (yeast)*	6.78	5.17E-04
7943998	NNMT	*Nicotinamide n-methyltransferase*	6.70	1.53E-03
7977933	SLC7A8	*Solute carrier family 7 (amino acid transporter, l-type), member 8*	6.62	3.24E-02
8130993	FAM20C	*Family with sequence similarity 20, member c*	6.55	3.12E-02
8140358	CCL26	*Chemokine (c-c motif) ligand 26*	6.54	2.54E-02
8122426	PHACTR2	*Phosphatase and actin regulator 2*	6.46	3.87E-02
8174576	AMOT	*Angiomotin*	6.45	1.07E-02
7903358	VCAM1	*Vascular cell adhesion molecule 1*	6.43	9.51E-03
8051241	ALK	*Anaplastic lymphoma receptor tyrosine kinase*	6.41	1.68E-02
8054731	IL1F8	*Interleukin 1 family, member 8 (eta)*	6.35	2.77E-03
8091678	VEPH1	*Ventricular zone expressed ph domain homolog 1 (zebrafish)*	6.29	1.38E-02
8091260	SLC9A9	*Solute carrier family 9 (sodium/hydrogen exchanger), member 9*	6.26	2.11E-02
8068022	MIR155HG	*Mir155 host gene (non-protein coding)*	6.11	5.17E-04
8066266	MAFB	*V-maf musculoaponeurotic fibrosarcoma oncogene homolog b (avian)*	6.09	1.16E-02
7960874	C3AR1	*Complement component 3a receptor 1*	6.02	2.24E-02
8134117	FZD1	*Frizzled homolog 1 (drosophila)*	6.01	3.51E-02
8099721	SEL1L3	*Sel-1 suppressor of lin-12-like 3 (c. Elegans)*	6.00	1.50E-02
8149448	MSR1	*Macrophage scavenger receptor 1*	5.94	4.80E-02
8121319	SOBP	*Sine oculis binding protein homolog (drosophila)*	5.94	1.15E-02
7901720	PRKAA2	*Protein kinase, amp-activated, alpha 2 catalytic subunit*	5.91	1.32E-02
8045637	KIF5C	*Kinesin family member 5c*	5.88	1.10E-02
8095680	IL8	*Interleukin 8*	5.88	3.47E-02
8166925	MAOA	*Monoamine oxidase a*	5.87	2.77E-03
8104124	FRG2	*FSHD region gene 2-like family*	5.85	1.74E-06
8084880	HES1	*Hairy and enhancer of split 1, (Drosophila)*	5.79	1.88E-06

Annex 1: List of genes differentially expressed in cluster 3 versus cluster 2 (continued)

Affymetrix gene ID	Gene symbol	Gene name	R-fold	NOM *p*-value
8154951	GLUL	*Glutamate-ammonia ligase*	5.74	2.68E-04
8007931	ITGB3	*Integrin, beta 3 (platelet glycoprotein iiia, antigen CD61)*	5.71	2.45E-05
7951703	DRD2	*Dopamine receptor D2*	5.67	3.94E-04
7957386	ACSS3	*Acyl-coa synthetase short-chain family member 3*	5.66	1.56E-05
7951309	MMP13	*Matrix metallopeptidase 13 (collagenase 3)*	5.65	6.64E-04
8142997	PLXNA4	*Plexin A4*	5.59	2.45E-04
8060963	SNAP25	*Synaptosomal-associated protein, 25kda*	5.51	3.84E-05
8103745	HAND2	*Heart and neural crest derivatives expressed 2*	5.51	9.49E-05
7923547	CHI3L1	*Chitinase 3-like 1 (cartilage glycoprotein-39)*	5.49	1.44E-04
8053551	REEP1	*Receptor accessory protein 1*	5.41	8.26E-04
7965941	GLT8D2	*Glycosyltransferase 8 domain containing 2*	5.32	3.72E-04
8180282	PCDHGB4	*Protocadherin gamma subfamily B, 4*	5.25	7.48E-04
7933488	C10orf72	*Chromosome 10 open reading frame 72*	5.24	6.26E-05
7917199	TTLL7	*Tubulin tyrosine ligase-like family, member 7*	5.20	3.31E-05
8152812	FAM84B	*Family with sequence similarity 84, member B*	5.18	5.50E-05
7961891	BHLHE41	*Basic helix-loop-helix family, member e41*	5.16	6.97E-04
7937251	FRG2	*FSHD region gene 2-like family*	5.16	8.96E-06
7918157	VAV3	*Vav 3 guanine nucleotide exchange factor*	5.04	8.13E-06
7960744	C1R	*Complement component 1, r subcomponent*	5.04	1.03E-04
8050427	FAM49A	*Family with sequence similarity 49, member A*	4.96	8.24E-05
8149825	STC1	*Stanniocalcin 1*	4.95	1.55E-05
8146533	FAM110B	*Family with sequence similarity 110, member B*	4.95	3.45E-04
7952205	MCAM	*Melanoma cell adhesion molecule*	4.92	3.83E-04
8056860	WIPF1	*WAS/WASL interacting protein family, member 1*	4.91	5.58E-07
8033257	C3	*Complement component 3*	4.91	7.06E-05
7972055	KCTD12	*Potassium channel tetramerisation domain containing 12*	4.83	4.09E-05
8139207	INHBA	*Inhibin, beta A*	4.82	1.13E-05
7913655	ID3	*Inhibitor of DNA binding 3, dominant negative helix-loop-helix protein*	4.77	3.41E-05
8068671	BACE2	*Beta-site APP-cleaving enzyme 2*	4.77	5.37E-04
7944722	UBASH3B	*Ubiquitin associated and SH3 domain containing B*	4.72	5.36E-04
8133860	GNAI1	*G protein, alpha inhibiting activity polypeptide 1*	4.68	6.49E-04
8113234	PCSK1	*Proprotein convertase subtilisin/kexin type 1*	4.66	5.77E-04
7921882	OLFML2B	*Olfactomedin-like 2B*	4.63	3.21E-04
7924987	AGT	*Angiotensinogen (serpin peptidase inhibitor, clade A, member 8)*	4.60	1.05E-04
7989365	RORA	*RAR-related orphan receptor A*	4.57	3.22E-04
8140478	PION	*Pigeon homolog (Drosophila)*	4.56	6.80E-08
7974366	PTGER2	*Prostaglandin E receptor 2 (subtype EP2), 53kda*	4.51	4.69E-06
7944751	C11orf63	*Chromosome 11 open reading frame 63*	4.49	1.03E-04
8152703	FBXO32	*F-box protein 32*	4.45	3.84E-04
7914580	FNDC5	*Fibronectin type III domain containing 5*	4.43	1.33E-04
8108744	PCDHB14	*Protocadherin beta 14*	4.41	1.12E-04
7925062	SIPA1L2	*Signal-induced proliferation-associated 1 like 2*	4.39	2.41E-04
8108733	PCDHB12	*Protocadherin beta 12*	4.39	1.66E-04
8157524	TLR4	*Toll-like receptor 4*	4.33	7.29E-04
8057578	CALCRL	*Calcitonin receptor-like*	4.31	2.73E-05
8114287	SPOCK1	*Sparc/osteonectin, cwcv and kazal-like dom. proteoglycan (testican) 1*	4.31	6.04E-04
8023828	NETO1	*Neuropilin (NRP) and tolloid (TLL)-like 1*	4.25	6.99E-05
8086600	CCR1	*Chemokine (C-C motif) receptor 1*	4.23	4.93E-05
8099633	PPARGC1A	*Peroxisome proliferator-activated receptor gamma, coactivator 1 alpha*	4.20	7.62E-08
8033767	ZNF560	*Zinc finger protein 560*	4.17	5.21E-05
8163202	SVEP1	*Sushi, von Willebrand factor A, EGF and pentraxin dom. containing 1*	4.15	4.07E-05
8074606	USP18/41	*Ubiquitin specific peptidase 18/41*	4.13	1.10E-04
8172425	SLC38A5	*Solute carrier family 38, member 5*	4.13	2.22E-04

Annex 1: List of genes differentially expressed in cluster 3 versus cluster 2 (continued)

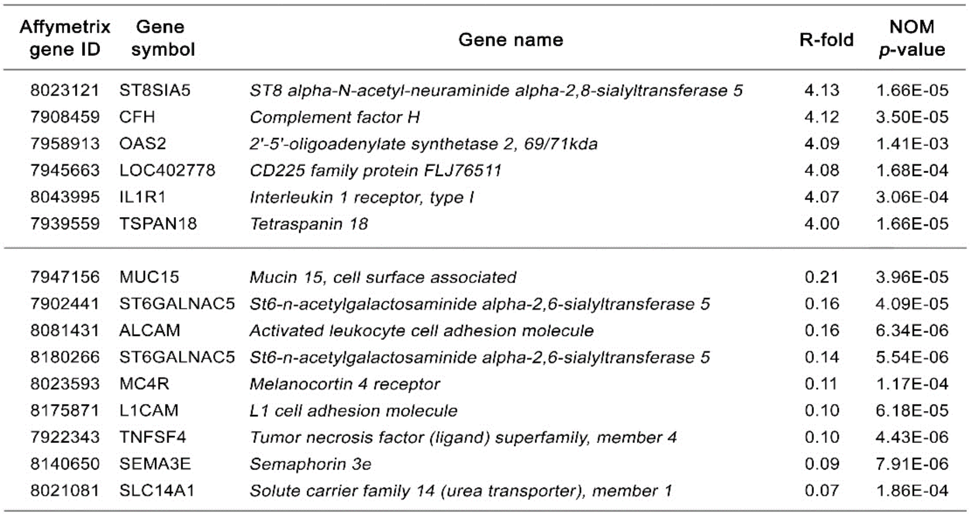

Affymetrix gene ID	Gene symbol	Gene name	R-fold	NOM *p*-value
8023121	ST8SIA5	*ST8 alpha-N-acetyl-neuraminide alpha-2,8-sialyltransferase 5*	4.13	1.66E-05
7908459	CFH	*Complement factor H*	4.12	3.50E-05
7958913	OAS2	*2'-5'-oligoadenylate synthetase 2, 69/71kda*	4.09	1.41E-03
7945663	LOC402778	*CD225 family protein FLJ76511*	4.08	1.68E-04
8043995	IL1R1	*Interleukin 1 receptor, type I*	4.07	3.06E-04
7939559	TSPAN18	*Tetraspanin 18*	4.00	1.66E-05
7947156	MUC15	*Mucin 15, cell surface associated*	0.21	3.96E-05
7902441	ST6GALNAC5	*St6-n-acetylgalactosaminide alpha-2,6-sialyltransferase 5*	0.16	4.09E-05
8081431	ALCAM	*Activated leukocyte cell adhesion molecule*	0.16	6.34E-06
8180266	ST6GALNAC5	*St6-n-acetylgalactosaminide alpha-2,6-sialyltransferase 5*	0.14	5.54E-06
8023593	MC4R	*Melanocortin 4 receptor*	0.11	1.17E-04
8175871	L1CAM	*L1 cell adhesion molecule*	0.10	6.18E-05
7922343	TNFSF4	*Tumor necrosis factor (ligand) superfamily, member 4*	0.10	4.43E-06
8140650	SEMA3E	*Semaphorin 3e*	0.09	7.91E-06
8021081	SLC14A1	*Solute carrier family 14 (urea transporter), member 1*	0.07	1.86E-04

Annex 1: List of genes differentially expressed in cluster 3 versus cluster 2 (continued)

Affymetrix gene ID	Gene symbol	Gene name	R-fold	NOM *p*-value
8046380	ITGA6	*Integrin, α 6*	59.33	0.000
8180100	HLA-DPA1	*Major histocompatibility complex, class ii, dp α 1*	38.07	0.001
8125556	HLA-DPA1	*Major histocompatibility complex, class ii, dp α 1*	33.80	0.002
8178891	HLA-DPA1	*Major histocompatibility complex, class ii, dp α 1*	33.80	0.002
8175871	L1CAM	*L1 cell adhesion molecule*	32.47	0.001
8048205	IGFBP2	*Insulin-like growth factor binding protein 2, 36kda*	25.20	0.004
8072626	TIMP3	*Timp metallopeptidase inhibitor 3*	22.22	0.002
8142981	PODXL	*Podocalyxin-like*	21.95	0.003
7902565	LPHN2	*Latrophilin 2*	20.71	0.000
8168678	FAM133A	*Family with sequence similarity 133, member a*	20.18	0.000
8021081	SLC14A1	*Solute carrier family 14 (urea transporter), member 1*	19.97	0.012
8092726	CLDN1	*Claudin 1*	19.41	0.002
7953200	CCND2	*Cyclin d2*	18.30	0.001
7922343	TNFSF4	*Tumor necrosis factor (ligand) superfamily, member 4*	17.03	0.001
8140668	SEMA3A	*Semaphorin 3a*	16.19	0.001
8105908	OCLN	*Occludin*	15.92	0.002
8140650	SEMA3E	*Semaphorin 3e*	14.52	0.004
8140556	HGF	*Hepatocyte growth factor (hepapoietin a; scatter factor)*	13.39	0.007
8180376	AKR1C1	*Aldo-keto reductase family 1, member c1*	12.26	0.028
8175562	MAGEC2	*Melanoma antigen family c, 2*	11.54	0.003
7922337	TNFSF18	*Tumor necrosis factor (ligand) superfamily, member 18*	11.07	0.045
7951297	MMP12	*Matrix metallopeptidase 12 (macrophage elastase)*	11.06	0.001
7983527	SEMA6D	*Semaphorin 6d*	10.64	0.011
8125289	TNXA	*Tenascin xa pseudogene*	9.99	0.021
8063536	TFAP2C	*Transcription factor ap-2 γ*	9.89	0.004
8054479	MALL	*Mal, t-cell differentiation protein-like*	9.83	0.011
8166202	GRPR	*Gastrin-releasing peptide receptor*	9.67	0.017
8178712	TNXB	*Tenascin xb*	9.50	0.027
8179935	TNXB	*Tenascin xb*	9.50	0.027
7947156	MUC15	*Mucin 15, cell surface associated*	9.40	0.003
8037283	PSG4	*Pregnancy specific beta-1-glycoprotein 4*	9.11	0.014
8023593	MC4R	*Melanocortin 4 receptor*	9.10	0.015
8126839	TNFRSF21	*Tumor necrosis factor receptor superfamily, member 21*	8.95	0.001
7979241	BMP4	*Bone morphogenetic protein 4*	8.92	0.004
8063923	SLCO4A1	*Solute carrier organic anion transporter family, member 4a1*	8.88	0.004
8175543	SPANXC	*Spanx family, member c*	8.74	0.005
8170249	SPANXA2	*Spanx family, member a2*	8.74	0.004
8175550	SPANXA2	*Spanx family, member a2*	8.74	0.004
8025402	ANGPTL4	*Angiopoietin-like 4*	8.65	0.001
8018652	RNF157	*Ring finger protein 157*	8.54	0.035
7961710	ABCC9	*Atp-binding cassette, sub-family c (cftr/mrp), member 9*	8.41	0.001
8132694	IGFBP1	*Insulin-like growth factor binding protein 1*	8.34	0.000
8066921	KCNB1	*Potassium voltage-gated channel, member 1*	7.94	0.020
7925929	AKR1C3	*Aldo-keto reductase family 1, member c3*	7.88	0.021
7910022	CNIH3	*Cornichon homolog 3 (drosophila)*	7.40	0.011
7904726	TXNIP	*Thioredoxin interacting protein*	7.19	0.007
7963427	KRT5	*Keratin 5*	7.16	0.018
7951271	MMP1	*Matrix metallopeptidase 1 (interstitial collagenase)*	6.94	0.013
7997332	NUDT7	*Nudix (nucleoside diphosphate linked moiety x)-type motif 7*	6.89	0.017

Annex 2: List of genes differentially expressed in unirradiated PG35s versus PG35

Genes significantly upregulated by more than four-fold and genes significantly downregulated below 0.25 R-fold. Significance level: $P < 0.05$. Indicated nominal *P*-value was calculated with two-tailed unpaired t-test.

Affymetrix gene ID	Gene symbol	Gene name	R-fold	NOM *p*-value
7917649	TGFBR3	*Transforming growth factor, beta receptor III*	6.82	0.006
7898655	CDA	*Cytidine deaminase*	6.65	0.024
8138459	TMEM196	*Transmembrane protein 196*	6.63	0.046
8162216	SHC3	*SHC transforming protein 3*	6.60	0.026
7949971	CPT1A	*Carnitine palmitoyltransferase 1A (liver)*	6.54	0.001
8173551	PHKA1	*Phosphorylase kinase, α 1 (muscle)*	6.38	0.001
8104901	IL7R	*Interleukin 7 receptor*	6.36	0.004
7993588	TMC7	*Transmembrane channel-like 7*	6.18	0.001
8023043	PSTPIP2	*Proline-serine-threonine phosphatase interacting protein 2*	6.18	0.022
8136200	CPA4	*Carboxypeptidase A4*	6.13	0.011
8046078	B3GALT1	*UDP-Gal:betaglcnac beta 1,3-galactosyltransferase1*	5.99	0.013
8032576	AES	*Amino-terminal enhancer of split*	5.98	0.040
8106210	ARHGEF28	*Rho guanine nucleotide exchange factor (GEF) 28*	5.93	0.005
7965335	DUSP6	*Dual specificity phosphatase 6*	5.93	0.007
8097098	USP53	*Ubiquitin specific peptidase 53*	5.66	0.001
8112428	CD180	*CD180 molecule*	5.60	0.018
8169061	PLP1	*Proteolipid protein 1*	5.58	0.010
7914342	FABP3	*Fatty acid binding protein 3*	5.56	0.012
7939215	KIAA1549L	*KIAA1549-like*	5.51	0.020
8121838	TPD52L1	*Tumor protein D52-like 1*	5.50	0.014
7950473	ARRB1	*Arrestin, beta 1*	5.50	0.010
8180266	ST6GALNAC5	*ST6-N-acetylgalactosaminide α-2,6-sialyltransferase 5*	5.49	0.004
7990545	CSPG4	*Chondroitin sulfate proteoglycan 4*	5.40	0.022
8178193	HLA-DRA	*Major histocompatibility complex, class II, DR α*	5.37	0.002
8057803	TMEFF2	*Tsm protein with EGF-like and two follistatin-like domains 2*	5.31	0.002
7950899	RAB38	*RAB38, member RAS oncogene family*	5.30	0.008
7902441	ST6GALNAC5	*ST6-N-acetylgalactosaminide α-2,6-sialyltransferase 5*	5.20	0.005
8154381	LURAP1L	*Leucine rich adaptor protein 1-like*	5.17	0.005
8163002	KLF4	*Kruppel-like factor 4 (gut)*	5.17	0.003
8033257	C3	*Complement component 3*	5.15	0.008
8040238	HPCAL1	*Hippocalcin-like 1*	5.14	0.007
8059279	EPHA4	*EPH receptor A4*	5.01	0.035
8007100	IGFBP4	*Insulin-like growth factor binding protein 4*	4.93	0.008
8180308	HMGA1	*High mobility group AT-hook 1*	4.92	0.012
8169378	RGAG1	*Retrotransposon gag domain containing 1*	4.83	0.009
7938702	NCR3LG1	*Natural killer cell cytotoxicity receptor 3 ligand 1*	4.77	0.001
8180307	HMGA1	*High mobility group AT-hook 1*	4.75	0.015
8121087	PM20D2	*Peptidase M20 domain containing 2*	4.71	0.008
8102468	PRSS12	*Protease, serine, 12 (neurotrypsin, motopsin)*	4.71	0.004
8131666	ITGB8	*Integrin, beta 8*	4.71	0.006
8083594	PTX3	*Pentraxin 3, long*	4.69	0.030
7956046	DGKA	*Diacylglycerol kinase, α 80kda*	4.64	0.023
8169898	RAB33A	*RAB33A, member RAS oncogene family*	4.63	0.009
8105302	FST	*Follistatin*	4.60	0.021
7983512	SQRDL	*Sulfide quinone reductase-like (yeast)*	4.52	0.010
8169389	PAK3	*P21 protein (Cdc42/Rac)-activated kinase 3*	4.50	0.041
8172220	NDP	*Norrie disease (pseudoglioma)*	4.50	0.008
7967544	SCARB1	*Scavenger receptor class B, member 1*	4.50	0.006
7928695	FAM213A	*Family with sequence similarity 213, member A*	4.49	0.003

Annex 2: List of genes differentially expressed in unirradiated PG35s versus PG35 (continued)

Affymetrix gene ID	Gene symbol	Gene name	R-fold	NOM *p*-value
8179481	HLA-DRA	*Major histocompatibility complex, class II, DR α*	4.47	0.003
8067409	LAMA5	*Laminin, α 5*	4.33	0.005
7927631	DKK1	*Dickkopf 1 homolog (Xenopus laevis)*	4.29	0.013
8114991	SH3TC2	*SH3 domain and tetratricopeptide repeats 2*	4.29	0.005
8172471	PIM2	*Pim-2 oncogene*	4.27	0.000
7899534	EPB41	*Erythrocyte membrane protein band 4.1*	4.24	0.002
8178802	HLA-DRB3	*Major histocompatibility complex, class II, DR beta 3*	4.23	0.007
7936856	CHST15	*Carbohydrate sulfotransferase 15*	4.23	0.004
8015268	KRT34	*Keratin 34*	4.19	0.047
8118548	HLA-DRA	*Major histocompatibility complex, class II, DR α*	4.16	0.004
8072382	OSBP2	*Oxysterol binding protein 2*	4.15	0.037
8103226	TMEM154	*Transmembrane protein 154*	4.13	0.000
8015179	KRTAP1-5	*Keratin associated protein 1-5*	4.10	0.020
8019588	KRTAP1-5	*Keratin associated protein 1-5*	4.10	0.020
8045688	TNFAIP6	*Tumor necrosis factor, α-induced protein 6*	4.05	0.018
7906919	RGS4	*Regulator of G-protein signaling 4*	4.05	0.044
7983239	CKMT1A	*Creatine kinase, mitochondrial 1A*	4.00	0.003
7983256	CKMT1A	*Creatine kinase, mitochondrial 1A*	4.00	0.003
8122150	EYA4	*Eyes absent homolog 4 (Drosophila)*	0.06	0.000
8148435	WISP1	*WNT1 inducible signaling pathway protein 1*	0.06	0.001
8078330	RBMS3	*RNA binding motif, single stranded interacting protein 3*	0.06	0.002
8052355	EFEMP1	*EGF containing fibulin-like extracellular matrix protein 1*	0.05	0.003
7962375	PRICKLE1	*Prickle homolog 1 (Drosophila)*	0.05	0.002
8170538	GABRQ	*Gamma-aminobutyric acid (GABA) A receptor, theta*	0.05	0.001
8082965	MRAS	*Muscle RAS oncogene homolog*	0.05	0.002
8068671	BACE2	*Beta-site APP-cleaving enzyme 2*	0.05	0.005
8176375	RPS4Y1	*Ribosomal protein S4, Y-linked 1*	0.04	0.003
7970954	DCLK1	*Doublecortin-like kinase 1*	0.04	0.001
7908204	HMCN1	*Hemicentin 1*	0.04	0.000
7927681	BICC1	*Bicaudal C homolog 1 (Drosophila)*	0.04	0.000
8046086	CERS6	*Ceramide synthase 6*	0.04	0.002
8103254	SFRP2	*Secreted frizzled-related protein 2*	0.04	0.000
8127563	COL12A1	*Collagen, type XII, α 1*	0.04	0.000
8031646	LOC100288114	*Hypothetical LOC100288114*	0.04	0.003
8081838	ARHGAP31	*Rho gtpase activating protein 31*	0.03	0.012
7964834	CPM	*Carboxypeptidase M*	0.03	0.001
8175217	GPC4	*Glypican 4*	0.03	0.001
8175696	GABRA3	*Gamma-aminobutyric acid (GABA) A receptor, α 3*	0.02	0.001
8001800	CDH11	*Cadherin 11, type 2, OB-cadherin (osteoblast)*	0.02	0.000
7965403	LUM	*Lumican*	0.01	0.000

Annex 2: List of genes differentially expressed in unirradiated PG35s versus PG35 (continued)

Annex 3: References of reagent and kits employ

REAGENT	REFERENCE	COMPANY
500 ml filter 0.2 µm	83.1823.101	Sarstedt
ACK	10-548E	Lonza
Acrylamide 19:1	A3658	AppliChem
AmpliTaq Gold®	4311814	Applied Biosystems
Apo-Transferrin	T2252	Sigma-Aldrich
bFGF	100-18B	PrepoTech
BSA	A9418	Sigma-Aldrich
Cell Strainer 70 µm	352350	BD Falcon
Collagenase I	C0130	Sigma-Aldrich
Complete	1697498	Roche
Cysteine	C7352	Sigma-Aldrich
DAB+ Chromogen	K5007	Dako
Dako REAL™	S2022	Dako
DMEM/F12	32500035	Invitrogen
DNase I	1284932	Roche
DNase I, RNase-free	EN0521	Thermo-Scientific
dNTPs (10 mM)	N8080260	Applied Biosystems
DRAQ5	DR05500	Biostatus
EGF	AF-100-15	PrepoTech
EZ DNA Methylation-	D5006	Zymo Research
Fluoroshield	F6182	Sigma-Aldrich
Glycogen type III	G8876	Sigma-Aldrich

REAGENT	REFERENCE	COMPANY
Heparin	H3393	Sigma-Aldrich
Hepes 1M	15630-056	Invitrogen
Hi-Di™ Formamide	4311320	Applied Biosystems
Insulin	I1882	Sigma-Aldrich
LIZ GeneScan 500	4322679	Applied Biosystems
MyTaq™ HS Mix	BIO-25045	Bioline
$NaHCO_3$	25080-060	Invitrogen
Normal Goat Serum	16210064	Invitrogen
o-Dianisidine (ODD)	D3252	Sigma-Aldrich
Papain	PAPL	Worthington
Pepstatin A	A2205	AppliChem
PGO enzymes	P7119	Sigma-Aldrich
PhosSTOP	04906845001	Roche
Plasmocin	ant-mpt	InvivoGen
Polybrene	107689	Sigma-Aldrich
Progesterone	P8783	Sigma-Aldrich
Puromycin	P8833	Sigma-Aldrich
Putrescine	P5780	Sigma-Aldrich
RNase A	A3832.0250	AppliChem
Selenium	S5261	Sigma-Aldrich
Sodium L-lactate	L7022	Sigma-Aldrich
Trisure	BIO-38033	Bioline

BIBLIOGRAPHY

Aggarwal B, Sung B and Gupta SC (2014). *Inflammation and Cancer* (Vol. 816). Springer Basel.

Aldape KD, Zadeh G, Mansouri S, Reifenberger G and von Deimling A (2015). Glioblastoma: pathology, molecular mechanisms and markers. *Acta Neuropathologica*, 129(6), 829–848.

Allen RG and Tresini M (2000). Oxidative stress and gene regulation. *Free Radical Biology and Medicine*, 28(3), 463–499.

Altman D, Atkinson D and Brat DJ (2007). Glioblastoma Multiforme. *Radiographics*, 27(3), 883–888.

Alvarez-Buylla A, Seri B and Doetsch F (2002). Identification of neural stem cells in the adult vertebrate brain. *Brain Research Bulletin*, 57(6), 751–758.

Anido J, Sáez-Borderías A, Gonzàlez-Juncà A, Rodón L, Folch G, Carmona M a, Prieto-Sánchez RM, Barba I, Martínez-Sáez E, … Seoane J (2010). TGF-β Receptor Inhibitors Target the CD44(high)/Id1(high) Glioma-Initiating Cell Population in Human Glioblastoma. *Cancer Cell*, 18(6), 655–668.

Astrahan M (2008). Some implications of linear-quadratic-linear radiation dose-response with regard to hypofractionation. *Medical Physics*, 35(9), 4161–4172.

Atun R, Jaffray DA, Barton MB, Bray F, Baumann M, Vikram B, Hanna TP, Knaul FM, Lievens Y, … Gospodarowicz M (2015). Expanding global access to radiotherapy. *The Lancet Oncology*, 16(10), 1153–1186.

Azare J, Leslie K, Al-Ahmadie H, Gerald W, Weinreb PH, Violette SM and Bromberg J (2007). Constitutively activated Stat3 induces tumorigenesis and enhances cell motility of prostate epithelial cells through integrin beta 6. *Molecular and Cellular Biology*, 27(12), 4444–4453.

Azzam EI, Jay-Gerin JP and Pain D (2012). Ionizing radiation-induced metabolic oxidative stress and prolonged cell injury. *Cancer Letters*, 327(1-2), 48–60.

Bao S, Wu Q, McLendon RE, Hao Y, Shi Q, Hjelmeland AB, Dewhirst MW, Bigner DD and Rich JN (2006). Glioma stem cells promote radioresistance by preferential activation of the DNA damage response. *Nature*, 444(7120), 756–760.

Barendsen GW (1997). Parameters of linear-quadratic radiation dose-effect relationships: dependence on LET and mechanisms of reproductive cell death. *International Journal Radiologiy Biology*, 71(6), 649 – 655.

Baumann M, Krause M and Hill R (2008). Exploring the role of cancer stem cells in radioresistance. *Nature Reviews. Cancer*, 8(7), 545–554.

Beier D, Hau P, Proescholdt M, Lohmeier A, Wischhusen J, Oefner PJ, Aigner L, Brawanski A, Bogdahn U and Beier CP (2007). CD133+ and CD133- glioblastoma-derived cancer stem cells show differential growth characteristics and molecular profiles. *Cancer Research*, 67(9), 4010–4015.

Beier D, Schulz JB and Beier CP (2011). Chemoresistance of glioblastoma cancer stem cells - much more complex than expected. *Molecular Cancer*, 10(1), e128.

Bellail AC, Hunter SB, Brat DJ, Tan C and Van Meir EG (2004). Microregional extracellular matrix heterogeneity in brain modulates glioma cell invasion. *International Journal of Biochemistry and Cell Biology*, 36(6), 1046–1069.

Bernstock J, Verheyen J, Huang B, Hallenbeck J and Pluchino S (2014). Typical and Atypical Stem Cell Niches of the Adult Nervous System in Health and Inflammatory Brain and Spinal Cord Diseases. In S. Wislet-Gendebien (Ed.), *Adult Stem Cell Niches* (pp. 211–288). InTech.

Bhat KPL, Balasubramaniyan V, Vaillant B, Ezhilarasan R, Hummelink K, Hollingsworth F, Wani K, Heathcock L, James JD, … Aldape K (2013). Mesenchymal Differentiation Mediated by NF-κB Promotes Radiation Resistance in Glioblastoma. *Cancer Cell*, 24(3), 331–346.

Bouwman P and Jonkers J (2012). The effects of deregulated DNA damage signalling on cancer chemotherapy response and resistance. *Nature Reviews Cancer*, 12(9), 587–598.

Braunstein S, Badura ML, Xi Q, Formenti SC and Schneider RJ (2009). Regulation of protein synthesis by ionizing radiation. *Molecular and Cellular Biology*, 29(21), 5645–5656.

Bredel M, Bredel C, Juric D, Harsh GR, Vogel H, Recht LD and Sikic BI (2005). Functional network analysis reveals extended gliomagenesis pathway maps and three novel MYC-interacting genes in human gliomas. *Cancer Research*, 65(19), 8679–8689.

Brell M, Tortosa A, Verger E, Gil JM, Viñolas N, Villá S, Acebes J-J, Caral L, Pujol T, … Graus F (2005). Prognostic Significance of O6-Methylguanine-DNA Methyltransferase Determined by Promoter Hypermethylation and Immunohistochemical Expression in Anaplastic Gliomas. *Clinical Cancer Research*, 11(14), 5167–5174.

Brennan CW, Verhaak RGW, McKenna A, Campos B, Noushmehr H, Salama SR, Zheng S, Chakravarty D, Sanborn JZ, … TCGA network (2013). The Somatic Genomic Landscape of Glioblastoma. *Cell*, 155(2), 462–477.

Brenner DJ (2008). The linear-quadratic model is an appropriate methodology for determining isoeffective doses at large doses per fraction. *Seminars in Radiation Oncology*, 18(4), 234–239.

Brescia P, Richichi C and Pelicci G (2012). Current strategies for identification of glioma stem cells: adequate or unsatisfactory? *Journal of Oncology*, 2012, e376894.

Brewer G, Torricelli J, Evege E and Price P (1993). Optimized survival of hippocampal neurons in B27-supplemented neurobasal^{TM}, a new serum-free medium combination. *Journal of Neuroscience Research*, 35(5), 567–576.

Bulat T, Keta O, Korićanac L and Žakula J (2016). Radiation dose determines the method for quantification of DNA double strand breaks. *Annals of the Brazilian Academy of Sciences*, 88(1), 127–136.

Buzzai M, Bauer DE, Jones RG, Deberardinis RJ, Hatzivassiliou G, Elstrom RL and Thompson CB (2005). The glucose dependence of Akt-transformed cells can be reversed by pharmacologic activation of fatty acid beta-oxidation. *Oncogene*, 24(26), 4165–4173.

Campos B and Herold-Mende CC (2011). Insight into the complex regulation of CD133 in glioma. *International Journal of Cancer*, 128(3), 501–510.

Cankovic M, Mikkelsen T, Rosenblum ML and Zarbo RJ (2007). A simplified laboratory validated assay for MGMT promoter hypermethylation analysis of glioma specimens from formalin-fixed paraffin-embedded tissue. *Laboratory Investigation*, 87(4), 392–397.

Carro MS, Lim WK, Alvarez MJ, Bollo RJ, Zhao X, Snyder EY, Sulman EP, Anne SL, Doetsch F, … Iavarone A (2010). The transcriptional network for mesenchymal transformation of brain tumours. *Nature*, 463(7279), 318–325.

Cerami E, Gao J, Dogrusoz U, Gross BE, Sumer SO, Aksoy BA, Jacobsen A, Byrne CJ, Heuer ML, … Schultz N (2012). The cBio Cancer Genomics Portal: An open platform for exploring multidimensional cancer genomics data. *Cancer Discovery*, 2(5), 401–404.

Chapman JD (2003). Single-hit mechanism of tumour cell killing by radiation. *International Journal of*

Radiation Biology, 79(2), 71–81.

Chapman JR, Taylor MRG and Boulton SJ (2012). Playing the End Game: DNA Double-Strand Break Repair Pathway Choice. *Molecular Cell*, 47(4), 497–510.

Charles NA, Holland EC, Gilbertson R, Glass R and Kettenmann H (2011). The brain tumor microenvironment. *Glia*, 59(8), 1169–1180.

Chen R, Nishimura MC, Bumbaca SM, Kharbanda S, Forrest WF, Kasman IM, Greve JM, Soriano RH, Gilmour LL, … Phillips HS (2010). A Hierarchy of Self-Renewing Tumor-Initiating Cell Types in Glioblastoma. *Cancer Cell*, 17(4), 362–375.

Chen Y-D, Feng J, Fang T, Yang M, Qui X and Jiang T (2013). Effect of intensity-modulated radiotherapy versus three-dimensional conformal radiotherapy on clinical outcomes in patients with glioblastoma multiforme. *Chinese Medical Journal*, 126(12), 2320–2324.

Cheng L, Wu Q, Huang Z, Guryanova OA, Huang Q, Shou W, Rich JN and Bao S (2011). L1CAM regulates DNA damage checkpoint response of glioblastoma stem cells through NBS1. *The EMBO Journal*, 30(5), 800–813.

Ciccia A and Elledge SJ (2010). The DNA Damage Response: Making It Safe to Play with Knives. *Molecular Cell*, 40(2), 179–204.

Clarke J, Butowski N and Chang S (2010). Recent Advances in Therapy for Glioblastoma. *Archives of Neurology*, 67(3), 279–283.

Clement V, Sanchez P, de Tribolet N, Radovanovic I, Ruiz i Altaba A, Tribolet N De, Radovanovic I and Ruiz A (2007). HEDGEHOG-GLI1 signaling regulates human glioma growth, cancer stem cell self-renewal, and tumorigenicity. *Current Biology*, 17(2), 165–172.

Clevers H (2011). The cancer stem cell: premises, promises and challenges. *Nature Medicine*, 17(3), 313–319.

Colman H, Zhang L, Sulman EP, McDonald J, Shooshtari NL, Rivera A, Popoff S, Nutt CL, Louis DN, … Aldape KD (2010). A multigene predictor of outcome in glioblastoma. *Neuro-Oncology*, 12(1), 49–57.

Colomiere M, Findlay J, Ackland L and Ahmed N (2009). Epidermal growth factor-induced ovarian carcinoma cell migration is associated with JAK2/STAT3 signals and changes in the abundance and localization of α6β1 integrin. *International Journal of Biochemistry and Cell Biology*, 41(5), 1034–1045.

Cordes N, Seidler J, Durzok R, Geinitz H and Brakebusch C (2006). Beta1-Integrin-Mediated Signaling Essentially Contributes To Cell Survival After Radiation-Induced Genotoxic Injury. *Oncogene*, 25(9), 1378–1390.

Craft JM and Hallahan DE (2012). Towards novel radiosensitizing agents: the role of cytosolic PLA2α in combined modality cancer therapy. *Future Medicinal Chemistry*, 3(7), 835–843.

Croft D, Mundo AF, Haw R, Milacic M, Weiser J, Wu G, Caudy M, Garapati P, Gillespie M, … D'Eustachio P (2014). The Reactome pathway knowledgebase. *Nucleic Acids Research*, 42(D1), 481–487.

D'Andrea FP, Safwat A, Kassem M, Gautier L, Overgaard J and Horsman MR (2011). Cancer stem cell overexpression of nicotinamide N-methyltransferase enhances cellular radiation resistance. *Radiotherapy and Oncology*, 99(3), 373–378.

De Llobet LI, Baro M, Figueras A, Modolell I, Da Silva M V., Muñoz P, Navarro A, Mesia R and Balart J (2013). Development and characterization of an isogenic cell line with a radioresistant phenotype. *Clinical and Translational Oncology*, 15(3), 189–197.

Delgado-López PD and Corrales-García EM (2016). Survival in glioblastoma: a review on the impact of treatment modalities. *Clinical and Translational Oncology*, [Epub ahea, 1–10.

Desgrosellier JS and Cheresh DA (2010). Integrins in cancer: biological implications and therapeutic opportunities. *Nature Reviews: Cancer*, 10(1), 9–22.

Dexheimer TS (2013). DNA Repair Pathways and Mechanisms. In *DNA Repair of Cancer Stem Cells* (pp. 19–32)

Dick JE (2008). Stem cell concepts renew cancer research. *Blood*, 112(13), 4793–4807.

Diehn M, Cho RW, Lobo NA, Kalisky T, Dorie MJ, Kulp AN, Qian D, Lam JS, Ailles LE, … Clarke MF (2009). Association of reactive oxygen species levels and radioresistance in cancer stem cells. *Nature*, 458(7239), 780–783.

Duluc D, Delneste Y, Tan F, Moles MP, Grimaud L, Lenoir J, Preisser L, Anegon I, Catala L, … Jeannin P (2007). Tumor-associated leukemia inhibitory factor and IL-6 skew monocyte differentiation into tumor-associated macrophage-like cells. *Blood*, 110(13), 4319–4330.

Eden E, Navon R, Steinfeld I, Lipson D and Yakhini Z (2009). GOrilla: a tool for discovery and visualization of enriched GO terms in ranked gene lists. *BMC Bioinformatics*, 10, e48.

Elinav E, Nowarski R, Thaiss CA, Hu B, Jin C and Flavell RA (2013). Inflammation-induced cancer: crosstalk between tumours, immune cells and microorganisms. *Nature Reviews. Cancer*, 13(11), 759–771.

Eljamel S (2015). 5-ALA fluorescence image guided resection of glioblastoma multiforme: A meta-analysis of the literature. *International Journal of Molecular Sciences*, 16(5), 10443–10456.

Ellis SJ and Tanentzapf G (2010). Integrin-mediated adhesion and stem-cell-niche interactions. *Cell and Tissue Research*, 339(1), 121–130.

Elstrom RL, Bauer DE, Buzzai M, Karnauskas R, Harris MH, Plas DR, Zhuang H, Cinalli RM, Alavi A, … Thompson CB (2004). Akt stimultes aerobic glycolysis in cancer cells. *Cancer Research*, 64(11), 3892–3899.

Emami B, Woloschak G and Small WJ (2015). Beyond the linear quadratic model : intraoperative radiotherapy and normal tissue tolerance. *Translational Cancer Research*, 4(2), 140–147.

Engler JR, Robinson AE, Smirnov I, Hodgson JG, Berger MS, Gupta N, James CD, Molinaro A and Phillips JJ (2012). Increased microglia/macrophage gene expression in a subset of adult and pediatric astrocytomas. *PLoS ONE*, 7(8), e43339.

Esteller M, Hamilton SR, Burger PC, Baylin SB and Herman JG (1999). Advances in Brief Inactivation of the DNA Repair Gene O6-Methylguanine-DNA Methyltransferase by Promoter Hypermethylation is a Common Event in Primary Human Neoplasia. *Cancer Research*, 59(4), 793–797.

Fabregat A, Sidiropoulos K, Garapati P, Gillespie M, Hausmann K, Haw R, Jassal B, Jupe S, Korninger F, … D'Eustachio P (2016). The Reactome pathway Knowledgebase. *Nucleic Acids Research*, 44(D1), D481–D487.

Fidoamore A, Cristiano L, Antonosante A, D'Angelo M, Di Giacomo E, Astarita C, Giordano A, Ippoliti R, Benedetti E and Cimini A (2016). Glioblastoma stem cells microenvironment: The paracrine roles of the niche in drug and radioresistance. *Stem Cells International*, 2016, e6809105.

Flavahan W a, Wu Q, Hitomi M, Rahim N, Kim Y, Sloan AE, Weil RJ, Nakano I, Sarkaria JN, … Hjelmeland AB (2013). Brain tumor initiating cells adapt to restricted nutrition through preferential glucose uptake.

Nature Neuroscience, 16(10), 1373–1382.

Fortunel NO, Otu HH, Ng H-H and Chen J (2003). Comment on "'Stemness": Transcriptional Profiling of Embryonic and Adult Stem Cells " and " A Stem Cell Molecular signature". *Science*, 302(5644), 393b.

Fouse SD, Nakamura JL, James CD, Chang S and Costello JF (2014). Response of primary glioblastoma cells to therapy is patient specific and independent of cancer stem cell phenotype. *Neuro-Oncology*, 16(3), 361–371.

Fowler J (2006). Practical time-dose evaluations, or how to stop worrying and learn to love linear quadratics. In L. W. Brady, H.-P. Heilmann & M. Molls (Eds.), *Technical Basis of Radiation Therapy* (4th ed., pp. 3–50). Heidel: Springer.

Franken N, Rodermond HM, Stap J, Haveman J and van Bree C (2006). Clonogenic assay of cells in vitro. *Nature Protocols*, 1(5), 2315–2319.

Franken N, van Bree C, ten Cate R, van Oven CH and Haveman J (2002). Importance of TP53 and RB in the repair of potentially lethal damage and induction of color junctions after exposure to ionizing radiation. *Radiation Research*, 158(6), 707–714.

Frey B, Hehlgans S, Rödel F and Gaipl US (2015). Modulation of inflammation by low and high doses of ionizing radiation: Implications for benign and malign diseases. *Cancer Letters*, 368(2), 230–237.

Fuller CD, Choi M, Forthuber B, Wang SJ, Rajagiriyil N, Salter BJ and Fuss M (2007). Standard fractionation intensity modulated radiation therapy (IMRT) of primary and recurrent glioblastoma multiforme. *Radiation Oncology*, 2, e26.

Galdzicki M, Clancy KP, Oberortner E, Pocock M, Quinn JY, Rodriguez CA, Roehner N, M, Wilson ML, … Sauro HM (2014). The Synthetic Biology Open Language (SBOL) provides a community standard for communicating designs in synthetic biology. *Nature Biotechnology*, 32(6), 545–550.

Galli R, Binda E, Orfanelli U, Cipelletti B, Gritti A, De Vitis S, Fiocco R, Foroni C, Dimeco F and Vescovi A (2004). Isolation and characterization of tumorigenic, stem-like neural precursors from human glioblastoma. *Cancer Research*, 64(19), 7011–7021.

Gambaletta D, Marchetti A, Benedetti L, Mercurio AM, Sacchi A and Falcioni R (2000). Cooperative signaling between α6β4 integrin and ErbB-2 receptor is required to promote phosphatidylinositol 3-kinase-dependent invasion. *Journal of Biological Chemistry*, 275(14), 10604–10610.

Gao J, Aksoy BA, Dogrusoz U, Dresdner G, Gross B, Sumer SO, Sun Y, Jacobsen A, Sinha R, … Schultz N (2013). Integrative analysis of complex cancer genomics and clinical profiles using the cBioPortal. *Science Signaling*, 6(269), pl1.

Gerweck LE and Wakimoto H (2016). At the Crossroads of Cancer Stem Cells, Radiation Biology, and Radiation Oncology. *Cancer Research*, 76(5), 994–998.

Gilbertson RJ and Rich JN (2007). Making a tumour's bed: glioblastoma stem cells and the vascular niche. *Nature Reviews. Cancer*, 7(10), 733–736.

Gritti A, Parati E, Cova L, Frolichsthal P, Galli R, Wanke E, Faravelli L, Morassutti D, Roisen F, … Vescovi AL (1996). Multipotential Stem Cells from the Adult Mouse and Self-Renew in Response to Basic Fibroblast. *The Journal of Neuroscience*, 16(3), 1091–1100.

Guo W and Giancotti FG (2004). Integrin signalling during tumour progression. *Nature Reviews. Molecular Cell Biology*, 5(10), 816–826.

Hakem R (2008). DNA-damage repair; the good, the bad, and the ugly. *The EMBO Journal*, 27(4), 589–605.

Halliday J, Helmy K, Pattwell SS, Pitter KL, LaPlant Q, Ozawa T and Holland EC (2014). In vivo radiation response of proneural glioma characterized by protective p53 transcriptional program and proneural-mesenchymal shift. *Proceedings of the National Academy of Sciences of the United States of America*, 111(14), 5248–5253.

Hamada N, Matsumoto H, Hara T and Kobayashi Y (2007). Intercellular and intracellular signaling pathways mediating ionizing radiation-induced bystander effects. *Journal of Radiation Research*, 48(2), 87–95.

Hambardzumyan D and Bergers G (2015). Glioblastoma: Defining Tumor Niches. *Trends in Cancer*, 1(4), 252–265.

Heddleston JM, Hitomi M, Venere M, Flavahan WA, Yang K, Kim Y, Minhas S, Rich JN and Hjelmeland AB (2011). Glioma stem cell maintenance: the role of the microenvironment. *Current Pharmaceutical Design*, 17(23), 2386–2401.

Hei TK, Zhou H, Ivanov VN, Hong M, Lieberman HB, Brenner DJ, Amundson SA and Geard CR (2008). Mechanism of radiation-induced bystander effects: a unifying model. *The Journal of Pharmacy and Pharmacology*, 60(8), 943–950.

Heiden MG Vander, Cantley LC and Thompson CB (2009). Understanding the Warburg Effect : The Metabolic Requirements of Cell Proliferation. *Science*, 324(5930), 1029–1033.

Heinrich PC, Behrmann I, Haan S, Hermanns HM, Müller-Newen G and Schaper F (2003). Principles of interleukin (IL)-6-type cytokine signalling and its regulation. *The Biochemical Journal*, 374, 1–20.

Hemmati HD, Nakano I, Lazareff J a, Masterman-Smith M, Geschwind DH, Bronner-Fraser M and Kornblum HI (2003). Cancerous stem cells can arise from pediatric brain tumors. *Proceedings of the National Academy of Sciences of the United States of America*, 100(25), 15178–15183.

Herman JG, Graff JR, Myohanen S, Nelkin BD and Baylin SB (1996). Methylation-specific PCR: a novel PCR assay for methylation status of CpG islands. *Proceedings of the National Academy of Sciences*, 93(18), 9821–9826.

Herrlich P and Böhmer FD (2000). Redox regulation of signal transduction in mammalian cells. *Biochemical Pharmacology*, 59(1), 35–41.

Heusinkveld M, de Vos van Steenwijk PJ, Goedemans R, Ramwadhdoebe TH, Gorter A, Welters MJ, van Hall T and van der Burg SH (2011). M2 macrophages induced by prostaglandin E2 and IL-6 from cervical carcinoma are switched to activated M1 macrophages by CD4+ Th1 cells. *The Journal of Immunology*, 187(3), 1157–1165.

Hochberg F and Pruitt A (1980). Assumptions in the radiotherapy of glioblastoma. *Neurology*, 30(9), 907–911.

Hopewell JW and Wright EA (1969). The importance of implantation site in cerebral carcinogenesis in rats. *Cancer Research*, 29(11), 1927–1931.

Hu Y and Smyth GK (2009). ELDA: extreme limiting dilution analysis for comparing depleted and enriched populations in stem cell and other assays. *Journal of Immunological Methods*, 347(1-2), 70–78.

Huang DW, Lempicki R a and Sherman BT (2009). Systematic and integrative analysis of large gene lists using DAVID bioinformatics resources. *Nature Protocols*, 4(1), 44–57.

Huang G, Yan H, Ye S, Tong C and Ying Q-L (2014). STAT3 Phosphorylation at Tyrosine 705 and Serine 727

Differentially Regulates Mouse ESC Fates. *Stem Cells*, 32(5), 1149–1160.

Ivanov VN and Hei TK (2014). Radiation-induced glioblastoma signaling cascade regulates viability, apoptosis and differentiation of neural stem cells (NSC). *Apoptosis*, 19(12), 1736–1754.

Jamal M, Rath BH, Tsang PS, Camphausen K and Tofilon PJ (2012). The brain microenvironment preferentially enhances the radioresistance of CD133(+) glioblastoma stem-like cells. *Neoplasia*, 14(2), 150–158.

Javle M and Curtin NJ (2011). The role of PARP in DNA repair and its therapeutic exploitation. *British Journal of Cancer*, 105(8), 1114–1122.

Johnson BE, Mazor T, Hong C, Barnes M, Aihara K, McLean C, Fouse SD, Yamamoto S, Ueda H, … Costello JF (2014). Mutational Analysis Reveals the Origin and Therapy-driven Evolution of Recurrent Glioma. *Science*, 343(6167), 189–193.

Joo KM, Kim SY, Jin X, Song SY, Kong D-S, Lee J-I, Jeon JW, Kim MH, Kang BG, … Nam D-H (2008). Clinical and biological implications of CD133-positive and CD133-negative cells in glioblastomas. *Laboratory Investigation*, 88(8), 808–815.

Kakarougkas A and Jeggo PA (2014). DNA DSB repair pathway choice: An orchestrated handover mechanism. *British Journal of Radiology*, 87(1035), e20130685.

Kanehisa M, Goto S, Sato Y, Furumichi M and Tanabe M (2012). KEGG for integration and interpretation of large-scale molecular data sets. *Nucleic Acids Research*, 40(D1), 109–114.

Kassem HS, Sangar V, Cowan R, Clarke N and Margison GP (2002). A potential role of heat shock proteins and nicotinamide N-methyl transferase in predicting response to radiation in bladder cancer. *International Journal of Cancer.*, 101(5), 454–460.

Kemper K, Sprick MR, De Bree M, Scopelliti A, Vermeulen L, Hoek M, Zeilstra J, Pals ST, Mehmet H, … Medema JP (2010). The AC133 epitope, but not the CD133 protein, is lost upon cancer stem cell differentiation. *Cancer Research*, 70(2), 719–729.

Kesanakurti D, Chetty C, Rajasekhar Maddirela D, Gujrati M and Rao JS (2013). Essential role of cooperative NF-κB and Stat3 recruitment to ICAM-1 intronic consensus elements in the regulation of radiation-induced invasion and migration in glioma. *Oncogene*, 32(43), 5144–5155.

Kim JE, Patel M, Ruzevick J, Jackson CM and Lim M (2014). STAT3 activation in glioblastoma: Biochemical and therapeutic implications. *Cancers*, 6(1), 376–395.

Korotchkina LG and Patel MS (2001). Probing the Mechanism of Inactivation of Human Pyruvate Dehydrogenase by Phosphorylation of Three Sites. *The Journal of Biological Chemistry*, 276(8), 5731–5738.

Kreth S, Heyn J, Grau S, Kretzschmar HA, Egensperger R and Kreth FW (2010). Identification of valid endogenous control genes for determining gene expression in human glioma. *Neuro-Oncology*, 12(6), 570–579.

Krex D, Klink B, Hartmann C, Von Deimling A, Pietsch T, Simon M, Sabel M, Steinbach JP, Heese O, … Schackert G (2007). Long-term survival with glioblastoma multiforme. *Brain*, 130(10), 2596–2606.

Kuwano T, Nakao S, Yamamoto H, Tsuneyoshi M, Yamamoto T, Kuwano M and Ono M (2004). Cyclooxygenase 2 is a key enzyme for inflammatory cytokine-induced angiogenesis. *FASEB Journal*, 18(2), 300–310.

Lal A, Lash AE, Altschul SF, Velculescu V, Zhang L, Mclendon RE, Marra MA, Prange C, Morin PJ, … Riggins GJ (1999). A Public Database for Gene Expression in Human Cancers. *Cancer Research*, 59(21), 5403–5407.

Laperriere N, Zuraw L, Cairncross G, Cancer T and Ontario C (2002). Radiotherapy for newly diagnosed malignant glioma in adults: a systematic review. *Radiotherapy and Oncology*, 64(3), 259–273.

Lathia JD, Gallagher J, Heddleston JM, Wang J, Eyler CE, Macswords J, Wu Q, Vasanji A, McLendon RE, … Rich JN (2010). Integrin alpha 6 regulates glioblastoma stem cells. *Cell Stem Cell*, 6(5), 421–432.

Lee J, Kotliarova S, Kotliarov Y, Li A, Su Q, Donin NM, Pastorino S, Purow BW, Christopher N, … Fine H (2006). Tumor stem cells derived from glioblastomas cultured in bFGF and EGF more closely mirror the phenotype and genotype of primary tumors than do serum-cultured cell lines. *Cancer Cell*, 9(5), 391–403.

Lee SW, Fraass BA, Marsh LH, Herbort K, Gebarski SS, Martel MK, Radany EH, Lichter AS and Sandler HM (1999). Patterns of failure following high-dose 3-D conformal radiotherapy for high-grade astrocytomas: A quantitative dosimetric study. *International Journal of Radiation Oncology Biology Physics*, 43(1), 79–88.

Ley K, Laudanna C, Cybulsky MI and Nourshargh S (2007). Getting to the site of inflammation: the leukocyte adhesion cascade updated. *Nature Reviews. Immunology*, 7(9), 678–689.

Li A, Walling J, Kotliarov Y, Steed ME, Ahn SJ, Rosenblum M, Mikkelsen T, Zenklusen JC and Fine HA (2008). Genomic Changes and Gene Expression Profiles Reveal That Established Glioma Cell Lines Are Poorly Representative of Primary Human Gliomas. *Molecular Cancer Research: MCR*, 6(1), 21–31.

Li W and Graeber MB (2012). The molecular profile of microglia under the influence of glioma. *Neuro-Oncology*, 14(8), 958–978.

Liberti M V and Locasale JW (2016). The Warburg Effect: How Does it Benefit Cancer Cells? *Trends in Biochemical Sciences*, 41(3), 211–218.

Liebelt BD, Shingu T, Zhou X, Ren J, Shin SA and Hu J (2016). Glioma Stem Cells: Signaling, Microenvironment, and Therapy. *Stem Cells International*, 2016, e7849890.

Lin GS, Chen YP, Lin Dr ZX, Wang XF, Zheng ZQ and Chen L (2014). STAT3 serine 727 phosphorylation influences clinical outcome in glioblastoma. *International Journal of Clinical and Experimental Pathology*, 7(6), 3141–3149.

Linkous A, Geng L, Lyshchik A, Hallahan DE and Yazlovitskaya EM (2009). Cytosolic phospholipase A2: targeting cancer through the tumor vasculature. *Clinical Cancer Research*, 15(5), 1635–1644.

Linkous A and Yazlovitskaya E (2010). Cytosolic phospholipase A2 as a mediator of disease pathogenesis. *Cellular Microbiology*, 12(10), 1369–1377.

Linkous AG, Yazlovitskaya EM and Hallahan DE (2010). Cytosolic phospholipase a2 and lysophospholipids in tumor angiogenesis. *Journal of the National Cancer Institute*, 102(18), 1398–1412.

Little SE, Popov S, Jury A, Bax DA, Doey L, Al-Sarraj S, Jurgensmeier JM and Jones C (2012). Receptor tyrosine kinase genes amplified in glioblastoma exhibit a mutual exclusivity in variable proportions reflective of individual tumor heterogeneity. *Cancer Research*, 72(7), 1614–1620.

Liu G, Yuan X, Zeng Z, Tunici P, Ng H, Abdulkadir IR, Lu L, Irvin D, Black KL and Yu JS (2006). Analysis of gene expression and chemoresistance of CD133+ cancer stem cells in glioblastoma. *Molecular Cancer*, 5(1), e67.

Locatelli M, Ferrero S, Martinelli Boneschi F, Boiocchi L, Zavanone M, Maria Gaini S, Bello L, Valentino S, Barbati E, … Garlanda C (2013). The long pentraxin PTX3 as a correlate of cancer-related inflammation and prognosis of malignancy in gliomas. *Journal of Neuroimmunology*, 260(1-2), 99–106.

Lomax ME, Folkes LK and O'Neill P (2013). Biological consequences of radiation-induced DNA damage: Relevance to radiotherapy. *Clinical Oncology*, 25(10), 578–585.

Lottaz C, Beier D, Meyer K, Kumar P, Hermann A, Schwarz J, Junker M, Oefner PJ, Bogdahn U, … Beier CP (2010). Transcriptional profiles of CD133+ and CD133- glioblastoma-derived cancer stem cell lines suggest different cells of origin. *Cancer Research*, 70(5), 2030–2040.

Louis DN, Ohgaki H, Wiestler OD and Cavenee WK (2007a). *WHO Classification of Tumours of the Central Nervous System* (4th ed.). Lyon, France: IARC Press.

Louis DN, Ohgaki H, Wiestler OD, Cavenee WK, Burger PC, Jouvet A, Scheithauer B and Kleihues P (2007b). The 2007 WHO classification of tumours of the central nervous system. *Acta Neuropathologica*, 114(2), 97–109.

Louis DN, Perry A, Reifenberger G, von Deimling A, Figarella-Branger D, Cavenee WK, Ohgaki H, Wiestler OD, Kleihues P and Ellison DW (2016). The 2016 World Health Organization Classification of Tumors of the Central Nervous System: a summary. *Acta Neuropathologica*, 131(6), 803–820.

Lü X, De La Peña L, Barker C, Camphausen K and Tofilon PJ (2006). Radiation-induced changes in gene expression involve recruitment of existing messenger RNAs to and away from polysomes. *Cancer Research*, 66(2), 1052–1061.

Ma H-I, Chiou S-H, Hueng D-Y, Tai L-K, Huang P-I, Kao C-L, Chen Y-W and Sytwu H-K (2011). Celecoxib and radioresistant glioblastoma-derived CD133(+) cells: improvement in radiotherapeutic effects. *Journal of Neurosurgery*, 114(3), 651–662.

Mäenpää A, Kovanen PE, Paetau A, Jääskeläinen J and Timonen T (1997). Lymphocyte adhesion molecule ligands and extracellular matrix proteins in gliomas and normal brain: Expression of VCAM-1 in gliomas. *Acta Neuropathologica*, 94(3), 216–225.

Maher EA, Marin-Valencia I, Bachoo RM, Mashimo T, Raisanen J, Hatanpaa KJ, Jindal A, Jeffrey FM, Choi C, … Deberardinis RJ (2012). Metabolism of [U-13C]glucose in human brain tumors in vivo. *NMR in Biomedicine*, 25(11), 1234–1244.

Maier P, Hartmann L, Wenz F and Herskind C (2016). Cellular pathways in response to ionizing radiation and their targetability for tumor radiosensitization. *International Journal of Molecular Sciences*, 17(1)

Mannino M and Chalmers AJ (2011). Radioresistance of glioma stem cells: Intrinsic characteristic or property of the "microenvironment-stem cell unit"? *Molecular Oncology*, 5(4), 374–386.

Mantovani a, Allavena P, Sica A and Balkwill F (2008). Cancer-related inflammation. *Nature*, 454(7203), 444.

Marin-Valencia I, Yang C, Mashimo T, Cho S, Baek H, Yang X-L, Rajagopalan KN, Maddie M, Vemireddy V, … Bachoo RM (2012). Analysis of tumor metabolism reveals mitochondrial glucose oxidation in genetically diverse human glioblastomas in the mouse brain in vivo. *Cell Metabolism*, 15(6), 827–837.

Markert JM, Fuller CM, Gillespie GY, Bubien JK, McLean L a, Hong RL, Lee K, Gullans SR, Mapstone TB and Benos DJ (2001). Differential gene expression profiling in human brain tumors. *Physiological Genomics*, 5(1), 21–33.

McCord AM, Jamal M, Williams ES, Camphausen K and Tofilon PJ (2009). CD133+ glioblastoma stem-like cells are radiosensitive with a defective DNA damage response compared with established cell lines.

Clinical Cancer Research, 15(16), 5145–5153.

Méndez-Lucas A, Hyrossová P, Novellasdemunt L, Viñals F and Perales JC (2014). Mitochondrial phosphoenolpyruvate carboxykinase (PEPCK-M) is a pro-survival, endoplasmic reticulum (ER) stress response gene involved in tumor cell adaptation to nutrient availability. *Journal of Biological Chemistry*, 289(32), 22090–22102.

Miao L, Holley AK, Zhao Y, St Clair WH and St Clair DK (2014). Redox-mediated and ionizing-radiation-induced inflammatory mediators in prostate cancer development and treatment. *Antioxidants & Redox Signaling*, 20(9), 1481–1500.

Miraglia S, Godfrey W, Yin a H, Atkins K, Warnke R, Holden JT, Bray R a, Waller EK and Buck DW (1997). A novel five-transmembrane hematopoietic stem cell antigen: isolation, characterization, and molecular cloning. *Blood*, 90(12), 5013–5021.

Mladenov E and Iliakis G (2011). Induction and repair of DNA double strand breaks: The increasing spectrum of non-homologous end joining pathways. *Mutation Research*, 711(1-2), 61–72.

Mootha VK, Lindgren CM, Eriksson K-F, Subramanian A, Sihag S, Lehar J, Puigserver P, Carlsson E, Ridderstråle M, … Groop LC (2003). PGC-1alpha-responsive genes involved in oxidative phosphorylation are coordinately downregulated in human diabetes. *Nature Genetics*, 34(3), 267–273.

Multhoff G and Radons J (2012). Radiation, Inflammation, and Immune Responses in Cancer. *Frontiers in Oncology*, 2, e58.

Nabors LB, Fink KL, Mikkelsen T, Grujicic D, Tarnawski R, Nam DH, Mazurkiewicz M, Salacz M, Ashby L, … Reardon DA (2015). Two cilengitide regimens in combination with standard treatment for patients with newly diagnosed glioblastoma and unmethylated MGMT gene promoter: Results of the open-label, controlled, randomized phase II CORE study. *Neuro-Oncology*, 17(5), 708–717.

Nabors LB, Mikkelsen T, Rosenfeld SS, Hochberg F, Akella NS, Fisher JD, Cloud GA, Zhang Y, Carson K, … Grossman SA (2007). Phase I and correlative biology study of cilengitide in patients with recurrent malignant glioma. *Journal of Clinical Oncology*, 25(13), 1651–1657.

Nakada M, Nakada S, Demuth T, Tran NL, Hoelzinger DB and Berens ME (2007). Molecular targets of glioma invasion. *Cellular and Molecular Life Sciences*, 64(4), 458–478.

Nakamura Y, Sakakibara SI, Miyata T, Ogawa M, Shimazaki T, Weiss S, Kageyama R, Okano H, Shakakibara S, … Okano H (2000). The bHLH gene Hes1 as a repressor of the neuronal commitment of CNS stem cell. *The Journal of Neuroscience*, 20(1), 283–293.

Nakano I (2014). Proneural-mesenchymal transformation of glioma stem cells: do therapies cause evolution of target in glioblastoma? *Future Oncology*, 10(9), 1527–1530.

Noushmehr H, Weisenberger DJ, Diefes K, Phillips HS, Pujara K, Berman BP, Pan F, Pelloski CE, Sulman EP, … Aldape K (2010). Identification of a CpG Island Methylator Phenotype that Defines a Distinct Subgroup of Glioma. *Cancer Cell*, 17(5), 510–522.

Ohgaki H and Kleihues P (2013). The definition of primary and secondary glioblastoma. *Clinical Cancer Research*, 19(4), 764–772.

Ouédraogo ZG, Müller-barthélémy M, Kemeny J, Dedieu V, Biau J, Khalil T, Raoelfils LI, Granzotto A, Pereira B, … Verrelle P (2015). STAT3 Serine 727 Phosphorylation : A Relevant Target to Radiosensitize Human Glioblastoma. *Brain Pathology*, 26(1), 18–30.

Ozawa T, Riester M, Cheng YK, Huse J, Squatrito M, Helmy K, Charles N, Michor F and Holland EC (2014). Most human non-GCIMP glioblastoma subtypes evolve from a common proneural-like precursor glioma. *Cancer Cell*, 26(2), 288–300.

Pagé B, Pagé M and Noel C (1993). A new fluorometric assay for cytotoxic measurements in vitro. *International Journal of Oncology*, 3(3), 473–476.

Pallini R, Ricci-Vitiani L, Banna GL, Signore M, Lombardi D, Todaro M, Stassi G, Martini M, Maira G, … De Maria R (2008). Cancer stem cell analysis and clinical outcome in patients with glioblastoma multiforme. *Clinical Cancer Research*, 14(24), 8205–8212.

Pallini R, Ricci-Vitiani L, Montano N, Mollinari C, Biffoni M, Cenci T, Pierconti F, Martini M, De Maria R and Larocca LM (2011). Expression of the stem cell marker CD133 in recurrent glioblastoma and its value for prognosis. *Cancer*, 117(1), 162–174.

Palmisano WA, Divine KK, Saccomanno G, Gilliland FD, Baylin SB, Herman JG and Belinsky SA (2000). Predicting Lung Cancer by Detecting Aberrant Promoter Methylation in Sputum. *Cancer Research*, 60(21), 5954–5958.

Parker NR, Khong P, Parkinson JF, Howell VM and Wheeler HR (2015). Molecular heterogeneity in glioblastoma: potential clinical implications. *Frontiers in Oncology*, 5, e55.

Parsons DW, Jones S, Zhan X, Cheng-Ho Lin J, Leary R, Angenendt P, Mankoo P, Carter H, Siu I-M, … Kinzler K (2008). An integrated genomic analysis of human glioblastoma multiforme. *Science*, 321(5897), 1807–1812.

Patel AP, Tirosh I, Trombetta JJ, Shalek AK, Gillespie SM, Wakimoto H, Cahill DP, Nahed B V, Curry WT, … Bernstein BE (2014). Single-cell RNA-seq highlights intratumoral heterogeneity in primary glioblastoma. *Science*, 344(6190), 1396–1401.

Petersen C, Petersen S, Milas L, Petersen C, Petersen S, Milas L, Lang FF and Tofilon PJ (2000). Enhancement of Intrinsic Tumor Cell Radiosensitivity Induced by a Selective Cyclooxygenase-2 Inhibitor. *Clinical Cancer Research*, 6(6), 2513–2520.

Phillips HS, Kharbanda S, Chen R, Forrest WF, Soriano RH, Wu TD, Misra A, Nigro JM, Colman H, … Aldape K (2006). Molecular subclasses of high-grade glioma predict prognosis, delineate a pattern of disease progression, and resemble stages in neurogenesis. *Cancer Cell*, 9(3), 157–173.

Pomp J, Wike JL, Ouwerkerk IJM, Hoogstraten C, Davelaar J, Schrier PI, Leer JWH, Thames HD and Brock WA (1996). Cell density dependent plating efficiency affects outcome and interpretation of colony forming assays. *Radiotherapy and Oncology*, 40(2), 121–125.

Prise KM and O'Sullivan JM (2009). Radiation-induced bystander signalling in cancer therapy. *Nature Reviews. Cancer*, 9(5), 351–360.

Pyonteck SM, Akkari L, Schuhmacher AJ, Bowman RL, Sevenich L, Quail DF, Olson OC, Quick ML, Huse JT, … Joyce JA (2013). CSF-1R inhibition alters macrophage polarization and blocks glioma progression. *Nature Medicine*, 19(10), 1264–1272.

Qi Q-R and Yang Z-M (2014). Regulation and function of signal transducer and activator of transcription 3. *World Journal of Biological Chemistry*, 5(2), 231–239.

Quatromoni JG and Eruslanov E (2012). Tumor-associated macrophages: function, phenotype, and link to prognosis in human lung cancer. *American Journal of Translational Research*, 4(4), 376–389.

Rardin MJ, Wiley SE, Naviaux RK, Murphy AN and Dixon JE (2009). Monitoring phosphorylation of the pyruvate dehydrogenase complex. *Analytical Biochemistry*, 389(2), 157–164.

Raso A, Vecchio D, Cappelli E, Ropolo M, Poggi A, Nozza P, Biassoni R, Mascelli S, Capra V, … Frosina G (2012). Characterization of Glioma Stem Cells Through Multiple Stem Cell Markers and Their Specific Sensitization to Double-Strand Break-Inducing Agents by Pharmacological Inhibition of Ataxia Telangiectasia Mutated Protein. *Brain Pathology*, 22(5), 677–688.

Reardon DA, Fink KL, Mikkelsen T, Cloughesy TF, O'Neill A, Plotkin S, Glantz M, Ravin P, Raizer JJ, … Nabors LB (2008). Randomized phase II study of cilengitide, an integrin-targeting arginine-glycine-aspartic acid peptide, in recurrent glioblastoma multiforme. *Journal of Clinical Oncology*, 26(34), 5610–5617.

Revet I, Feeney L, Bruguera S, Wilson W, Dong TK, Oh DH, Dankort D and Cleaver JE (2011). Functional relevance of the histone gammaH2Ax in the response to DNA damaging agents. *Proceedings of the National Academy of Sciences of the United States of America*, 108(21), 8663–8667.

Reya T, Morrison SJ, Clarke MF and Weissman IL (2001). Stem cells, cancer, and cancer stem cells. *Nature*, 414(6859), 105–111.

Reynolds B a and Vescovi AL (2009). Brain cancer stem cells: Think twice before going flat. *Cell Stem Cell*, 5(5), 466–467.

Richardson RB and Harper M (2016). Mitochondrial stress controls the radiosensitivity of the oxygen effect: Implications for radiotherapy. *Oncotarget*, [Epub ahea, e7412.

Ropolo M, Daga A, Griffero F, Foresta M, Casartelli G, Zunino A, Poggi A, Cappelli E, Zona G, … Frosina G (2009). Comparative analysis of DNA repair in stem and nonstem glioma cell cultures. *Molecular Cancer Research : MCR*, 7(3), 383–392.

Rőszer T (2015). Understanding the Mysterious M2 Macrophage through Activation Markers and Effector Mechanisms. *Mediators of Inflammation*, 2015, e816460.

Russell W and Burch R (1959). *The Principles of Humane Experimental Technique*. Retrieved from http://altweb.jhsph.edu/pubs/books/humane_exp/het-toc

Sanai N, Varez-Buylla A and Berger MS (2005). Neural stem cells and the origin of gliomas. *The New England Journal of Medicine*, 353(8), 811–822.

Sandfort V, Koch U and Cordes N (2007). Cell adhesion-mediated radioresistance revisited. *International Journal of Radiation Biology*, 83(11-12), 727–32.

Sasaki R, Aoki S, Yamato M, Uchiyama H, Wada K, Ogiuchi H, Okano T and Ando T (2010). A protocol for immunofluorescence staining of floating neurospheres. *Neuroscience Letters*, 479(2), 126–127.

Schneider M, Ströbele S, Nonnenmacher L, Siegelin MD, Tepper M, Stroh S, Hasslacher S, Enzenmüller S, Strauss G, … Halatsh M-E (2016). A paired comparison between glioblastoma "stem cells" and differentiated cells. *International Journal of Cancer*, 138(7), 1709–1718.

Schulte RR, Linkous AG, Hallahan DE and Yazlovitskaya EM (2011). Cytosolic phospholipase A2 as a molecular target for the radiosensitization of ovarian cancer. *Cancer Letters*, 304(2), 137–143.

Seystahl K, Wick W and Weller M (2016). Therapeutic options in recurrent glioblastoma-An update. *Critical Reviews in Oncology/Hematology*, 99, 389–408.

Shattil SJ, Kim C and Ginsberg MH (2010). The final steps of integrin activation: the end game. *Nature Reviews. Molecular Cell Biology*, 11(4), 288–300.

Shen Q, Wang Y, Kokovay E, Lin G, Chuang SM, Goderie SK, Roysam B and Temple S (2008). Adult SVZ Stem

Cells Lie in a Vascular Niche: A Quantitative Analysis of Niche Cell-Cell Interactions. *Cell Stem Cell*, 3(3), 289–300.

Shimizu T, Kurozumi K, Ishida J, Ichikawa T and Date I (2016). Adhesion molecules and the extracellular matrix as drug targets for glioma. *Brain Tumor Pathology*, 33(2), 97–106.

Shono T, Tofilon PJ, Bruner JM, Owolabi O and Lang FF (2001). Cyclooxygenase-2 Expression in Human Gliomas: Prognostic Significance and molecular correlations. *Cancer Research*, 61(11), 4375–4381.

Shrivastav M, De Haro LP and Nickoloff JA (2008). Regulation of DNA double-strand break repair pathway choice. *Cell Research*, 18(1), 134–147.

Singh SK, Clarke ID, Terasaki M, Bonn VE, Hawkins C, Squire J and Dirks PB (2003). Identification of a Cancer Stem Cell in Human Brain Tumors. *Cancer Research*, 63(18), 5821–5828.

Singh SK, Hawkins C, Clarke ID, Squire JA, Bayani J, Hide T, Henkelman RM, Cusimano MD and Dirks PB (2004). Identification of human brain tumour initiating cells. *Nature*, 432(7015), 396–401.

Smith-Sorensen B, Lind G, Skotheim R, Fossa S, Fodstad O, Stenwig A, Jakobsen K and Lothe R (2002). Frequent promoter hypermethylation of the O6-Methylguanine-DNA Methyltransferase (MGMT) gene in testicular cancer. *Oncogene*, 21(57), 8878–8884.

Snuderl M, Fazlollahi L, Le LP, Nitta M, Zhelyazkova BH, Davidson CJ, Akhavanfard S, Cahill DP, Aldape KD, … Iafrate a J (2011). Mosaic amplification of multiple receptor tyrosine kinase genes in glioblastoma. *Cancer Cell*, 20(6), 810–817.

Solecki DJ, Liu X, Tomoda T, Fang Y and Hatten ME (2001). Activated Notch2 signaling inhibits differentiation of cerebellar granule neuron precursors by maintaining proliferation. *Neuron*, 31(4), 557–568.

Sottoriva A, Spiteri I, Piccirillo SGM, Touloumis A, Collins VP, Marioni JC, Curtis C, Watts C and Tavaré S (2013). Intratumor heterogeneity in human glioblastoma reflects cancer evolutionary dynamics. *Proceedings of the National Academy of Sciences of the United States of America*, 110(10), 4009–4014.

Srichai MB and Zent R (2010). Integrin Structure and Function. In R. Zent & A. Pozzi (Eds.), *Cell-Extracellular Matrix Interactions in Cancer* (1st ed., pp. 19–41). New York: Springer-Verlag New York.

Stopschinski BE, Beier CP and Beier D (2013). Glioblastoma cancer stem cells - From concept to clinical application. *Cancer Letters*, 338(1), 32–40.

Strojnik T, R??sland GV, Sakariassen PO, Kavalar R and Lah T (2007). Neural stem cell markers, nestin and musashi proteins, in the progression of human glioma: correlation of nestin with prognosis of patient survival. *Surgical Neurology*, 68(2), 133–143.

Stupp R, Brada M, van den Bent MJ, Tonn JC and Pentheroudakis G (2014a). High-grade glioma: ESMO clinical practice guidelines for diagnosis, treatment and follow-up. *Annals of Oncology*, 25(Supplement 3), 93–101.

Stupp R, Hegi ME, Gorlia T, Erridge SC, Perry J, Hong YK, Aldape KD, Lhermitte B, Pietsch T, … Weller M (2014b). Cilengitide combined with standard treatment for patients with newly diagnosed glioblastoma with methylated MGMT promoter (CENTRIC EORTC 26071-22072 study): a multicentre, randomised, open-label, phase 3 trial. *The Lancet Oncology*, 15(10), 1100–1108.

Stupp R, Hegi ME, Mason WP, van den Bent MJ, Taphoorn MJ, Janzer RC, Ludwin SK, Allgeier A, Fisher B, … Mirimanoff RO (2009). Effects of radiotherapy with concomitant and adjuvant temozolomide versus radiotherapy alone on survival in glioblastoma in a randomised phase III study: 5-year analysis of the EORTC-NCIC trial. *The Lancet Oncology*, 10(5), 459–466.

Stupp R, Mason WP, van den Bent MJ, Weller M, Fisher B, Taphoorn MJ, Belanger K, Brandes AA, Marosi C, … Mirimanoff RO (2005). Radiotherapy plus concomitant and adjuvant temozolomide for glioblastoma. *The New England Journal of Medicine*, 352(10), 987–996.

Subramanian A, Tamayo P, Mootha VK, Mukherjee S, Ebert BL, Gillette M a, Paulovich A, Pomeroy SL, Golub TR, … Mesirov JP (2005). Gene set enrichment analysis: a knowledge-based approach for interpreting genome-wide expression profiles. *Proceedings of the National Academy of Sciences of the United States of America*, 102(43), 15545–15550.

Sullivan JP, Nahed B V., Madden MW, Oliveira SM, Springer S, Bhere D, Chi AS, Wakimoto H, Michael Rothenberg S, … Haber DA (2014). Brain tumor cells in circulation are enriched for mesenchymal gene expression. *Cancer Discovery*, 4(11), 1299–1309.

Svendsen CN, ter Borg MG, Armstrong RJ, Rosser a E, Chandran S, Ostenfeld T and Caldwell M a (1998). A new method for the rapid and long term growth of human neural precursor cells. *Journal of Neuroscience Methods*, 85(2), 141–152.

Szerlip NJ, Pedraza A, Chakravarty D, Azim M, McGuire J, Fang Y, Ozawa T, Holland EC, Huse JT, … Brennan CW (2012). Intratumoral heterogeneity of receptor tyrosine kinases EGFR and PDGFRA amplification in glioblastoma defines subpopulations with distinct growth factor response. *Proceedings of the National Academy of Sciences of the United States of America*, 109(8), 3041–3046.

Tamura K, Aoyagi M, Ando N, Ogishima T, Wakimoto H, Yamamoto M and Ohno K (2013). Expansion of CD133-positive glioma cells in recurrent de novo glioblastomas after radiotherapy and chemotherapy. *Journal of Neurosurgery*, 119(5), 1145–1155.

TCGA network (2008). Comprehensive genomic characterization defines human glioblastoma genes and core pathways. *Nature*, 455(7216), 1061–1068.

Thotala D, Craft JM, Ferraro DJ, Kotipatruni RP, Bhave SR, Jaboin JJ and Hallahan DE (2013). Cytosolic PhospholipaseA2 Inhibition with PLA-695 Radiosensitizes Tumors in Lung Cancer Animal Models. *PLoS ONE*, 8(7), e69688.

Tirino V, Desiderio V, d'Aquino R, De Francesco F, Pirozzi G, Graziano A, Galderisi U, Cavaliere C, De Rosa A, … Giordano A (2008). Detection and characterization of CD133+ cancer stem cells in human solid tumours. *PloS One*, 3(10), e3469.

Tomida M, Ohtake H, Yokota T, Kobayashi Y and Kurosumi M (2008). Stat3 up-regulates expression of nicotinamide N-methyltransferase in human cancer cells. *Journal of Cancer Research and Clinical Oncology*, 134(5), 551–559.

Trusolino L, Bertotti A and Comoglio PM (2001). A signaling adapter function for α6 β4 integrin in the control of HGF-dependent invasive growth. *Cell*, 107(5), 643–654.

Tu WZ, Li B, Huang B, Wang Y, Liu XD, Guan H, Zhang SM, Tang Y, Rang WQ and Zhou PK (2013). γH2AX foci formation in the absence of DNA damage: Mitotic H2AX phosphorylation is mediated by the DNA-PKcs/CHK2 pathway. *FEBS Letters*, 587(21), 3437–3443.

Valente V, Teixeira S a, Neder L, Okamoto OK, Oba-Shinjo SM, Marie SKN, Scrideli C a, Paçó-Larson ML and Carlotti CG (2009). Selection of suitable housekeeping genes for expression analysis in glioblastoma using quantitative RT-PCR. *BMC Molecular Biology*, 10, e17.

Valerie K, Yacoub A, Hagan MP, Curiel DT, Fisher PB, Grant S and Dent P (2007). Radiation-induced cell signaling: inside-out and outside-in. *Molecular Cancer Therapeutics*, 6(3), 789–801.

Verhaak RGW, Hoadley K a, Purdom E, Wang V, Qi Y, Wilkerson MD, Miller CR, Ding L, Golub T, … TCGA network (2010). Integrated genomic analysis identifies clinically relevant subtypes of glioblastoma characterized by abnormalities in PDGFRA, IDH1, EGFR, and NF1. *Cancer Cell*, 17(1), 98–110.

Vescovi AL, Galli R and Reynolds B a (2006). Brain tumour stem cells. *Nature Reviews. Cancer*, 6(6), 425–436.

Villanueva MT (2012). United colors of glioblastoma. *Nature Reviews. Clinical Oncology*, 9(2), 68.

Visvader JE and Lindeman GJ (2008). Cancer stem cells in solid tumours: accumulating evidence and unresolved questions. *Nature Reviews Cancer*, 8(10), 755–768.

Vlashi E, Lagadec C, Vergnes L, Matsutani T, Masui K, Poulou M, Popescu R, Della Donna L, Evers P, … Pajonk F (2011). Metabolic state of glioma stem cells and nontumorigenic cells. *Proceedings of the National Academy of Sciences of the United States of America*, 108(38), 16062–16067.

Walker M, Alexander E, Hunt WE, MacCarty CS, Mahaley MS, Mealey J, Norrell H a, Owens G, Ransohoff J, … Strike T (1978). Evaluation of BCNU and/or radiotherapy in the treatment of anaplastic gliomas. A cooperative clinical trial. *Journal of Neurosurgery*, 49(3), 333–343.

Walker M, Strike T and Sheline G (1979). An analysis of dose-effect relationship in the radiotherapy of malignant gliomas. *International Journal of Radiation Oncology, Biology, Physics*, 5(10), 1725–1731.

Walker SR, Xiang M and Frank DA (2014). STAT3 activity and function in cancer: Modulation by STAT5 and mir-146b. *Cancers*, 6(2), 958–968.

Wang H, Lathia JD, Wu Q, Wang J, Li Z, Heddleston JM, Eyler CE, Elderbroom J, Gallagher J, … Rich JN (2009). Targeting Interleukin 6 Signaling Suppresses Glioma Stem Cell Survival and Tumor Growth. *Stem Cells*, 27(10), 2393–2404.

Wang J, Duncan D, Shi Z and Zhang B (2013). WEB-based GEne SeT AnaLysis Toolkit (WebGestalt): update 2013. *Nucleic Acids Research*, 41(Web Server issue), 77–83.

Wang J, Sakariassen P, Tsinkalovsky O, Immervoll H, Bøe SO, Svendsen A, Prestegarden L, Røsland G, Thorsen F, … Enger P (2008). CD133 negative glioma cells form tumors in nude rats and give rise to CD133 positive cells. *International Journal of Cancer*, 122(4), 761–768.

Wang L, Long L, Wang W and Liang Z (2015). Resveratrol, a potential radiation sensitizer for glioma stem cells both in vitro and in vivo. *Journal of Pharmacological Sciences*, 129(4), 216–225.

Wang T, Niu G, Kortylewski M, Burdelya L, Shain K, Zhang S, Bhattacharya R, Gabrilovich D, Heller R, … Yu H (2004). Regulation of the innate and adaptive immune responses by Stat-3 signaling in tumor cells. *Nature Medicine*, 10(1), 48–54.

Warburg O (1925). The Metabolism of Carcinoma Cells. *Journal of Cancer Research*, 9(1), 148–163.

Warburg O (1956). On Respiratory Impairment in Cancer Cells. *Science*, 124(3215), 269–270.

Warburg O, Wind F and Negelein E (1927). The metabolism of tumors in the body. *The Journal of General Physiology*, 8(6), 519–530.

Weller M, van den Bent M, Hopkins K, Tonn JC, Stupp R, Falini A, Cohen-Jonathan-Moyal E, Frappaz D, Henriksson R, … Wick W (2014). EANO guideline for the diagnosis and treatment of anaplastic gliomas and glioblastoma. *The Lancet Oncology*, 15(9), 395–403.

Wen PY and Kesari S (2008). Malignant gliomas in Adults. *The New England Journal of Medicine*, 359(5), 492–507.

Wolf A, Agnihotri S and Guha A (2010). Targeting Metabolic Remodeling in Glioblastoma Multiforme. *Oncotarget*, 1(7), 552–577.

Woodfin A, Beyrau M, Voisin MB, Ma B, Whiteford JR, Hordijk PL, Hogg N and Nourshargh S (2016). ICAM-1-expressing neutrophils exhibit enhanced effector functions in murine models of endotoxemia. *Blood*, 127(7), 898–907.

Wu Y, Siadaty MS, Berens ME, Hampton GM and Theodorescu D (2008). Overlapping gene expression profiles of cell migration and tumor invasion in human bladder cancer identify metallothionein 1E and nicotinamide N-methyltransferase as novel regulators of cell migration. *Oncogene*, 27(52), 6679–6689.

Xu K, Wang L and Shu H-KG (2014). COX-2 overexpression increases malignant potential of human glioma cells through Id1. *Oncotarget*, 5(5), 1241–1252.

Yan H, Parsons DW, Jin G, McLendon R, Rasheed BA, Yuan W, Kos I, Batinic-Haberle I, Jones S, … Bigner DD (2009). IDH1 and IDH2 Mutations in Gliomas. *The New England Journal of Medicine*, 360(8), 765–773.

Yang YP, Chang YL, Huang PI, Chiou GY, Tseng LM, Chiou SH, Chen MH, Chen MT, Shih YH, … Chang CJ (2012). Resveratrol suppresses tumorigenicity and enhances radiosensitivity in primary glioblastoma tumor initiating cells by inhibiting the STAT3 axis. *Journal of Cellular Physiology*, 227(3), 976–993.

Yazlovitskaya EM, Linkous a G, Thotala DK, Cuneo KC and Hallahan DE (2008). Cytosolic phospholipase A2 regulates viability of irradiated vascular endothelium. *Cell Death and Differentiation*, 15(10), 1641–1653.

Yeaman SJ, Hutcheson ET, Roche TE, Pettit FH, Brown JR, Reed LJ, Watson DC and Dixon GH (1978). Sites of phosphorylation on pyruvate dehydrogenase from bovine kidney and heart. *Biochemistry*, 17(12), 2364–2370.

Yi L, Xiao H, Xu M, Ye X, Hu J, Li F, Li M, Luo C, Yu S, … Feng H (2011). Glioma-initiating cells: A predominant role in microglia/macrophages tropism to glioma. *Journal of Neuroimmunology*, 232(1-2), 75–82.

Young L, Sung J, Stacey G and Masters JR (2010). Detection of Mycoplasma in cell cultures. *Nature Protocols*, 5(5), 929–934.

Yu H, Lee H, Herrmann A, Buettner R and Jove R (2014). Revisiting STAT3 signalling in cancer: new and unexpected biological functions. *Nature Reviews Cancer*, 14(11), 736–746.

Yu K-R, Yang S-R, Jung J-W, Kim H, Ko K, Han DW, Park S-B, Choi SW, Kang S-K, … Kang K-S (2012). CD49f enhances multipotency and maintains stemness through the direct regulation of OCT4 and SOX2. *Stem Cells*, 30(5), 876–87.

Zeppernick F, Ahmadi R, Campos B, Dictus C, Helmke BM, Becker N, Lichter P, Unterberg A, Radlwimmer B and Herold-Mende CC (2008). Stem cell marker CD133 affects clinical outcome in glioma patients. *Clinical Cancer Research*, 14(1), 123–129.

Zhou B-BS, Zhang H, Damelin M, Geles KG, Grindley JC and Dirks PB (2009). Tumour-initiating cells: challenges and opportunities for anticancer drug discovery. *Nature Reviews. Drug Discovery*, 8(10), 806–823.